The properties of galaxies in supercluster filaments

by
Scott Clive Porter

A Thesis submitted to
The University of Birmingham
for the degree of
Doctor of Philosophy

Astrophysics and Space Research Group
School of Physics and Astronomy
University of Birmingham
England

October 2006

Synopsis

Superclusters appear as large-scale structures in the form of a network of filaments, and can be up to $100\,h_{100}^{-1}$ Mpc in extent. In this dissertation, we investigate in detail the spatial structure of the three richest superclusters of galaxies closer to us then z=0.1.

We investigate the rate of star formation in galaxies at various positions among the filaments and clusters in the Pisces-Cetus Supercluster. We use an index of star formation derived from a principal component analysis of optical spectra. We have shown that galaxies which are members of these filaments, show a steady decline in star formation rate, from the periphery of a cluster, into the cluster core. However, on top of this trend, we find a nearly instantaneous enhancement of the rate of star formation at $\sim 3\,h_{70}^{-1}$ Mpc from its centre. We conclude that the most likely reason for this sudden enhancement in star formation rate is galaxy-galaxy harassment. Further work shows that the enhancement in star formation occurs mainly in the infalling dwarf galaxies ($-20 < M_B < -17.5$) and that there is little evidence that the tidal effect of the dark matter haloes of the clusters is responsible for the enhanced star formation.

The results of an anaylsis performed on a larger ensemble of 52 filaments were consistent with the those from our smaller sample drawn from the Pisces-Cetus supercluster.

We conclude this study with the analysis of a sample of spectra from the 6dF redshift survey. In the absence of spectrophotometric calibration, for these galaxies we were only able to obtain an uncalibrated star formation rate, but we could examine the effect of correction due to dust extinction, and could separate the star-forming galaxies from the active galactic nuclei. From our small sample, there was interesting evidence of enhanced star formation in galaxies at similar distances from the centres of the clusters in the Shapley Supercluster.

Acknowledgements

Over the course of my PhD I have received help and support from a range of people, but my foundation of strength has come from my parents as it has throughout my life. They supported me both financially and emotionally throughout my degree and PhD and have always encouraged without applying pressure. Without them I would never have completed this work. I would also like to say a massive thank you to my supervisor Dr Somak Raychaudhury for his constant support and inspiration. He has always been able to pull me forwards when everything seemed to be going wrong and re-light the fires of determination to continue. I am indebted to Philip Lah for his contribution of 6dF spectroscopic data and Kevin Pimbblet for sharing with us his work on filaments in the 2dFGRS. I am also grateful to Stuart Aston, Stephen Fletcher and Robert Satchwell for their support and friendship which helped pull me through my degree. Going further back I would like to thank my A level mathematics teachers at Stourbridge College, Shangara Baines and Lhaktar Dhaga. When others had told me to quit, they believed in me and their efforts, above and beyond the call of duty, enabled me to continue my education. I would also like to mention the other inhabitants of G27 and members of the extragalactic group for their scientific advice and discussions on football and cricket which always lightened a day of programming. Finally I would like to thank all the members of Astrosoc over the years and the committee members I served with. They provided a much needed distraction from the technical side of astrophysics and enabled me to see the beauty of the Universe I was studying.

Publications

Publications in Refereed Journals

1. The Pisces-Cetus Supercluster a remarkable filament of galaxies in the 2dF Galaxy Redshift and Sloan Digital Sky surveys: Scott C. Porter and Somak Raychaudhury, 2005, MNRAS, 364, 1387-1396 (astro-ph/0511050). (This paper is integrated into chapters 3 and 4)

2. Star formation in galaxies along the Pisces-Cetus Supercluster filaments: Scott C. Porter and Somak Raychaudhury, 2006, MNRAS, accepted, (astro-ph/0612357). (This paper is integrated into chapter 4)

3. Star formation properties of galaxies in supercluster filaments in the 2dF Galaxy Redshift Survey: Scott C. Porter, Somak Raychaudhury and Kevin A. Pimbblet, in preparation. (This paper is integrated into chapter 5) [Kevin Pimbblet contributed the initial filament catalogue]

Publications in Contributed Conference Proceedings

1. The Pisces-Cetus Supercluster: the largest filament of galaxies in the 2dF-GRS region, Scott C. Porter and Somak Raychaudhury 2004, abstract in the proceedings of the RAS National Astronomy Meeting, Milton Keynes, April 2004.

2. Enhanced star formation in group galaxies in the Pisces-Cetus supercluster: Scott C. Porter and Somak Raychaudhury, 2005, abstract in the proceedings of the RAS National Astronomy Meeting, Birmingham, April 2005.

3. Star formation properties in Supercluster Filaments: Somak Raychaudhury and Scott C. Porter, 2005, abstract, Bulletin of the American Astronomical Society, 207, 177.15

Contents

List of Figures

List of Tables

Chapter 1

Captain James Cook: "I had ambition not only to go farther than any man had ever been before, but as far as it was possible for a man to go."

Introduction

Throughout history humans have become more and more aware of the universe in which they live. Boundaries have moved beyond the hunting grounds of ancient times, expanded beyond the horizon by explorers who dared to go where "here be dragons" marked the map. Today we have gone beyond the bounds of our little blue planet and out into the depths of space. Our vision has advanced out beyond our solar system, out through the billions of stars of the Milky Way, to gaze upon Andromeda and the other galaxies that form the local group. Then even further we are drawn out into a universe of other groups of galaxies, huge clusters of galaxies and a massive network of filaments linking them all together. Finally we arrive at superclusters of galaxies. These are massive chains of clusters of galaxies linked by filaments of galaxy groups and individual galaxies.

The term supercluster has been used to denote various entities in literature (see § 1.3). However, in this thesis we define the term to denote Large-scale structures that are much larger than the virial radii of individual rich clusters ($\gtrsim 10\,h_{70}^{-1}$ Mpc).

Observations and simulations of the large-scale structure of the Universe have revealed the presence of a network of filaments and voids in which most galaxies seem to be found (Zucca et al., 1993; Einasto et al., 1994; Jenkins et al., 1998). This implies that that the Universe is not homogeneous on scales below $\sim 100\,h_{70}^{-1}$ Mpc (Bharadwaj, Bhavsar, & Sheth, 2004; Shandarin, Sheth, & Sahni, 2004), which is the scale of the largest common structures of galaxies, though the discovery of structures

far larger than these have been claimed (e.g., Brand et al., 2003; Miller et al., 2004).

Perturbations on the scale of superclusters are likely to still be in a linear growth regime and have not yet reached equilibrium, or to have only recently left the linear growth regime. If this is the case they have yet to condense out of the Hubble expansion and can be analytically tractable containing valuable information about the processes that occurred during their formation. Superclusters are an essential tool to study the largest-scale density perturbations that have given rise to structure in the Universe (e.g., Bahcall, 2000). They can be useful in quantifying the the high-end mass function of collapsing systems and ratio of mass to light on the largest scales, thus being useful in discriminating between dark matter and structure formation models (e.g., Kolokotronis, Basilakos, & Plionis, 2002; Bahcall, 1988).

1.1 Structure formation

When the universe was much younger than it is now it was smoother and denser. Superposed on this smooth background were small fluctuations in the density of matter and the temperature of the Cosmic Microwave Background (CMB). According to the most popular current theory, initial Gaussian density perturbations in the primordial universe lead to the formation of structure on different scales as the universe expanded. The linear theory of gravitational instability shows that density perturbations grow at best in proportion to the expansion factor of the universe. As the universe has expanded by a factor of approximately 1000 since the decoupling of radiation and matter at recombination, density perturbations can only have grown by a factor of about 1000 since this time. Therefore, the fluctuations should be detectable as small-scale anisotropies in the cosmic microwave background radiation. This is indeed the case and such anisotropies have been observed by COBE (Smoot et al., 1992) and more recently the Wilkinson Microwave Anisotropy Probe, WMAP (Bennett et al., 1997), which used differential microwave radiometers to measure temperature differences between two points on the sky.

1.1.1 The power spectrum

The cosmological density perturbations or matter overdensities are specified by the quantity:

$$\delta(x) = \frac{\rho(x) - \langle\rho\rangle}{\langle\rho\rangle}, \tag{1.1}$$

where $\langle\rho\rangle$ is the mean density of the universe and $\rho(x)$ is the mass density at position x.

These spherically overdense regions in the otherwise uniform density universe will start off decreasing in density at almost the same rate as the rest of the universe, following linear theory. However, the density gradually stops decreasing and then starts to increase radically when a critical density is reached. For $\delta(x) \ll 1$, the region is in the linear regime and it is possible to analytically model the collapse. However, for $\delta(x) \gtrsim 1$ the collapse is in the non-linear regime and becomes too complicated to model analytically and numerical simulations are needed. Superclusters have been shown to have overdensities of the order of 2 or 3 (e.g., Fabian, 1991; Fleenor et al., 2005) over scales of larger than $20\,h_{70}^{-1}$ Mpc and will therefore have only recently have left the linear regime.

Fluctuations in the CMB

The fluctuations in the smooth background must have been created by some kind of mechanism. The only mechanism which fits with todays observations is inflation, which refers to a period of exponential expansion of the universe which occurred soon after the Big Bang (e.g., Albrecht et al., 1982). This process solves two major problems, that of the flatness problem and the horizon problem. The rapid inflation of the universe would have smoothed out spacetime allowing the flat universe we see today. At the same time it explains how regions that are on opposite sides of the universe today could once have been close enough to have been in communication allowing for their almost identical CMB conditions. It also allows for seed fluctuations for galaxy formation to have originated from quantum fluctuations that were

then inflated to a macroscopic scale.

1.1.2 The growth of perturbations

The initial Gaussian density perturbations are assumed to have a power-law spectrum,

$$P_i(k) = Ak^n, \tag{1.2}$$

where n is the spectral index and $k = 2\pi/L$, where L is the size of the perturbation.

Zel'Dovich (1970) approximated the perturbations to be scale invariant or grow at the same rate as the universe. This led to the Harrison-Zeldovich spectrum, with $n = 1$,

$$P(k) \propto k. \tag{1.3}$$

Recent observations by WMAP, have shown the actual value of n in a flat Λ dominated universe, to be remarkably close to the Harrison-Zeldovich approximation with a value of 0.99 ± 0.04 (Spergel et al., 2003).

The power spectrum at any given time depends on this initial power spectrum and the transfer function which describes how the initial power spectrum is modified over time by the physical processes present in the universe. Thus the power spectrum at a given time in its dimensionless form is described by,

$$\Delta^2(k) = k^{n+3}\, T^2(k,t), \tag{1.4}$$

where $T(k,t)$ is the transfer function. The amplitude of the perturbations will continue to grow with time with the shape of the initial spectrum being maintained in the linear regime. When δ approaches unity on a scale of size L the region collapses and becomes non-linear, where $\rho = \rho_0(1+\delta)$, ρ being the density of the region and ρ_0 the mean density of the universe.

The Press-Schechter formalism

As mentioned above, the non-linear phases of collapse of the matter are too complex to allow completely analytic solutions. Press & Schechter (1974) created a simplified analytic approach where structure has formed hierarchically from initial Gaussian fluctuations. They adopted initially overdense regions that would expand at the same rate as the density of the rest of the universe until z approaches z_{vir}, the redshift at which the region starts to collapse and becomes virialised. At this time the region will start to free fall until it collapses to a point. They formulate an equation which tracks the evolution of the density across regions containing a mass M on average. This results in an analytical solution where the form of the mass distribution remains constant, even as the scale of the collapsing objects increases. This is shown in Eq. 1.5 which defines the fraction of mass f_g that is in virialised structures exceeding mass M at a given redshift.

$$f_g(M, z) = \mathrm{erfc}\left[\frac{(1+z)\delta_c}{\sqrt{2}\sigma(M, 0)}\right], \tag{1.5}$$

where erfc is a complementary error function, δ_c is the critical overdensity and σ is the r.m.s mass fluctuation over the spherical region containing the mass M

1.2 Dark matter and cosmological models

It has now become obvious that that the luminous matter in the universe only makes up a very small percentage of the mass in the universe. Observations as far back as 1933 (Zwicky, 1933) showed that the coma cluster had insufficient mass to explain the velocity dispersion of the galaxies. Further evidence came in the form of the rotation curves of galaxies. Rubin & Ford (1970) showed that rather than rising to a peak velocity then dropping as predicted the rotation curve of Andromeda was in fact flat out to large radii. This has been confirmed for many other galaxies of varying morphology. More recently X-ray derived masses of clusters of galaxies and those from gravitational lensing have confirmed the presence of an excess of mass over that which can be explained from optical observations. The additional

missing mass is referred to as dark matter. Dark matter plays an important role in the formation of structure as its gravitational influence dominates that of the other components for most of the life of the universe. It is therefore essential to understand the properties, amount and distribution of dark matter before large scale structure can be explained. Dark matter is the dominant influence on the form that the transfer function and hence the power spectrum described by Eq. 1.4 takes.

A possible candidate for dark matter is massive astrophysical compact halo objects (MACHOs) such as brown dwarfs and neutron stars. These like the luminous matter in the universe are baryonic. However, due to constraints on the contribution of baryons to the critical density Ω_b imposed by Big Bang Nucleosynthesis (e.g., Burles, Nollett, & Turner, 2001) only a small fraction can be baryonic ($\Omega_b h^2 = 0.020 \pm 0.002$). Therefore, models were proposed that incorporated non-baryonic matter in structure formation.

Each of the model types results in a unique form of the power spectrum which in turn, if correct should describe the universe that we observe today. Examples of the forms taken by two possible models are shown in Fig. 1.1. The actual power spectrum of the universe can be found by using the two point correlation function of galaxies in large scale galaxy surveys, e.g., the APM Galaxy survey (Maddox et al., 1990) and compared with dark matter models.

1.2.1 Hot Dark Matter

Hot dark matter (HDM) consists of particles that decouple when relativistic. These particles have a number density roughly equal to that of the microwave background photons. To remain relativistic for longer periods requires their masses to be less than $\approx$ 100 eV. A major advantage of HDM is that it has a definite candidate in the neutrino which had been suggested to oscillate from one species to another and hence have non-zero mass (Fukuda et al., 1998). The major problem with HDM is that in the early universe most of the matter density would have been due to neutrinos. At this time their speeds would have been too great to be caught in any overdense regions. Therefore, density fluctuations could only appear after the universe had expanded enough to let the neutrinos cool and slow down. This

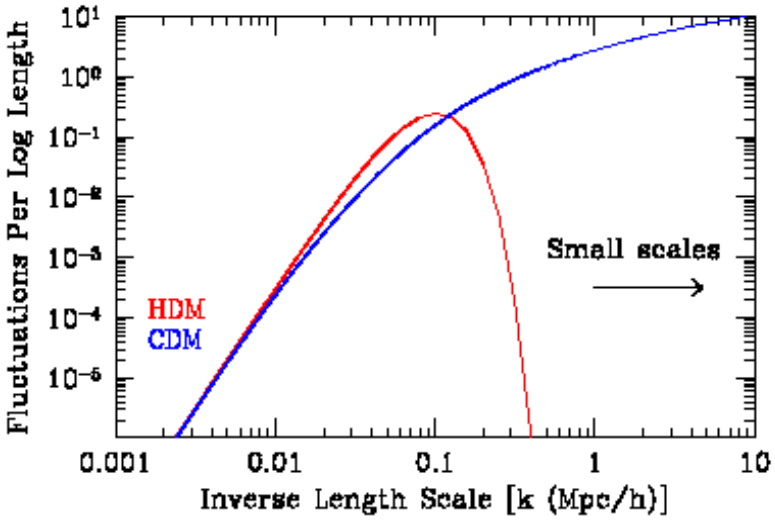

Figure 1.1: The power spectrum of density perturbations as a function of scale size for the standard HDM and CDM models. (White, 2006). (§1.2)

means that the HDM model would have insufficient power on small scales, i.e., less small scale structure than that observed (e.g., White, Frenk, & Davis, 1983; White, Davis, & Frenk, 1984; Zeng & White, 1991). This can be seen in Fig. 1.1 where the HDM peaks for values of approximately $k = 0.1$ which corresponds to scales of $L \sim 10\,h^{-1}$ Mpc. For scales smaller than $10\,h^{-1}$ Mpc the HDM model rapidly loses power and predicts no structures at scales of a few h^{-1} Mpc or less, excluding galaxy size structures at the current epoch. The power spectrum changes over time, with structures forming when a certain threshold of power is exceeded. It can be seen that the first part of the HDM model to pass a threshold will be at its peak value, at approximately $k = 0.1$ and so structures of approximately 10 Mpc will be formed first. At all times there will be more large scale structure due to the gradual slope towards low values of k, compared with the steep slope at higher values of k. Thus HDM is a top down model with larger structures forming first.

Cold Dark Matter

Cold dark matter dominated universes (CDM) have been extensively modelled with the use of N-body simulations and show a bottom-up structure formation (e.g., Peebles, 1982). The most likely candidates for non-baryonic CDM are Weakly in-

teracting massive particles (WIMPS) such as neutralinos, gravitinos, photinos and higgsinos predicted by supersymmetric theories. Structure grows out of Gaussian fluctuations with the scale invariant spectrum proposed by Harrison and Zeldovich , see equation (1.3). The perturbations in the CDM begin to grow at the epoch of matter-radiation equality but are unstable prior to decoupling. Only after recombination can the perturbations in the baryons begin to grow by falling into the CDM potential wells. As material continues to flow into the density fluctuation, the fluctuation continues to grow in size and accrete more matter. Galaxies are eventually made by the coalescence of larger and larger clumps of matter, and later clusters and superclusters of galaxies form as the gravitational clustering continues. Thus the smallest structures are made first and a bottom up formation is observed. This can be seen in Fig. 1.1 where the CDM model has no peak and the highest point in the model is for high values of k. As the power spectrum evolves over time, this point at high values of k will be the first to exceed the power threshold needed for structure to form and so the smallest structures will form first. One of the greatest successes of this model is its ability to produce structures with masses ranging from small galaxies to those of rich clusters with simulations being indistinguishable from surveys. This success is only possible though if the galaxies and the dark matter are distributed differently (see §1.2.4). However, CDM does have its problems which include an excess of faint galaxies at low luminosities and a lack of power on large scales ($> 10\,h^{-1}$ Mpc), i.e. less large scale structure than is seen (Davis et al., 1992, e.g.,). The lack of power can be seen in Fig. 1.1 where the power of the CDM model has dropped by a factor of nearly 10^6 from that of scales of a few h^{-1} Mpc by the time it reaches scales $> 10\,h^{-1}$ Mpc. The lack of power can be solved in three main ways:

1. Reducing the the mean mass density, thus reducing Ω which forms part of the transfer equation. However, without another parameter in the universe the value of Ω can't be reduced and still be consistent with a flat universe and CMB fluctuations. This can however, be solved with the introduction of Dark Energy (see §1.2.3).

2. Tilting the initial power spectrum by changing the spectral index, n (Lidsey,

1994).

3. CDM and HDM to get warm dark matter (Colín, Avila-Reese, & Valenzuela, 2001)(see §1.2.2).

1.2.2 Warm Dark Matter

Warm dark matter (WDM), is a simple modification to the CDM model where the dark matter particles have an initial kinetic energy. WDM particles have masses of $\sim$ 1 keV compared to $\sim$ 1 GeV in CDM and $\sim$ 10 keV in HDM models. The higher velocities than the CDM particles leads to a smoothing out of small-scale fluctuations and hence the number of small haloes formed is suppressed reducing the excess of small scale structures found in CDM. However WDM retains enough of the CDM characteristics to allow for early structure formation on small scales. However, achieving this balance on large and small scales puts stringent limits on the mass of the various neutrino species.

1.2.3 Cold Dark Matter with Dark Energy

Data from sources such as cosmic microwave background (CMB) (e.g., Spergel et al., 2003), measurements of the brightness of distant supernovae (e.g., Perlmutter et al., 1999) and the abundance of present day of massive galaxy clusters (e.g., Bahcall & Fan, 1998) to name just a few are all suggesting a universe where matter only makes up less than 30% of the critical density ($\Omega_M < 0.3$). A dark energy component ($\Omega_\Lambda < 0.3$) accounts for the other 70% and maintains a flat cosmology. Λ cold dark matter models ΛCDM are also most commonly considered in the scale invariant spectrum of density perturbations proposed by Harrison and Zeldovich. Some of the CDM is replaced with a cosmological constant Λ but a flat geometry such that $\Omega = \Omega_m + \Omega_\Lambda = 1$ is maintained. The latest values from WMAP finds $\Omega_m h^2 = 0.14 \pm 0.02$, $\Omega_b h^2 = 0.024 \pm 0.001$ and $h = 0.72 \pm 0.05$ (Spergel et al., 2003). Therefore, further models must be created to incorporate the new data. (Efstathiou, Sutherland, & Maddox, 1990, e.g.,). A ΛCDM model due to its lower value of Ω_m is able to predict more large scale structure than the standard CDM model. With

the current best values from WMAP of $\Omega_m = 0.27$ and $h = 0.72$, structures of over $70\,h^{-1}$ Mpc are possible, better recreating supercluster sized structure.

1.2.4 Bias

Bias is a measure of how well the observed large scale structure such as galaxies, clusters and superclusters trace the underlying mass distribution from models. The concept of bias was first introduced by Kaiser (1984) to explain the clustering properties of Abell clusters. An object of a certain mass will collapse at an early time if it is a region of a peak in the initial density field. So galaxies forming in these overdense regions will form sooner and hence there will be an enhanced abundance of these galaxies. They will be more clustered and show increased bias. In the linear regime, where density fluctuations are small the mass overdensity and the galaxy overdensity can be related by the linear bias parameter b, where,

$$\left(\frac{\delta\rho}{\rho}\right)_{galaxies} = b\left(\frac{\delta\rho}{\rho}\right)_{mass}. \tag{1.6}$$

Hence, observations of clustering on large scales only allow us to determine the mass fluctuations if we know the value of b. Lahav et al. (2002), using 2dF Galaxy Redshift Survey (2dFGRS) and CMB data in a ΛCDM universe, find that optically selected galaxies are almost unbiased, with $b \sim 0.96$. However, Simon et al. (2004) find that galaxies are less clustered than the total matter, and thus are anti-biased, demonstrating that biasing is still an open subject.

1.2.5 Peculiar velocities

The high intensity activity in the study of the large scale motions in the universe was launched by the finding of the "seven samurai" (Burstein et al., 1986) that the Local Group participates in a large streaming motion. Under the assumption that fluctuations are linear, the continuity equation, the Euler equation of motion and the Poisson field equation can be used to to obtain the relation between density and velocity, given by:

$$\bigtriangledown \cdot \upsilon = -\Omega_m^{0.6}\ \delta_m, \tag{1.7}$$

where $\delta_m = (\delta\rho/\rho)_{mass}$ is the mass density contrast, υ is the peculiar velocity and Ω_m is the mass density parameter. This relation can be used to predict peculiar velocity fields from the galaxy density fields of all-sky redshift surveys and this can be compared with measured peculiar velocities. From these comparisons a dimensionless quantity, $\beta = \Omega_m^{0.6}/b$ is obtained. The redshift surveys used now usually result in regions of over 100 h^{-1} Mpc being studied. Such large regions should still be in the linear regime and so the linear fluctuation assumptions are valid. With the value of Ω_m being tightly constrained by WMAP these studies can give an estimate of the bias, b, over large scales. Radburn-Smith, Lucey, & Hudson (2004) used the peculiar velocities of type 1a supernovae to obtain $\beta = 0.55 \pm 0.06$, while Hudson et al. (2004) obtain a lower value of $\beta = 0.39 \pm 0.17$ from the study of the streaming motions of Abell clusters.

1.2.6 N-body simulations

As mentioned earlier when a region leaves the linear regime it is no longer possible to analytically predict its evolution and hence numerical simulations are needed. The Virgo consortium used the Millennium simulation of over 10^{10} particles to trace the evolution of the matter distribution in a ΛCDM universe (Springel, 2005). The model used a ΛCDM model with $\Omega_{dm} = 0.205$, $\Omega_b = 0.045$, $\Omega_\Lambda = 0.75$, $h = 0.73$ and an initial spectral index of $n = 1$. This has resulted in a sufficient mass resolution over volumes similar to those of the large redshift surveys (2dFGRS, SDSS) to allow direct comparisons with observations. The simulation volume was a box of 500 h^{-1} Mpc which resulted in the 10 billion particles, each having a mass of $8.6 \times 10^8\ h^{-1}\mathrm{M}_\odot$. This was enough for dwarf galaxies ($L > 0.1L_*$) to be represented by approximately 100 particles, galaxies like the Milky way by approximately 1000 particles and rich clusters of galaxies several million particles.

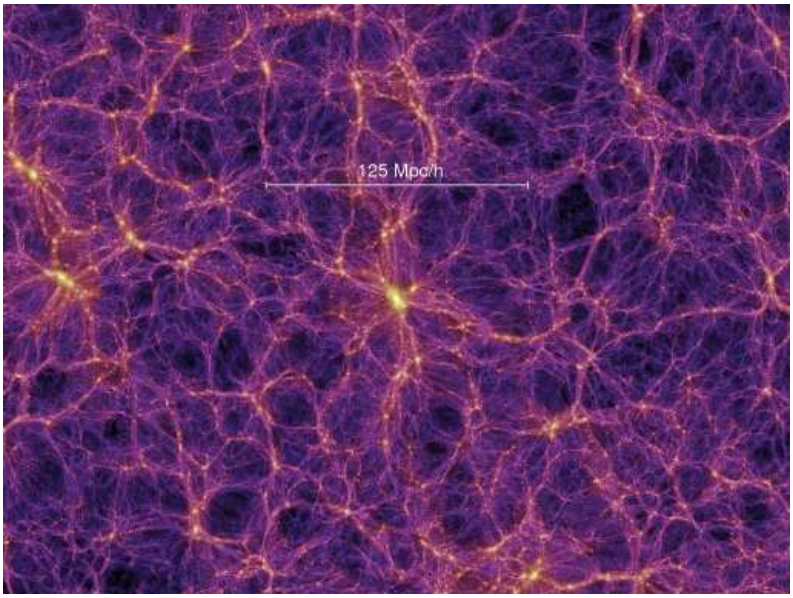

Figure 1.2: The distribution of dark matter in a $15\,h^{-1}$ Mpc thick slice at a redshift of zero from the millennium simulation. The intensity shows the surface density with the brightest regions being the densest. The linear scale is shown by the bar. (§1.2.6)

1.3 The definition of a supercluster

The term supercluster has been used to describe structures from just a couple of clusters separated by just a few h_{70}^{-1} Mpc (e.g., the A1367-Coma supercluster, Gavazzi et al., 1998) up to structures larger than our ours (Brand et al., 2003), spanning distances of 100 h_{70}^{-1} Mpc or more. In this thesis our superclusters are defined in the supercluster catalogue of Raychaudhury et al. (2007). These superclusters have been defined with the use of a minimal spanning tree (MST) algorithm with a maximum linking length of 20 h_{100}^{-1} Mpc (i.e. no links between adjacent clusters on the tree larger than 20 h_{100}^{-1} Mpc are considered). This length is approximately where the cluster-cluster correlation function becomes one, i.e. the length scale at which there is no clustering above that of a random sample. Even on slightly larger scales, say, at 25 h_{100}^{-1} Mpc, the correlation function has the same value, but the detailed structure of the supercluster changes. Raychaudhury et al. (2007) considers both 20 h_{100}^{-1} Mpc and 25 h_{100}^{-1} Mpc as maximum linking length, and produces two different catalogues. An example of this is the Pisces-Cetus supercluster which consists of two unlinked parts of 5 and 11 clusters when a linking length of 20 h_{100}^{-1} Mpc is used.

This however increases to one large supercluster of 19 members if the 25 h_{100}^{-1} Mpc links are used. The linking length of 25 h_{100}^{-1} Mpc results in superclusters which have a maximum size of the order 100 h_{70}^{-1} Mpc. It is therefore important to know at which size superclusters become just a random collection of galaxies rather than a statistically significant structure.

Pandey & Bharadwaj (2005) use SDSS data to find the maximum length of filament which is statistically significant. They take a volume limited sample over the redshift range $0.08 \leq z \leq 0.2$, extinction corrected Petrosian r band apparent magnitude $14.5 \leq m_r \leq 17.5$ and absolute magnitude range $-22.6 \leq M_r \leq -21.6$. This results in 5315 galaxies distributed in two wedges, spanning 91 degrees (NGP) and 65 degrees (SGP) in RA. and thickness 2 degrees.

They use a technique where the 2D galaxy distribution is embedded in a 1 h_{100}^{-1} Mpc by 1 h_{100}^{-1} Mpc rectangular grid. Grid cells having a galaxy within them are termed as filled (assigned a value of 1) and those without a galaxy present are termed as empty (assigned a value of 0). The filamentarity of a cluster is defined based on a single 2D "shapefinder" statistic (Bharadwaj et al., 2000), where a value of 1 is a filament, a value of 0 is a square and the values change from 0 to 1 as a square is deformed into a filament. They then use a statistical technique called shuffle to determine the largest scale length at which the filamentarity is significant.

The shuffle technique involves taking squares with sides of length L. These squares are then randomly interchanged, thus destroying structures larger than L but maintaining those smaller than L. For a fixed value of L, if the shuffled data has an average filamentarity lower than the initial data then the original data had more filaments with length longer than L. They calculate the difference in the filamentarity of the shuffled and original cluster data (χ^2 per degree of freedom) at each value of L. They find that shuffling the data with L>90 h_{100}^{-1} Mpc does not result in a significant difference in the filamentarity of the two samples. Therefore, the longest filament which is statistically significant is 80 h_{100}^{-1} Mpc, or 114 h_{70}^{-1} Mpc. Therefore, our superclusters which have a maximum size of the order 100 h_{70}^{-1} Mpc, should therefore be statistically significant.

1.4 Observational Surveys

1.4.1 The Two Degree Galaxy Redshift Survey

The Two degree Galaxy Redshift Survey (2dFGRS) is a large spectroscopic survey in the southern celestial hemisphere covering approximately 1500 square degrees. Spectra for 245,591 galaxies were obtained in three regions, the North Galactic pole region , South Galactic pole region and a series of random fields. This makes it the second largest redshift survey to date, coming above the VIRMOS galaxy redshift survey (Le Fèvre et al., 2004) of approximately 150000 galaxies but falling below the Sloan Survey which is discussed later in this section. The survey is performed with the Two-degree Field multifibre spectrograph on the Anglo-Australian telescope, capable of observing up to 400 objects at once within the two degree field. The survey is based on an extended version of the Automated Plate Measuring catalogue of over 5 million objects.

The overall incompleteness of the source catalogue varying with apparent magnitude is $10-15\%$, the incompleteness being due to effects such as merged images, misclassification of some galaxies as stars and the misclassification of some low surface brightness galaxies as noise. The survey magnitude limit varies across the survey regions and is detailed in the survey magnitude mask. Initially before improvements to the photometric calibrations target galaxies were limited to extinction corrected magnitudes of $b_J > 19.45$. The 2dFGRS is the first survey to be large enough to study effects over scales of larger than 100 h^{-1} Mpc. One such effect that has been studied is the Kaiser effect (Kaiser, 1987), which studies the gravitational collapse of cosmological structures. In the collapsing regions there should exist coherent infall velocities of galaxies which will cause an apparent flattening of structures along the line of sight. Peacock et al. (2001) used the galaxy two-point correlation function to show that the Kasier effect is observed for these large scales and combined with CMB data their results are consistent with a $\Omega_m = 0.3$ universe. Other results have included calculating the galaxy power spectrum (Percival et al., 2001), the luminosity dependence of galaxy clustering (Norberg et al., 2001) and the environmental effects on star formation rates near clusters (Lewis et al., 2002) to name just a few.

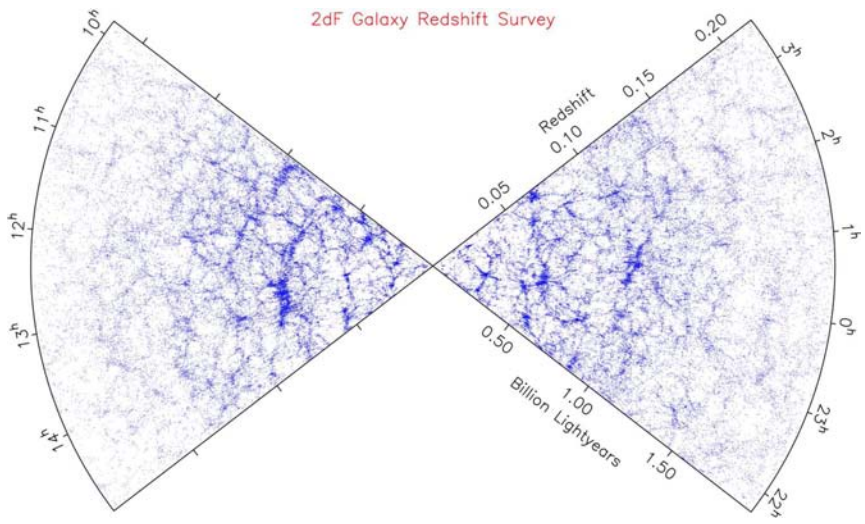

Figure 1.3: Map of the galaxy redshift distribution for the completed 2dFGRS survey. .Taken from Colless et al. (2003). (§1.4.1)

1.4.2 The 2dFGRS Percolation-Inferred Galaxy Group catalogue

The 2dFGRS Percolation-Inferred Galaxy Group (2PIGG) catalogue is a catalogue of groups based on the North and South strips of the 2dFGRS catalogue consisting of approximately 220,000 galaxies (Eke et al., 2004). They chose a friend-of-friends algorithm to find the groups. These algorithms link together all the galaxies within a certain linking distance of the centre of each galaxy. So that the groups all have a similar overdensity throughout the sample, this linking length was varied with redshift to counter the reduced number density of galaxies detected at larger redshifts. The linking length should ideally be scaled in the perpendicular direction (plane of the sky) and the parallel (line of sight) directions such that a group sampled at different completeness should have its edges in approximately the same position. However, care has to be taken that the linking lengths do not become too large compared to the size of gravitationally bound structures. The shape of the linking volume was taken to be a cylinder to account for elongation in the redshift direction, and to best recover groups that trace the underlying dark matter halo.

Eke et al. (2004) also showed that the overdensity enclosed in the group was dependent on the mass of the underlying halo. This can result in a systematic

bias in the projected size and velocity dispersion, resulting in small groups with overestimated sizes or large clusters with underestimated sizes. To correct for this they estimated the halo mass in which each galaxy is found. This was done by measuring the galaxy density relative to the background, and then using this density contrast to scale the size and aspect ratio of the linking cylinder. The size of the linking volume is thus dependent on the maximum size of the perpendicular linking length ($L_\perp$) , the aspect ratio of the linking cylinder (R_{gal}) and the number of mean intergalaxy separations defining the perpendicular linking length (b_{gal}). These values are in physical coordinates and set at optimum values while the parameters in co-moving space vary with redshift and galaxy density.

Optimum values were found by comparing groups found from a mock 2dFGRS catalogue with their parent dark matter halos. The 220,000 galaxies in the initial sample were reduced to 191,000 after all galaxies within fields with less than 70% completeness, and in all sectors (overlapping field areas) with completeness less than 50%, were removed. Weights were then applied to these galaxies by assigning all the galaxies in the parent APM catalogues with no recorded redshift to the nearest 10 members with redshifts. The co-moving number density of galaxies was calculated at each angular position and redshift. This mean observed galaxy density for each galaxy was then used with the friend-of-friends algorithm with optimum values of $L_\perp = 2\,h^{-1}$ Mpc, $R_{gal} = 11$ and $b_{gal} = 0.13$ to find real groups in the 190,000 galaxy sample. This resulted in 55 % of galaxies being part of groups of at least two members. 28,877 groups were found with at least 2 members and 7,020 groups with at least 4 members.

1.4.3 The Six degree Galaxy Survey

Since 2001 the Six degree Galaxy Survey (6dFGS) has obtained over 120,000 redshifts in the southern sky. The final release is due in late 2006, by which time the survey will have covered an area 8 times larger than that of the 2dFGRS. The survey is performed with the six-degree field multi-object fibre spectroscopy system on the UK Schmidt telescope at the Anglo-Australian Observatory (6dF). The 6dF is capable of taking 150 simultaneous spectra in a field of a 5.7 degree diameter. The

primary sample for the survey is extracted from the near infrared (NIR) two micron all sky survey (2MASS)(Jarrett et al., 2000). The use of a NIR survey means that the bias towards currently star forming galaxies, found in the SDSS and 2dFGRS, would be minimalised. Each field takes approximately 1.5 hours and repositioning of fibres and other overheads take about 40 minutes, resulting in 5 fields being observed a night on average.

1.4.4 The Sloan Digital Sky Survey

Funded by the Alfred P. Sloan Foundation, the Sloan Digital Sky Survey (SDSS) is the largest redshift survey to date and is still growing. The fifth data release contained spectra for approximately 675,000 galaxies and 79,000 quasars with the aim being to get over 1 million galaxies by the end of the survey. Imaging is carried out in drift scan mode using a wide-field 2.5 m telescope at Apache Point Observatory, New Mexico. Photometry is gathered in five broad bands, (u,g,r,i,z) in the range from 3000 to 10,000 $\mathring{A}$. Each plate can accommodate 640 fibres, about 50 of which are reserved for calibration targets, which leaves approximately 590 fibres for targets. Plates are exposed in a series of 15 minute sessions after which signal-to-noise ratio (S/N) diagnostics are performed. The 15 minute exposures are continued until until the cumulative median $(S/N)^2 > 15$ at g* = 20.2 and i* = 19.9 in each of the 4 CCD detectors (One red and one blue in each of the two spectrographs). The nominal exposure time is 45 minutes. The spectroscopic survey aims to observe a complete sample of galaxies, selected to be brighter than r* = 17.77, using Petrosian magnitudes [1]. Like the 2dFGRS the SDSS has been used extensively to investigate the large scale structure of the universe. Studies have included, the clustering properties of galaxy clusters (Basilakos & Plionis, 2004), constraining the amplitude of the matter power spectrum (Viana, Nichol, & Liddle, 2002) and large scale galaxy

[1] Galaxies do not all have the same radial surface brightness profile, and have no sharp edges, Therefore, a method is needed to measure a constant fraction of the total light, independent of the position and distance of the object. The SDSS has adopted a modified form of the Petrosian (1976) system, measuring galaxy fluxes within a circular aperture whose radius is defined by the shape of the azimuthally averaged light profile.

clustering (Gaztañaga, 2002), to name just a few.

1.4.5 Super COSMOS

SuperCOSMOS is a machine used to digitise Sky Survey plates taken with the UK Schmidt telescope, the ESO Schmidt, and the Palomar Schmidt telescopes. The photographic plates are digitised to 15 bits with a resolution of 10 microns. The resulting database is approximately 2.5 terabytes in size and contains 3.7 billion individual object detections. The database covers the southern sky (dec $< +3.0°$) in three wavebands (BRI), with the R band represented at two epochs. Initially the source pairing was done "on-the-fly" but a more detailed analysis of merged objects is performed in the SuperCOSMOS Science Archive (SSA). Each scanned plate in the SSA results in a pixel map. This map is then processed using Image Analysis Mode, or IAM, software to produce a list of parameterised detections on each plate. The "on-the-fly" method uses a series of pair index pointers between any two given plate datasets, however this can result in the same slave detection being paired with more than one master image. The SSA uses the same pair indices but removes any multiple pairings based on absolute proximity, i.e. the nearest slave is chosen.

1.5 Cosmology in this thesis

Throughout this thesis the cosmology used is $\Omega_M = 1$ and $H_0 = 70$ km s^{-1} Mpc^{-1}, though the trends we present do not crucially depend on these parameters. It can be shown that for the Shapley supercluster, for example, a dark energy dominated cosmology $\Omega_\Lambda = 0.7$, $\Omega_m = 0.3$, at the mean redshift of $z = 0.0476$ would be at a distance of $211 h_{70}^{-1}$ Mpc compared with $206\, h_{70}^{-1}$ Mpc for our $\Omega_M = 1$ cosmology. This amounts to a 2.5 % difference in the distances, which is within the error budget of most of the calculations we perform.

1.6 Thesis Outline

In Chapter 2 we give a brief introduction into star formation in galaxies, covering areas such as trends with time and environment, star formation indicators and a summary of the 2dFGRS star formation parameter η. Chapter 3 investigates the Pisces-Cetus, Horologium-Reticulum and Shapley superclusters, looking at their spatial structure and obtaining estimates of their minimum mass and consequently their mass overdensities. The star formation properties of the Pisces-Cetus supercluster are looked at in Chapter 4 using the η parameter. The dependency of star formation on its environment is investigated in a range of areas including within clusters and groups, within the supercluster and in the field, in dwarf and giant galaxies and around low and high velocity dispersion clusters. Chapter 5 looks at some of the same star formation environmental relations in much larger samples of filaments of galaxies using the same η parameter. Star formation is also investigated in Chapter 6, but this time 6dF equivalent widths are used to estimate star formation within the Shapley supercluster region. Our findings are summarised in Chapter 7 and future work discussed.

Chapter 2

Lady Astor: "Winston, if I were your wife I'd put poison in your coffee."
Sir Winston Churchill: "Nancy, if I were your husband I'd drink it."

Star formation in galaxies

2.1 Star formation as a function of time

It is generally accepted that the stellar populations in galaxies in the cores of clusters are predominantly old. Most of the galaxies have early type morphology with suppressed star formation, with the bulk of stars forming at $z > 2$. The tight correlation of colour magnitude relations support this, as recent star formation would result in a much greater scatter than that observed (Bower, Lucey, & Ellis, 1992; Gladders et al., 1998). Other relations such as that between the Mg_2 line strength (metallicity indicator) and central velocity dispersion (e.g. Guzman et al., 1992) or that in the fundamental plane of early type galaxies (e.g. Fritz & Ziegler, 2003) also show little scatter.

With little star formation at the current epoch it is sensible to assume that as you go back in time you will reach a period where the relations break down and star formation is more prevalent. van Dokkum & Stanford (2003) have shown that the fundamental plane relation remains tight at $z = 1.27$, but there is little or no evidence for tight relations beyond $z = 2$. However, studying only the early type galaxies or any subset of the total cluster population can result in biases. An example of this is the "progenitor bias" described by van Dokkum & Franx (2001), where by the progenitors of the youngest present day early type galaxies drop out of the sample at high redshift. i.e. a significant fraction of present-day, early-type

galaxies was transformed from star-forming galaxies at $z < 1$ and so for $z > 1$, galaxies which are early-type now may not be included in the sample.

The star formation rate (SFR) in cluster cores has also been studied as a function of redshift. This has been extensively performed on the basis of colours. Butcher & Oemler (1984) showed that clusters show a larger proportion of bluer (higher temperature and higher SFR) galaxies at progressively higher redshifts. This effect has become known as the "Butcher-Oemler effect" and has been confirmed by more recent studies (Margoniner et al., 2001). This has helped establish clusters as evolving systems where star formation and galaxy morphology are dependent on the environment. However, once again care has to be taken to consider possible biases. The magnitude limit can be a potential bias where by blue galaxies will fade by up to a magnitude when star formation ends and thus are not directly comparable to the red galaxies. Another potential bias can come from the contamination of cluster members by field galaxies due to projection effects. At low redshifts this effect may be minimal, but at larger redshifts, with their bluer field populations, this effect will be greater. De Propris et al. (2004) have concluded that the observed changes in the blue fraction are dependent on the luminosity limit, cluster-centric radius and more generally the local galaxy density but not the properties of the individual clusters. Poggianti et al. (2006) also confirm the "Butcher-Oemler effect" but also show that the morphology of galaxies change to later-type toward higher redshifts. Thus, there is also a morphological version of the "Butcher-Oemler effect".

The fraction of star forming galaxies as a function of redshift can also be studied spectroscopically. Poggianti et al. (2006) use the Equivalent Width (EW) of the [OII] line as an indicator of ongoing star formation in a high (z=0.4–0.8) and low (z=0.04–0.08) redshift galaxy sample to find the fraction of passive galaxies. They propose a scenario in which the passive galaxies consist of two populations, primordial which had all their star formation at $z > 2.5$ and quenched galaxies where the SFR had been reduced due to dense environments at later times. The Millennium simulation is used to show that their observed relations between the fraction of passive galaxies and velocity dispersion at high redshifts is consistent with that of galaxies that were in groups at $z = 2.5$, with primarily a primordial passive population. The high

redshift sample is found to be consistent with galaxies that have been in clusters over the last 3 Gyr, with 60% quenched galaxies. This would mean that galaxy star formation histories of galaxies are closely linked with the environment, even at high redshift..

2.2 Star formation as a function of environment

Early works have also shown that the relative morphological content of galaxies in a given volume of space is dependent on the local projected galaxy density, with more elliptical galaxies and less spirals at higher densities (e.g. Dressler, 1980). Menanteau et al. (2006) have shown that the SFR is dependent on the morphology of the galaxy with spiral galaxies being the main provider to the star formation density at all redshifts. However, Ravindranath et al. (2006) use high redshift Lyman-break galaxies $2.5 < z < 5$ to show that at higher redshifts many star forming galaxies have elongated structures. Thus at higher redshifts a significant fraction of star formation may be occurring in galaxies which are comprised of gas rich filaments. Therefore, morphological type can not always be used as a proxy for SFR.

The effect of the density of the environment has been studied extensively in clusters of galaxies, where a large range of projected surface density can be probed. There is clear evidence that SFRs are highly suppressed in galaxies within the cores of rich clusters (Dressler, 1980). Furthermore, the current SFR is shown to increase with decreasing density and increasing distance from a cluster core. Balogh et al. (1999) were one of the first to study the SFR away from cluster cores. They found a strong radial dependence on SFR and that the SFR had not yet reached the field value as far out as the virial radius. The arrival of the 2dFGRS and SDSS has allowed much more accurate work to be done with the detailed redshift information removing contamination from interlopers. From these surveys, Lewis et al. (2002) and Gómez et al. (2003) have shown a correlation between the median SFR and the local density. There is a sharp transition in the correlation at approximately 1 galaxy per h^{-2} Mpc^{-2}. Beyond 1 galaxy per h^{-2} Mpc^{-2} the median SFR has values very similar to the field values but below 1 galaxy per h^{-2} Mpc^{-2} the median SFR

begins to drop rapidly.

The SFR in clusters away from the core does not reach that of the field until beyond 3 h^{-1}Mpc ($\sim$2 times the virial radius) from the centre of the clusters. This shows that ram pressure stripping can't be the only process that is suppressing the SFR as this is only present in the most dense environments. They also conclude that the SFR dependence on density is independent of the velocity dispersion of the cluster and hence the SFR is independent of the large scale structure of the environment (group or cluster). However, while Balogh et al. (2004) also find that the correlation is independent of velocity dispersion, they suggest that fewer galaxies in supercluster like environments have significant Hα emission and that there may be some correlation at lower densities on scales $> 5\,h^{-1}$ Mpc.

Haines et al. (2006a) compare the environmental dependence of giant ($M_R < -20$) and dwarf galaxies. They find that the SFR in giant galaxies are in agreement with the above studies with SFR approaching field values at 3–4 virial radii. However, the dwarf galaxies show a sharp transition at approximately the virial radius from predominantly passive to predominantly star forming. This means that dwarf galaxies may preferentially lose their gas reserves and hence become passive when they encounter effects such as ram pressure striping or galaxy harassment.

2.3 Star formation indicators

2.3.1 Recombination lines of Hydrogen

High temperature OB stars cause the ionisation of the HII nebular gas that surrounds them. The hydrogen electrons ionised by Lyman continuum photons with energies above 13.6 eV, recombine with the atoms. The initially excited atom jumps down to less excited states, and, in doing so, releases energy at specific wavelengths, which is seen as emission lines in the spectrum. For a radiation bounded system, the flux of the hydrogen recombination lines scales directly with the flux of the ionising radiation from the stars. The strongest emission line is the Lyman Hα , the strength of which can be determined by taking the equivalent width. Equivalent Width is defined as the rectangular section of a surface counted between the level of the con-

tinuum, normalised to unity, and reference zero, having a surface area identical to the profile of the line. The relation of Kennicutt (1998b),

$$\mathrm{SFR(IR)}\,(\mathrm{M_{\odot}yr^{-1}}) = 7.9 \times 10^{-42}\mathrm{L_{H\alpha}}\,(\mathrm{erg\ s^{-1}}), \tag{2.1}$$

where $\mathrm{L_{H\alpha}}$ is the total Hα luminosity, can be used to gain an estimate the SFR.

Because nearly half of the ionising atoms produce a H_{α} photon (Kennicutt et al., 1998a) this technique is very sensitive. This combined with the direct coupling between nebular emission and SFR and the ability of even small telescopes to obtain high resolutions has enabled this technique to provide the most detailed information on SFRs in galaxies.

However, the observed spectrum of the galaxy is a combination of the nebular emission lines and the combined spectra of the constituent stellar population. Therefore, the accurate measurement of the nebular emission lines relies on the removal of the absorption lines in the underlying stellar spectrum. The stellar spectrum can be recreated by either spectral synthesis or evolutionary synthesis models (e.g., Bruzual & Charlot, 2003). Spectral synthesis creates the model spectrum by integrating the spectra of star clusters spanning the range of types of star expected to be present in the galaxy population. This is best used in elliptical galaxies and spiral bulges where the population types are well constrained. In active star forming galaxies the evolutionary synthesis is best used. These use a theoretical stellar evolution model, coupled with models of stellar atmospheres and an assumed initial mass function to create integrated spectra over a range of star formation histories. These are then compared with the observed spectrum to find the stellar properties of the galaxy.

Extinction due to dust in the interstellar medium remains the main problem with this technique. The extinction in normal galaxies can be estimated from the reddening of [HII] regions or comparing the integrated Hα and thermal radio fluxes (e.g., Ruffle et al., 2004). The nuclear regions of galaxies and the starburst regions found in many mergers, can have much higher extinctions than those calculated for normal galaxies. The emission line flux only traces the most massive stars requiring the extrapolation of the Initial Mass Function (IMF) to lower stellar masses. The

[NII] doublet (6548 Å and 6584 Å) are very close to the Hα emission line and are sometimes blended together. When separated high [NII]/Hα ratios can suggest photo-ionisation due to the presence of an Active Galactic Nucleus (AGN) (Veilleux et al., 1994).

While the Hα emission line is the strongest and hence most commonly used, any hydrogen recombination line can be used, Brγ and Brα hydrogen emission lines in Infrared wavelengths are often used for dusty regions. At higher redshifts the Hα emission lines become unobservable in optical spectra ($z \gtrsim 0.4$) and the higher order Balmer lines such as Hβ or the [OII] doublet are substituted.

Using the Hβ emission line has essentially the same strengths and weaknesses as the use of the Hα line. It too is sensitive only to the most massive stars and suffers from the same dependence on dust extinction. In fact, Hβ encounters more interstellar dust attenuation and is slightly more sensitive to the underlying stellar absorption. Kennicutt (1992) regards its use as limited in normal galaxies, due to the difficulty in accounting for the underlying stellar absorption, although population synthesis models can try to account for this (Tremonti et al., 2004). There is a strong correlation between the equivalent widths of Hβ and Hα+[NII] (Kennicutt, 1992). [OIII] has been used as a crude estimator of SFR but shows such a large dispersion in relations to Hα that it has little significance (Kennicutt, 1992).

2.3.2 Ultraviolet continuum emission from hot stars

Young stars ($< 10^7$ yr) contribute most of the Ultraviolet (UV) flux in a galaxy, hence the UV continuum in the range 1300-2500Å is an indicator of the galaxies SFR. This method allows the tracing of stars that are not hot or massive enough to produce [HII] regions. The SFR in this way can be found using the relation of Kennicutt (1998b),

$$\mathrm{SFR(UV)}\ \ (\mathrm{M_\odot yr^{-1}}) = 1.4 \times 10^{-28} \mathrm{L}_\nu\,(\mathrm{erg\ s^{-1} Hz^{-1}}), \tag{2.2}$$

where L_ν is the total luminosity per frequency interval.

While this method is undoubtedly a useful indicator it has several drawbacks.

The most serious of these is that the UV flux is very sensitive to interstellar extinction, meaning that the UV spectrum is of little use in the dusty starburst regions of galaxies. The wavelength band used is also visible from the ground only for high redshift systems.

2.3.3 Infrared thermal emission

Infrared (IR) emission in the 8–1000 μm band in star forming galaxies can arise from three different processes, (a) emission from dust heated by young OB stars, (b) emission from the photospheres of evolved stars as they lose mass, and (c) from dust distributed throughout the interstellar medium, which is heated by the general stellar radiation. The absorption cross section of the dust is highly peaked in the UV and the absorbed radiation is re-emitted in the IR. If it is assumed that young stars dominate the radiation field in the UV and visible bands, then the last two of these processes are negligible. It is then also assumed that the opacity of the dust in a galaxy is infinite, then the IR SFR is a good representation of the actual galaxy SFR. The relation of Kennicutt (1998b),

$$\mathrm{SFR(IR)}\,(\mathrm{M_{\odot}yr^{-1}}) = 4.5 \times 10^{-44}\mathrm{L_{IR}}\,(\mathrm{erg\ s^{-1}}), \tag{2.3}$$

where $\mathrm{L_{IR}}$ is the total Ir luminosity in the 8-1000μ m band, can be used to gain the IR SFR.

Calibration of the SFR for normal galaxies is not an easy task. The dust grains absorb radiation with a broad range in wavelengths and hence radiation from young and old stars. Conclusively separating the star forming component has proven elusive. However, in the case of dusty starburst regions, the young stars dominate, and the optical depth of the dust is so high that the IR emission is effectively the bolometric luminosity of the starburst.

2.3.4 X-ray Luminosity

It has been shown (e.g., Grimm, Gilfanov, & Sunyaev, 2003; Gilfanov, Grimm, & Sunyaev, 2004) that high-mass X-ray binaries (HMXB) can be used as SFR indicators. The X-ray luminosity (L_x) distribution of HMXBs can approximately be described by a luminosity function which is a power law with a slope of ~ 1.6 and a cut off at $\log(L_x) \sim 40.5$, the normalisation of which is proportional to the SFR. The 2-10 KeV L_x of a normal galaxy with sufficiently high SFR/M_* ratio, where M_* is the total stellar mass, is dominated by the emission from HMXBs. Therefore, L_x can be used as a SFR indicator for normal galaxies. The L_x–SFR relation is only linear for higher SFRs, the break in the relation occurring at SFR ~ 4.5 $M_\odot$ yr^{-1} or $L_x \sim 3 \times 10^{40}$ erg s^{-1}. In the linear regime the SFR of stars with $M > 5$ $M_\odot$ is given by,

$$\mathrm{SFR}(L_x)\,(M_\odot \mathrm{yr}^{-1}) = \frac{L_{2-10\mathrm{KeV}}}{6.7 \times 10^{39}\,(\mathrm{erg\ s}^{-1})}, \tag{2.4}$$

where $L_{2-10\mathrm{KeV}}$ is the X-ray luminosity in the range 2-10 KeV. However, contamination of the SFR from the emission of the central supermassive black holes in which even low luminosity AGNs can outshine the X-ray binaries and the contribution of low-mass X-ray binaries which are unrelated to SFR and may be important for low SFR can be a problem. The latter has been suggested by Gilfanov, Grimm, & Sunyaev (2004) to be responsible for Ranalli, Comastri, & Setti (2003) obtaining a linear L_x–SFR relation for all SFRs.

2.4 Star formation in interacting galaxies

2.4.1 Star formation mechanisms

The diversity of the star forming environments in interacting galaxies suggests that several physical processes are responsible for the increased SFR seen in starburst galaxies. Potential mechanisms for causing varying levels of increased SFR in different environments are discussed below.

Gravitational star formation thresholds

Nonlinear star formation features are seen in a wide range of interacting and normal galaxies. An abrupt transition is seen in most late-type spirals where at a certain radius SFR drops to very low values. Thresholds are also seen in gas-rich S0 galaxies and low surface brightness galaxies. Kennicutt (1989) proposed that these thresholds could be associated with large scale gravitational thresholds for the growth of density perturbations. The Toomre parameter (Q) is the ratio of the critical density for star formation at a given radius to the actual gas density. Regions that have $Q \gg 1$ have suppressed star formation while regions with $Q \ll 1$ would have unimpeded star formation. However, regions with $Q \sim 1$ would be stable but easily perturbed. When galaxies interact, local compressions in density waves could cause the gas in these stable regions to exceed the critical threshold, leading to an increase in SFR.

Cloud collisions

The variation in star formation thresholds can only account for a variation in SFR by $\sim 5\%$, which is not high enough to explain the large increases in strongly interacting systems. When two galaxies closely interact, clouds of gas from the two galaxies may collide with each other. Collision velocities may be high enough to cause shocks, which can compress clouds inducing small-scale gravitational collapse and star formation (e.g., Olson & Kwan, 1990). If the galaxies do not touch, but still interact, small perturbations could cause gas clouds with orbits close to one another to collide and start star formation (e.g., Lin, Pringle, & Rees, 1988). The rate of collisions depends on the ratio between the lifetime of a cloud and the time interval of the collision (Struck-Marcell & Scalo, 1987).

Tidally induced bars

One of the most critical pre-requisites for the most active starbursts is the transport of large masses of interstellar gas at the centre of the merger. If one of two tidally interacting systems has a large solid-body like rotation curve, then its partner can induce a bar which out-lives the interaction itself. This can channel gas into the nuclear region perhaps leading to a nuclear starburst (Noguchi, 1988). The gas and

star formation is often found in nuclear rings of dense young star clusters known as "hotspots" or twin "peaks" (Kenney, 1994) often surrounding an AGN. This process is unlikely to produce very luminous starbursts but may be important in the lower level nuclear activities of many interacting galaxies.

2.4.2 Environmental influences

The environment of a galaxy is an essential ingredient of its evolution and SFR properties. The relations between the density of galaxies, the presence of an intra cluster medium (ICM), gas reserves, temperature and the velocity of encounters influence the resulting SFR, either enhancing or suppressing the rate. Many studies of Hα and IR have shown increased SFR in merging and interacting galaxies (e.g., Bushouse, 1987; Kennicutt et al., 1987; Xu & Sulentic, 1991; Liu & Kennicutt, 1995). On average the equivalent widths of the interacting galaxies show an enhancement in SFR of approximately double that of an isolated sample. The majority of interactions show only modest enhancements. However, they range from practically no SFR enhancements to systems where a significant fraction of their total stellar mass is star forming. Some of the main interacting processes which may influence the onset of the above mechanisms are described below.

Galaxy Harassment

One of the most important influences on induced SFRs in galaxy-galaxy interactions is tidal in nature, where the gravitational attraction of galaxies influence each other. Multiple close encounters between galaxies at high speeds can deform gas clouds and/or cause them to collide leading to an increased SFR. Moore et al. (1996) used high resolution numerical simulations to study the effect of these multiple encounters and termed the phrase "galaxy harassment". They conclude that "galaxy harassment has the potential to change any internal property of a galaxy within a cluster, including the gas distribution and content, the orbital distribution of stars and the overall shape". From these early results galaxy harassement has been investigated in numerous papers and used to explain the morphological transformation of galaxies in clusters, in particular the formation of dwarf ellipticals, and even as

a source of fuel for quasars (e.g., Lake & Moore, 1999; Matković & Guzmán, 2003; Davies, Roberts, & Sabatini, 2005; Haines et al., 2006b). Observationally galaxy harassment can be seen on galaxies with long tidal tails, drawn out by the close encounters and rings around a stellar bar.

Tidal influence of a cluster potential

Galaxies falling into a cluster potential will experience a strong differential force the strength of which depends on the galaxies orbit. The tidal force experienced is of the order of,

$$F_{tide} \sim \frac{GM(r)}{r^3} \sim \frac{\sigma_{cl}^2}{r^2}, \tag{2.5}$$

where σ_{cl} is the cluster velocity dispersion, r is the distance from the cluster centre, $M(r)$ is the enclosed mass within radius r and G is the gravitational constant. The tidal forces of the cluster potential can cause density waves in the gas of the infalling galaxies leading to enhanced star formation where the densities become high enough.

Strangulation

It has been shown that galaxies can be surrounded by a halo of hot gas with a temperature of up to a few million degrees Kelvin (e.g., Pedersen et al., 2006). However, warm halos of gas with a temperature of a few hundred thousand degrees Kelvin, which is too cool to be seen in X-ray detections and too warm to be seen in radio detections, may be present around most galaxies. This halo of warm gas would provide a reserve of gas which can be used to fuel star formation in the future. As a galaxy falls into a cluster potential well, tidal effects can strip this reserve of gas from the halo. This will result in a "strangulation" (e.g. Larson, Tinsley, & Caldwell, 1980) of star formation, where star formation in the disk continues until gas in the disk of the galaxy is used up, with no reserve of gas to fuel further star formation. More massive galaxies will be more able to retain their warm gas haloes.

Ram pressure stripping

As a galaxy falls in towards the centre of a cluster it will encounter the ICM. The ICM is hot gas which has been ejected from galaxies by early supernovae-driven winds. In the centres of clusters the density of the ICM is high enough that the galaxies moving through it will experience a strong drag force known as ram pressure. Ram pressure can strip the gas from the disk of a galaxy causing the suppression of star formation at the current time. Gunn & Gott (1972) give the conditions for ram pressure stripping to be if the force due to ram pressure exceeds the restoring gravitational force, given by,

$$P_{ram} \geq 2\pi G \sigma_{star} \sigma_{gas}, \tag{2.6}$$

and,

$$P_{ram} = \rho_{icm} V_{gal}^2, \tag{2.7}$$

where P_{ram} is the ram pressure, G is the gravitational constant, σ_{star} is the stellar surface density, σ_{gas} is the surface density of the gas, V_{gal} is the velocity of the galaxy and ρ_{icm} is the density of the ICM.

Mergers

Evidence for the merging of galaxies in clusters has been demonstrated optically and with X-ray data (e.g. Mahdavi et al., 1996; Mohr, Geller, & Wegner, 1996). This is consistent with the hierarchical growth of structure with highly evolved galaxies being found in clusters which are not yet in equilibrium. The process of merging can cause bursts of star formation through effects such as cloud collisions. Larger galaxies have a greater merger cross section and hence mergers between dwarf galaxies will be rare. Gnedin (2003) show that the number of close encounters experienced by a galaxy can be given as,

$$N_{enc} \approx \frac{N_g}{\frac{4\pi}{3} R_{cl}^3} \pi R_g^2 \sqrt{2} \sigma_{cl} t_H, \tag{2.8}$$

where σ_{cl} is the cluster velocity dispersion, R_{cl} is the cluster virial radius, N_g is the number of galaxies in the cluster and t_H is the Hubble time. The probability of a merger is then given by,

$$P_{mer} \sim N_{enc} \left(\frac{\sigma_g}{\sigma_{cl}} \right)^4, \tag{2.9}$$

where σ_g is the galactic velocity dispersion.

Evaporation

As the cool gas in a galaxy encounters the hot ICM the galaxy can lose the gas through evaporation. Fujita & Goto (2004b) show the time scale of the evaporation of the cool gas can be given as,

$$t_e \approx \frac{3k_b T_{icm} M_{cold}}{2\mu m_H |L|}, \tag{2.10}$$

where k_b is the Boltzman constant, T_{icm} is the temperature of the ICM, $\mu(= 0.6)$ is the mean molecular weight, m_H is the Hydrogen mass, M_{cold} is the mass of cold gas in the galaxy and L is the energy flux from the hot ICM surrounding the galaxy via thermal conduction. The loss of the cool gas will curtail the ability of the galaxy to form stars.

Active galactic nuclei

The process of interaction between galaxies can also trigger non-thermal nuclear activities, creating active galactic nuclei (AGN). These AGN and the nuclear starbursts are closely intertwined and occur together in many interacting and normal galaxies. However, it has been shown that galaxies dominated by nuclear star formation are more prevalent in interacting systems (Sekiguchi & Wolstencroft, 1993), and galaxies with AGN or composites may be as low as 15% (Brinchmann et al., 2004) overall.

2.5 A star formation index from 2dFGRS spectra: the η parameter

The flux calibration of the 2dF spectra is unreliable due to instrumental limitations. The calibration of fibre spectra is difficult to achieve due to, (a) astrometric/positioning errors, which combined with the small fibre aperture prevent reproducible sampling of each galaxy's light distribution, (b) chromatic variations in distortion, and (c) residual errors in the atmospheric dispersion correction (see Colless et al., 2001). Consequently a comprehensive study of the shape of the spectral continuum is not possible. In order to find a parameter sensitive to SFR that can be extracted from the uncalibrated 2dFGRS spectra, a Principal Component Analysis of the galaxy spectra is the best method of gaining spectroscopic data . This essentially measures the strength of the emission and absorption lines while remaining insensitive to the continuum.

2.5.1 The Principal Component Analysis

Madgwick et al. (2002) initially took all the 2dFGRS observations until January 2001. This comprised a total of 111,404 galaxy spectra in the northern region and 60,062 in the southern region. They removed those galaxies which did not have an accurate redshift ($Q < 3$, which is those galaxies which have a redshift which is, probable, reliable, or reliable with a high quality redshift (see Colless et al., 2001)) , repeated observations and spectra with a signal to noise ratio of less than or equal to 10. With a redshift cut of $z \leq 0.15$ to avoid corruption due to sky emission and atmospheric absorption this left a total sample of 75,589 galaxies.

From this sample they defined a new parameter η based upon a Principal Component Analysis (PCA) of the galaxy spectra. PCA is a statistical technique which is used to reduce the dimensionality of the data to summarise the parts that are useful to the user. In this case it does this by identifying the components of the spectra that best discriminate between the galaxies. A detailed description of the technique can be found in Glazebrook, Offer, & Deeley (1998).

The significance of each successive principal component was found to drop off

so sharply that the first two components retained two-thirds of the total variance within the population. Thus from the initial 738 channels needed to describe each spectrum, now only 2 were needed. The principal components were determined from a subsample of the main sample, and these used to find the projections of the rest of the sample. The subsample was chosen to have an absolute magnitude limit of –18.0 corresponding to a redshift of approximately 0.1. This makes the process less prone to bias from relationships between the luminosity and type of galaxy.

It was found that the first eigenspectrum derived from the PCA contains approximately an equal contribution from both the continuum and the emission/absorption lines. However, the second eigenspectrum is dominated by the emission and absorption lines. Therefore by taking linear combinations of the two, the line features can be maximised, see Fig. 2.1. By maximising the emission and absorption features they were in effect high-pass filtering the spectra. This meant that the projection was relatively stable to uncertainties in continuum measurements. Therefore, once the projection was chosen, the η parameter was defined as: $\eta = apc_1 - pc_2$. Where pc_1 and pc_2 are the first and second projections onto the principal axes and a is a constant which maximises the absorption and emission features. Identifying the most stable projection in the pc_1, pc_2 plane between repeated pairs of spectral observations gave a value of $a = 0.5 \pm 0.1$.

By comparing the values from approximately 2000 repeat observations an estimate of the uncertainties in the PCA was obtained. The difference in the two projections between repeat observations had 1σ dispersions of 2.9 and 1.7 for $pc1$ and $pc2$ respectively. However the combination of the two in the η parameter is greatly reduced having a 1σ dispersion of 0.7.

The analysis has been expanded to now contain 192,982 galaxies with an η value from a total of 245,591 galaxies in the final catalogue.

2.5.2 Relationships with other parameters

Madgwick et al. (2002) plotted the relation between the η parameter and its morphological type for the spectrophotometric standard galaxies in Kennicutt's atlas (Kennicutt, 1992). It can be seen in Fig. 2.2 that there is a relation between the

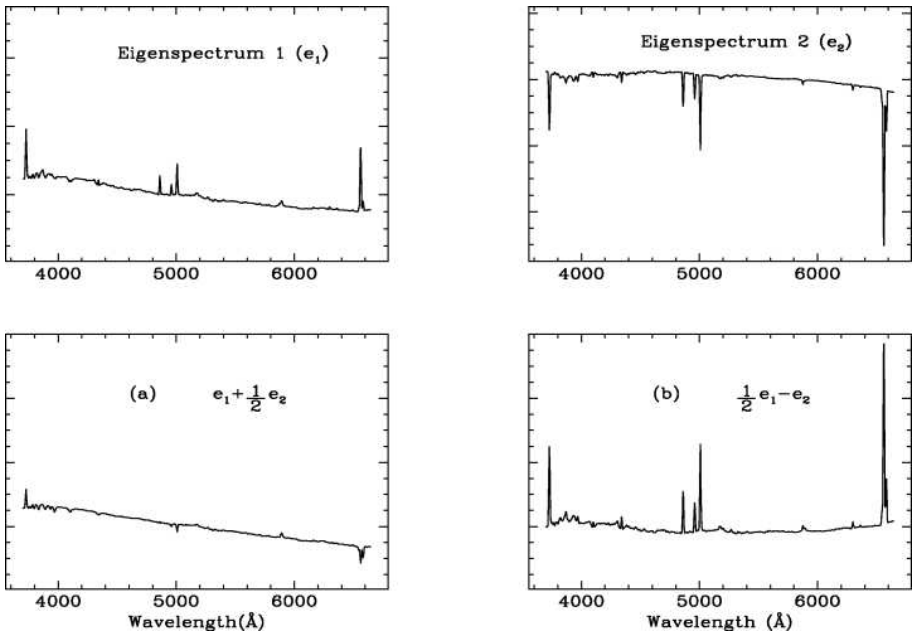

Figure 2.1: The first two principal components identified from the 2dF galaxy spectra and the linear combinations which isolate either (a) the continuum slope or (b) the line features (Madgwick et al., 2002). (§2.5.1)

morphological type and the value of η. Thus our own galaxy, the Milky way (Sb), would have a η of between approximately 0 and 2. It is also possible to see that a histogram of the η parameter is bimodal. The first peak corresponds to mainly E/S0 galaxies, which would be consistent with little or no star formation at the current time at these low η values. Approximately 40% of the galaxies are in the first passive galaxy peak.

Madgwick et al. (2003) compared the value of η derived for each galaxy to the equivalent width of the Hα emission-line spectra. It can be seen in Fig. 2.3 that with some scatter there is a strong linear correlation between the two quantities. A Hα EW of 0.0 corresponds to $\eta \approx -2.0$ and A Hα EW of 50.0 corresponds to $\eta \approx 7.0$.

Madgwick et al. (2003) also compare the η with the birth rate parameter, b, which is the ratio of the current SFR to the past averaged SFRs. They initially derive b using a simple model of the star formation history in terms of an exponential function of time (Bruzual, 1983) with a Kennicutt (1983) initial mass function of:

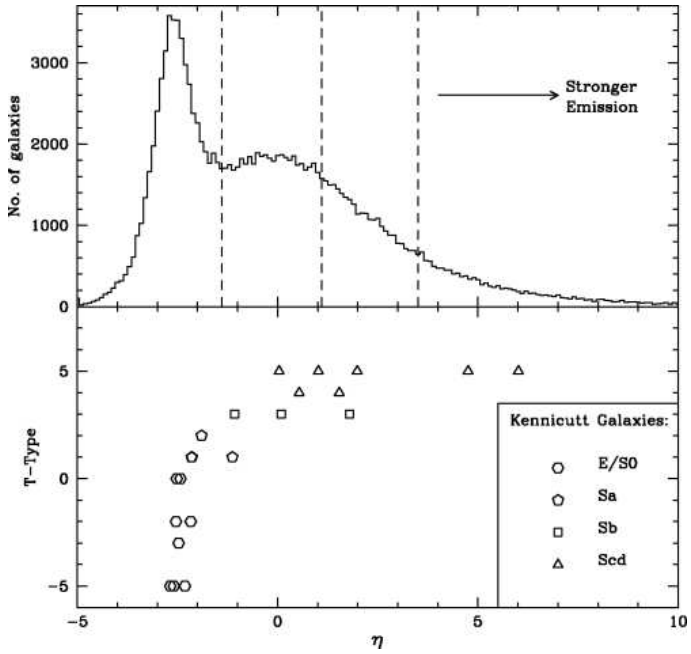

Figure 2.2: (Top) The distribution of η projections for the volume-limited sample of 2dF galaxies.Vertical lines show the devisions in η that correspond roughly to E/S0, early type S, late type S and Irr, used in the analysis of Madgwick et al. (2002) (Bottom) The η projections calculated for a subset of the Kennicutt Atlas galaxies. This plot is taken from Madgwick et al. (2003). (§2.5.2)

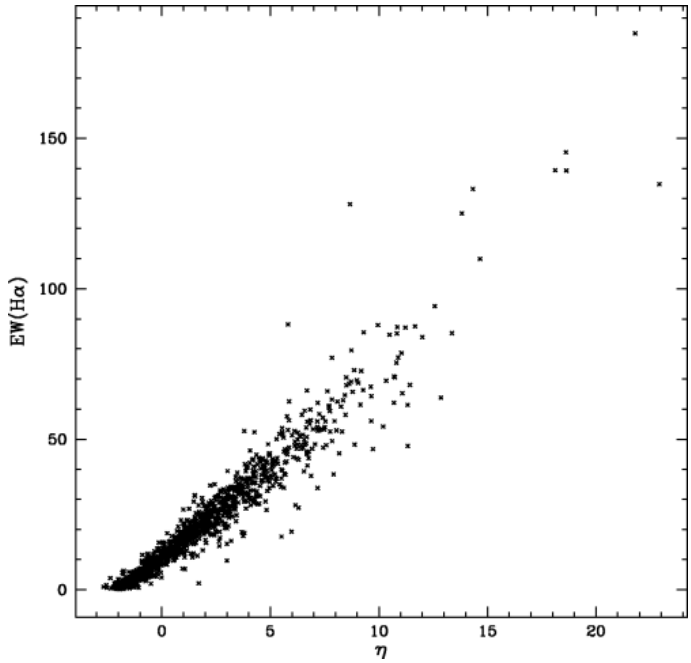

Figure 2.3: The correlation between η and the equivalent width of the Hα emission line for a sample of high signal-to-noise ratio emission-line spectra (Madgwick et al., 2003). (§2.5.2)

$$\mathrm{SFR(t)} = \frac{1}{\tau} e^{-(t-t_f)/\tau}, \tag{2.11}$$

where t_f is the time at which star formation first commences and τ is the characteristic timescale of the star formation.

The PEGASE software package is used to realize the model and deals with other tasks such as determining the strengths of nebula emission lines and dust extinction. Spectral histories of a given galaxy are compiled for a range of formation times (0–20 Gyr) and lengths of star formation activity (0–2 Gyr). The value of b is determined from:

$$\frac{\mathrm{SFR(t)}}{\langle \mathrm{SFR(t)} \rangle_{past}} = \frac{(t-t_f)}{\tau} \frac{e^{-(t-t_f)/\tau}}{(1-e^{-(t-t_f)/\tau})} = b. \tag{2.12}$$

The same analysis is also performed using a semi-analytic model. In the hierarchical model for the universe galaxies have built up from mergers and accretion. Mergers can trigger bursts of star formation, which in turn may inhibit future formation by expelling gas from the galaxy on stellar winds. This model can be convolved with stellar population models to produce model spectra. Madgwick et al. (2003) use a multi-metalicity GISSEL model (Bruzual, 1983) and a Salpeter IMF. They construct a mock 2dF catalogue of 2,611 model galaxies with the same magnitude limit, wavelength coverage, spectral resolution and redshift range as the actual 2dFGRS. They derive the principal components of the mock catalogue and the birth rate parameter b for each galaxy. They show that b has a strong relationship to the η parameter in both the simple model and the semi-analytic model. This relation is shown for the semi-analytic model in Fig. 2.4. It can be seen that galaxies with an η of less than approximately –1.4 have a value of $b < 0.1$, where the current SFR is only 10% of what it was in the past.

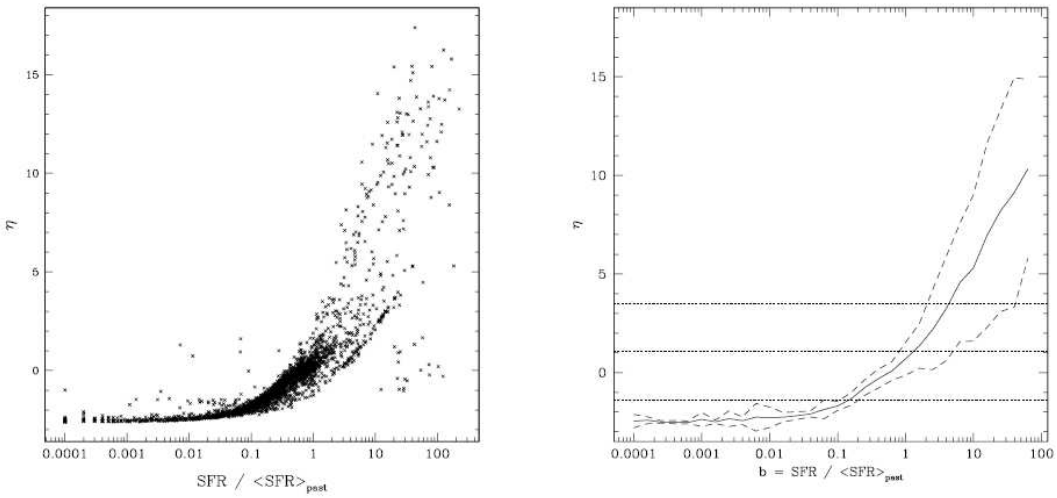

Figure 2.4: (Left) η plotted versus b for each galaxy in the SAM mock-galaxy catalogue. (Right) The mean value of η versus b for these galaxies (the dashed lines show the 1 σ uncertainties). Also shown on this plot (dotted lines) are the cuts in η used in Madgwick et al. (2002) to calculate the 2dFGRS luminosity functions per spectral type. It can be seen, for example, that the Type I galaxies of that paper ($\eta < -1.4$) correspond to galaxies with $b < 0.1$, or, alternatively, galaxies with current star formation activity that is only 10 per cent of their past-averaged rate. Figure taken from Madgwick et al. (2003). (§2.5.2)

2.5.3 Separating the star-forming and non star-forming populations

As mentioned previously (also see Fig. 2.5) a histogram of the η parameter is extremely bimodal. The first narrow peak corresponding to the non star-forming galaxies (approximately 30 % of all $z < 0.1$ galaxies) and the wider second peak the galaxies with current star formation.

To obtain the probability that a given galaxy falls within the first or second peak, $P(\eta)$, a series of likely functions were fitted to the two peaks such that,

$$\mathrm{P}(\eta) = \alpha g(\eta) + (1 - \alpha)\, f(\eta), \tag{2.13}$$

where $f(\eta)$ is a function of η to fit the first peak, $g(\eta)$ is a function of η to fit the second peak and α is a constant. $P(\eta)$ can be maximised such that,

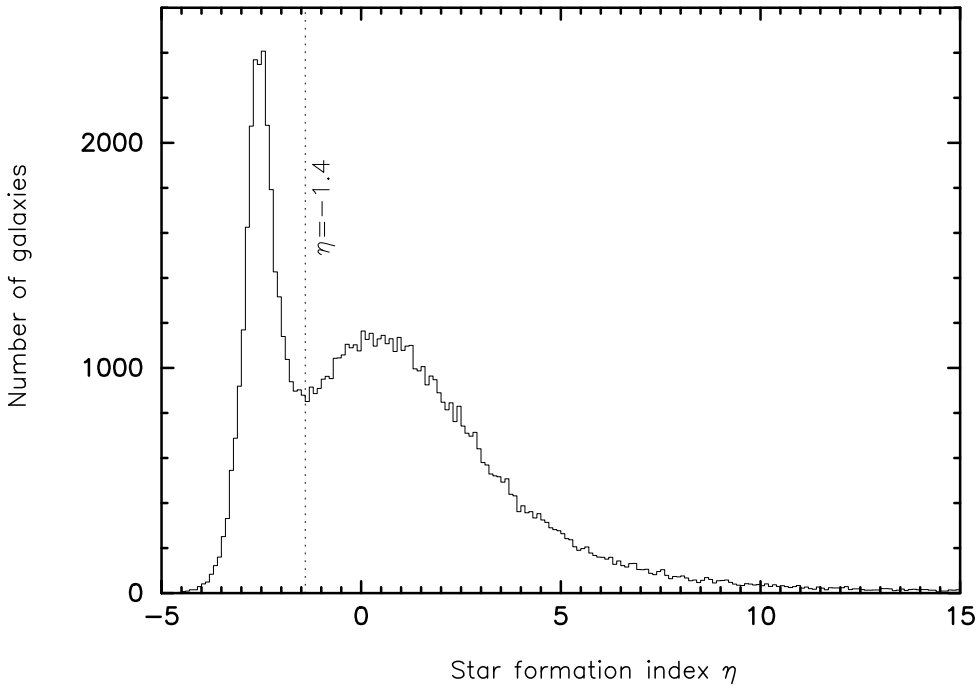

Figure 2.5: A histogram of the η parameter for all 2dFGRS galaxies with $z < 0.1$ binned in 0.1 η bins. (§2.5.3)

$$L = \sum lnP(\eta). \tag{2.14}$$

The first peak was fitted with a standard Gaussian function such that,

$$f(\eta) = \frac{1}{\sigma\sqrt{2\pi}} e^{\frac{-(\eta-\mu)^2}{2\sigma^2}}, \tag{2.15}$$

where μ is the position of highest point of the peak and σ is the standard deviation of the peak.

The second peak was fitted with an extreme value distribution such that,

$$g(\eta) = \frac{e^{(\sigma-\eta)/\mu - e^{(\sigma-\eta)/\mu}}}{\mu}. \tag{2.16}$$

L was fitted using the NAG routine E04JYF and the resulting fit can be seen as the dashed line in Fig. 2.6. However, it can be seen in Fig. 2.7 when the values of μ and σ obtained are used to plot the individual functions the Gaussian seen as the dashed red line is not an appropriate fit to the first peak.

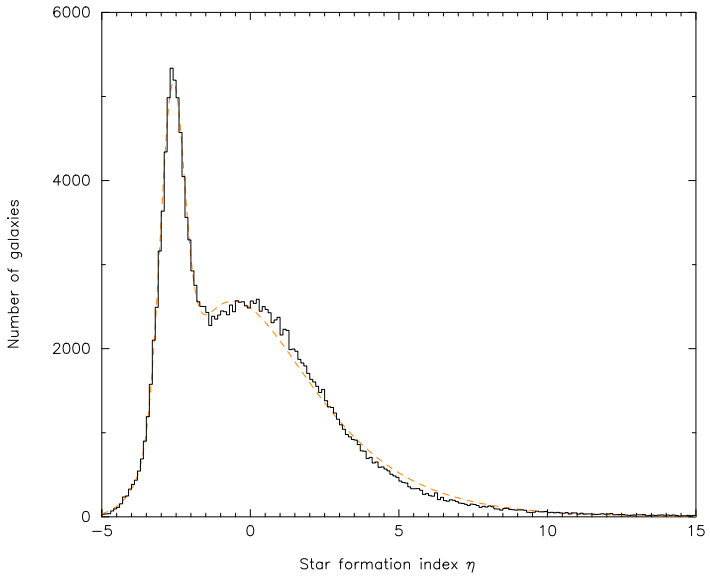

Figure 2.6: Composite fit to the 2dFGRS η parameter distribution. The resulting fit shown as the dashed orange line is a combination (eq.Fig. 2.13) of a Gaussian and an extreme value distribution. The histogram shown is for the entire 2dFGRS binned in 0.1η bins. (§2.5.3)

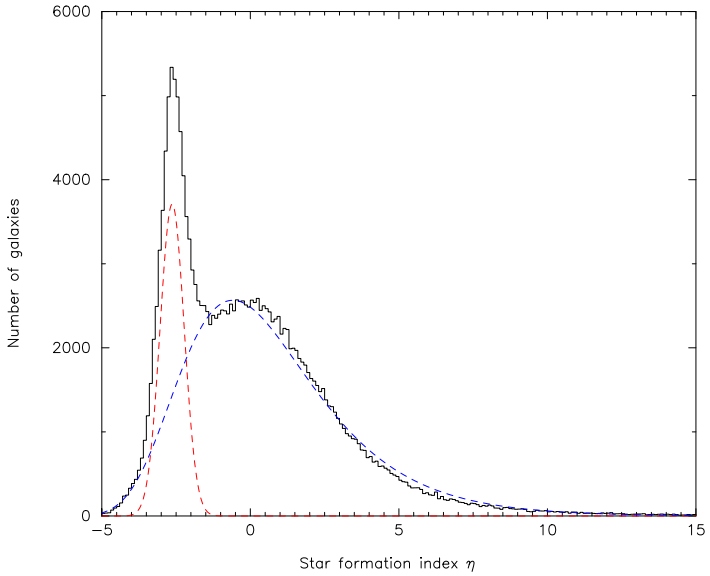

Figure 2.7: Individual fits to the 2dFGRS η parameter distribution. The red dashed line is the Gaussian function and the dashed blue line the extreme value distribution plotted with the values of μ and σ obtained from the composite fit. The histogram shown is for the entire 2dFGRS binned in 0.1η bins. (§2.5.3)

The above fitting of a sum of two distributions did not lead to a more elegant separation of the star-forming and non star-forming populations. A KMM algorithm (Ashman, Bird, & Zepf, 1994) could also have been used to partition the data in two subpopulations. However in the end it was decided that a complex solution to the bimodality was not needed and a transitional value set at $\eta = -1.4$, below which all galaxies will be classified as "passive" was chosen. This corresponds to, the divide between E/S0 and Sa galaxies in Fig. 2.2, a Hα EW$\sim$ 3 in Fig. 2.3 and a $b < 0.1$ in Fig. 2.4, where the current SFR is only 10% that it was in the past.

Chapter 3

Viscount Horatio Nelson: "Thank God I have done my duty."

Supercluster structure

Superclusters are an essential tool to study the largest-scale density perturbations that have given rise to structure in the Universe (e.g., Bahcall, 2000). These are particularly interesting since they have always evolved in the linear regime and can be analytically tractable. Superclusters can be useful in quantifying the the high-end mass function of collapsing systems and ratio of mass to light on the largest scales, thus being useful in discriminating between dark matter and structure formation models (e.g., Kolokotronis, Basilakos, & Plionis, 2002; Bahcall, 1988).

3.1 Minimal spanning tree supercluster structure

Superclusters are expected to be predominantly filamentary structures. Numerical simulations of the evolution of large-scale structure (e.g., Bond, Kofman, & Pogosyan, 1996; Colberg, Krughoff, & Connolly, 2005), as well as the analysis of large-volume surveys like the 2dFGRS (e.g., Pimbblet, Drinkwater, & Hawkrigg, 2004) or studies of individual systems of superclusters (e.g., Bagchi et al., 2002; Ebeling, Barrett, & Donovan, 2004) show the pre-eminence of filamentary structures. Nevertheless, supercluster catalogues are usually constructed (e.g., Einasto et al., 1994; Zucca et al., 1993) using percolation or friends-of-friends algorithms which do not take this geometrical feature into consideration.

Recently, Raychaudhury et al. (2007) have compiled a catalogue of supercluster-size structures from a redshift survey of Abell clusters ($z < 0.1$) using the minimal

spanning tree statistic, which contains all the information used in a percolation analysis (Bhavsar & Splinter, 1996), and is particularly sensitive to filaments (Bhavsar & Raychaudhury, 2000).

In this Chapter we investigate the structure of the three richest superclusters in the catalogue of Raychaudhury et al. (2007), Horologium-Reticulum, Shapley and Pisces-Cetus. We also gain estimates of the mass overdensity within each of the superclusters.

3.1.1 The Pisces-Cetus supercluster

More than a decade ago, in a series of papers, Tully (1986, 1987, 1988) pointed out the Pisces-Cetus supercluster to be one of the five richest systems of clusters of galaxies in the $z < 0.1$ Universe, and speculated that it could be as large as $300\,h_{70}^{-1}$ Mpc across, and might include the Local Group. Subsequent work (e.g., Zucca et al., 1993; Einasto et al., 1994) has pointed out interesting features of significantly smaller substructures of this remarkable web of galaxies, groups and clusters, and at least one unusually large void (Burns et al., 1988).

The Pisces-Cetus supercluster is found to straddle the 2dF galaxy redshift survey (Colless et al., 2003) [2dFGRS] and the Sloan Digital Sky Survey (Abazajian et al., 2005) [SDSS] regions.

In the supercluster catalogue of Raychaudhury et al. (2007), the Pisces-Cetus supercluster occupies a region of about 700 sq. deg. of the (equatorial) southern sky. While using the Minimal Spanning Tree (MST) in constructing this catalogue, if a maximum edge-length of $20\,h_{100}^{-1}$ Mpc is used, the system breaks up into two filaments (A, B) of 11 and 5 clusters respectively, at mean redshifts of 0.0625 and 0.0545 respectively. If, however, adjacent clusters on the tree are allowed to be separated by a distance of up to $25\,h_{100}^{-1}$ Mpc, the supercluster becomes a long filament of 19 clusters at a mean redshift of 0.0591, making the supercluster the third richest in the catalogue (following the Shapley and Horologium-Reticulum superclusters). This is illustrated in Fig. 3.1, where the clusters excluded by the former consideration are shown to be connected to the main tree by dashed lines.

The clusters comprising the Pisces-Cetus supercluster from the MST analysis of

Raychaudhury et al. (2007) form the core of our sample, and are listed in Table 3.1. Unlike MST analyses of galaxy catalogues, where completeness is an important consideration, the supercluster list obtained in this catalogue is considered reasonably complete since it arises from an analysis of rich Abell clusters in the volume closer than $z < 0.1$ (Galactic latitude $|b| > 20^{\circ}$).

To the member list of the Pisces-Cetus Supercluster from the above list, we added a few clusters, in the same volume as the filament, from the Supplementary Abell cluster catalogue (Abell et al., 1989) and the Edinburgh-Durham Southern Galaxy Cluster Catalogue (Lumsden et al., 1997). These extra clusters were taken as potential members of the supercluster if their redshift as derived in §3 was found to be consistent with the other members.

A plot of these clusters within the supercluster region and redshift range, including the connecting MST, can be seen in Fig. 3.1. Also plotted are the groups of galaxies in the region of the supercluster covered by the 2dFGRS ($\delta < -25^{\circ}$) from the 2dFGRS Percolation-inferred Galaxy Group (2PIGG) catalogue (Eke et al., 2004), which are seen to follow a filamentary structure (though not necessarily the tree defined by the MST), as expected from numerical simulations where groups are seen to preferentially form on filaments and move along filaments to fall into clusters. For comparison, Fig. 3.2 shows all galaxies with spectroscopic redshifts from the SDSS and 2dFGRS catalogues, where only galaxies within 3000 km s $^{-1}$ of the upper and lower redshift bounds of the supercluster have been plotted. Overdensities of galaxies are clearly visible in the regions around the richer clusters and the filamentary structure of the supercluster is also visible.

A combined look at Figs. 3.1 and 3.5 through 3.7 reveals that the supercluster is made of two main filaments. From Fig. 3.5 which plots redshift against Right Ascension for the groups and clusters in the region, it is evident that the filament containing A85 is at a lower redshift than the longer filament, which has A133 at the near end and A2716 at the more distant end. The poorer clusters E0332 and S1155, appear to be in a clump separated from both of the main filaments, with a filament of groups joining these three clusters to the principal filament. These trends are also seen in Fig. 3.7 which plots redshift against declination for the groups and clusters

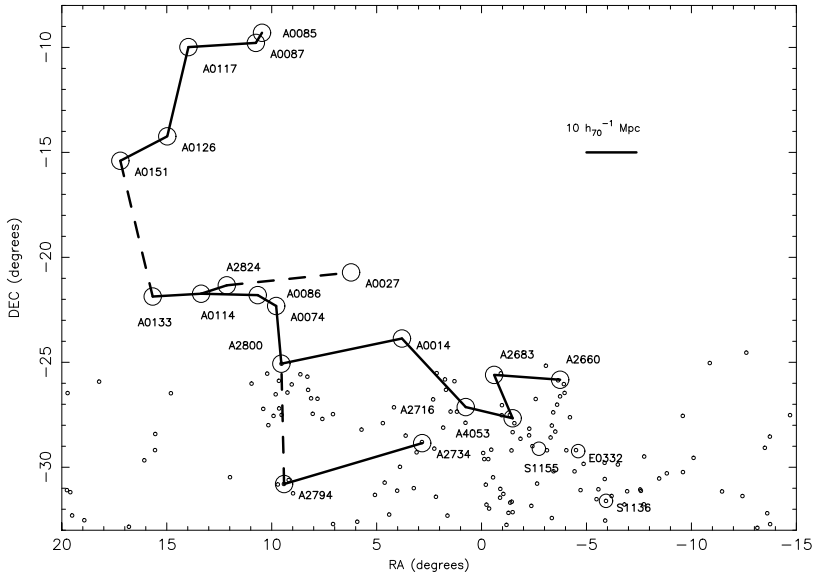

Figure 3.1: Clusters of galaxies belonging to Pisces-Cetus supercluster. The minimal spanning tree used to identify the supercluster (Raychaudhury et al., 2007) is shown connecting the clusters. Edges in the tree with length $20\,h_{100}^{-1} < L \leq 25\,h_{100}^{-1}$ Mpc are shown as dashed lines. The groups of galaxies (2PIGG) identified from a friends-of-friends analysis of the 2dFGRS (Eke et al., 2004) are shown as little circles between redshifts of 13507 and 22810 km s^{-1}, which is $\pm$ 3000 km s^{-1} from the lowest/highest cluster redshifts of chain A 20 h_{100}^{-1} Mpc links. (§3.1.1)

in the region. Although, the filament of groups linking the E0332, S1155 clump to the main chain is less visible.

It is also possible to see the filamentary structure and concentration of galaxies at the cluster positions in Fig. 3.3. All of all the galaxies in the SuperCOSMOS galaxy catalogue within the Pisces-Cetus supercluster bounds are shown. All galaxies had to be classified as a galaxy in each of the three bands B, I and R2. In addition, the quality of the detection had to be less than 128 in each band and $gCorMagB < 20.0$, where $gCorMagB$ is the magnitude if the object is assumed to be a galaxy. By eye, circular concentrations can be seen at the junction of long thin filaments at the positions of Abell clusters. This is confirmed in Fig. 3.4 showing the density contours of the galaxies in Fig. 3.3. Green contours showing the higher density regions can be seen at the positions of Abell clusters.

Fig. 3.6 shows all the galaxies with redshifts from 2dFGRS and ZCAT in the declination range $-32^\circ < \delta < -20^\circ$. The diagram shows clearly the filamentary nature of the supercluster and the positions of the Abell clusters on the filaments.

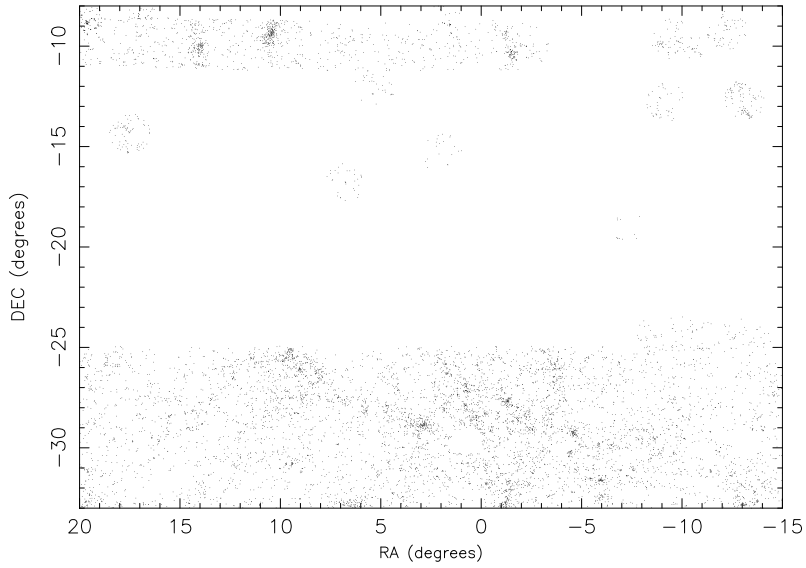

Figure 3.2: All galaxies with measured redshifts from the 2dFGRS and SDSS surveys in the Pisces-Cetus region, between redshifts of 13507 and 22810 km s^{-1}, which is ± 3000 km s^{-1} from the lowest/highest cluster redshifts of chain A 20 h_{100}^{-1} Mpc links. The SDSS reaches down to $\delta = -10°$ in this R.A. range, and covers the clusters A85, A87 and A117. The SDSS reaches up to $\delta = -25°$, and thus a large part of the supercluster falls in the gap between the two surveys, except for the occasional isolated two-degree fields of the 2dFGRS. (§3.1.1)

There are some clusters not obviously associated with overdensities, these are in the declination range not covered by the 2dFGRS.

3.1.2 The Horologium-Reticulum Supercluster

Harlow Shapley (Shapley, 1935) was the first to note that the Horologium region was abnormally rich in galaxies. Since then further studies have confirmed the presence of an overdense region of clusters and galaxies (e.g., Lucey et al., 1983; Einasto et al., 2003; Fleenor et al., 2005, 2006). Lucey et al. (1983) were the first to obtain redshifts and find velocity dispersions for the clusters in the Horologium-Reticulum supercluster region, thus confirming the superclusters existence. More recently the region has been shown to have entered the non-linear regime with a mass overdensity of 2.4 (Fleenor et al., 2005).

In the supercluster catalogue of Raychaudhury et al. (2007) if a maximum edge length of 25 h_{100}^{-1} Mpc is used in the MST analysis the Horologium-Reticulum su-

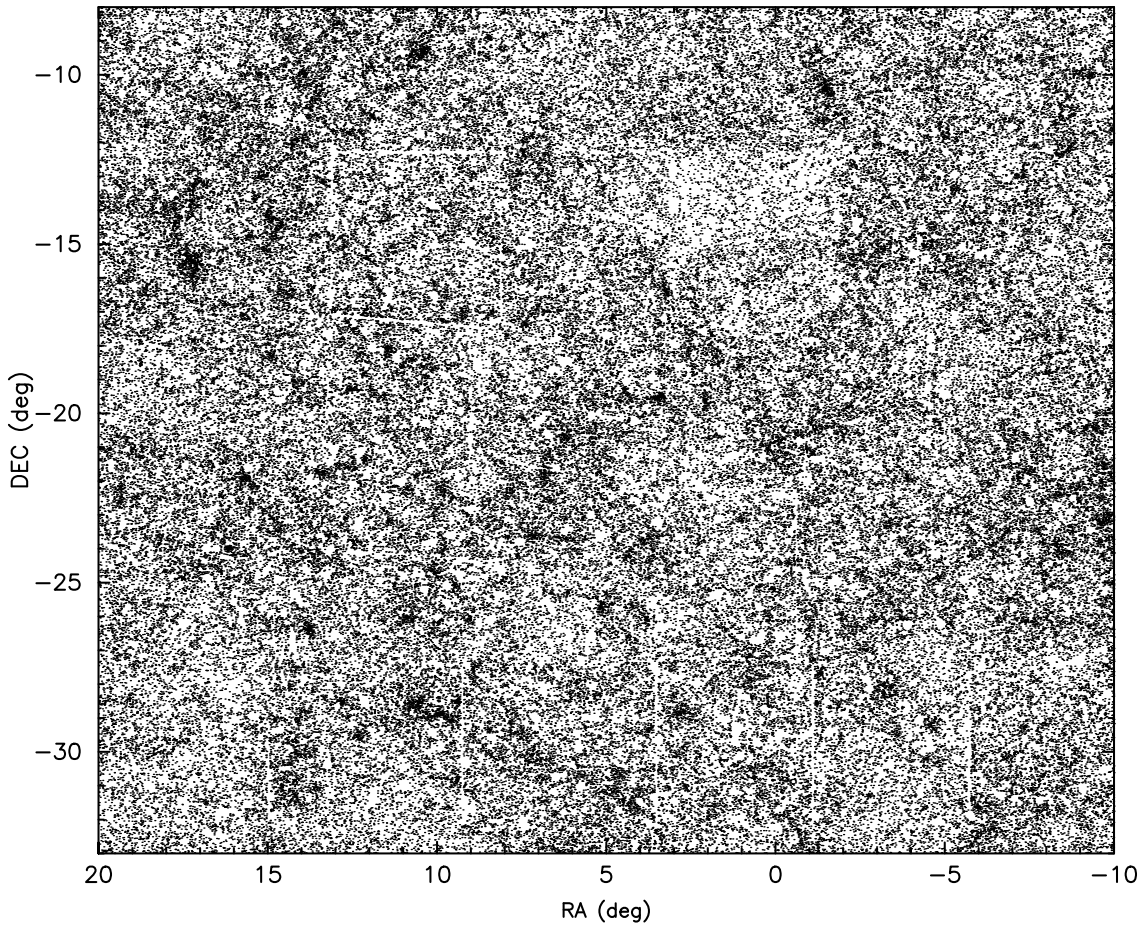

Figure 3.3: All galaxies in the SuperCOSMOS galaxy catalogue within the Pisces-Cetus supercluster bounds. All galaxies are classified as a galaxy in each of the three bands B,I and R2. In addition the quality of the detection is less than 128 in each band and gCorMagB$<$ 20.0 (magnitude if the object is assumed to be a galaxy). (§3.1.1)

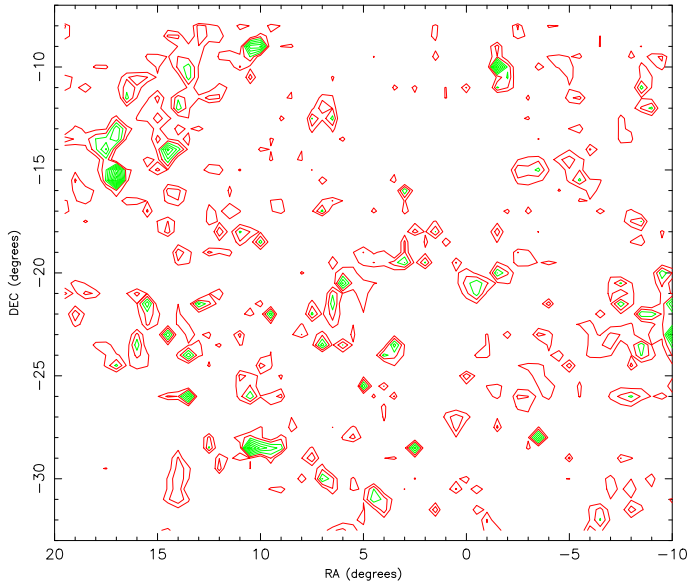

Figure 3.4: Density contours of all galaxies in the SuperCOSMOS galaxy catalogue within the Pisces-Cetus supercluster bounds. All galaxies are classified as a galaxy in each of the three bands B,I and R2. In addition the quality of the detection is less than 128 in each band and gCorMagB< 20.0 (magnitude if the object is assumed to be a galaxy) Contours range from 75 to 225 galaxies per 1 $degree^2$ bin in 10 increments of 15 galaxies. Contours are shown in red below and green for and above the 120 galaxies per bin level. (§3.1.1)

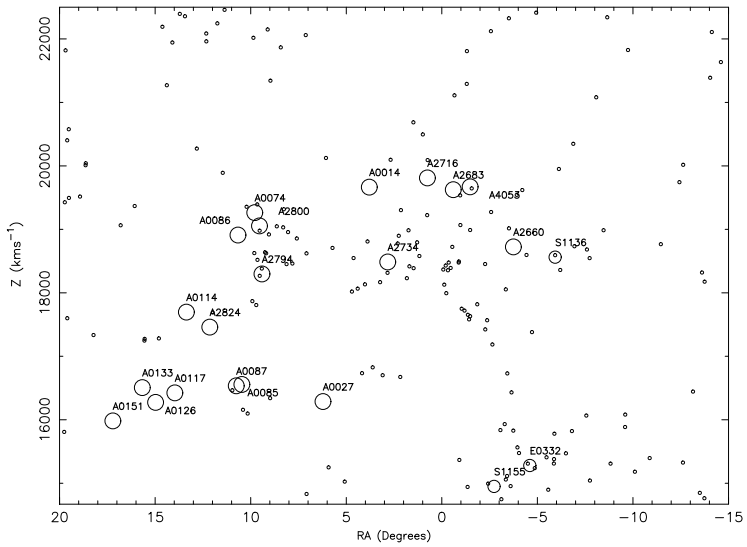

Figure 3.5: Clusters of galaxies belonging to Pisces-Cetus supercluster, covering the declination range $-32° < \delta < -9°$). The 2PIGG groups of galaxies are shown as little circles, but only in the declination range covered by the 2dFGRS $-32° < \delta < -25°$). (§3.1.1)

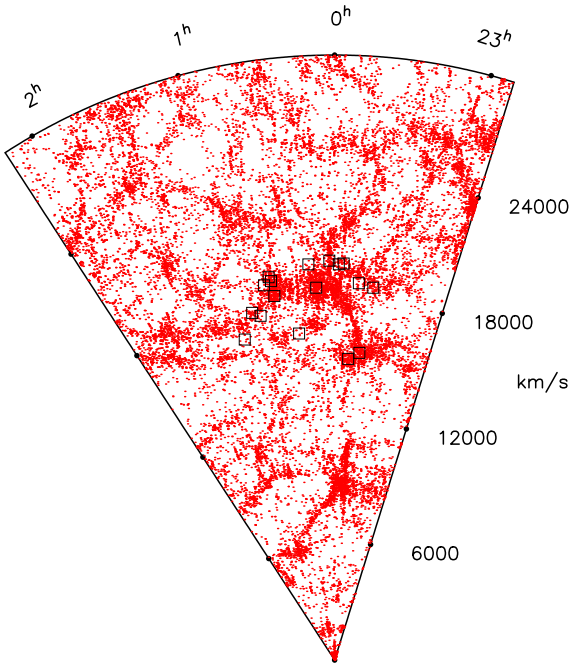

Figure 3.6: Galaxies with redshifts (mostly from 2dFGRS, see §3) in the Pisces-Cetus supercluster region (Declination range $-32° < \delta < -20°$). The mean positions of the clusters in the supercluster are marked. The 2dFGRS only goes up to $\delta < -25°$, which is why some of the clusters don't seem to be associated with obvious concentrations. (§3.1.1)

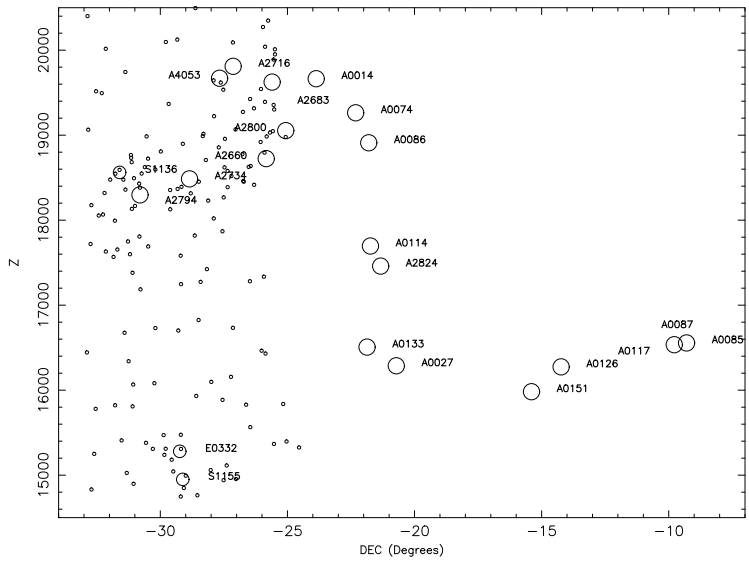

Figure 3.7: Clusters of galaxies belonging to Pisces-Cetus supercluster, covering the Right Ascension range $345° < \delta < 20°$). The 2PIGG groups of galaxies are shown as little circles. (§3.1.1)

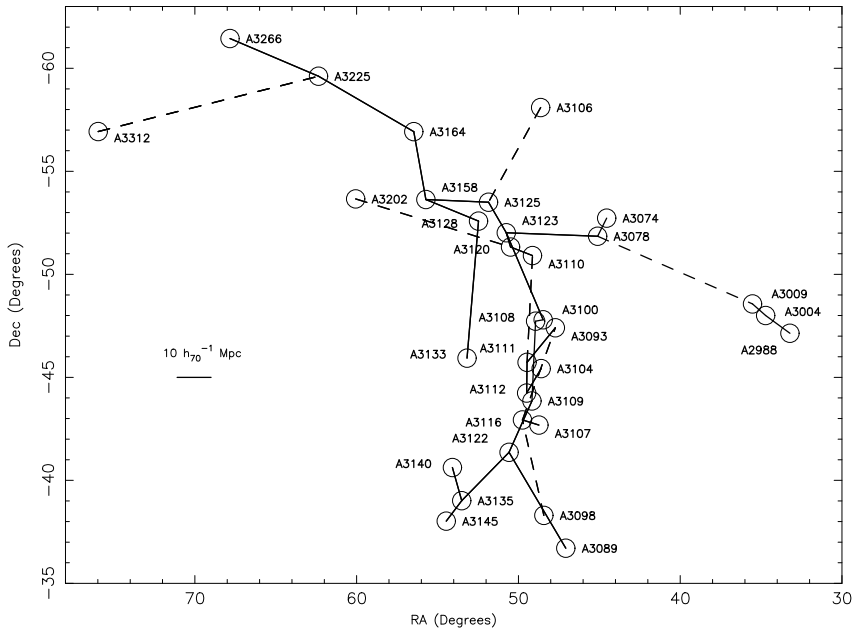

Figure 3.8: Clusters of galaxies belonging to Horologium-Reticulum supercluster. The minimal spanning tree used to identify the supercluster (Raychaudhury et al., 2007) is shown connecting the clusters. Edges in the tree with length $20\,h_{100}^{-1} < L \leq 25\,h_{100}^{-1}$ Mpc are shown as dashed lines. (§3.1.2)

percluster comprises 33 Abell clusters making it the richest in the catalogue. The supercluster occupies approximately 1300 degrees^2 of the equatorial southern sky. The mean redshift of the supercluster is 0.067 but with a range in z from 0.0567 to 0.084 a lot of the structure is radial direction. The clusters comprising the Horologium-Reticulum supercluster are those of the MST analysis of Raychaudhury et al. (2007), and are listed in Table 3.2.

A plot of these clusters within the supercluster region and redshift range, including the connecting MST, can be seen in Fig. 3.8. The radial nature of the supercluster is evident with many clusters and links falling on top of each other in R.A.-Dec. space.

For comparison, Fig. 3.9 shows all galaxies with spectroscopic redshifts from the latest version of ZCAT, where only galaxies between 13000 km s $^{-1}$ and 30000 km s $^{-1}$ have been plotted. Overdensities of galaxies are clearly visible in the regions around the richer clusters.

Fig. 3.11 and Fig. 3.10 clearly show the large radial component to the superclusters structure using the redshift information described below.

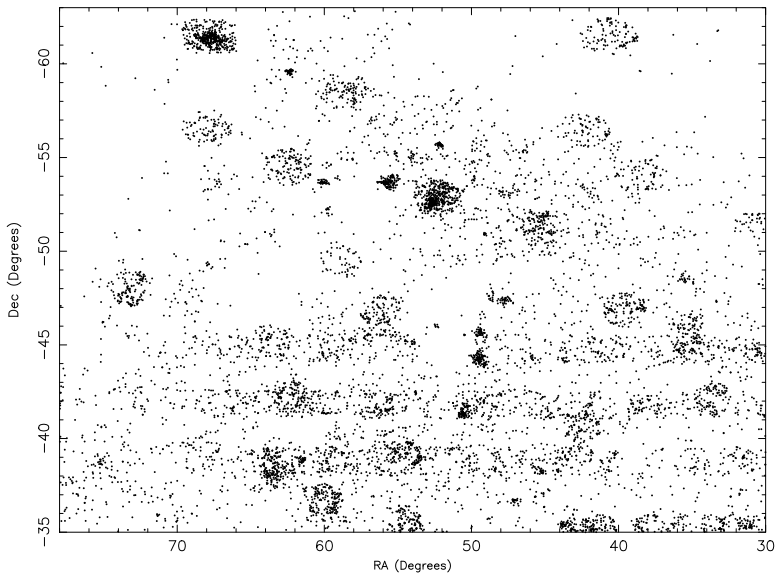

Figure 3.9: All galaxies with measured redshifts from the latest version of ZCAT (http://cfa-www.harvard.edu/∼huchra/zcat/) in the Horlogium-Reticulum region, between redshifts of 13965 and 28337 km s^{-1}, which is ± 3000 km s^{-1} from the lowest/highest cluster redshifts. (§3.1.2)

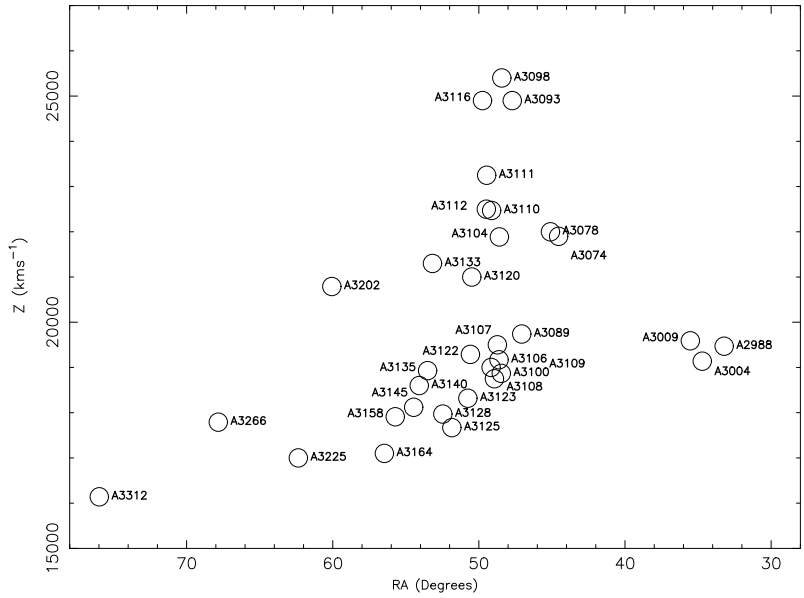

Figure 3.10: Clusters of galaxies belonging the Horologium-Reticulum supercluster in R.A.-redshift space, covering the declination range $-63° < \delta < -35°$. (§3.1.2)

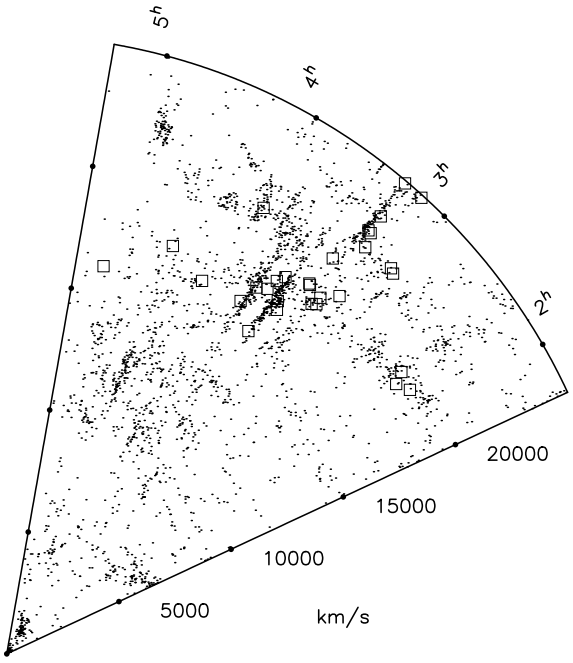

Figure 3.11: Galaxies with redshifts from the latest version (2005) of ZCAT in the Horologium-Reticulum supercluster region (Declination range $-63° < \delta < -35°$). The mean positions of the clusters in the supercluster are marked. (§3.1.2)

3.1.3 The Shapley supercluster

The clusters comprising the Shapley supercluster are those of the catalogue of Raychaudhury et al. (2007). A plot of the resulting members including the MST links can be seen in Fig. 3.12 and a list of the clusters can be found in table 3.3. Fig. 3.12 shows all galaxies with measured redshifts from NED in the region, overdensities of galaxies at the cluster positions are clearly visible.

With a maximum edge length of 25 h_{100}^{-1} Mpc in the MST analysis, the Shapley supercluster forms one large structure of 29 Abell clusters which can be seen in Fig. 3.12 at a mean redshift of $z = 0.0476$. Fig. 3.14 clearly shows that the supercluster is separated into two sections in the radial direction. The main group containing the core of A3555, A3556 and A3558 centred around 15000 km s^{-1} and the smaller group containing A3571 is at approximately 12000 km s^{-1}. While being within the central regions in R.A.-Dec. space, A3546 is quite isolated in the radial direction from the two main groups.

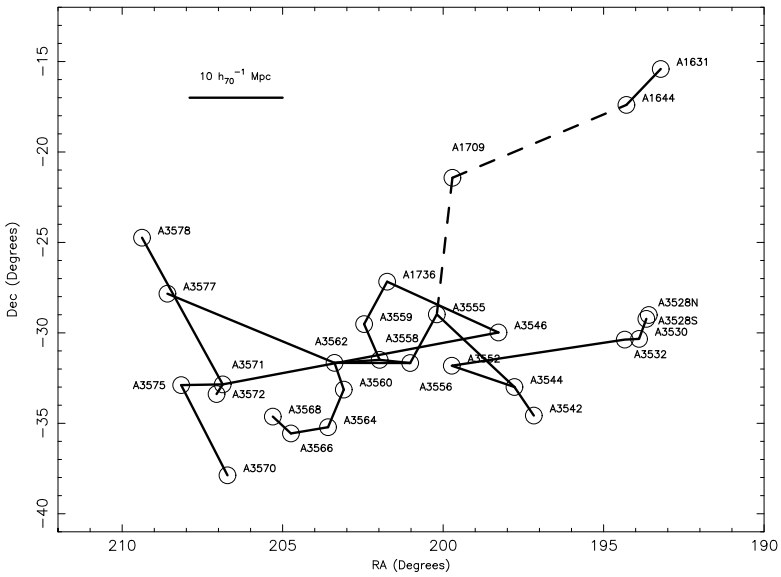

Figure 3.12: Clusters of galaxies belonging to the Shapley supercluster. The minimal spanning tree used to identify the supercluster (Raychaudhury et al., 2007) is shown connecting the clusters. Edges in the tree with length $20\,h_{100}^{-1} < L \leq 25\,h_{100}^{-1}$ Mpc are shown as dashed lines. (§3.1.3)

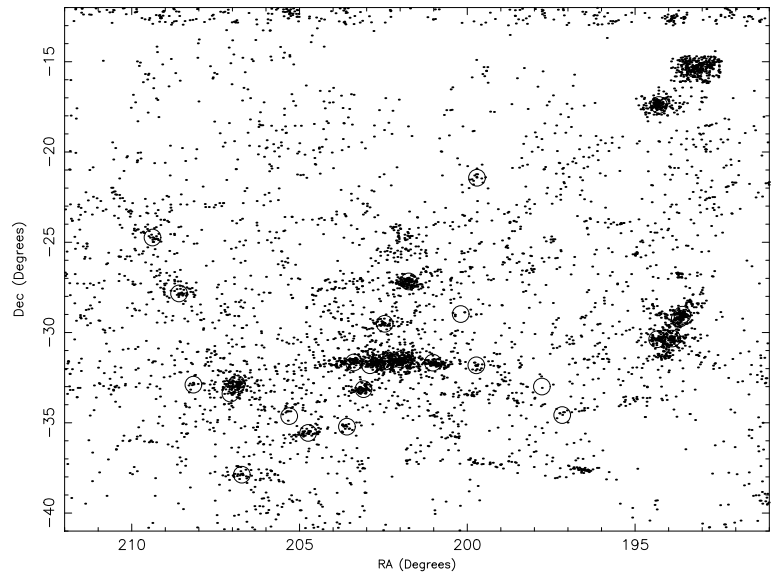

Figure 3.13: All galaxies with measured redshifts from NED in the Shapley supercluster region, between redshifts of 10462 and 19480 km s^{-1}, which is ± 3000 km s^{-1} from the lowest/highest cluster redshifts of the main chain at a mean redshift of approximately 15000 km s^{-1}. (§3.1.3)

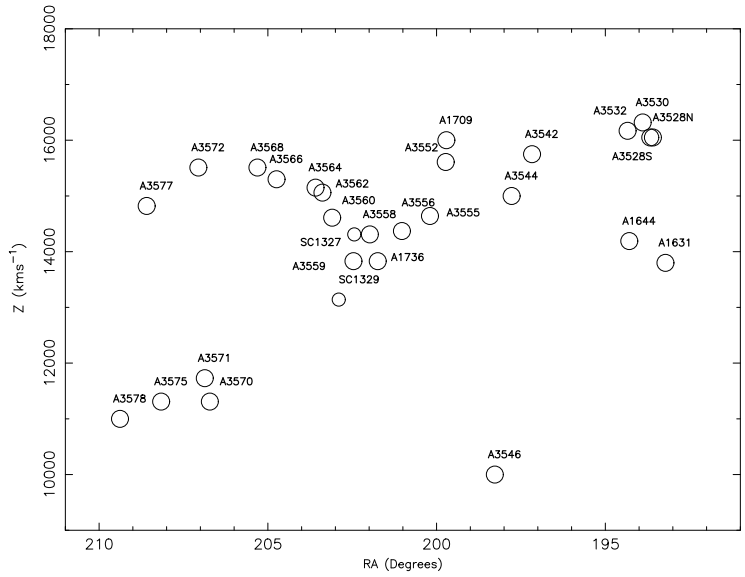

Figure 3.14: Clusters of galaxies belonging the Shapley supercluster in R.A.-redshift space, covering the declination range $-41° < \delta < -12°$. (§3.1.3)

3.2 Mean redshift and velocity dispersion

Positions from the NASA/IPAC Extragalactic Database (NED) were taken as a starting point for the cluster centres, and then they were located on UK Schmidt Telescope (UKST) B_J plates. The NED positions, particularly those from Abell et al. (1989), were largely inadequate. Therefore, centres were determined from available X-ray data whenever possible, and from a visual inspection of the appropriate UKST plates otherwise.

Redshifts were taken from all available sources including NED, ZCAT (http://cfa-www.harvard.edu/∼huchra/zcat/), the second data release of the 6dF Galaxy Survey Database (Jones et al., 2005) [6dFGS DR2], the 2dF galaxy redshift survey (Colless et al., 2003) and the second release (DR2) of the Sloan Digital Sky Survey (Abazajian et al., 2005). In the case of Horologium-Reticulum supercluster additional redshifts were gained from Fleenor et al. (2005) and Fleenor et al. (2006). For the Shapley supercluster the NED redshifts came largely from Kaldare et al. (2003).

Galaxies were initially extracted from these catalogues within an Abell radius (2.14 h_{70}^{-1} Mpc, 1.5 h_{100}^{-1} Mpc) of the new cluster centres and filtered for repeated galaxies. In the case of the very dense Shapley supercluster, an initial circle of radius of 2.14 h_{70}^{-1} Mpc was tried around each cluster. If this did not overlap any

other clusters this was adopted as the extraction radius for galaxies. If an overlap was present the size was modified accordingly till each extraction area was unique.

In the case of Abell 85/87 it has been shown (Durret et al., 2003) while Abell 85 is a strong X-ray source Abell 87 is not detected. It is likely that Abell 87 is in fact a system of filaments and groups of galaxies merging with A85. Therefore, while the same extraction was performed for A87 as the other clusters it is likely that many of the extracted galaxies are members of the large merging cluster of Abell 85. Because of this ambiguity A87 is not used in our virial mass estimates described below.

For clusters that have redshifts available for ≥ 4 galaxies, within the extraction radius, mean recessional velocities were calculated, using an iterative process clipping 3σ about the median, and finally calculating the mean. If ≥ 12 galaxies with known redshift remained, the velocity dispersion of the cluster and its error were calculated, using a method that takes into account observational errors on individual redshift measures (Danese, de Zotti, & di Tullio, 1980). The dispersion is given by,

$$\sigma_{\parallel}^2 = \sum_i \frac{\upsilon_{\parallel i}^2}{(n-1)} - \frac{\delta^2}{(1+\frac{\bar{\nu}_{\parallel}}{c})^2}, \tag{3.1}$$

where $\upsilon_{\parallel}$ is the radial velocity of a galaxy relative to the mean cluster velocity, $\bar{\nu}_{\parallel}$ is the mean cluster velocity, n is the number of galaxies in the cluster and δ is the sum of the uncertainties on the individual galaxy radial velocities. The 68% uncertainties on the velocity dispersion are given by,

$$(\Delta\sigma_{\parallel\pm})^2 \cong \Big[\Big(\frac{\nu}{\chi_{\mp}^2} - 1\Big)^{1/2}\Big]^2 \sigma_{\parallel}^2 + \frac{\bar{\delta}_*^2}{n}\Big(1 + \frac{\bar{\delta}_*^2}{2\sigma_{\parallel}^2}\Big), \tag{3.2}$$

where $\bar{\delta}_*^2 = \frac{\bar{\delta}^2}{\left(1+\frac{\bar{\nu}_{\parallel}}{c}\right)^2}$, n is the number of galaxies in the cluster, ν is $n-1$ and $\chi_{\mp}^2$ is taken from the table of Danese, de Zotti, & di Tullio (1980) for small values or from,

$$\chi_{\pm}^2 \cong \nu\Big[1 - \frac{2}{9\nu} \pm \chi_p\big(\frac{2}{9\nu}\big)^{1/2}\Big]^3 \tag{3.3}$$

for $\chi^2 > 30$.

The resulting mean velocities, velocity dispersions and the number of cluster members used to calculate them can be found in Table 3.1, Table 3.2 and Table 3.3, for each cluster belonging to the Pisces-Cetus, Horologium-Reticulum and Shapley superclusters respectively.

Our mean velocities for the clusters of the Horologium-Reticulum supercluster are in good agreement with those of Fleenor et al. (2006). 16 out of 18 clusters agree to within 240 km s^{-1} and the remaining 2 to within 370 km s^{-1}.

The velocity dispersions of Fleenor et al. (2006) are in reasonable agreement with our own, 5 out of 7 of the clusters agreeing within 170 km s^{-1}. While the remaining two, A3109 and A3164 agreeing within 441 km s^{-1} and 286 km s^{-1} respectively both have some ambiguity on the edges of the cluster in the velocity histograms of figs 3.18 and 3.19.

Velocity histograms for the clusters can be seen in figs. 3.16 to 3.19. Where more than a peak is obviously present, the velocity dispersion of the peak closest to the current literature value of the clusters mean velocity has been adopted. When an accepted current mean velocity is unavailable, the peak closest to the mean recessional velocity of the supercluster has been adopted.

Fig. 3.16 shows the radial velocity histograms for the Pisces-Cetus supercluster. Fig. 3.19 shows the velocity histograms for clusters in the Shapley supercluster that had an extraction radius equal to the Abell radius while Fig. 3.19 shows those with a reduced extraction radius. The reduced extraction radius is shown in the top centre of each clusters panel as a fraction of the Abell radius. Fig. 3.17 shows the velocity histograms for the Horologium-Reticulum supercluster.

3.2.1 Models of Surface brightness

To obtain an estimate of the mass of each of the clusters (see §3.3), it was necessary to obtain a surface brightness profile for each cluster. For all clusters belonging

Table 3.1: Clusters belonging to the Pisces-Cetus Supercluster

Cluster.	R.A. (J2000)	Dec. (J2000)	cz km s^{-1}	# z	$L_{\rm x}$ $\times 10^{44}$ ergs^{-1}	T keV	Rich	Survey	σ_r km s^{-1}	r_{200} Mpc	r_v Mpc	$M_{\rm NFW}$ $10^{15}\,M_\odot$
A0014	00 15 10.9	-23 52 56	19665	13	0.51_b	$2.8_{b,*}$	0	-	643^{+185}_{-100}	2.01	3.85	0.72
A0027	00 24 52.1	-20 43 14	16287	6	$<0.028_d$	1.0_*	0	-		0.63	3.08	
A0074	00 39 08.8	-22 19 49	19264	11	0.021_a	1.1_*	0	-		0.88	3.47	
A0085	00 41 50.8	-09 18 18	16556	294	12.47_c	6.2_a	1	S	1016^{+44}_{-39}	2.08	0.82	0.67
A0086	00 42 40.0	-21 48 01	18911	12	0.094_a	1.3_*	0	-		1.71	3.67	
A0087	00 43 01.0	-09 47 36	16535	194			1	S	987^{+54}_{-46}			
A0114	00 53 27.5	-21 44 42	17696	24	0.055_a	1.4_*	0	-	525^{+100}_{-65}	1.57	2.95	0.34
A0117	00 55 51.9	-09 59 09	16424	101	0.26_a	1.5_*	0	S	604^{+47}_{-38}	1.77	3.13	0.45
A0126	00 59 53.8	-14 14 41	16274	11	0.027_d	1.2_*	1	-		1.31	3.06	
A0133	01 02 41.2	-21 52 45	16507	20	3.81_c	3.8_a	0	-	687^{+146}_{-90}	1.97	2.97	0.69
A0151	01 08 51.1	-15 24 23	15982	73	0.70_b	$3.1_{b,*}$	1	-	699^{+66}_{-52}	1.58	1.01	0.32
A2660	23 45 16.0	-25 50 09	18724	17	0.049_d	1.7_*	0	0.73	800^{+189}_{-111}	2.29	3.41	1.00
A2683	23 57 36.7	-25 36 44	19625	11			0	0.88		0.65	3.96	
A2716	00 03 01.3	-27 08 11	19810	77			0	0.85	812^{+75}_{-59}	2.27	3.84	0.77
A2734	00 11 19.5	-28 51 41	18486	141	2.22_c	$4.4_{b,*}$	1	0.82	848^{+55}_{-46}	1.64	0.62	0.38
A2794	00 37 38.1	-30 48 59	18298	34			1	0.97	365^{+56}_{-40}	0.73	0.39	0.04
A2800	00 38 09.4	-25 04 51	19054	79			1	0.81	567^{+52}_{-41}	1.67	3.43	0.36
A2824	00 48 34.0	-21 20 36	17460_e	7	0.47_b	$2.8_{b,*}$	0	-				
A4053	23 54 46.0	-27 40 18	19670	26			1	0.88	398^{+72}_{-48}	1.54	3.44	
S1136	23 36 16.9	-31 36 20	18562	54	1.25_b	$3.7_{b,*}$	0	0.89	602^{+68}_{-51}	1.86	4.41	0.59
S1155	23 49 44.0	-29 07 13	14950	33			0	1.00	345^{+57}_{-42}	1.20	2.92	0.17
ED332	23 41 35.5	-29 14 11	15280	84				1.00	477^{+43}_{-35}	1.46	2.61	0.30

(1) Name of cluster (A*** and S*** Abell et al. (1989), ED332 Lumsden et al. (1997).

(2,3) Equatorial J2000 centres (we use centroids of X-ray emission where available).

(4) Redshift (see §3.2).

(5) Number of cluster member redshifts used to find the mean cluster redshift ((e) Struble & Rood (1999) and §3.2).

(6)Bolometric X-ray luminosities ((a)Jones & Forman (1999). (b) Cruddace et al. (2002); (c) Reiprich & Böhringer (2002); (d) Ledlow et al. (2003)).

(7) Temperature (∗=estimated from $L_X - T$ relation Osmond & Ponman (2004)).

(8) Abell richness (Abell et al. (1989)).

(9) Survey coverage [S=Sloan, Number= completeness in 2dFGRS field].

(10) Velocity dispersion (see §3.2).

(11) r_{200} in h_{70}^{-1} Mpc (see Eq. (3.26)).

(12) Virial radius (see Eq. (7)).

(13) Cluster virial mass within an Abell radius (2.14 h_{70}^{-1} Mpc) (see Eq. (3.19)).

Table 3.2: Clusters belonging to the Horologium-Reticulum Supercluster

Cluster	R.A. (J2000)	Dec. (J2000)	cz km s^{-1}	# z	Rich	σ_r km s^{-1}	r_{200} Mpc	r_v Mpc	$M_{\rm NFW}$ $10^{15}\,M_\odot$
A2988	02 12 52.3	-47 08 24	19663	8	1			0.31	
A3004	02 18 51.8	-47 59 57	19565	7	0			3.31	
A3009	02 22 06.9	-48 33 50	19713	16	1	493^{+122}_{-71}	1.50	3.44	0.32
A3074	02 58 11.2	-52 43 42	21580	7	0			3.64	
A3078	03 00 25.0	-51 50 53	21768	42	0	499^{+66}_{-48}	1.30	1.90	0.23
A3089	03 08 16.8	-36 42 31	19779	31	0	628^{+100}_{-68}	1.18	0.44	0.15
A3093	03 10 52.6	-47 24 19^{dx}	24667	30	2	685^{+111}_{-75}	1.82	4.23	0.43
A3098	03 13 43.1	-38 18 03	25337	12	0	311^{+96}_{-51}	1.04	3.68	0.11
A3100	03 13 52.7	-47 47 34	18901	22	0	312^{+63}_{-41}	1.06	3.40	0.12
A3104	03 14 22.8	-45 25 23^{ex}	21822	66	0	731^{+73}_{-56}	1.98	3.75	0.62
A3106	03 14 29.8	-58 05 48	19529	12	0	429^{+124}_{-67}	0.88	0.47	0.07
A3107	03 14 56.4	-42 41 07	19108	23	1	1045^{201}_{127}		4.10	
A3108	03 15 44.9	-47 43 39^{b}	18931	21	1	382^{+79}_{-50}		3.15	
A3109	03 16 39.2	-43 51 19	18925	21	0	1520^{+209}_{-148}	1.31	4.80	0.20
A3110	03 16 31.1	-50 54 44	22489	7	0		3.63		
A3111	03 17 51.6	-45 43 43	23257	47	1	931^{+114}_{-84}	2.35	3.89	0.87
A3112	03 17 57.8	-44 14 18^{dx}	22401	82	2	1087^{+96}_{-76}	2.67	3.75	1.33
A3116	03 19 00.0	-42 56 02	24015	13	0	1334^{+407}_{-212}	3.48	4.60	2.66
A3120	03 21 56.4	-51 19 36	21247	5	0				
A3122	03 22 18.6	-41 21 34^{fx}	18427	102	2	872^{+68}_{-55}	1.70	0.38	0.37
A3123	03 23 00.0	-52 01 00^{c}	18105	18	0	524^{+120}_{-73}	1.58	3.53	0.36
A3125	03 27 24.0	-53 30 00^{c}	17998	75	0	789^{+74}_{-58}	2.10	3.29	0.80
A3128	03 29 51.5	-52 35 07^{gx}	18010	198	3	840^{+45}_{-39}	1.53	0.62	0.33
A3133	03 32 42.0	-45 56 00^{c}	21256	12	0	428^{+131}_{-68}	1.47	3.06	0.21
A3135	03 34 01.7	-39 00 54^{dx}	18777	54	2	872^{+99}_{-74}	2.27	3.39	1.00
A3140	03 36 18.7	-40 37 20^{fx}	18777	5	0			0.36	
A3145	03 37 51.0	-38 01 12^{a}	19144	7	0			0.26	
A3158	03 42 53.5	-53 37 50^{dx}	17758	138	2	994^{+66}_{-55}	2.41	2.93	1.16
A3164	03 45 52.6	-56 55 37^{ex}	17769	18	0	861^{+196}_{-117}	2.14	2.76	0.84
A3202	04 00 14.9	-53 39 37^{a}	20779	27	1	427^{+74}_{-49}	1.34	3.52	0.23
A3225	04 09 25.6	-59 36 55	16965	36	0	658^{+95}_{-66}	1.78	2.89	0.51
A3266	04 31 19.4	-61 26 50^{dx}	17800	272	2	1209^{+55}_{-48}	2.08	0.81	0.75
A3312	05 03 54.1	-56 55 55^{a}			2			2.52	

(1) Name of cluster (A*** and S*** Abell et al. (1989)).

(2,3) Equatorial J2000 centres; (a)Abell et al. (1989), (b)Katgert et al. (1998), (c)(Fleenor et al., 2005), X-ray centres; (dx)David, Forman, & Jones (1999), (ex)Ebeling et al. (1996), (fx)Böhringer et al. (2004), (gx)Rose et al. (2002);

(4) Redshift (see §3.2).

(5) Number of cluster member redshifts used to find the mean cluster redshift.

(6) Abell richness (Abell et al. (1989)).

(7) Velocity dispersion (see §3.2).

(8) r_{200} in h_{70}^{-1} Mpc (see Eq. (3.26)).

(9) Virial radius (see Eq. (10)).

(10) Cluster virial mass within an Abell radius (2.14 h_{70}^{-1} Mpc) (see Eq. (3.19)).

Table 3.3: Clusters belonging to the Shapley Supercluster

Cluster	R.A. (J2000)	Dec. (J2000)	cz km s^{-1}	# z	Rich	σ_r km s^{-1}	r_{200} Mpc	r_v Mpc	$M_{\rm NFW}$ $10^{15}\,M_\odot$
A1631	12 52 52.7	-15 24 46	13836	271	1	696^{+32}_{-28}	1.98	3.64	0.67
A1644	12 57 9.8	-17 24 1[c]	14268	129	1	982^{+67}_{-56}	1.89	1.00	0.57
A1709	13 18 50.6	-21 25 34	15725	12	0	404^{+127}_{-71}	0.75	0.32	0.05
A1736	13 26 58.9	-27 10 13[b]	13462	111	0	1157^{+86}_{-70}	2.85	3.40	1.78
A3542	13 08 41.6	-34 34 28	15428	7	0			3.56	
A3544	13 11 6.4	-32 59 34	15252	8	1			0.79	
A3546	13 13 6.0	-29 58 46	9706	13	0	307^{+90}_{-50}	0.89	2.92	0.07
A3552	13 18 55.2	-31 49 4	15628	18	1	350^{+80}_{-49}	1.06	3.54	0.11
A3555	13 20 47.0	-28 58 48	14072	12	1	698^{+201}_{-108}	1.47	1.06	0.29
A3556	13 24 6.7	-31 40 10	14409	137	0	717^{+47}_{-39}	1.93	3.71	0.50
A3559	13 29 50.9	-29 30 51	14075	71	3	979^{+94}_{-73}	2.51	3.36	1.30
A3560	13 32 22.6	-33 8 22[c]	14672	69	3	742^{+73}_{-56}	1.53	1.06	0.33
A3564	13 34 20.8	-35 12 57	15220	26	1	572^{+102}_{-67}	1.68	3.52	0.42
A3566	13 38 58.0	-35 33 36	15460	44	2	483^{+62}_{-45}	1.08	0.99	0.13
A3568	13 41 13.9	-34 37 53	15550	18	1	675^{+154}_{-92}	1.88	3.75	0.52
A3570	13 46 52.5	-37 52 28[c]	11004	69	0	792^{+78}_{-60}	2.19	3.71	0.83
A3575	13 52 38.6	-32 53 16	11522	29	0	748^{+124}_{-83}	1.55	1.01	0.33
A3577	13 54 21.8	-27 50 11	14817	28	2	439^{+75}_{-50}	1.40	3.64	0.26
A3578	13 57 31.6	-24 44 21	11145	25	1	381^{+70}_{-58}	1.15	3.38	0.14
A3528N	12 54 22.1	-29 00 46[a]	16056	75		1030^{+96}_{-75}	1.36	0.13	0.24
A3528S	12 54 40.6	-29 13 44[a]	16215	49		1109^{+133}_{-97}	2.04	0.98	0.70
A3558	13 27 54.8	-31 29 32[b]	14257	126	4	1010^{+70}_{-58}	2.00	1.30	0.71
A3562	13 33 31.9	-31 39 37[b]	14508	62	2	1099^{+114}_{-87}	2.22	1.52	0.93
A3530	12 55 34.6	-30 20 9[b]	16291	47	0	755^{+92}_{-68}	1.53	1.07	0.34
A3532	12 57 22.1	-30 22 26[b]	16480	33	0	894^{+136}_{-93}	1.73	1.02	0.46
A3571	13 47 28.4	-32 50 59[c]	11702	58	2	1015^{+110}_{-83}	1.95	1.11	0.66
A3572	13 48 14.0	-33 22 56	15031	2	0			1.09	
SC1327	13 29 45.4	-31 36 12[b]	14646	45		964^{+121}_{-88}	1.79	1.19	0.61
SC1329	13 31 36.0	-31 48 45[b]	13606	54		1060^{+120}_{-89}	1.95	0.50	0.53

(1) Name of cluster (A*** and S*** Abell et al. (1989).

(2,3) Equatorial J2000 centres, X-ray positions: a=Gastaldello et al. (2003), b=Breen et al. (1994), c=Böhringer et al. (2004).

(4) Redshift.

(5) Number of cluster member redshifts used to find the mean cluster redshift.

(6) Abell richness (Abell et al. (1989)).

(7) Velocity dispersion (see §3.2).

(8) r_{200} in h_{70}^{-1} Mpc.

(9) Virial radius (see Eq. (7)).

(10) Cluster virial mass within an Abell radius (2.14 h_{70}^{-1} Mpc).

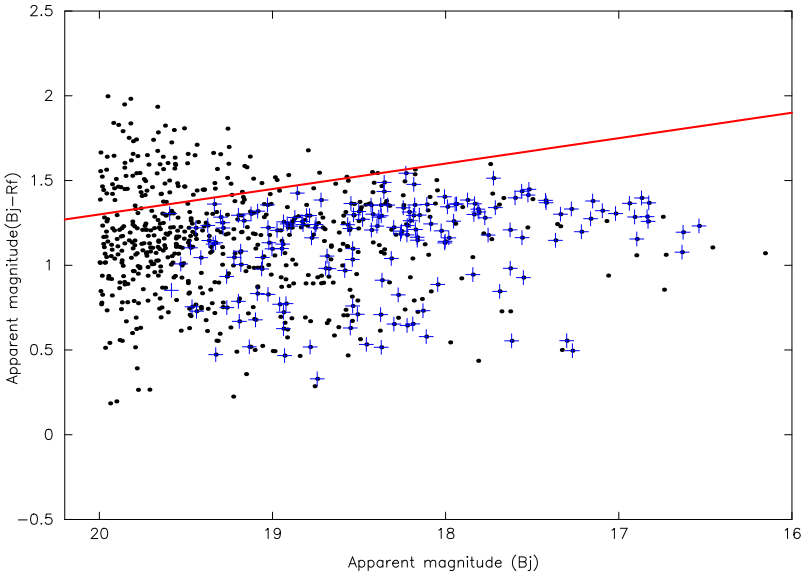

Figure 3.15: Colour magnitude plot for 4 supercluster clusters within the 2dFGRS region. Black dots represent all SuperCosmos galaxies selected in the manner described in section 3.1.1, within an Abell radius of the cluster centres. Blue crosses represent redshift selected cluster members. The red line shows the adopted red sequence cut. (§3.2.1)

to the superclusters, all galaxies within the same extraction radii as for the radial velocity calculations were extracted from the SuperCosmos Science archive (Hambly et al., 2001). All galaxies had to be classified as a galaxy in each of the three bands B, I and R2. In addition the quality of the detection had to be less than 128 in each band and $gCorMagB < 20.0$ (magnitude if the object is assumed to be a galaxy).

UK Schmidt blue, B_j (B) and UK Schmidt red magnitudes (R2) were selected for each galaxy. To remove background galaxies a colour magnitude cut was applied to the the SuperCosmos samples. To obtain the cut, galaxies from four clusters which had 2dFGRS redshifts available were overlayed on a colour magnitude plot for all the SuperCosmos galaxies for the same clusters. The 2dFGRS galaxies were only selected if they were within 3000 km s^{-1} of the mean cluster redshift and hence were likely cluster members. From this overlay (see Fig. 3.15) a red sequence cut was placed along the top of the redshift selected galaxies by eye. The line was found to have a relation of $b_J - r_F = -0.15\, b_j + 4.3$. The application of this cut to each SuperCosmos sample left the likely members for each cluster for further analysis.

In order to obtain a profile of the optical surface brightness of the clusters we

required an analytical model which would fit the surface brightness curve of the galaxies selected as cluster members. The models chosen did not have to be actual optical surface brightness models, as long as their mathematical form fitted the shape of our profiles. We selected four potential models which are described below.

The Navarro Frenk White Model

Navarro, Frenk & White (1996) used N-body simulations to investigate dark halos in the Standard cold dark matter cosmology. They simulated the formation of 19 different systems with scales ranging from those of dwarf galaxies to those of rich clusters. It was found that a model of the form shown in Eq. 3.4 provided a good fit to the density profiles of four systems with a halo mass range of nearly four orders of magnitude (Navarro, Frenk, & White, 1995).

$$\rho(r) = \frac{\delta_c \, \rho_c}{\frac{r}{r_c}\left(1 + \frac{r}{r_c}\right)^2}, \tag{3.4}$$

where $r_c = r_{200}/c$ is a characteristic radius, $\rho_c = 3H_0^2/8\pi G$ is the critical density (H_0 is the current value of Hubble's constant), and δ_c and c are two dimensionless parameters, representing the mean overdensity and central concentration of the radial profile respectively.

The mass densities of the usual NFW profile are scaled to light density profiles assuming light traces mass, at least in the visible cores of each cluster, such that $\delta_\lambda = \delta_c/\Upsilon$, where $\Upsilon \equiv M/L$ is the mean mass-to-light ratio of the cluster. This results in the light profile,

$$\lambda(r) = \frac{\delta_\lambda \, \rho_c}{\frac{r}{r_c}\left(1 + \frac{r}{r_c}\right)^2}, \tag{3.5}$$

where $r_c = r_{200}/c$ is a characteristic radius, $\rho_c = 3H_0^2/8\pi G$ is the critical density (H_0 is the current value of Hubble's constant), and δ_c and c are two dimensionless parameters, representing the mean overdensity and central concentration of the radial profile respectively. The two dimensional projected surface brightness of galaxies

on the sky can be computed by integrating Eq. 3.4 according to the Abell integral equation given by,

$$\Lambda\left(R\right) = 2\int_{R}^{\infty} \rho\left(r\right) \frac{r}{\sqrt{r^2 - R^2}} dr \tag{3.6}$$

Bartelmann (1996) show this results in the projected surface brightness of,

$$\Lambda\left(R\right) = \frac{2\rho_c \delta_\lambda r_c}{x^2 - 1} f(x), \tag{3.7}$$

with

$$\begin{aligned} f(x) = &\quad 1 - \tfrac{2}{\sqrt{x^2-1}} \arctan\sqrt{\tfrac{x-1}{x+1}} \quad (x > 1) \\ f(x) = &\quad 1 - \tfrac{2}{\sqrt{1-x^2}} \arctan\sqrt{\tfrac{1-x}{1+x}} \quad (x < 1) \\ f(x) = &\qquad\qquad 1 \qquad\qquad\qquad\quad (x = 1), \end{aligned} \tag{3.8}$$

where $x = r/r_c$, R being the projected radius from the centre of the cluster.

The Hernquist Model

Hernquist (1990) presented a potential density pair which closely approximates the de Vaucouleurs $R^{1/4}$ law for elliptical galaxies. A modification of the distribution of Jaffe (1983) allowed the intrinsic properties and projected distributions to be evaluated analytically,

$$\rho(r) = \frac{M}{2\pi} \frac{a}{r} \frac{1}{(r+a)^3}, \tag{3.9}$$

where M is the total mass and a is a scale length. So as to be able to apply this form to our optical data, in the same manner as for the NFW profile, we divide through by a constant mass to light ratio, Υ, obtaining the relation,

$$\lambda(r) = \frac{L}{2\pi} \frac{a}{r} \frac{1}{(r+a)^3}, \tag{3.10}$$

where L is the total light and a is a scale length. The two dimensional projected surface brightness of galaxies on the sky can be computed by integrating Eq. 3.10 according to Eq. 3.6. This results in the projected surface brightness of,

$$\Lambda(R) = \frac{L}{2\pi a^2(1-s^2)^2}[(2+s^2)\,X(s) - 3], \tag{3.11}$$

where $s = R/a$, R is the projected radius, L is the total light and

$$X(s) = \frac{1}{\sqrt{1-s^2}}\,\mathrm{sech}^{-1}s \quad \text{for } (0{\leq}s{\leq}1) \tag{3.12}$$

$$X(s) = \frac{1}{\sqrt{1-s^2}}\,\mathrm{sech}^{-1}s \quad \text{for } (1{\leq}s{\leq}\infty). \tag{3.13}$$

The Plummer Model

The Plummer model was first used by Plummer (1911) to fit observations of globular clusters and the density profile takes the form,

$$\rho(r) = \frac{3Mb^2}{4\pi}\frac{1}{(b^2+r^2)^{5/2}}, \tag{3.14}$$

where M is the total mass of the cluster, and b is the Plummer radius, a scale parameter which sets the density of the cluster. In the same manner as the previous models dividing by a constant mass to light ratio, Υ, results in the following light profile,

$$\lambda(r) = \frac{3Lb^2}{4\pi}\frac{1}{(b^2+r^2)^{5/2}}, \tag{3.15}$$

where L is the total light of the cluster. By integrating according to Eq. 3.6 the

projected surface brightness profile can be obtained as,

$$\Lambda(R) = \frac{L}{\pi} \frac{b^2}{(b^2 + R^2)^2} \tag{3.16}$$

The standard "beta" model

Traditionally models assume that the intra-cluster X-ray emitting gas is isothermal and that the gas and the galaxies are in hydrostatic equilibrium. King (1962) presented an analytical approximation to the isothermal sphere which is often referred to as the standard beta model. The surface X-ray brightness at projected distance R is given by

$$\Sigma(R) = \Sigma_0[1 + (R/r_c)^2]^{-3\beta+0.5}, \tag{3.17}$$

where r_c is the core radius of the gas distribution and β is the ratio of the specific energy in galaxies to the specific energy in the hot gas. We can simply apply this to our optical data fitting optical surface brightness instead of X-ray, such that,

$$\Lambda(R) = \Lambda_0[1 + (R/r_c)^2]^{-3\beta+0.5}. \tag{3.18}$$

Model choice

Each of the above projected models were fitted to the observed optical surface brightness profiles obtained from the SuperCOSMOS galaxy data as described in §3.2.1, using the Numerical Algorithm Groups (NAG) E04JYF algorithm. The models were fitted with the following variables

1. Beta model: from Eq. 3.18, three variables were fitted, a=Λ_0, b=β and c=r_c.
2. Hernquist model: from Eq. 3.11 two variables were fitted, a=L and b=$2\pi a^2$.
3. NFW model: from Eq. 3.7 two variables were fitted, a=r_c and b=$\rho_c\,\delta_\lambda$.
4. Plummer model: from Eq. 3.16 two variables were fitted, a=L and b=b.

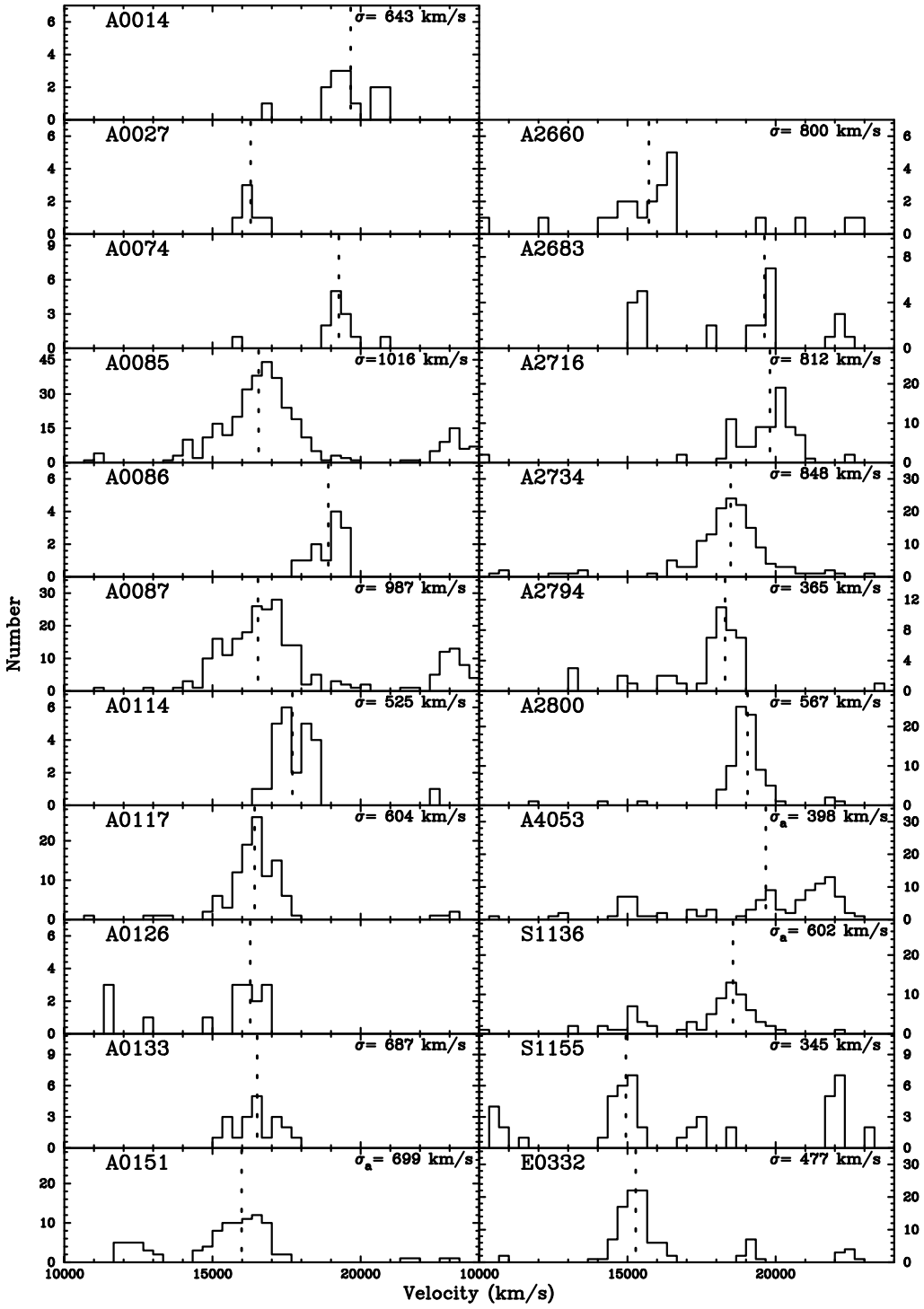

Figure 3.16: Radial velocities of galaxies lying within the Abell radius of 2.14 h_{70}^{-1} Mpc of each galaxy cluster, belonging to the Pisces-Cetus supercluster, compiled from NED, 6dFGS, 2dFGRS and SDSS. For each cluster, the mean recessional velocity is shown as a dotted line, and for those with $\geq$12 redshifts, the velocity dispersion is shown on the upper right. (§3.2)

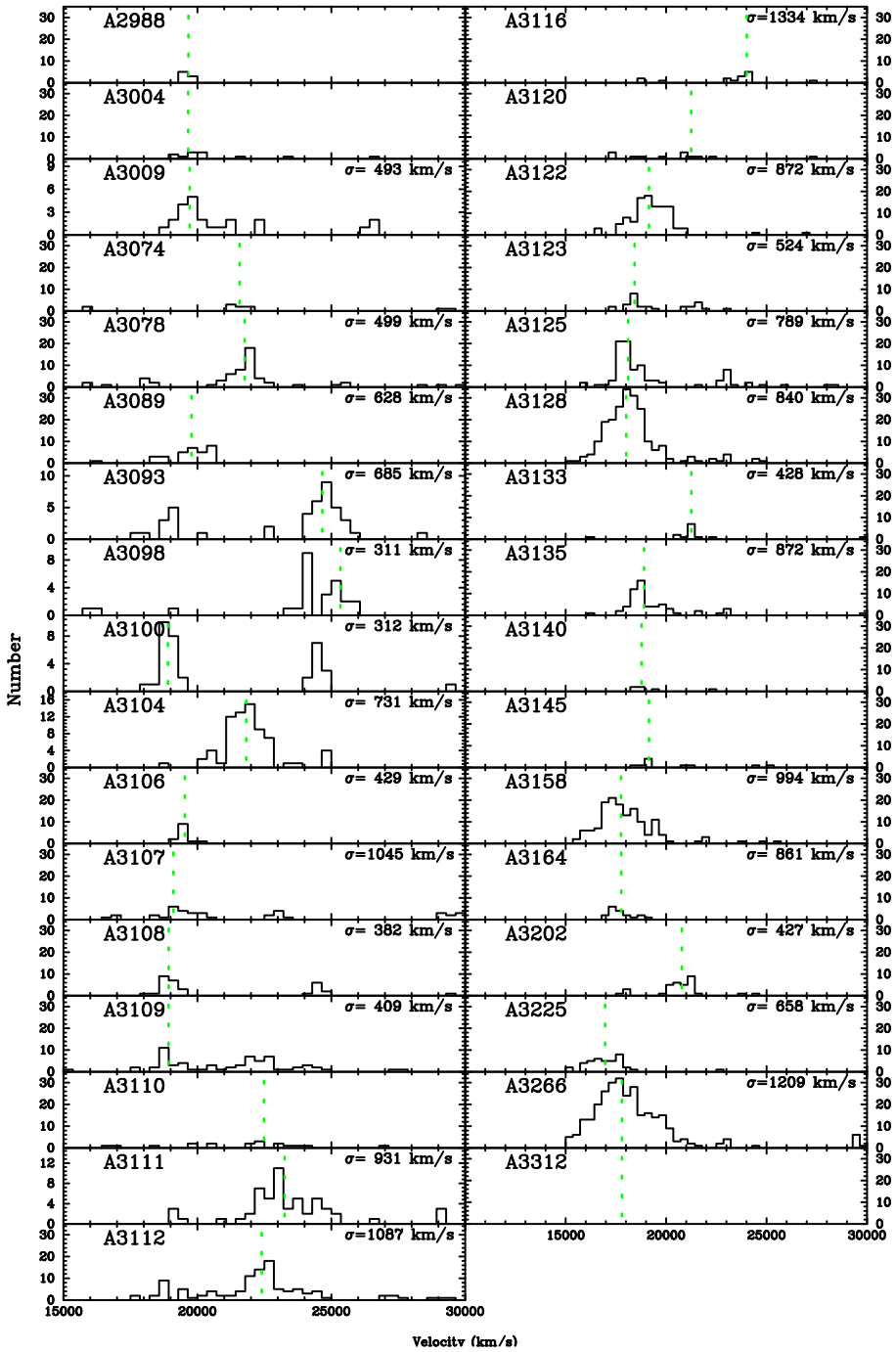

Figure 3.17: Radial velocities of galaxies lying within the Abell radius of 2.14 h_{70}^{-1} Mpc of each galaxy cluster, belonging to the Horologium-Reticulum supercluster, compiled from NED, 6dFGS, (Fleenor et al., 2005) and (Fleenor et al., 2006). For each cluster, the mean recessional velocity is shown as a dotted line, and for those with $\geq$8 redshifts, the velocity dispersion is shown on the upper right. (§3.2)

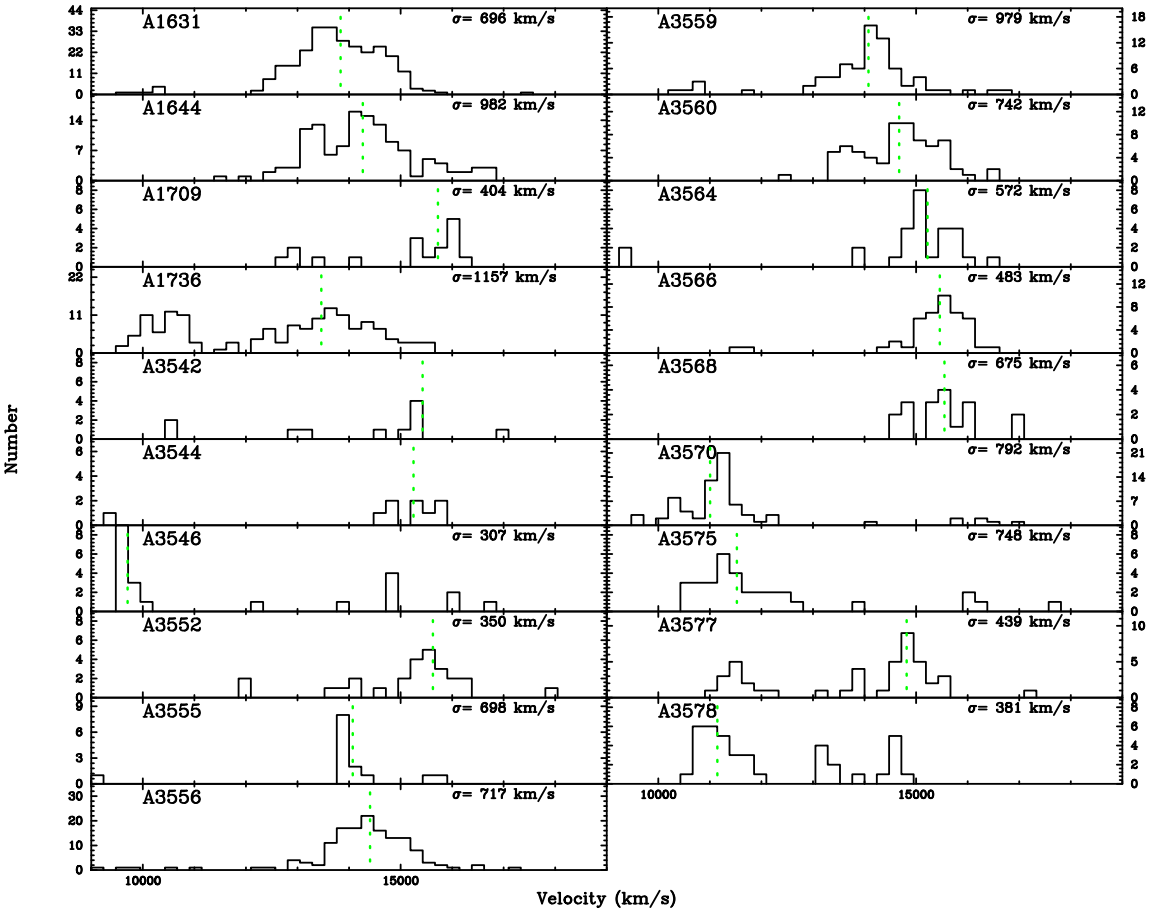

Figure 3.18: Radial velocities of galaxies lying within the Abell radius of 2.14 h_{70}^{-1} Mpc of each galaxy cluster, belonging to the Shapley supercluster, compiled from NED, 6dFGS and ZCAT. For each cluster, the mean recessional velocity is shown as a dotted line, and for those with $\geq$9 redshifts, the velocity dispersion is shown on the upper right. (§3.2)

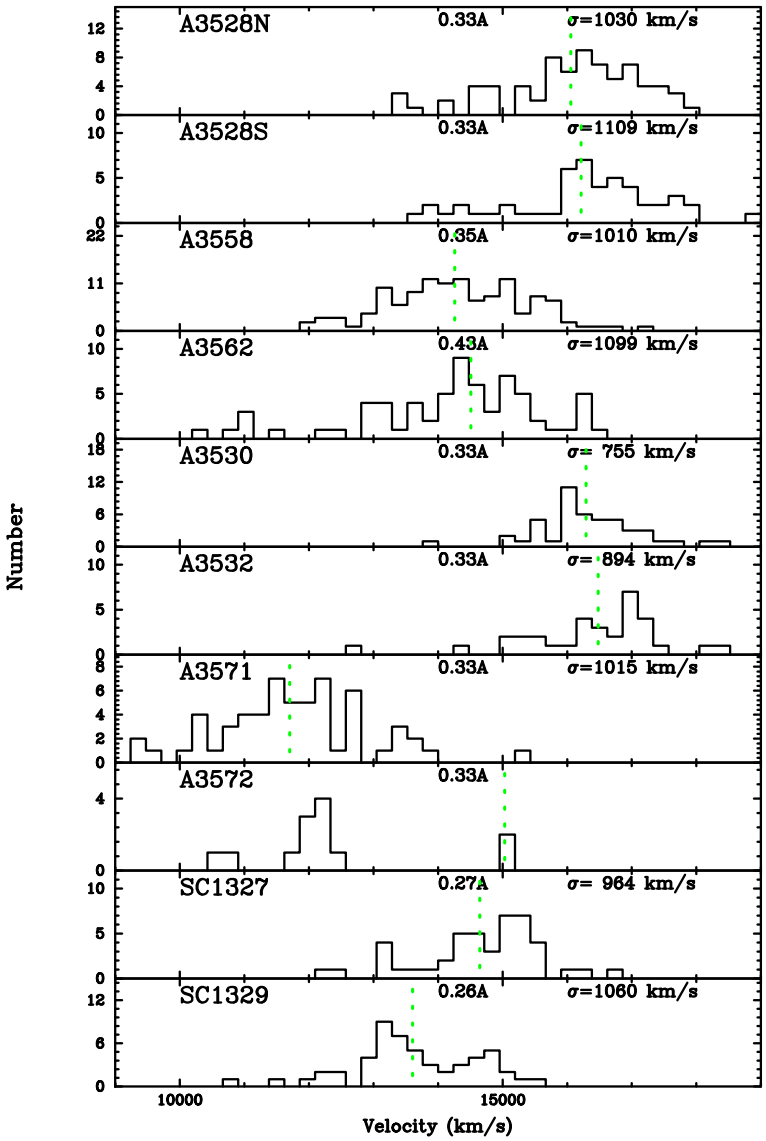

Figure 3.19: Radial velocities of galaxies lying with an extraction radius of each galaxy cluster, belonging to the Shapley supercluster. The extraction radii are shown in the top centre of each cluster panel and are expressed as a fraction of the Abell radius (2.14 h_{70}^{-1} Mpc). All clusters belong to the Shapley supercluster and galaxies are compiled from NED, 6dFGS and ZCAT. For each cluster, the mean recessional velocity is shown as a dotted line, and for those with $\geq$9 redshifts, the velocity dispersion is shown on the upper right. (§3.2)

An additional constant term to represent foreground/background galaxies was also added as an extra +c term to all the models. For the majority of the clusters the galaxies were binned in variable radius annuli around the cluster centre, such that each annulus contains an equal number of galaxies. The luminosity per unit area in each annulus was then calculated to plot the surface brightness profiles. However, a satisfactory fit could not be found for some clusters using this method. Therefore, for these profiles, equal radius annuli with a variable number of galaxies were used.

From this process the NFW model was seen to be the best overall model, fitting the most cluster profiles accurately. Therefore, the NFW fit was used as the final fit all of the clusters profiles to enable estimates of their mass to be performed. The resulting surface brightness profiles and their associated NFW fits are shown in Appendix A, Appendix B, and Appendix C for the clusters of the Pisces-Cetus, Horologium-Reticulum and Shapley superclusters respectively.

3.3 Virial mass estimates

The mass within a radius r from the centre of a cluster can be derived from the modelled velocity dispersion and spatial density profiles $\lambda\,(r)$ (Koranyi & Geller, 2000). On assumption of a constant mass-to-light ratio $\Upsilon \equiv M/L$, the mass density $\rho\,(r) \equiv \Upsilon\,\lambda\,(r)$, following (3.4), results in the enclosed mass profile,

$$M(< r) = 4\pi\delta_c\rho_c r_c^3 \Big[\ln(1+\frac{r}{r_c}) - \frac{r/r_c}{1+r/r_c}\Big]. \tag{3.19}$$

The core radius r_c has already been found in the fitting of the surface brightness profile as described in §3.2.1. The quantity δ_c and c are linked by the requirement that the mean density within r_{200} should be $200\times\rho_c$, i.e.,

$$\delta_c = \frac{200}{3}\frac{c^3}{[\ln(1+c) - c/(1+c)]}, \tag{3.20}$$

where $c = r_{200}/r_c$. With the value of r_c already being calculated the NFW model would be completely specified if we knew r_{200}.

From the definition of r_{200}, we have that,

$$\rho_{200} = 200\rho_c, \tag{3.21}$$

where ρ_{200} is the density inside r_{200} and ρ_c is the critical density of the universe. This leads to,

$$M_{200} = 200 \times \frac{4\pi r_{200}^3 \rho_c}{3}, \tag{3.22}$$

where M_{200} is the mass inside r_{200}. It can be shown that the critical density of the universe can be expressed as,

$$\rho_c = \frac{3H_0^2(1+z)^3}{8\pi G}, \tag{3.23}$$

where H_0 is Hubble's constant, G is the gravitational constant and z is the redshift. Substituting Eq. 3.23 into Eq. 3.22 gives,

$$M_{200} = \frac{100 r_{200}^3 H_0^2 (1+z)^3}{G} \tag{3.24}$$

It can be shown that the virial mass can be defined as,

$$M_v = \frac{3\sigma^2 r_v}{G}, \tag{3.25}$$

where r_v is the virial radius. Dividing Eq. 3.24 by Eq. 3.25 gives,

$$\frac{M_{200} r_v}{M_\nu r_{200}^3} = 100 H_0^2 \frac{(1+z)^3}{3\sigma_r^2}, \tag{3.26}$$

where σ_r^2 is the radial velocity dispersion of the cluster and r_v is the approximate virial radius determined by

$$r_v \sim \frac{\pi}{2} \frac{N(N-1)}{\sum_i \sum_{i<j} R_{ij}^{-1}}, \tag{3.27}$$

where N is the number of galaxies in the system. The summation is over all pairs of galaxies (i, j) within the Abell radius, where the projected separation for each pair is R_{ij} (Binney & Tremaine, 1987). This should provide a radius at which most cluster members are included.

The enclosed mass profile (3.19) can be used to find M_{200} and M_ν in terms of δ_c. The calculated cluster masses within the Abell radius of 2.14 h_{70}^{-1} Mpc, their core radii and virial radii found from the model fitting, can be found in Table 3.1,Table 3.2 and Table 3.3 for the Pisces-Cetus. Horologium-Reticulum and Shapley supercluster clusters respectively.

The virial estimate will fail to represent the gravitating mass of a cluster which is very obviously in the process of rapid evolution, e.g. a collapsing or interacting system, since the virial theorem does not strictly apply to systems whose moment of inertia is significantly changing with time. Abell 87 is obviously such a system and hence its mass has been omitted.

3.4 A lower limit to the Mass of the Superclusters

The sum of the individual virial masses of the clusters, as calculated in the previous section, can be treated as a lower limit to the mass of each supercluster.

3.4.1 Pisces-Cetus supercluster

For the filament containing A85, we use a cylindrical column of length equal to the sum of the distances between the constituent clusters from the MST analysis equalling 47.9 h_{70}^{-1} Mpc. Adopting a radius of 6 h_{70}^{-1} Mpc (Approximately 3 Abell radii) gives a volume of 5421 h_{70}^{-3} Mpc^3, we obtain the total mass of the clusters as $2.44 \times 10^{15}\, h_{70}^{-1}\, M_\odot$. As discussed in section 3.2 Abell 87 is likely to be a filament of galaxies rather than a cluster and therefore its mass is not included.

For the filament containing A133, we use a cylindrical column of length of 167.8 h_{70}^{-1} Mpc again equal to the sum of the cluster separations form the MST analysis. The radius of 6 h_{70}^{-1} Mpc for the cylinder gives a volume of 18996 h_{70}^{-3} Mpc^3, we obtain the total mass of the clusters as $3.88 \times 10^{15}\, h_{70}^{-1}\, M_\odot$.

With the critical density of the universe having a value of $\rho_c = 1.36 \times 10^{11}\, h_{70}^2$ $M_\odot$ Mpc^{-3}, these values for the mass of the Supercluster represent matter overdensities of $\delta_M \equiv \Delta\rho/\rho_{crit}$ >1.96 (over 5400 h_{70}^{-3} Mpc^3) and δ_M >1.51 (over 19000 h_{70}^{-3} Mpc^3) for the A85-related and A133-related filaments respectively. Thus a mean for the supercluster region of 1.74. These values are slightly lower than those found in the core of the Shapley supercluster (5.2 over $\sim$ 22 h_{100}^{-1} Mpc scale (Bardelli et al., 2000)(extended sample)), (2.4 over $\sim$ 26 h_{70}^{-1} Mpc scale (Fabian, 1991)), (5.0 over $\sim$ 38 h_{70}^{-1} Mpc scale (Drinkwater et al., 2004)), (2.4 over $\sim$ 40 h_{70}^{-1} Mpc scale (Fleenor et al., 2005)) and (5.4 over $\sim 30 - 46$ h_{70}^{-1} Mpc scale (Proust et al., 2006)). The cosmological significance of such overdensities in a supercluster filament has been discussed in the literature (Raychaudhury, 1989; Ettori, Fabian, & White, 1997). However, that these represent just the mass with some clusters omitted, no filament galaxies included, and that the matter density of the Universe is $\Omega_M \sim 0.3$, these amount to significant overdensities over very large volumes. This supports the possibility that galaxies in these regions may evolve differently to galaxies which are present in less dense regions and have different properties such as enhanced or suppressed star formation.

3.4.2 Horologium-Reticulum supercluster

For the purposes of the estimate of a lower limit of the mass for the Horologium-Reticulum supercluster we will take the super cluster to consist of those clusters that are part of the main chain, joint by links of less than 20 h_{100}^{-1} Mpc, represented by solid lines in Fig. 3.8. The main chain spans from Abell 3089 through to Abell 3266, containing 18 clusters (A3089, A3122, A3125, A3140, A3145, A3135, A3109, A3108, A3100, A3123, A3120, A3110, A3078, A3074, A3125, A3158, A3164, A3225).

A lower limit of the mass of this structure found by summing all of the available masses of the constituent clusters results in a total mass of $6.60 \times 10^{15}\, h_{70}^{-1}\, M_\odot$.

Taking the volume of the supercluster to consist of a series of cylinders of radius 6 h_{70}^{-1} Mpc and length of the MST link between the clusters results in a total length of 202.1 h_{70}^{-1} Mpc and a total volume of $22,800\,h_{70}^{-3}$ Mpc^3. With the critical density of the universe having a value of $\rho_c = 1.36 \times 10^{11}\,h_{70}^2$ M$_\odot$ Mpc^{-3}, this value for the mass of the Supercluster represents a matter overdensity of δ_M >2.1 (over $23,000\,h_{70}^{-3}$ Mpc^3)

Again given that these represent just the mass with some clusters omitted, no filament galaxies included, and that the matter density of the Universe is $\Omega_M \sim 0.3$, these amount to significant overdensities and the possibility of environmental effects on the evolution of galaxies in the region.

3.4.3 Shapley supercluster

For the Shapley supercluster the main chain consisting of all clusters joined by links of less than 20 h_{100}^{-1} Mpc included all clusters accept for A1631, A1644 and A1709. The total length of the MST links between these clusters was 195.31 giving a volume of $22,089\,h_{70}^{-3}$ Mpc^3 for the adopted cylinder radius of 6 h_{70}^{-1} Mpc. The total mass is $1.2 \times 10^{16}\,h_{70}^{-1}\,M_\odot$. With the critical density of the universe having a value of $\rho_c = 1.36 \times 10^{11}\,h_{70}^2$ M$_\odot$ Mpc^{-3}, this value for the mass of the Supercluster represents a matter overdensity of δ_M >4.06 (over $22,000\,h_{70}^{-3}$ Mpc^3).

This value is even higher than the previous two superclusters making the supercluster even more likely to effect the evolution of galaxies.

3.5 Conclusions

We have used survey redshifts (mainly from 2dFGRS, 6dFGS, SDSS, NED and ZCAT) and photometry (from SuperCosmos) of galaxies belonging to the clusters belonging to three superclusters to investigate its nature, extent and orientation.

The Pisces-Cetus supercluster consists of two main filaments, consisting of 11 and 5 clusters respectively, at mean redshifts of z =0.0625 and 0.0545 respectively. The Horologium-Reticulum supercluster consists of 33 clusters of galaxies at a mean redshift of z =0.0670 (MST maximum edge length = 25 h_{100}^{-1} Mpc) and mainly

extends in the radial direction. Finally the Shapley supercluster consists of 29 clusters at a mean redshift of z =0.0476 MST maximum edge length = 25 h_{100}^{-1} Mpc).

While there is some suggestion of filamentary structure in all three of the superclusters the position of the Pisces-Cetus supercluster with some coverage in both the SDSS and 2dFGRS leads to the most compelling evidence. Most of chain A of the Pisces-Cetus supercluster lies in the 2dFGRS region, and gives us a remarkable three-dimensional view of a string of clusters, with groups delineating the filamentary structure. Chain B, partially covered by the Sloan Digital sky survey, contains the clusters A85 & A87, for which independent evidence exists (from X-ray observations) of collapse along the filament.

Virial masses were calculated from NFW fits to surface brightness profiles and velocity dispersions for the constituent clusters, the sum of these masses being taken as a lower limit to the mass of each of the superclusters. These were found to be $6.0 \times 10^{15}\, h_{70}^{-1}\, M_{\odot}$ and $5.2 \times 10^{15}\, h_{70}^{-1}\, M_{\odot}$ respectively for the chain A and chain B of the Pisces-Cetus supercluster, $6.6 \times 10^{15}\, h_{70}^{-1}\, M_{\odot}$ for Horologium-Reticulum and $1.2 \times 10^{16}\, h_{70}^{-1}\, M_{\odot}$ for Shapley. These correspond to mass overdensities of δ_M >1.5, δ_M >2.0, δ_M >2.1 and δ_M >4.1, for Pisces-Cetus chain A, Pisces-Cetus chain B, Horologium-Reticulum and Shapley respectively.

These values indicate that in all three superclusters, it is likely that the systems are just in the linear regime or have just left it. Furthermore, these overdensities suggest that the regions may have different environmental conditions to other regions and hence may have different effects on the evolution of galaxies.

Ever since the discovery of the "Great Wall"(Geller & Huchra, 1989), which seemed to be a structure almost $< 200\, h_{70}^{-1}$ Mpc long, the discovery of comparable structures have been claimed at higher redshift (e.g., Bagchi et al., 2002; Brand et al., 2003; Miller et al., 2004). To be cosmologically significant, it is necessary to show that these large structures are gravitationally bound, which is difficult to demonstrate. In this work, we have found cluster filaments between approximately $50\, h_{70}^{-1}$ Mpc and $130\, h_{70}^{-1}$ Mpc long. This is consistent with statistical analyses of the LCRS and 2dF redshift surveys, which indicate that the scale of homogeneity sets in beyond the scale of $\sim 100\, h_{70}^{-1}$ Mpc or so.

A limited X-ray analysis of the $L_X - \sigma$ relation in the clusters of the Pisces-Cetus supercluster, based on literature X-ray data can be found in Appendix D.

Chapter 4

Benjamin Disraeli: "There are three kinds of lies: lies, damned lies, and statistics."

Star formation in the Pisces-Cetus supercluster

4.1 Introduction

Studies of the environmental effects on galaxy evolution in the past have shown that star formation is suppressed in the cores of rich clusters (Dressler, 1980; Couch & Sharples, 1987; Balogh et al., 1998). More recently, from the high-quality spectra of the 2dFGRS and SDSS archives, the difference between the properties of star-forming and quiescent galaxies have been further characterised, and shown to depend on the local density of galaxies. For instance, studies (Lewis et al., 2002; Gómez et al., 2003; Balogh et al., 2004) identifying star formation activity with the equivalent width of the Hα emission line W(Hα), show that the fraction of galaxies with W(Hα)$>$4 Å steadily declines with increase in the local three-dimensional density of galaxies. Kauffmann et al. (2004) show similar effects, with the star formation history being quantified from line indices measured elsewhere in the spectrum as well, including the Hδ absorption line and the strength of the 4000Å break.

In the hierarchically merging scenario supported by large-volume numerical simulations such as Jenkins et al. (1998), much of this merger-driven evolution in the history of a galaxy is expected to occur in small groups forming in and falling along a supercluster filament towards regions of higher density. In the absence of direct mergers, the close encounters between galaxies brought closer by dynamical friction,

can lead to galaxy harassment, which can also play a very important role in galaxy evolution, and can affect the star formation properties of galaxies.

To investigate the star formation rate (SFR) within the galaxies that form the Pisces-Cetus supercluster we use the 2dFGRS η parameter as discussed in Chapter 2.

4.2 Star formation within Pisces-Cetus supercluster filaments

A supercluster filament is a snapshot of a cluster in formation, and the study of the properties of galaxies as a function of position along a filament is expected to provide insights into the processes involved in galactic evolution and cluster formation. This section looks at galaxies in a few filaments of the Pisces-Cetus supercluster.

The clusters comprising the Pisces-Cetus supercluster, taken from the minimal spanning tree (MST) analysis of Raychaudhury et al. (2007), form the core of our sample. The filamentary nature of the region can clearly be seen in the distribution of galaxies in the groups in Fig. 4.2, where the 2dFGRS galaxies within 1840 kms^{-1} (three times the velocity dispersion of the clusters belonging to the supercluster), are plotted. The 2PIGG groups found within the same velocity bounds (Eke et al., 2004), also show the same large-scale structure. The rich clusters, plotted as large circles on the same plot, can be seen to be mostly along these filaments forming the supercluster structure.

4.2.1 Filament membership

Our sample of galaxies was taken from the 2PIGG (Eke et al., 2004) subsample of the 2dFGRS comprising 191,328 galaxies. This leaves out about 20 % of galaxies in the parent sample in under-sampled regions and ensures a uniform completeness limit all over the survey. This enables comparisons with 2PIGG statistics to be made without bias. Hereafter, 2dFGRS refers to this subsample.

From this subsample, galaxies which belong to the three most prominent fila-

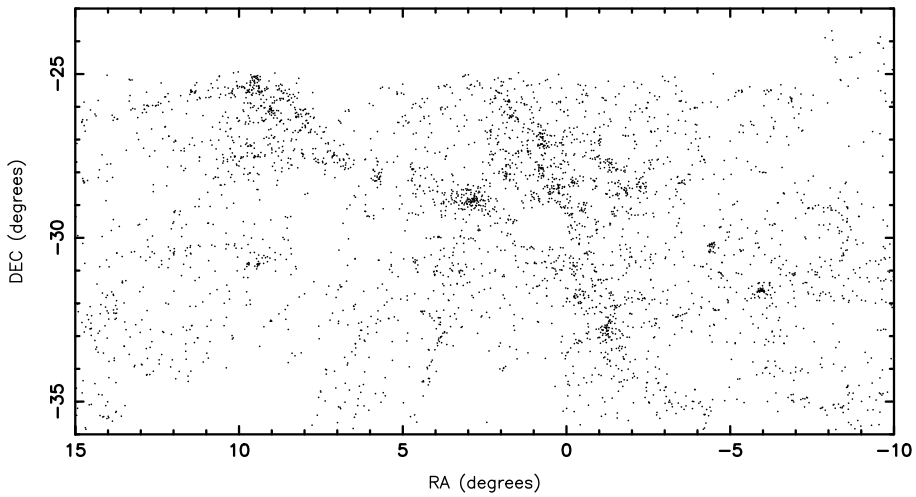

Figure 4.1: (a, Left) All 2dFGRS Galaxies within 1840 km s^{-1} (3σ) of the mean recessional velocity of the Pisces-Cetus supercluster. The filamentary structure is clearly visible. (§4.2)

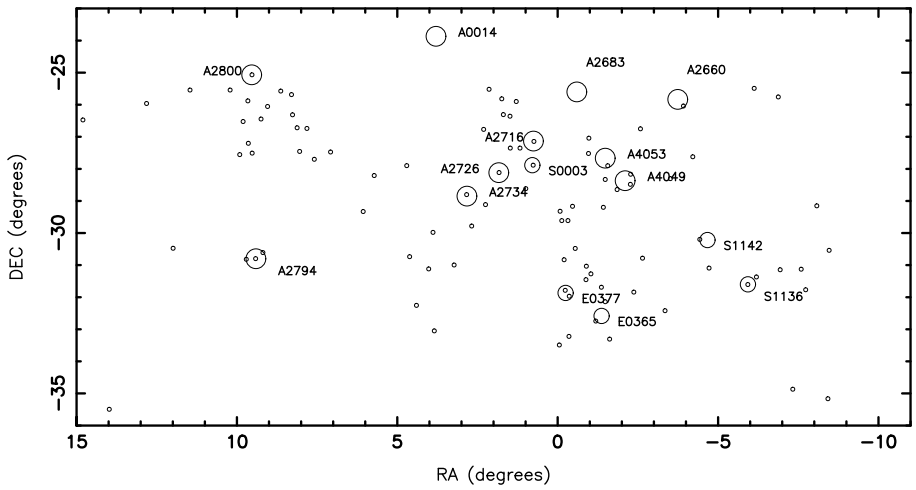

Figure 4.2: Clusters of galaxies belonging to Pisces-Cetus supercluster filaments within the 2dFGRS region and within 1840 km s^{-1} (3σ) of the mean supercluster velocity. The largest circles represent Abell clusters, and the medium-sized ones are supplementary Abell and Edinburgh-Durham clusters within the same redshift range. The groups of galaxies (Eke et al., 2004, 2PIGG) within the same velocity bounds, identified from a friends-of-friends analysis of the 2dFGRS are shown as the smallest circles. (§4.2)

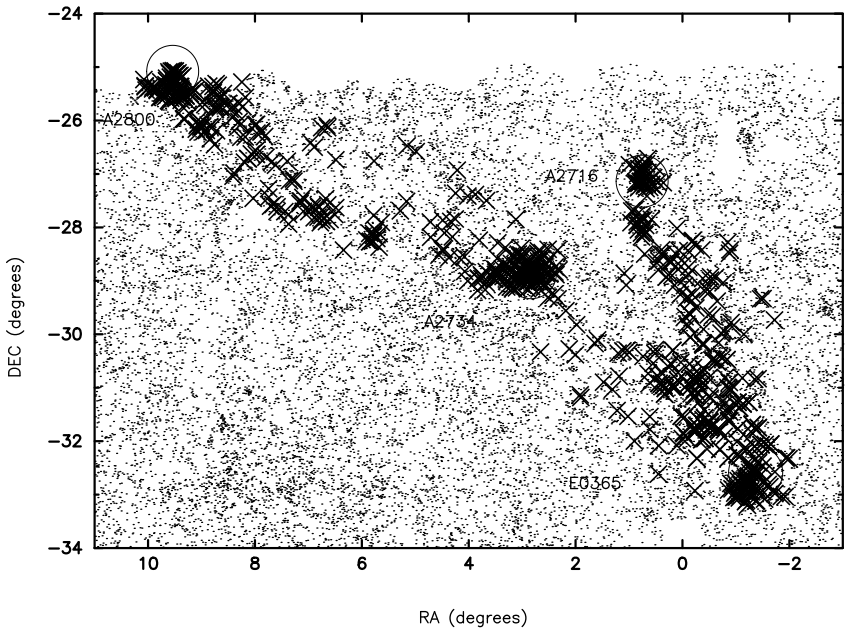

Figure 4.3: The 2dFGRS galaxies that form the three filaments as defined in the text are shown as crosses. All galaxies within the 2dFGRS in the region are shown as dots. (§4.2.1)

ments, longer than $20\,h_{70}^{-1}$ Mpc, seen in Fig. 4.2, namely those joining A2800-A2734, A2734-E0365 and E0365-A2716, were extracted.

We define the extent of each filament as an prolate spheroid, with the centres of the two clusters involved being at each end, the distance between them being the major axis of the spheroid, and $6\,h_{70}^{-1}$ Mpc being the semi-minor axis. All galaxies falling inside this spheroid were taken to be members of the filament. So as to not omit cluster galaxies at each end of the filament, we added the galaxies found, from a percolation analysis, to belong to the corresponding 2PIGG "group" in (Eke et al., 2004). The resulting 965 filament members can be seen in Fig. 4.3.

The distance between two clusters, and between a galaxy and a cluster, was calculated as the co-moving proper distance between them (see Hogg, 1999). We used the measured redshift of each galaxy as a measure of its distance from us, except if it is a member of a rich cluster, where the mean redshift of the cluster was used.

Fig 4.2.1 shows the distribution of the 2dFGRS galaxies for the 2PIGG group corresponding to Abell 2734. The red circle in the left hand plot shows the Abell radius (2.14 Mpc h_{70}^{-1}). This demonstrates that simply taking cluster members to

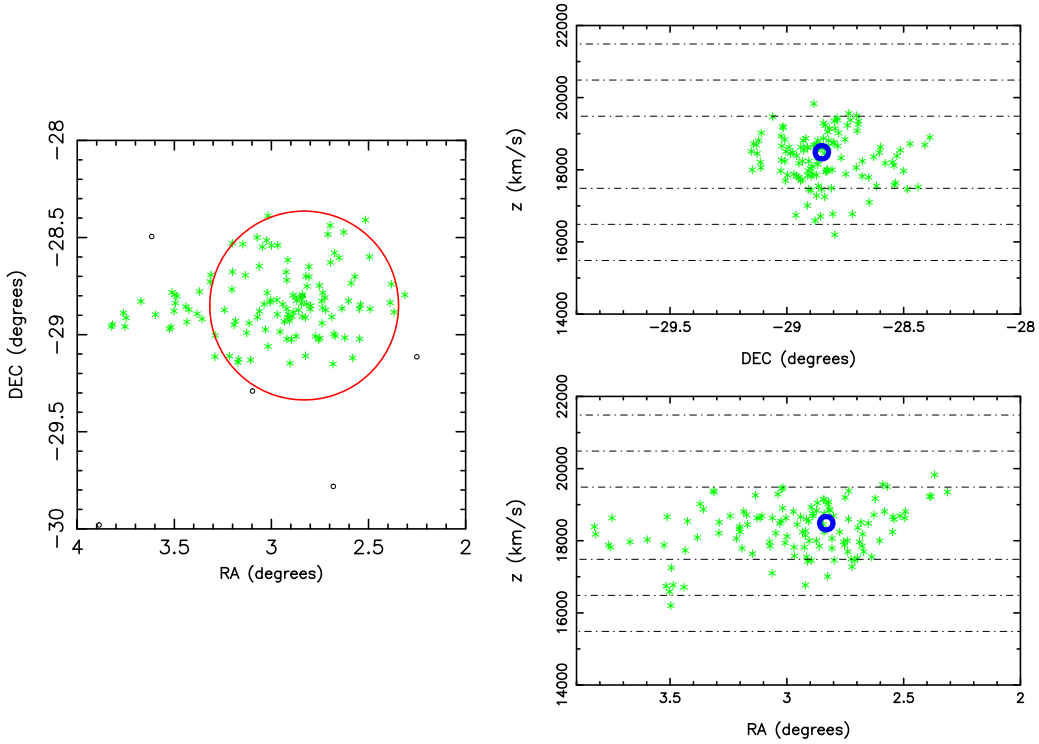

Figure 4.4: The distribution of the 2dFGRS galaxies for the 2PIGG group corresponding to Abell 2734. (left) Distribution in R.A.-Dec. space with the Abell radius ($2.14\,h_{70}^{-1}$ Mpc) shown as a red circle. (top, right) Distribution in redshift-Dec. space, where the centre of the cluster is shown as a blue circle. Dot-dash lines show 1000 km s^{-1} increments of redshift from the mean cluster redshift. (bottom, right) Distribution in redshift-R.A. space , the centre of the cluster is shown as a blue circle, dot-dash lines show 1000 km s^{-1} increments of redshift from the mean cluster redshift. (§4.2.1)

be within the Abell radius would omit some cluster members.

4.2.2 Star formation along the A2734-A2800 filament

We start our exercise by looking in detail at the most prominent filaments in the Pisces-Cetus supercluster, that linking A2734 and A2800, which is about $32\,h_{70}^{-1}$ Mpc long. The co-moving distance of each of the filament galaxies from one end (A2734) was calculated as described above. Members of A2800 were assigned a distance equal to the separation of the two clusters minus their projected distance from the centre of A2800.

Along the filament, we chose bins of varying size according to the numbers of galaxies available. Closer to the two clusters, we chose smaller bins of $0.3 -$

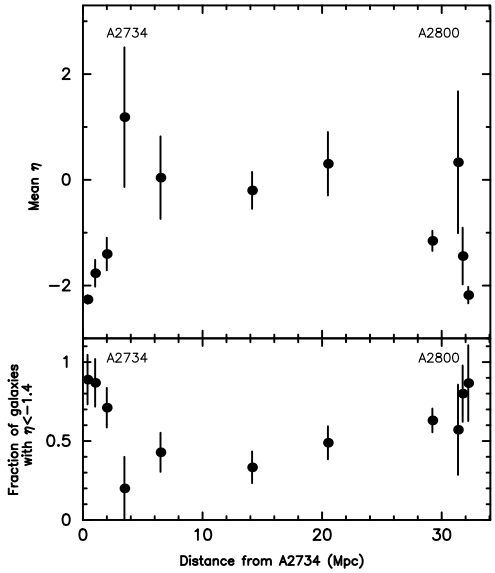

Figure 4.5: For the filament of galaxies linking A2734 and A2800, the mean η is plotted as a function of the distance from the centre of A2734. The "field" value, the mean η for all galaxies of the 2dFGRS, is around zero. The bottom panel shows the fraction of passive galaxies ($\eta < -1.4$) in each bin. It can be seen, as expected, that the SFR is lowest at the cores of the two rich clusters, where the number of passive galaxies is the highest. The mean η seems to peak between 3–4 h_{70}^{-1} Mpc from each end. (§4.2.2)

$0.6\,h_{70}^{-1}$ Mpc to sample the rapid variation of SFR within the virial radius of the cluster. For each bin, the the mean distance of all member galaxies, and the mean η, were calculated.

Fig. 4.5 shows the resulting plot of mean η as a function of distance from A2734. We also plot, in the bottom panel, the fraction of passive ($\eta < -1.4$) galaxies in each bin. It can be seen, as expected, that the SFR is minimum at the cores of the two rich clusters, where the number of passive galaxies is the highest. The mean value of the η parameter increasing with distance to approximately the field value (the mean η for all galaxies of the 2dFGRS is around zero).

However, it can also be seen that between 3–4 h_{70}^{-1} Mpc from the centre of A2734 there is a peak in the mean η. There is another peak at the A2800 end of the plot at a slightly closer distance from the cluster centre. Although within errors one of them does not rise above the field, there is enough of an indication of a peak to warrant further investigation by increasing numbers. To investigate the reality of the signal, we will now stack all three filaments in our sample, and fold Fig. 4.5 such

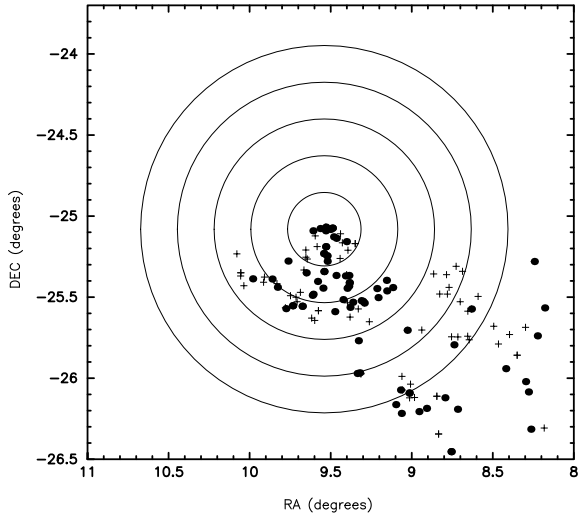

Figure 4.6: The distribution of passive ($\eta < -1.4$) galaxies shown as filled circles and star forming ($\eta > -1.4$) galaxies shown as crosses in the region surrounding Abell 2800. Only galaxies belonging to the A2734–A2800 filament are shown. The concentric circles are at $1\,h_{70}^{-1}$ Mpc intervals. (§4.2.2)

that we consider distances along the filament from the nearest cluster.

Fig. 4.6 and Fig. 4.7 show the distribution of the passive and star forming galaxies for Abell 2800 and Abell 2734 respectively. The concentric circles are at $1\,h_{70}^{-1}$ Mpc intervals and it can be seen that in the 3–4 h_{70}^{-1} Mpc annulus there are more star forming than passive galaxies for both clusters.

4.2.3 Star formation properties of galaxies in all three filaments combined

The distance of each of the filament members from the nearest of the two clusters at either end was calculated using the same method as above.

Here we combine the three filaments longer than $20\,h_{70}^{-1}$ Mpc, namely those joining A2800–A2734, A2734–E0365 and E0365–A2716, seen in Fig. 4.3. All galaxies belonging to the three filaments were grouped in bins of varying size according to their distance from the nearest cluster (representing the extremities of the filaments). As above, we plot the mean value of η and the fraction of passive galaxies in each bin in Fig. 4.8. For comparison between the trend with distance for the filament galaxies with galaxies elsewhere, we compute "field" values from the whole 2dFGRS,

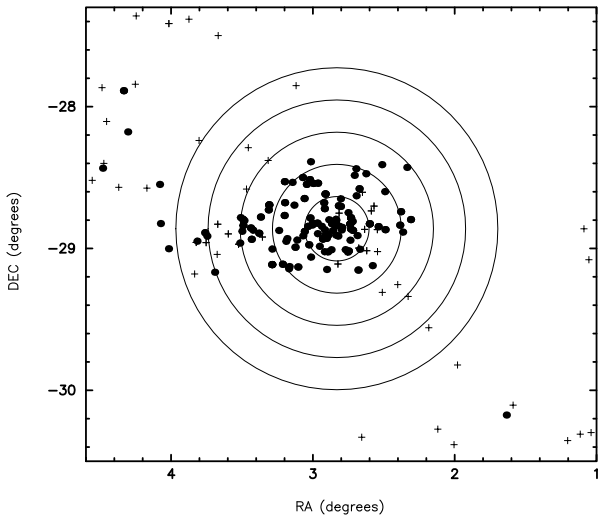

Figure 4.7: The distribution of passive ($\eta < -1.4$) galaxies shown as filled circles and star forming ($\eta > -1.4$) galaxies shown as crosses in the region surrounding Abell 2734. Only galaxies belonging to the A2734–A2800 filament are shown. The concentric circles are at $1\,h_{70}^{-1}$ Mpc intervals. (§4.2.2)

Table 4.1: Virial radii for Pisces-Cetus filament clusters

Cluster	σ (kms^{-1})	Virial radius (Mpc)
A2800	567	1.62
A2734	848	2.42
A2716	812	2.32
E0365	442	1.26

where distances are calculated from the nearest 2PIGG group of ≥ 30 members (the equivalent of a rich cluster), shown as the dashed line.

While the "field" values of mean η increase steadily with distance from the centre of the nearest cluster, the galaxies in the filaments, binned in the same way, show a peak between 3–4 h_{70}^{-1} Mpc, confirming our finding from the single filament above.

A rough estimate of the virial radius of each of the clusters is calculated using the formula of Girardi et al. (1998), $R_v = 0.002\sigma(\mathrm{h}^{-1}\mathrm{Mpc})$, where σ is the one-dimensional velocity dispersion. These are shown in Table 4.1.

The peak region therefore corresponds to about 2 virial radii. A corresponding dip in the percentage of passive galaxies is also seen at this distance. Of course, star

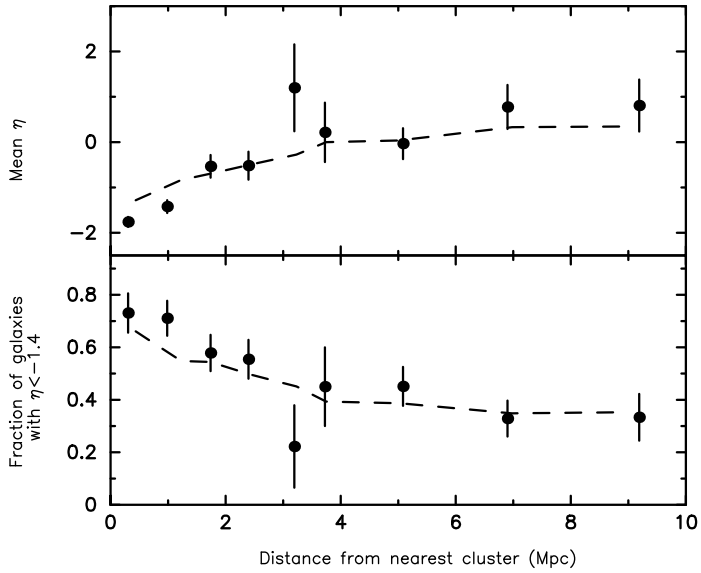

Figure 4.8: (a, Top) For the three filaments combined, the mean η as function of distance from the nearest cluster is shown. The dashed line shows the mean η as function of distance from the nearest 2PIGG group with ≥ 30 members for all 2dFGRS galaxies. (b, Bottom) For the same galaxies as above, the fraction of these galaxies with an $\eta < -1.4$ is shown as a function of distance from the nearest cluster. The dashed line showing the same fraction as a function of distance from the nearest 2PIGG group with ≥ 30 members for the whole 2dFGRS. (§4.2.3)

formation is suppressed as the galaxy approaches the core of the cluster, leading to a low mean η and a higher fraction of passive galaxies interior to this distance. The cause of the enhanced star formation is discussed in more detail in (§4.3).

To get a better picture of how the values of η for the individual galaxies contribute to the means, a histogram of η in each of the 8 bins is shown in Fig. 4.9. It can be seen that the large peak of galaxies at the lowest levels of SFR seen in the first three bins is missing in bins 5 and 6. This combines with a relatively high percentage of galaxies having high η values of above 0 is consistent with the corresponding peak in the mean η of Fig. 4.8.

4.2.4 Star formation in high and low velocity dispersion clusters

If tidal forces were an important influence on the peak in star formation, we would expect that the position of any region of enhanced star formation would vary ac-

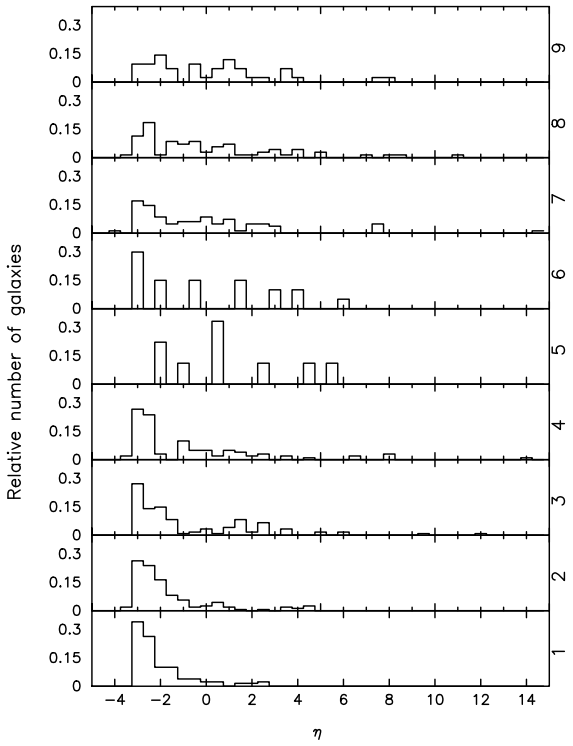

Figure 4.9: For the three filaments combined, histograms of the galaxy η's in each of the 8 distance bins. (§4.2.3)

cording to the velocity dispersion of the cluster that it was nearest to. Tidal forces are proportional to M/R^3, where M is the mass of the cluster and R the distance from the cluster at which tidal forces are encountered. Since the mass of a cluster is proportional to $\sigma^2 R_v$, where σ is the velocity dispersion, you would expect galaxies falling into clusters of larger velocity dispersion to encounter tidal forces at larger distances.

We therefore split the four clusters that form our filaments into those with high velocity dispersions (A2716 = 812 km s^{-1}, A2734 = 848 km s^{-1}) and those with low velocity dispersions (A2800 = 567 km s^{-1}, E0365 = 426 km s^{-1}). Distances from the clusters in each of the two samples were then calculated for the galaxies from the three filaments. Fig. 4.10 shows the resulting values for mean η as a function of distance for the high and low velocity dispersion cluster samples. It can be seen that there is no significant difference in the position of the low velocity dispersion cluster peak in mean η (filled circles) and the peak in the high velocity dispersion cluster peak (open circles).

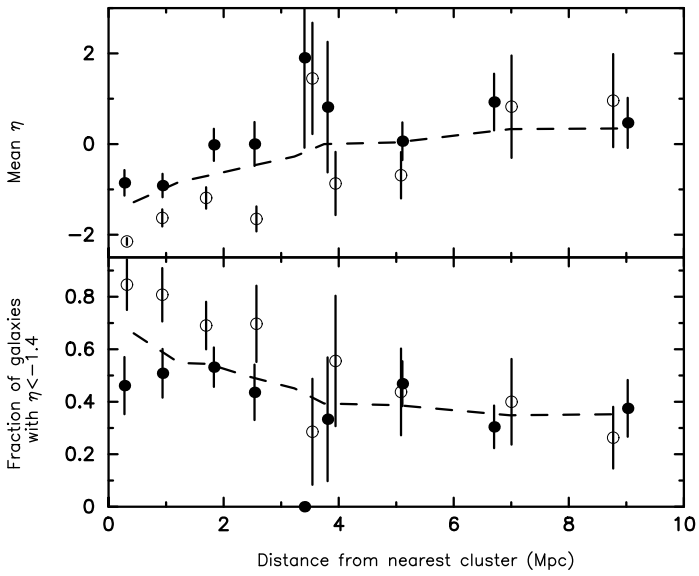

Figure 4.10: (a, Top) For the three filaments combined, the mean η as function of distance from the nearest high or low velocity dispersion cluster is shown. Distances from low velocity dispersion clusters (A2800 and E0365) are shown as filled circles, while distances from high velocity dispersion clusters (A2734 and A2716) are shown as open circles. The dashed line shows the mean η as function of distance from the nearest 2PIGG group with ≥ 30 members for all 2dFGRS galaxies. (b, Bottom) For the same galaxies as above, the fraction of these galaxies with an $\eta < -1.4$ is shown as a function of distance from the nearest cluster. The dashed line showing the same fraction as a function of distance from the nearest 2PIGG group with ≥ 30 members for the whole 2dFGRS. (§4.2.4)

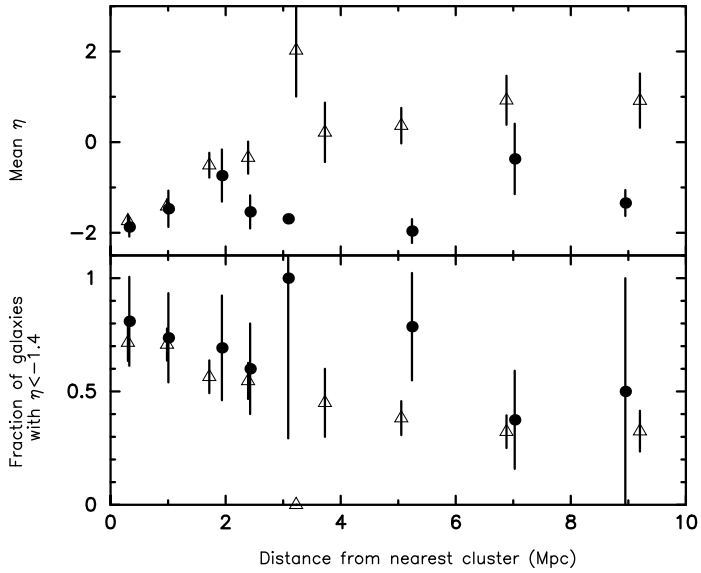

Figure 4.11: Star formation in giant galaxies ($M_B \leq -20$) vs that in dwarfs ($-20 < M_B \leq -17.5$), in the three filaments combined. (a, Top) The mean star formation rate parameter η is shown as function of distance from the nearest cluster, for dwarfs (open triangles) and giants (filled circles). (b, Bottom) The fraction of these galaxies with $\eta < -1.4$ is shown as a function of distance from the nearest cluster. (§4.2.5)

4.2.5 Star formation in giant and dwarf galaxies

As samples of galaxies with estimated star formation properties grow larger, it would become easier to study the relation between star formation in a galaxy and various properties of its environment, and those of the galaxies themselves (e.g., Haines et al., 2006a).

Here, in Fig. 4.11, we break up the galaxies plotted above in Fig. 4.8 into two subsamples: giant galaxies ($M_B \leq -20$) and dwarf galaxies ($-20 < M_B \leq -17.5$). As a result there are are 119 giants and 846 dwarfs in the three filaments used above. As in Fig. 4.8, we plot the mean value of η as a measure of star formation, and the fraction of passive galaxies, as a function of their distance from the nearest cluster, with dwarfs plotted as open triangles and giants as filled circles.

It seems that the peak in mean η seen in Fig. 4.8, between $3 - 4\,h_{70}^{-1}$ Mpc, is almost entirely due to enhanced star formation in dwarfs, indeed there are no passive dwarf galaxies in the bin containing the peak in mean η.

It can be seen in Fig. 4.12, especially for the giant galaxies that there are more

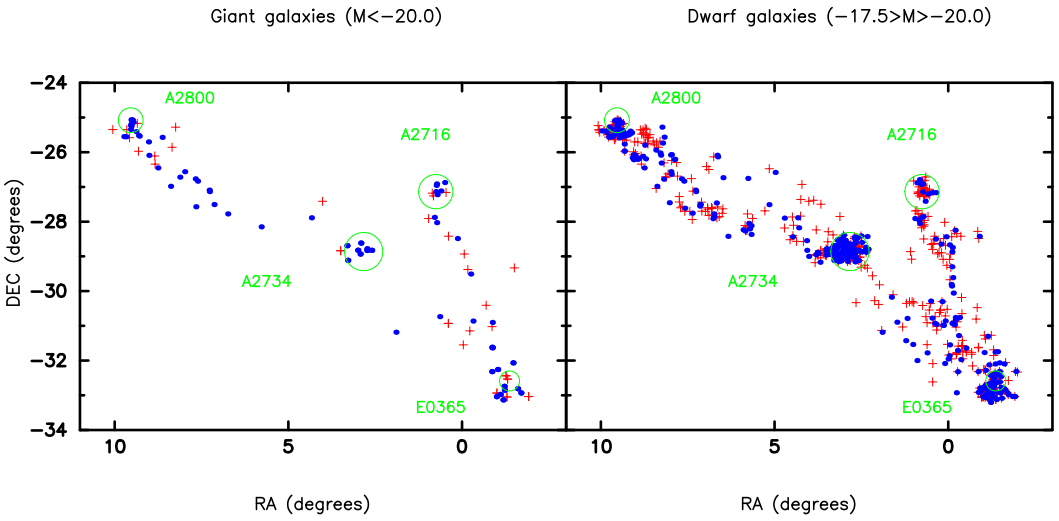

Figure 4.12: The distribution of giant ($M_B \leq -20$) and dwarf ($-20 < M_B \leq -17.5$) galaxies, in the three filaments combined in R.A.-Dec. space. Also shown is the current star formation of these galaxies with passive ($\eta < -1.4$) galaxies shown as blue and star forming ($\eta < -1.4$) as red. The green circles show the virial radius of each cluster. (§4.2.5)

passive galaxies within the virial radius than star forming. The virial radii are taken from Table 4.1.

While the differences in the populations would appear to be real it is worth remembering that the populations were determined from the blue magnitudes. The blue magnitude will be boosted by star formation and therefore the high η galaxies will have preferentially higher blue magnitudes, This will result in some dwarf galaxies being shifted into the giant population. This might explain why our populations overlap at lower radii unlike the completely separate lines of Haines et al. (2006a) who use SDSS R band data. Ideally K-band magnitudes would have been used to separate our populations, but we do not have such magnitudes available from the 2MASS survey for all our galaxies.

4.2.6 Star formation in Groups

The suppression of star formation with increasing local density of galaxies has been observed to occur in giant galaxies at very low values of the local projected density ($\sim 1\, h_{70}^{-1}$ Mpc^{-2}) (e.g. Lewis et al., 2002; Gómez et al., 2003), which are typical of densities well-outside the virialised regions in clusters, indicating that the cause

does not lie entirely in the influence of the cluster environment. One suggestion is that much of the evolution of galaxies occurs in groups during their life on the filaments, before the groups are assimilated in clusters. Evidence supporting this is found in the virialised structure of some galaxy groups (O'Sullivan, Forbes, & Ponman, 2001). If so, the trend seen in the previous section would be different for filament galaxies that belong to groups and those that are relatively isolated.

We divide our sample of galaxies that are members of the three Pisces-Cetus filaments into those that belong to groups (2PIGG groups with 4 or more members, (Eke et al., 2004), and relatively isolated galaxies, which are galaxies that are not members of 2PIGG groups. Fig. 4.13 shows the variation of mean η and the fraction of passive galaxies for these two subsamples, as a function of the distance from the nearest cluster for the filament galaxies. There is a large scatter in the points corresponding to non-group galaxies (representing only 8% of the total number in the sample). There is very weak evidence that the peak in mean η occurs in groups at smaller distances than in the non-group galaxies, which in general have a higher fraction of star forming galaxies. However, as non-group galaxies can not be found within approximately $3\,h_{70}^{-1}$ Mpc of the cluster centres there will be a considerable selection bias against having a peak in star-formation in non-group galaxies at $3\,h_{70}^{-1}$ Mpc or less.

Fig. 4.14 compares the same quantities for galaxies that belong to groups (2PIGG, $N \geq 4$) in these three filaments to similar group galaxies elsewhere in the 2dFGRS. The black dots represent the variation of mean η and passive galaxy fraction as a function of distance from the nearest cluster in the 2dFGRS. The plots suggest that in the sample representing the whole 2dFGRS the SFR is more or less uniform in all group galaxies irrespective of their distance from the nearest cluster, except for those galaxies within the virial radii of clusters. In sharp contrast, the trend we find of a peak in SFR between $3 - 4\,h_{70}^{-1}$ Mpc is seen in the group galaxies that belong to filaments.

To investigate whether the groups that we were comparing the SFR in were the same basic entities in the three filaments and in the whole 2dFGRS, we have plotted histograms of the richness and velocity dispersion for these group samples. These

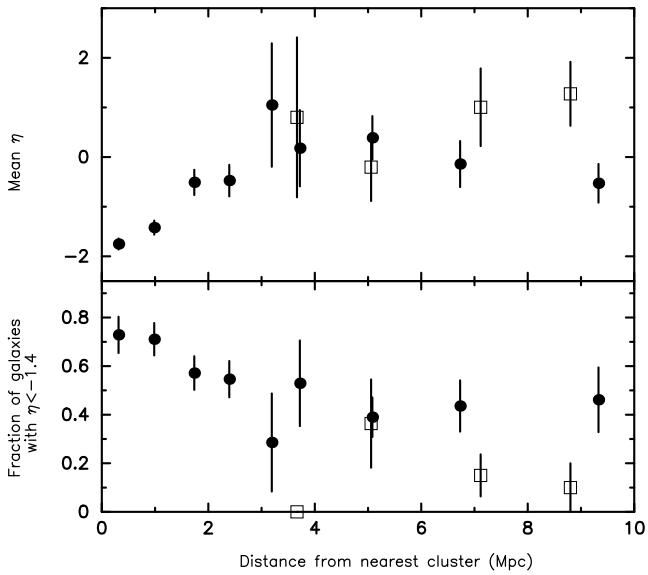

Figure 4.13: (a, Top) The mean value of the η as a function of distance from the nearest cluster, for all galaxies in the three filaments combined. Galaxies that are members of groups (2PIGG groups with $N \geq 4$) are shown as filled circles while galaxies that are not part of a group as squares. (b, Bottom) The fraction of filament galaxies with $\eta < -1.4$ is plotted as a function of distance from the nearest cluster for the same samples. (§4.2.6)

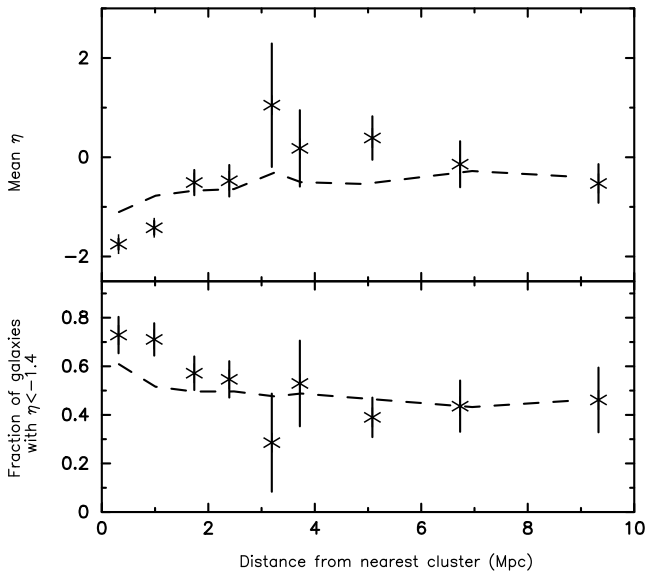

Figure 4.14: Star formation in galaxies in 2dFGRS groups: those in filaments vs the entire 2dFGRS: (a, Top) The mean value of the η as a function of distance from the nearest cluster. Filament galaxies that are members of groups (2PIGG groups with $N \geq 4$) are shown as crosses. This is compared to a sample of ALL galaxies in the 2dFGRS that are members of similar 2PIGG groups (dashed line). The peak in η is not seen in the latter category. (b, Bottom) The fraction of filament galaxies with $\eta < -1.4$ as a function of distance from the nearest cluster for the same samples. (§4.2.6)

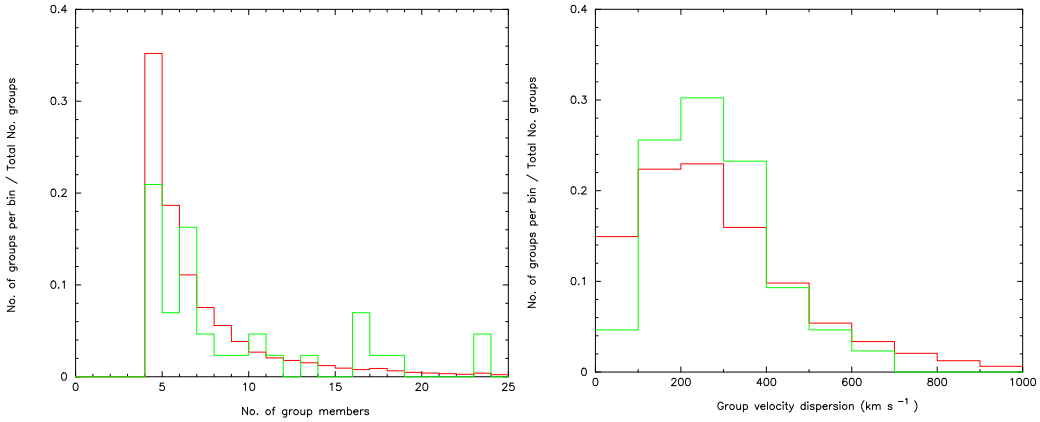

Figure 4.15: (a, Left) Histograms of the relative number of groups with richness 0-25 for groups (2PIGG groups with $N \geq 4$) within the 3 filaments of the Pisces-Cetus supercluster (green) and groups within the entire 2dFGRS (Red). (b, Right) Histograms of the relative number of groups with velocity dispersion 0-1000 Kms^{-1} for groups within the 3 filaments of the Pisces-Cetus supercluster (green) and groups within the entire 2dFGRS (Red). (§4.2.6)

histograms can be seen in Fig 4.15a and Fig 4.15b. It can be seen that there is some evidence that the group galaxies in the filaments (green histograms) have richer groups. There is also marginal evidence that the group galaxies in the filaments have larger velocity dispersions in the range up to 400 kms^{-1}. This may be due to the filamentary structure of the region causing the percolation algorithm used in finding the groups to include more group members and hence the groups to have larger velocity dispersions. Due to this effect and the marginal results of our group work we have chosen not to emphasise the group results.

4.2.7 Welch's test results

Given two data sets, each characterised by its mean, standard deviation and number of data points, we can use some kind of t test to determine whether the means are distinct, provided that the underlying distributions can be assumed to be normal. All such tests are usually called Student's t tests, though strictly speaking that name should only be used if the variances of the two populations are also assumed to be equal. In our case the variances of our means do not have the same variance and so we use a variant of the Student's t tests, Welch's t test. Welch's t test is an adaptation of Student's t-test intended for use with two samples having unequal

Table 4.2: Welch's test results for Pisces-Cetus filaments

Figure	Probability									
number	1	2	3	4	5	6	7	8	9	Joint (4-9)
Fig. 4.8	7.6E-5	2.4E-3	0.53	0.93	0.14	0.74	0.83	0.36	0.42	0.01
Fig. 4.10 *	5.2E-5	0.027	0.006	0.004	0.83	0.28	0.25	0.93	0.67	1.4E-4
Fig. 4.11	0.57	0.89	0.72	0.02	0.0076		4.4E-6	0.17	0.001	1.14E-13
Fig. 4.13						0.71	0.46	0.20	0.16	0.01
Fig. 4.14	3.1E-7	3.1E-5	0.53	0.61	0.28	0.38	0.04	0.77	0.74	1.4E-3

(*) Note that in the case of Fig. 4.10, the test is performed between the low and high velocity dispersion samples, represented by the filled and open circles respectively.

variances, with the statistic given by,

$$t = \frac{\bar{X}_a - \bar{X}_b}{[\mathrm{var}(X_a)/N_a + \mathrm{var}(X_b)/N_b]^{1/2}}, \tag{4.1}$$

where $\bar{X}_a$ is the mean value in dataset 1, $\bar{X}_b$ is the mean value in dataset 2, $\mathrm{var}(X_a)$ is the variance of dataset 1, $\mathrm{var}(X_b)$ is the variance of dataset 2, N_a is the number of data in datset 1 and N_b is the number of data in datset 2. The number of degrees of freedom, v, is given by,

$$v_{\bar{X}_a - \bar{X}_b} = \frac{\left[\frac{\mathrm{var}(X_a)}{N_a} + \frac{\mathrm{var}(X_b)}{N_b}\right]^2}{\frac{[\mathrm{var}(X_a)/N_a]^2}{N_a - 1} + \frac{[\mathrm{var}(X_b)/N_b]^2}{N_b - 1}}, \tag{4.2}$$

The above formulas as part of the "tutest" routine from Press et al. (1992) were applied to the mean η in each bin of our SFR as a function of distance from the centre of a cluster and gave the results seen in Table 4.2. The joint probability for the filament region outside of the cluster radius (bins 4-9) is also shown in Table 4.2. It can be seen that for Fig. 4.8 the point at which the SFR of the filament galaxies peaks, has a probability of 0.14 of the means being equal. This corresponds approximately to a 1.5 σ result, which while not overwhelmingly significant, the result persisted in various subsets of the Pisces-Cetus sample, i.e. the filaments taken independently, as well as the high and low velocity dispersion cluster samples. With the sample drawn from the entire 2dFGRS having no such result this suggests that the result may be stronger than that which the statistics show. The first 4 bins of Fig. 4.10 show significant differences between the high and low velocity dispersion clusters (see §4.3) with three of the bins having probabilities of approximately 3 σ

or greater. The joint probabilities shows that the populations that are the most different to each other are the dwarf and giant samples of Fig. 4.11.

4.3 Discussion

The most striking of our results are those seen in Fig. 4.8, where we look at galaxies which are members of filaments joining pairs of rich clusters of galaxies. We see a decline in SFR in these galaxies, from the filament environment on the periphery of a cluster, to the galaxies in the cluster core, that indicate a physical mechanism at work that quenches star formation progressively as a galaxy approaches the core of the cluster potential well. This trend is consistent with that seen in other environmental studies (e.g., Balogh et al., 1998; Moran et al., 2005). However the unusual feature in our own case is that, on top of this decline we see a nearly instantaneous effect which causes a burst of star formation at $\sim 3\,h_{70}^{-1}$ Mpc from its centre, which is about 1.5–2 times the virial radius of the cluster.

It has been shown that galaxies can be surrounded by a halo of hot gas with a temperature of up to a few million degrees Kelvin (e.g., Pedersen et al., 2006). However, it is likely that many more galaxies have a warm halo of gas with a temperature of a few hundred thousand degrees Kelvin which is too cool to be seen in X-ray detections and too warm to be seen in radio detections. This halo of warm gas would provide a store of gas which can be used as fuel for continued star formation in galaxies.

As galaxies approach the gravitational potential well of cluster, they will start to encounter the Intracluster Medium (ICM), possibly at a distance much larger than the virial radius. Approaching the outer regions of the cluster along a filament, at the same time, the density of galaxies will begin to increase rapidly. At this stage the galaxies will start to lose their warm gas haloes through evaporation and possibly ram pressure stripping, as the gaseous halo of the galaxy interacts with the hot ICM. This will lead to a steep decline in the SFR of galaxies between about $\sim 3\,h_{70}^{-1}$ Mpc, progressively to the centre. This is seen in Fig. 4.8. When the galaxies reach the very dense core region of the clusters at $< 1\,h_{70}^{-1}$ Mpc, galaxy harassment

(Moore et al., 1999) will become an important effect. With a lot of their gas already removed by this stage, star formation will not be induced by the harassment, and the remaining gas of the galaxy will now be stripped, leading to the observed steep dip in SFR in the first two bins from the centre of the cluster.

Superposed on this trend, a rapidly acting process such as galaxies experiencing the ICM for the first time or galaxy harassment are the most likely candidates for our observed sudden burst in SFR at $\sim 3\,h_{70}^{-1}$ Mpc from the cluster. As galaxies just start to encounter the ICM they will not yet have had their gas stripped or evaporated, but the interaction with the ICM will lead to shocks leading to a burst of star formation. Similarly, with their gas still intact, galaxy harassment may lead to density fluctuations in the gas which may trigger a burst of star formation. In the infall region of the cluster at a few h_{70}^{-1} Mpc, the galaxies will just have started to encounter the density of galaxies needed for galaxy harassment to become an important factor. The sharpness of the peak in SFR is another indicator that galaxy harassment may be important, since Moore et al. (1999) show that harassment is a rapid effect.

The effects of "backsplash" (Gill, Knebe, & Gibson, 2005) which are strongest in approximately the $1-2\,h_{70}^{-1}$ Mpc range are not likely to have a strong effect on our peak in SFR, which is further out, but it may mean that the increase in SFR in some galaxies in the sharp peak region may be even stronger than our mean suggests.

Moran et al. (2005) also observe a peak in SFR in the approach to the rich cluster CL0024 at z=0.4. Their peak however is observed at $1.8\,h_{70}^{-1}$ Mpc, i.e. at approximately half the distance of our peak. It is possible the discrepancy between the two may stem from the fact that we are looking at galaxies falling into clusters along filaments. In the case of CL0024, galaxies are falling into the cluster isotropically, while ours are falling in along a denser filament of galaxies, which can lead to a higher local density. This may lead to our galaxies encountering galaxy harassment further from the cluster core.

Our peak in SFR may even contribute to our steep gradient within $\sim 3\,h_{70}^{-1}$ Mpc, making it steeper. The galaxies that are star forming will have had their gas temperature raised and thus when they encounter the ICM they will be more prone to

evaporation and stripping and hence have a rapidly decreasing SFR (for a similar effect on groups see Rasmussen, Ponman, & Mulchaey, 2006).

The principal component analysis used in obtaining the η parameter will not have removed contributions from active galactic nuclei (AGN). It therefore remains a possibility that our peak in SFR is due to AGN activity rather than conventional star formation. In fact this would be fairly consistent with the X-ray results of Ruderman & Ebeling (2005) who find a prominent spike in the number of cluster AGN at $\sim 2.5\,h_{70}^{-1}$ Mpc. However, the detection of X-ray AGN does not necessarily confirm the presence of an optical AGN (Shen et al., 2007) and the above arguments are more suggestive of galaxy harassment being the dominant effect leading to starbursts.

Fig. 4.10 shows that there is no real difference in the position of the peak in SFR in the infall regions of high or low velocity dispersion clusters. Therefore, either the enhanced star formation that we are seeing is not due to the tidal effects of the cluster or the tidal forces are being masked by stronger effects such as those described above. However this plot does show a marked difference between the low and high velocity dispersion distributions in the first 4 bins. In this region the high velocity dispersion clusters are at significantly lower SFRs, this is consistent with the higher velocities resulting in more ram pressure stripping and hence there is less gas available for star formation.

Fig. 4.11 shows that our dwarf galaxies generally have a higher SFR than the giant galaxies. This is consistent with the results of Haines et al. (2006a) and Moran et al. (2005). This also provides more evidence for galaxy harassment being the dominant influence on the burst in star formation, dwarf galaxies are expected to be more vulnerable to galaxy harassment than giants. Moran et al. (2005) shows this, where almost all the galaxies in their peak in the [OII] equivalent width are dwarfs.

The fact that our peak in SFR is mainly due to the dwarf galaxies also means that the burst in SFR is unlikely to be due to merging of galaxies. The small merger cross sections of dwarfs make them unlikely candidates for mergers.

Fig. 4.13 suggests that non group galaxies may have higher SFR at greater distances from the cluster core. However, the low numbers of galaxies used here

make the trend inconclusive. This will be investigated with a larger sample of galaxies in Chapter 5.

4.4 Conclusions

We investigated the environmental dependence of star formation within a supercluster environment. We have done this by finding the variation of the η parameter with distance from cluster centres along filaments of galaxies joining rich clusters.

For galaxies belonging to three filaments (each over $20\,h_{70}^{-1}$ Mpc long), connecting three pairs of rich clusters, we have looked at the variation of the mean η parameter with distance along the filaments, in bins of one to a few h_{70}^{-1}Mpc, starting from the cores of the rich clusters out to the sparser reaches of the filament. We have also looked at similar dependence on distance of the fraction of passive galaxies ($\eta < -1.4$, which is equivalent to the equivalent width of the Hα emission being less than 4 Å), in each distance bin. In doing so, we have also noted whether these galaxies are giant ($M_B \leq -20$) or a dwarf, or member of a group or a cluster. Where possible, we have compared these results to similar properties of galaxies elsewhere in the 2dF galaxy redshift survey.

It is well known that in the cores of rich clusters, the star formation rate in a galaxy is very low, irrespective of its mass, and and this we confirm by showing that the value of mean η and the fraction of passive galaxies falls to its lowest value for both giant and dwarf galaxies in the cores of clusters, both in the supercluster filaments as well as elsewhere in the 2dFGRS. As one moves away from the cores of clusters along the filaments, there is an increased activity of star formation, peaking in the range $3 - 4\,h_{70}^{-1}$ Mpc, which is 1.5–2 times the virial radius of the clusters. This peak in star formation in filament galaxies is seen to be entirely due to dwarf galaxies ($-20 < M_B \leq -17.5$). More luminous galaxies ($M_B \leq -20$) have much lower star formation in general in agreement with previous work done by others.

We have also examined the influence of the group environment on the SFR in the galaxies within the filament. There is some evidence to suggest that the peaks in mean η are present in more or less the same position in both group and non-group

galaxies. It is also seen that there is little variation in mean η with distance for the group galaxies taken from the whole 2dFGRS. This is in contrast with the group galaxies within the filaments which again show a peak at approximately $3\,h_{70}^{-1}$ Mpc. This would suggest that the filament environment is dominant over the group environment with respects to SFR at this distance.

The possible physical mechanisms for the gradient in SFR and the peak in SFR at $\sim 3\,h_{70}^{-1}$ Mpc have been discussed in §4.3 and galaxy harassment is seen as the most likely candidate for the rapid burst in star formation.

Finally, although these results in this work are indicative of interesting environmental effects on star formation in galaxies, investigated at a level beyond the usual projected local densities that are more commonly found in the literature, they come from a small sample of about a thousand galaxies in three filaments in a single supercluster. Moreover, we have used an indirect measure for star formation (the η parameter) in these galaxies. It would therefore be useful to explore these effects in a large ensemble of filaments from both the 2dFGRS and 6dFGRS, not only using various measures of star formation, but also scrutinising the effects of various environmental parameters that large samples can afford.

Chapter 5

The 1st Duke of Wellington: "Wise people learn when they can; fools learn when they must."

Star formation in 2dFGRS filaments

5.1 Introduction

In Chapter 4 we investigated the environmental dependence of star formation within three filaments joining rich clusters of the Pisces-Cetus supercluster region. We observed that as one moves away from the cluster cores there is an increased activity of star formation, with a peak in the 3-4 h_{70}^{-1} Mpc range along the filaments over and above the gradual increase in star formation rate (SFR) away from the cluster cores. While this is a striking result, these results come only from approximately 1,000 galaxies in three filaments, and in one supercluster. To confirm that the observed effect is not confined to this one supercluster, a larger sample of filaments is therefore required. Since the Pisces-Cetus supercluster is the only supercluster of the Raychaudhury et al. (2007) catalogue within the 2dFGRS region, we sought another source of filaments.

In this Chapter, we have drawn from the filament catalogue of Pimbblet, Drinkwater, & Hawkrigg (2004) which listed 805 "filaments" identified among the galaxies of the 2dFGRS, this sample will be referred to as the PIM04 sample. Since the catalogue is compiled from the 2dFGRS, the η parameter was once again available as an estimator of star formation for all the member galaxies.

5.2 The filament catalogue

The source catalogue of potential filaments was composed from the cluster catalogue of De Propris et al. (2002) consisting of over 800 cross correlations with the Abell (Abell et al., 1989), the Edinburgh Durham Cluster Catalogue (Lumsden et al., 1992) and the APM survey cluster catalogue (Dalton et al., 1997). From this catalogue, they select potential intercluster filaments, by applying the following criteria:

1. The clusters must be spatially close, < 10 degrees on the sky. At a median redshift of $z = 0.1$, this corresponds to a projected length of $\approx 45h^{-1}$ Mpc.

2. Their recession velocities must not differ by more than $z = 1000$ km s^{-1}.

3. Clusters common to the Abell, EDCC and APMCC catalogues are removed to prevent self-pairing. This resulted in 805 unique potential intercluster filaments.

Based on the method of Colberg, Krughoff, & Connolly (2005) the potential filaments are then classified into types. This is done by drawing a vector from one cluster centre to the other and then extracting all galaxies within 20 h_{100}^{-1} Mpc of this axis with a depth of 5 h_{100}^{-1} Mpc. These galaxies are then placed onto two orthogonal planes containing the intercluster axis and smoothed with a circular top-hat function of radius 1 h_{100}^{-1} Mpc. The two projections were then visually inspected and classified according to Table 5.1.

5.3 The samples

5.3.1 Filament selection

Further criteria were applied to narrow down the initial sample of 805 potential filaments. Only filaments having a length of between 10 and 40 h_{70}^{-1} Mpc were selected. Further more, potential filaments that had a classification (see Table 5.1) of "near coincidental clusters" or "Nil" were also removed. This resulted in a sample of 432 filaments to study visually. Each of the 432 filaments had two clusters from which Pimbblet, Drinkwater, & Hawkrigg (2004) had identified a filament. In addition

Table 5.1: Filament type classification in the PIM04 sample

Type	Filament description
Nil	No filament is detected.
0	Near-coincident clusters. The cluster pair overlaps to such a degree that any filament present cannot be isolated.
1	Straight. The filament of galaxies runs along the axis from one cluster centre to the other.
2	Warped (Curved). The galaxies lie off the axis and continuously curve (in a 'C' or 'S'-shape for example) from one cluster centre to the other.
3	Sheet (Planar; Wall). The filament appears as Type I or II viewed from one direction but the galaxies are approximately evenly spread out in the orthogonal view.
4	Uniform. Galaxies fill the space between the clusters in an approximately uniform manner viewed from any direction.
5	regular (Complex). There are one or more connections between both cluster centres, but the connections are irregular in shape and often have large density fluctuations.

to these clusters other clusters fall within the same region of space. These extra clusters were deemed to be part of the filament if they had a redshift within 0.01 of the mean redshift of the two initial clusters and were coincident with the filament galaxies in R.A. and Dec. space. In addition, to confirm the presence of a cluster of galaxies at the cluster positions, each of the clusters had to have greater than ten members to be part of the filament. Cluster membership was determined by finding all 2PIGG (Eke et al., 2004) group centres within 1 h_{70}^{-1} Mpc of the cluster centres. The members of these groups were then taken as the cluster members. Most clusters would correspond with a single 2PIGG "group" but for some, the 2PIGG catalogue had separated the cluster members into multiple "groups".

From the sample of 432 filaments we created a "clean sample" of filaments. The filaments had to be between two clear clusters of galaxies and have to be relatively clean from contamination from other filaments and clusters. Therefore, by a visual inspection of the 432 filaments, 52 pairs of clusters on these filaments that had a clear run of galaxies, with no other intruding clusters within 6 h_{70}^{-1} Mpc, were found.

These can be seen in Table 5.2. To avoid contamination from the complex weave of other filaments, and to enable comparisons with our previous work, the galaxies joining the two filament clusters were selected using the prolate spheroid method as described in section 4.2.1. This resulted in 6,222 galaxies within the 52 filaments.

As in Chapter 4 all references to 2dFGRS galaxies are taken from the 2PIGG subsample of the 2dFGRS (Eke et al., 2004) comprising 191,328 galaxies. This subsample had all the galaxies within fields with less than 70% completeness, and in all sectors (overlapping field areas) with completeness less than 50%, removed This enables comparisons with 2PIGG statistics to be made without bias.

Table 5.2: Filament information for the 52 visually selected sample.

Clusters	Mean redshift	Filament length
Abell 2829 Abell 0118	0.1133	20.75
Abell 3094 Abell S0333	0.0675	13.07
Abell 1419 Abell 1364	0.1072	27.51
Abell 1411 Abell 1407	0.1334	21.41
Abell 1692 Abell 1663	0.0834	17.41
Abell 1620 Abell 1663	0.0839	21.58
Abell 2553 EDCC 0275	0.1458	13.05
Abell 3980 EDCC 0268	0.1894	27.04
APMCC 0869 APMCC 0840	0.1125	47.62
Abell 2601 Abell 4009	0.1091	42.68
EDCC 0365 Abell S1155	0.0547	38.71
Abell 2741 APMCC 0039	0.1050	12.92
Abell 2780 APMCC 0039	0.1031	33.62
EDCC 0465 Abell 2780	0.1046	40.13
Abell 2741 APMCC 0051	0.1060	21.07
EDCC 0445 APMCC 0094	0.0617	17.94
APMCC 0094 EDCC 0457	0.0613	20.86

continued on next page

Clusters	Mean redshift	Filament length
EDCC 0465 Abell 2814	0.1084	12.44
Abell 2814 Abell 2829	0.1097	22.08
Abell 2734 EDCC 0445	0.0623	17.94
EDCC 0457 EDCC 0445	0.0620	10.24
Abell 2829 EDCC 0511	0.1112	23.01
EDCC 0517 EDCC 0511	0.1107	19.03
Abell 2878 EDCC 0511	0.1090	24.14
Abell 2915 EDCC 0581	0.0862	23.51
APMCC 0167 Abell S0160	0.0688	7.98
Abell 2943 APMCC 0222	0.1498	21.36
Abell 2961 APMCC 0245	0.1242	25.60
Abell 2967 Abell 2972	0.1122	12.03
Abell 2981 Abell 2999	0.1083	15.84
EDCC 0119 Abell 3837	0.0885	28.84
EDCC 0057 Abell 3837	0.0922	25.07
EDCC 0057 APMCC 0721	0.0963	30.55
Abell 3878 Abell 3892	0.1179	22.31
EDCC 0230 APMCC 0827	0.1103	15.80
APMCC 0827 Abell 3892	0.1142	31.64
EDCC 0128 Abell 3880	0.0586	15.12
Abell 3959 APMCC 0853	0.0876	17.09
Abell S1075 Abell 3978	0.0854	26.87
EDCC 0457 Abell 2794	0.0613	20.86
EDCC 0492 Abell 2804	0.1169	44.83
EDCC 0202 EDCC 0187	0.0768	8.85
EDCC 0187 APMCC 0810	0.0769	7.24
EDCC 0317 Abell 4011	0.1371	8.76

continued on next page

Clusters	Mean redshift	Filament length
EDCC 0321 Abell 4012	0.0533	9.49
Abell 3854 Abell 3844	0.1505	29.89
Abell S1064 EDCC 0153	0.0571	17.95
Abell 2967 Abell 2981	0.1103	16.12
EDCC 0239 APMCC 0853	0.0871	17.62
EDCC 0248 Abell 3959	0.0876	17.09
EDCC 0217 EDCC 0202	0.0784	19.94
Abell 2493 EDCC 0215	0.0773	21.88
Abell 2493 EDCC 0215	0.0773	21.88

5.4 Star formation properties

5.4.1 Properties of galaxies in the field

It has been shown on many occasions (Dressler, 1980; Couch & Sharples, 1987; Balogh et al., 1998) that star formation is suppressed in cluster cores and then increases with decreasing galaxy density away from the dense cores. Here we seek to confirm this for the 2dFGRS using the star formation parameter η which is described in detail in Section 2.5.

The distance of each of the 191,328 2dFGRS galaxies was calculated from the nearest 2PIGG group of ≥ 30 members (the equivalent of a rich cluster). This was done for all 2dFGRS galaxies with a measured η value which comprised 167,602 galaxies. The galaxies were then binned in distance in 0.5 h_{70}^{-1} Mpc bins within the approximate cluster bounds of 2.5 h_{70}^{-1} Mpc. Around the 3 h_{70}^{-1} Mpc region of interest, from past results, 0.1 h_{70}^{-1} Mpc bins were used, while beyond this 1 h_{70}^{-1} Mpc bins were used. These small bin sizes were only possible due to the large sample size.

It can be seen in Fig. 5.1 that our results agree with the literature, with the star formation being at a minimum within the cluster cores and gradually rising with increasing distance from the core and hence decreasing galaxy density. The means of this sample are taken as a field level with which other distributions can be

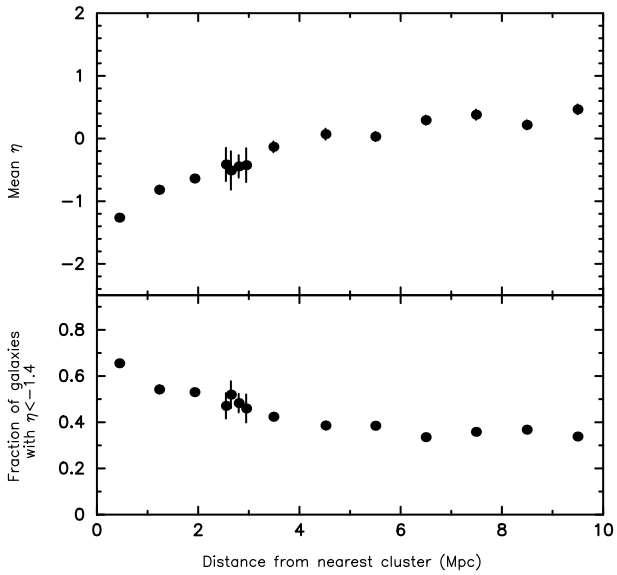

Figure 5.1: (a, Top) For galaxies with a measured η, from the entire 2dFGRS (N=167602), the mean η as function of distance from the nearest cluster (defined as 2PIGG groups with ≥ 30 members) is shown. Finer bins are chosen between 2–4 h_{70}^{-1} Mpc to investigate the presence of enhanced SFR in this region. (b, Bottom) For the same galaxies as in a the fraction of these galaxies with an $\eta < -1.4$ is shown as a function of distance from the nearest cluster. (§5.4.1)

compared.

5.4.2 Star formation in galaxies belonging to filaments

Once the members of each filament had been determined the same method used in their selection was used to find the distance of each filament member from the nearest of the two clusters at either end. The distances were then binned with the first two bins extending out to 2.14 h_{70}^{-1} Mpc (Abell radius) to contain all the cluster galaxies. The area of greatest interest just outside of the cluster was covered in 0.25 h_{70}^{-1} Mpc bins while in the outer regions 2 h_{70}^{-1} Mpc bins were used. Within each bin the mean η was calculated. The data for galaxies from all the filaments were combined and the means plotted against the mean distance in each bin and can be seen in see Fig. 5.2. For comparison between the trend with distance for the filament galaxies with galaxies elsewhere, we take the field values calculated in section 5.4.1, shown as the dashed line. We also plot, in the bottom panel, the fraction of passive ($\eta < -1.4$) galaxies in each bin.

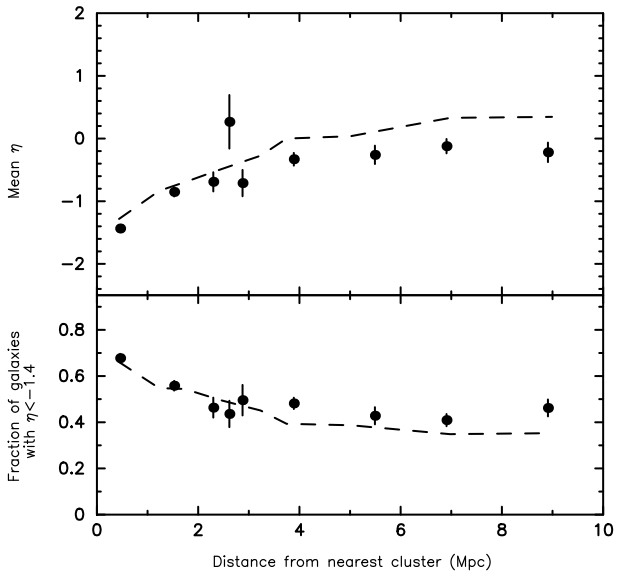

Figure 5.2: (a, Top)For the "clean filament" sample (N=52), the mean η of each galaxy as function of distance from the nearest cluster is shown. The dashed line shows the mean η as function of distance from the nearest cluster (defined as a 2PIGG group with ≥ 30 members) for all 2dFGRS galaxies. (b, Bottom) For the same galaxies as in the top panel the fraction of these galaxies with an $\eta < -1.4$ is shown as a function of distance from the nearest cluster. The dashed line showing the same fraction as a function of distance from the nearest 2PIGG group with ≥ 30 members for the whole 2dFGRS. (§5.4.2)

Fig. 5.2 shows, as expected, the mean η and hence SFR is at a minimum in the first bin, within the cluster and the fraction of passive galaxies is at a maximum. The field value shown as a dotted line on average has a gradual increase in SFR with increasing distance from the cluster centre. However, the filament galaxies show a distinct peak in the gradual increase in SFR at approximately $2.5\,h_{70}^{-1}$ Mpc. This region corresponds to about 1.5 virial radii. This is in agreement with the results of the Pisces-Cetus filaments used in Chapter 4. There is a very slight corresponding dip in the percentage of passive galaxies in the 2.0–2.5 h_{70}^{-1} Mpc range.

Fig. 5.3 shows a histogram of the values of η for each of the 8 bins for the galaxies of the 52 filaments and the field. It can be seen that the mean η value for the field represented by the dashed vertical line increases gradually with increasing bin number while the filament galaxies have a peak in bin 4. It can be seen in the histograms, that in bin 4, there is a reduction in the number of filament galaxies in the first passive peak and a slight increase in the numbers above this at higher

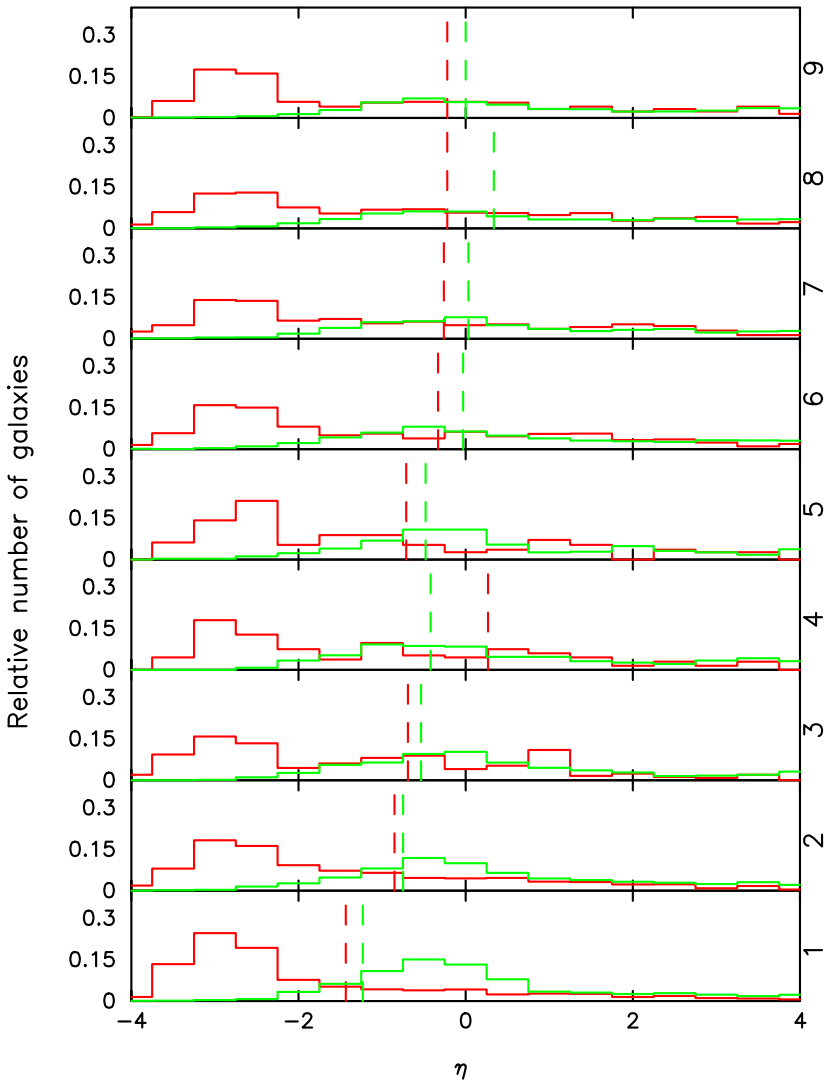

Figure 5.3: For the "clean filament" sample (N=52), histograms of the η parameter for the galaxies in each of the 8 distance bins are shown in red. The corresponding histograms for the field galaxies are shown in green. The mean η in each bin is shown as a dashed vertical line. (§5.4.2)

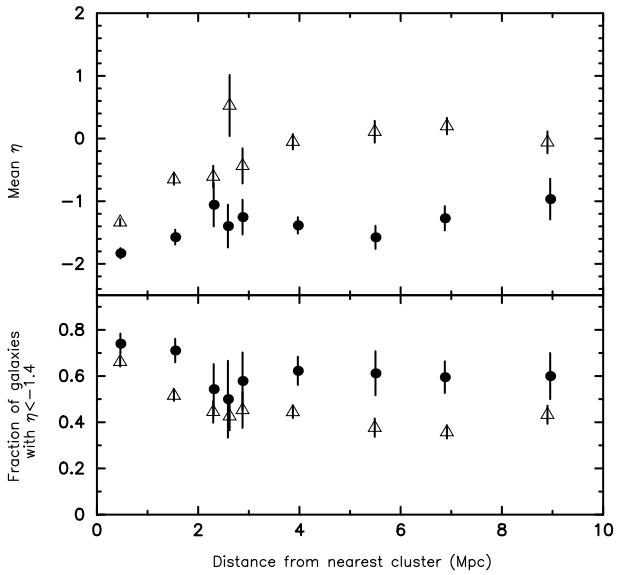

Figure 5.4: (a, Top)For the "clean filament" sample (N=52), the mean η as function of distance from the nearest cluster is shown. Giant galaxies ($M < -20$) are shown as closed circles while dwarf galaxies ($M > -20$) are shown as open triangles. (b, Bottom) For the same galaxies as in a the fraction of these galaxies with an $\eta < -1.4$ is shown as a function of distance from the nearest cluster. (§5.4.3)

values of η for the filament galaxies with respect to the field.

5.4.3 Star formation in giant and dwarf galaxies

Continuing the investigation of star formation with respects to environment, the "clean filament" sample (N=6,222 galaxies) was further segregated by environment into giant and dwarf galaxies. The samples were defined as giant galaxies ($M_B \leq -20$) and dwarf galaxies ($-20 < M_B \leq -17.5$) of 1,392 galaxies and 4,830 galaxies respectively.

As before we plot the mean value of η, and the fraction of passive galaxies, as a function of their distance from the nearest cluster, which can be seen in Fig. 5.4. However, the two separate samples are now plotted as open triangles for dwarf galaxies and filled circles for giant galaxies.

It seems that the peak in mean η seen in Fig. 5.4, at approximately $2.5\,h_{70}^{-1}$ Mpc, is almost entirely due to enhanced star formation in dwarfs. This is in agreement with our results for the Pisces-Cetus filaments. The two populations are completely

segregated with the dwarf galaxies having more SFR at all distances. This is in good agreement with Haines et al. (2006a) who gets a lower fraction of passive galaxies in giants for all values of local density.

As in Chapter 4 it is worth remembering that the populations were determined from the blue magnitudes. The blue magnitude will be boosted by star formation and therefore the high η galaxies will have preferentially higher blue magnitudes. However, this effect would serve to pull the two populations closer together so the real separation may be even greater than that seen here.

5.4.4 Star formation in short and long filaments

Continuing the investigation of star formation with respects to environment, the "clean filament" sample (N=6,222 galaxies) was further segregated by environment into those falling in short filaments (length $\leq$ 15 h_{70}^{-1} Mpc) and long filaments (length $>$ 15 h_{70}^{-1} Mpc). The samples had of 1,452 galaxies and 4,770 galaxies respectively.

As before we plot the mean value of η, and the fraction of passive galaxies, as a function of their distance from the nearest cluster, which can be seen in Fig. 5.5. However, the two separate sample are now plotted as open triangles for long filament galaxies and filled circles for short filament galaxies.

The peak in mean η seen in Fig. 5.5, at approximately 2.5 h_{70}^{-1} Mpc, is seen in both samples. However, there is some evidence that the short filament galaxy sample peak is higher than that of the longer filament sample. In fact in general the shorter filament sample galaxies have a higher SFR. This is reflected in the fraction of passive galaxies which is in general lower for the shorter filaments.

5.4.5 Star formation in groups

The suppression of star formation with increasing local density of galaxies has been observed to occur at very low values of the local projected density ($\sim$1 h_{70}^{-1} Mpc^{-2} (e.g. Lewis et al., 2002; Gómez et al., 2003), indicating that the cause does not lie entirely in the influence of the cluster environment. One suggestion is that much of

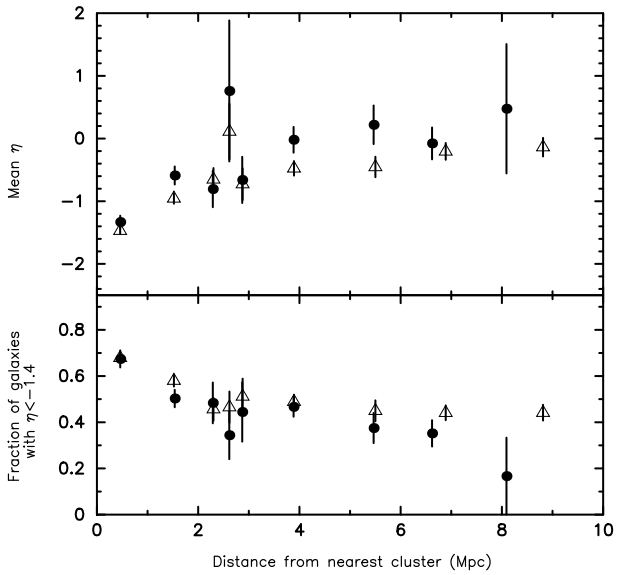

Figure 5.5: (a, Top)For the "clean filament" sample (N=52), the mean η as function of distance from the nearest cluster is shown. Short filament ($length \leq 15\ h_{70}^{-1}$ Mpc) galaxies are shown as closed circles while long filament ($length > 15\ h_{70}^{-1}$ Mpc) galaxies are shown as open triangles. (b, Bottom) For the same galaxies as in a the fraction of these galaxies with an $\eta < -1.4$ is shown as a function of distance from the nearest cluster. (§5.4.4)

the evolution of galaxies occurs in groups during their life on the filaments, before the groups are assimilated in clusters. If so, the trend seen in the previous section would be different for filament galaxies that belong to groups and those that are relatively isolated.

As in Chapter 4 We therefore split our galaxy sample into those that are a member of a group and those that are not. A group member is defined to be a member of a 2PIGG group (Eke et al., 2004) that has 4 or more members and a non-group or relatively isolated galaxy is defined as a galaxy which is not a member of a 2PIGG group of any number of members. The majority of the galaxies are part of groups with 4,921 falling in this category, with 669 galaxies being classified as relatively isolated. As in the other sections the mean value of η, and the fraction of passive galaxies, as a function of their distance from the nearest cluster are plotted in Fig. 5.6.

Fig. 5.6 shows the variation of mean η and the fraction of passive galaxies for these two subsamples, as a function of the distance from the nearest cluster for the filament galaxies. The mean η is seen to occur in groups and non-group galaxies at

approximately the same distance, but with the non-group galaxies generally having a higher fraction of star forming galaxies.

Fig. 5.7 compares the same quantities for galaxies that belong to groups (2PIGG, $N \geq 4$) in the 52 filaments to similar group galaxies elsewhere in the 2dFGRS. The black dots represent the variation of mean η and passive galaxy fraction as a function of distance from the nearest cluster in the 2dFGRS (defined as 2PIGG groups with $N \geq 30$).

In agreement with the results of Chapter 4 the plots suggest that the star formation rate is more or less uniform in all groups galaxies irrespective of their distance from the nearest cluster, except for those galaxies within the virial radii of clusters. There is some indication that the trend we find of a peak in SFR at approximately $2.5\,h_{70}^{-1}$ Mpc is seen in the group galaxies that belong to filaments, indicating that the presence of the filaments influences star formation properties in galaxies that belong to groups in this region. In general the non-group galaxies are seen to have higher mean values of η and a lower fraction of passive galaxies than the group galaxies both in the filament and in the 2dFGRS as a whole.

In the same manner as in Chapter 4 we have investigated whether the groups that we were comparing the SFR in were the same basic entities in the filaments and in the whole 2dFGRS. We have therefore plotted histograms of the richness and velocity dispersion for these group samples. These histograms can be seen in Fig 5.8a and Fig 5.8b. It can be seen, that in agreement with the smaller group sample in Chapter 4, the filament groups (green histograms) have a higher proportion of richer galaxies and higher proportion with larger velocity dispersions. This is not unexpected as the filamentary nature of the region will cause the percolation algorithm that the groups were formed by to pick out more group members and hence the groups have larger velocity dispersions.

5.4.6 Welch's test results

As in Chapter 4 we have used Welch's t test to determine if the means of our two populations are distinct from one another. Applying Welch's t test to the mean η in each bin of our SFR as a function of distance from the centre of a cluster gives

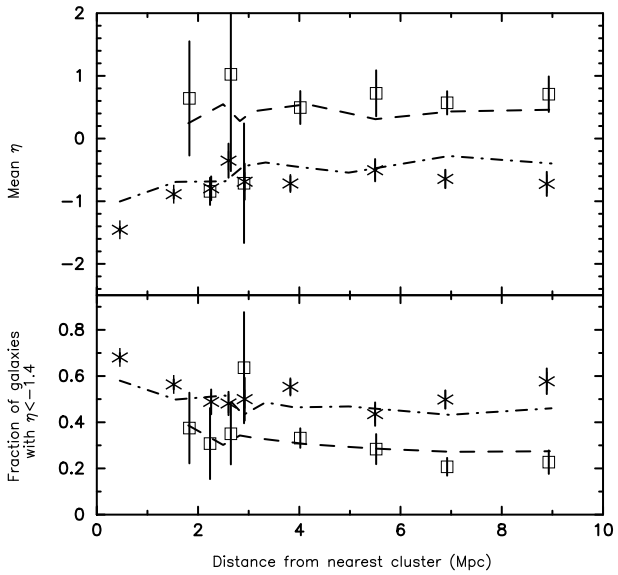

Figure 5.6: (a, Top)For the "clean filament" sample (N=52), the mean η as a function of distance from the nearest cluster. Galaxies that are members of groups and part of the filament are shown as crosses while galaxies that are not part of a group are shown as squares. A group is defined as a 2PIGG group with greater than or equal to 4 members, while non-group galaxies are those 2PIGG groups which are not part of a group of any number of members. The dashed line shows the mean η for non-group galaxies in the whole 2dFGRS, while the dot-dashed line shows the mean η for group galaxies in the whole 2dFGRS. (b, Bottom) The fraction of filament galaxies with $\eta < -1.4$ as a function of distance from nearest cluster within the same galaxy and group samples as defined for a. (§5.4.5)

the results seen in Table 5.3. The joint probability for the filament region outside of the cluster radius (bins 4-9) is also shown in Table 5.3.

It can be seen that for Fig. 5.2 the point at which the SFR of the filament galaxies peaks has a probability of 0.03 of the means being equal. This corresponds approximately 2.0 σ result, which while still not overwhelmingly significant, it is an improvement on the 1.5 σ result of Chapter 4, strengthening the reality of the enhancement. Furthermore, reproducing the results of our earlier work of just one and three filaments, in various samples within 52 filaments, enhances the robustness of our results beyond that shown by the formal significance. The lowest joint probability is again for the giant and dwarf populations of Fig. 5.4, although most of the joint probabilities are so small as to make them effectively zero.

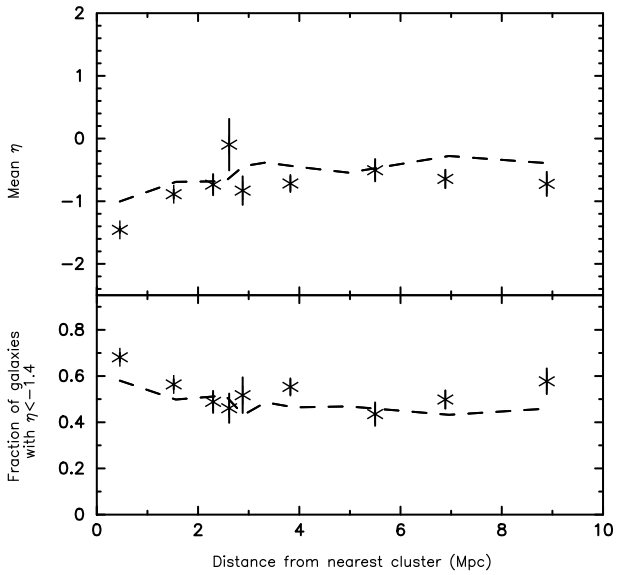

Figure 5.7: (a, Top)For the "clean filament" sample (N=52), the mean η as a function of distance from the nearest cluster. Galaxies that are members of groups and part of the filament sample are shown as crosses This is compared to galaxies that are part of groups within the entire 2dFGRS shown as a dashed line. A group is a 2PIGG group with greater than or equal to 4 members, while non-group galaxies are those 2PIGG groups which are not part of a group of any number of members. (b, Bottom) The fraction of filament galaxies with $\eta < -1.4$ as a function of distance from nearest cluster within the same galaxy and group samples as defined for a. (§5.4.5)

5.5 Star formation in the PIM04 sample filaments

We have shown that within filaments of galaxies which meet our tight definition for a "clean filament" there is a marked difference between filament galaxies and the rest of the field. In this section we investigate whether the same trends are seen within the more broadly defined filaments of the PIM04 sample.

We take two filament samples from the PIM04 sample, the length of filament being between 10 and 40 h_{70}^{-1} Mpc in each. From these filaments we extract the

Table 5.3: Welch's test results for "clean sample" filaments

Figure	Probability									
number	1	2	3	4	5	6	7	8	9	Joint (4-9)
Fig. 5.2	0.02	0.87	0.97	0.08	0.03	0.04	0.06	3.9E-3	6.5E-3	1.8E-9
Fig. 5.4	1.1E-6	6.23E-10	0.24	0.001	0.04	3.9E-13	2.5E-10	1.5E-9	0.02	1.2E-36
Fig. 5.5	0.23	0.03	0.65	0.59	0.88	0.06	0.05	0.65	0.56	5.7E-4
Fig. 5.6			0.86	0.37	0.98	3.7E-5	0.003	4.3E-7	4.2E-5	4.5E-19
Fig. 5.7	0	0.09	0.53	0.47	0.76	3.2E-5	0.003	2.9E-5	3.0E-5	2.9E-17

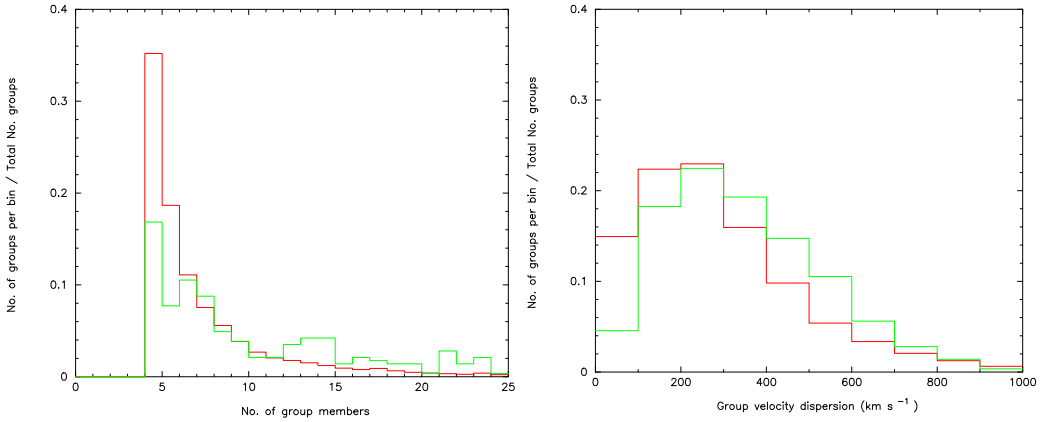

Figure 5.8: (a, Left)Histograms of the relative number of groups with richness 0-25 for groups (2PIGG groups with $N \geq 4$) within the 52 filaments of the clean filament sample (green) and groups within the entire 2dFGRS (Red). (b, Right) Histograms of the relative number of groups with velocity dispersion 0-1000 kms^{-1} for groups within the 52 filaments of the clean sample (green) and groups within the entire 2dFGRS (Red). (§5.4.5)

galaxies that formed the orthoginal plains used in the classification process and remove any repeated galaxies. The samples were defined as:

1. Galaxies from filaments classified as type 1, straight or 2, warped in the PIM04 sample. This resulted in 307 filaments and 24,420 galaxies (PIM04a).

2. Galaxies in filaments of all types including those that are classified as being near coincidental clusters and as not being a filament. This resulted in 552 filaments and 35,609 galaxies (PIM04b).

5.5.1 Star formation within the filaments

As in the other sections the mean value of η, and the fraction of passive galaxies, as a function of their distance from the nearest cluster are plotted for each of the samples.

The galaxies of PIM04a while being from more broadly defined definition of filament than ours, the filament type is still constrained. It can be seen in Fig. 5.9 that while the peak in mean η at approximately 2.5 h_{70}^{-1} Mpc is less pronounced than that in our own filaments there is definite evidence for a peak in mean η and a very slight dip in the fraction of passive galaxies.. However, one difference to note is that

for this sample the majority of the points fall under the field value, with only the peak values approaching field levels. This can also be seen in Fig. 5.11 where the mean in each bin of the PIM04a sample shown in red is below that of the field. It can be seen that in most bins the red histogram is above the green for the lower η values below -2.0. This is in contrast to the results of our tightly defined filaments where only the higher radii points drop significantly below the field, and the results of Chapter 4 where the filament points closely follow the field and the peak values are well above it.

The galaxies of PIM04b include all of the potential filaments and thus will include those that are complex, coincidental clusters and even those classified as not being a filament. Therefore, these galaxies will simply be from the regions between two clusters with the potential to be a filament. The resulting plot can be seen in Fig. 5.10 and there is little or no evidence for a peak at $2.5\,h_{70}^{-1}$ Mpc in this very loose definition of filament. Once again the points are below that of the field values with not even the peak reaching the field level.

5.5.2 Star formation within giants and dwarfs

For the PIM04a galaxies which have shown some evidence for the trends seen in our other work the 24420 galaxy sample was further segregated by environment into giant and dwarf galaxies. The samples were defined as giant galaxies ($M_B \leq -20$) and dwarf galaxies ($-20 < M_B \leq -17.5$) of 5867 galaxies and 18553 galaxies respectively.

As before we plot the mean value of η, and the fraction of passive galaxies, as a function of their distance from the nearest cluster, which can be seen in Fig. 5.12. However, the two separate sample are now plotted as open triangles for dwarf galaxies filled circles for giant galaxies.

Fig. 5.12 again shows the results to be consistent with our previous results both in this Chapter and Chapter 4 and with the results of Haines et al. (2006a), with the dwarf galaxies having a higher mean SFR at all distances. The peak at approximately $2.5\,h_{70}^{-1}$ Mpc is clearly seen in the dwarf galaxies once again with slight evidence for a corresponding dip in the fraction of passive galaxies. The same peak is a little more ambiguous in the giant galaxies with only the two outside points of

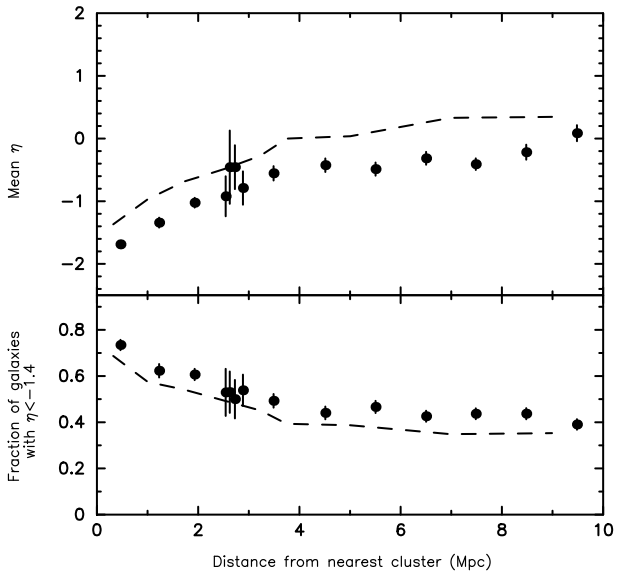

Figure 5.9: (a, Top)For galaxies within the filaments of PIM04a of the PIM04 sample , the mean η as function of distance from the nearest cluster is shown. The dashed line shows the mean η as function of distance from the nearest 2PIGG group with ≥ 30 members for all 2dFGRS galaxies. (b, Bottom) For the same galaxies as in a the fraction of these galaxies with an $\eta < -1.4$ is shown as a function of distance from the nearest cluster. The dashed line showing the same fraction as a function of distance from the nearest 2PIGG group with ≥ 30 members for the whole 2dFGRS. (§5.5.1)

the four normally associated with the peak actually being at a raised value.

5.5.3 Star formation in groups

As before we split our PIM04a filament galaxies into those that are a member of a group and those that are not. A group member is defined to be a member of a 2PIGG group (Eke et al., 2004) that has 4 or more members and a non-group or relatively isolated galaxy is defined as a galaxy which is not a member of a 2PIGG group of any number of members. A larger percentage of the galaxies are part of groups with 11,204 falling in this category, with 7,457 galaxies being classified as relatively isolated. As in the other sections the mean value of η, and the fraction of passive galaxies, as a function of their distance from the nearest cluster are plotted in Fig. 5.13.

Fig. 5.13 shows the variation of mean η and the fraction of passive galaxies for these two subsamples, as a function of the distance from the nearest cluster for

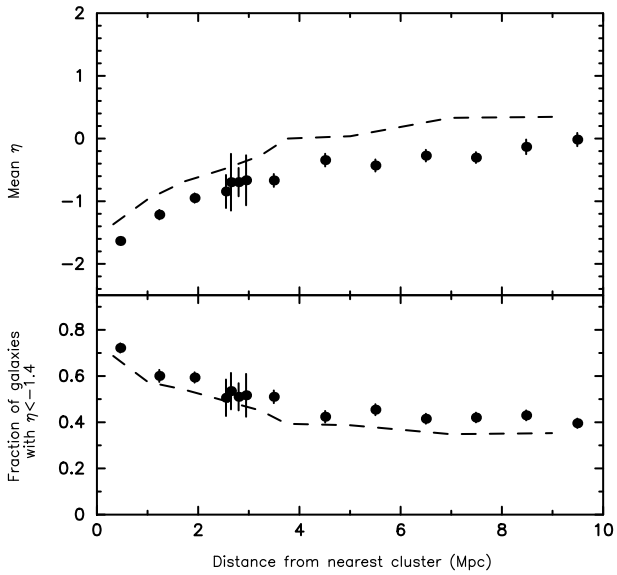

Figure 5.10: (a, Top)For galaxies within the filaments of PIM04b taken from the PIM04 sample , the mean η as function of distance from the nearest cluster is shown. The dashed line shows the mean η as function of distance from the nearest 2PIGG group with ≥ 30 members for all 2dFGRS galaxies. (b, Bottom) For the same galaxies as in a the fraction of these galaxies with an $\eta < -1.4$ is shown as a function of distance from the nearest cluster. The dashed line showing the same fraction as a function of distance from the nearest 2PIGG group with ≥ 30 members for the whole 2dFGRS. (§5.5.1)

the filament galaxies. It can be seen in Fig. 5.13 that the peak in mean η seen at approximately $2.5\,h_{70}^{-1}$ Mpc for all the PIM04a filament galaxies in section 5.5.1 is mainly due to the group galaxies, with the non group galaxies actually having a dip in mean η in the same region. This is matched by a corresponding peak in the fraction of passive galaxies for the non-group galaxies and a dip in the group galaxies. However, the large errors on the non group galaxies leaves the possibility of a sizable contribution from these galaxies to the peak in mean η for this sample and an equal possibility of little contribution from the non group galaxies of our previous results. In agreement with all of our previous results the non group galaxies are in general at higher mean values of η and lower fractions of passive galaxies.

Fig. 5.14 compares the same quantities for galaxies that belong to groups (2PIGG, $N \geq 4$) within PIM04a and group galaxies elsewhere in the 2dFGRS. The dashed line represent the variation of mean η and passive galaxy fraction as a function of distance from the nearest cluster in the 2dFGRS. In agreement with our previous

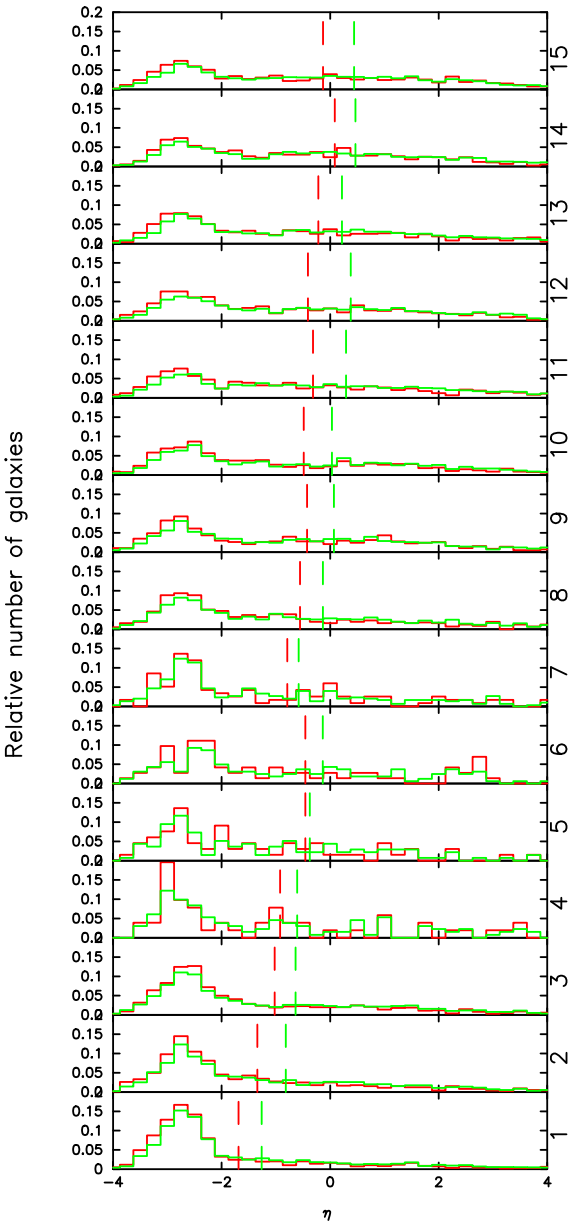

Figure 5.11: For galaxies within the filaments of PIM04a taken from the PIM04 sample , a histogram of η within each of the 15 distance bins is shown in red. The equivalent histogram but for the field sample is shown in green. The mean eta in each bin is shown as a dashed vertical line. (§5.5.1)

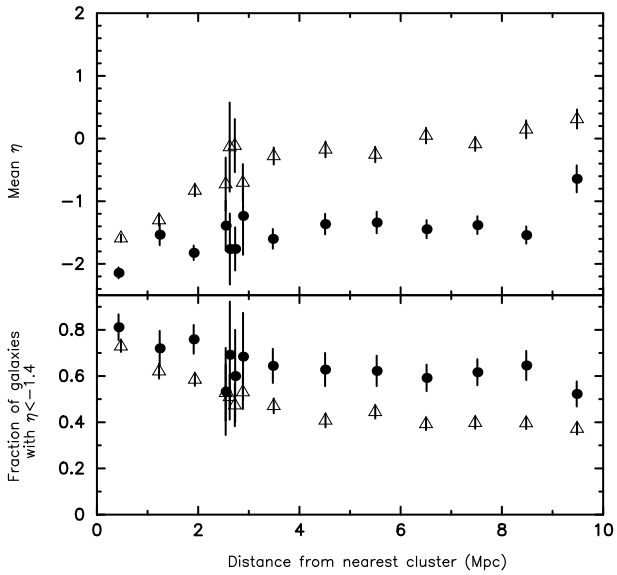

Figure 5.12: (a, Top)For the PIM04a galaxies, the mean η as function of distance from the nearest cluster is shown. Giant galaxies ($M < -20$) are shown as closed circles while dwarf galaxies ($M > -20$) are shown as open triangles. (b, Bottom) For the same galaxies as in a the fraction of these galaxies with an $\eta < -1.5$ is shown as a function of distance from the nearest cluster. (§5.5.2)

results there seems to be little evidence of a peak in the mean η of group galaxies in the whole 2dFGRS beyond the fluctuations introduced through the increase in bins from the earlier work. There is though some evidence for a peak in the filament group galaxies mean η at approximately $2.5\,h_{70}^{-1}$ Mpc. In the same manner as the results for all the filament galaxies in section 5.5.1 the filament group galaxies are in general at lower mean values of η and higher fractions of passive galaxies than the groups in the 2dFGRS as a whole.

5.6 Conclusions

We have investigated the environmental dependence of star formation within filaments of galaxies with quite stringent criteria. These filaments have to be between just two clusters of galaxies and the filaments have to have no intervening clusters within $6h_{70}^{-1}$ Mpc. Within this "clean sample", star formation variation has been observed by finding the variation of the η parameter with distance from the cluster centres along the filaments.

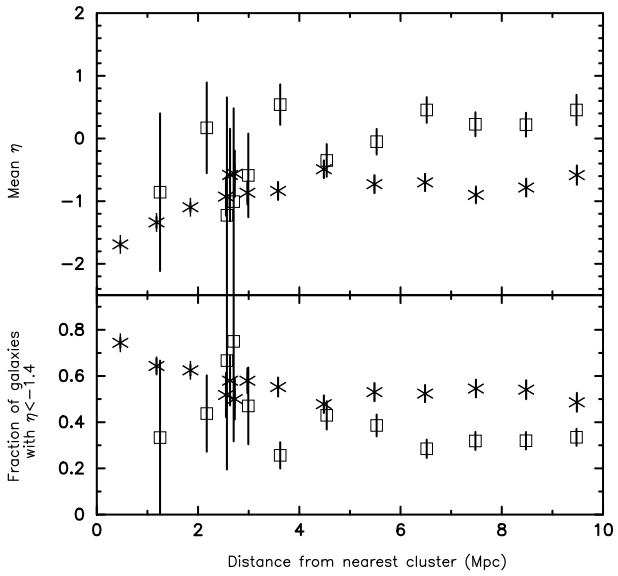

Figure 5.13: (a, Top)For the galaxies of PIM04a, the mean η as a function of distance from nearest cluster. Galaxies that are members of groups and part of the filament are shown as crosses while galaxies that are not part of a group are shown as squares. A group is a 2PIGG group with greater than or equal to 4 members, while non-group galaxies are those 2PIGG groups which are not part of a group of any number of members. (b, Bottom) The fraction of filament galaxies with $\eta < -1.4$ as a function of distance from nearest cluster within the same galaxy and group samples as defined for a. (§5.5.3)

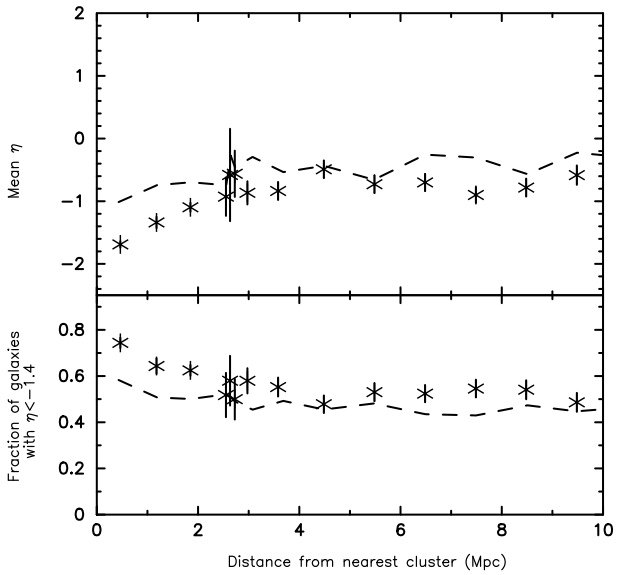

Figure 5.14: (a, Top)For the galaxies of PIM04a, the mean η as a function of distance from nearest cluster. Galaxies that are members of groups and part of the filament are shown as crosses This is compared to galaxies that are part of a group within the entire 2dFGRS shown as a dashed line. A group is a 2PIGG group with greater than or equal to 4 members, while non-group galaxies are those 2PIGG groups which are not part of a group of any number of members. (b, Bottom) The fraction of filament galaxies with $\eta < -1.4$ as a function of distance from nearest cluster within the same galaxy and group samples as defined for a. (§5.5.3)

For galaxies belonging to the "clean sample" filaments we have looked at the variation of the mean η parameter with distance along the filaments, in bins ranging from 0.25 h_{70}^{-1} Mpc within the 2-3 h_{70}^{-1} Mpc region up to 2 h_{70}^{-1} Mpc, starting from the cores of the rich clusters out to the sparser reaches of the filament. We have also looked at similar dependence on distance of the fraction of passive galaxies, in each distance bin. In doing so, we have also noted whether these galaxies are giant ($M_B \leq -20$) or a dwarf, member of a group or a cluster, or are part of a short filament ($length \leq 15$ h_{70}^{-1} Mpc) or long. Where possible, we have compared these results to similar properties of galaxies elsewhere in the 2dFGRS galaxy redshift survey.

We confirm that in the cores of rich clusters, the star formation rate in a galaxy is very low, irrespective of its mass, by showing that the value of mean η and the fraction of passive galaxies falls to its lowest value for both giant and dwarf galaxies in the cores of clusters. As one moves away from the cores of clusters along the

filaments, there is an increased activity of star formation, peaking at approximately $2.5\,h_{70}^{-1}$ Mpc, at approximately 1.5 times the virial radius of the clusters. This peak in star formation in filament galaxies is seen to be mostly due to dwarf galaxies ($-20 < M_B \leq -17.5$). All of this is in agreement with the much smaller sample of filament galaxies used in Chapter 4. More luminous galaxies ($M_B \leq -20$) have much lower star formation than less luminous galaxies at all distances from the centre of the cluster. This is in better agreement with the results of Haines et al. (2006a) than for the smaller sample in Chapter 4 where there was some overlap at lower radii. The peak in SFR is observed in both the short and long filaments at the same distance, but with the short filaments having higher SFR in the peak and higher SFR in general.

With the increased numbers in the "clean sample" compared with the Pisces-Cetus sample of Chapter 4, it is more clear that in filaments the mean η of the non-group galaxies are at much higher values than the group galaxies. However, this does not appear to be an effect of the filament, with the non-group galaxies within the whole 2dFGRS showing a similar enhancement in mean η over the group galaxies.

It is also seen that there is little variation in mean η with distance for the group galaxies taken from the whole 2dFGRS. This is in contrast with the group galaxies within the filaments which again show a peak at approximately 3 h_{70}^{-1} Mpc. This would suggest that the effects such as galaxy harassment are more important in the denser filament environment and effects all galaxies, including those in groups.

We have also investigated the same environments and effects in the more broadly defined filaments of the Pimbblet, Drinkwater, & Hawkrigg (2004) catalogue. While the peaks in the mean η are less well defined they are clearly present in those filaments that are designated as being genuine filaments of type 1 or 2, straight or curved. However, when more dubiously defined filaments are included the peak becomes less significant. Within the genuine filaments the same general trends in giant and dwarf, group and non-group distributions are observed as in the "clean sample" of filaments .

The results of this Chapter closely follow those seen in Chapter 4 and hence the

same physical processes are likely to be the cause of the enhancements in SFR (see §4.3) seen in this large sample of filaments. Therefore, galaxy harassment will once again be the most likely candidate for the enhancement in SFR.

Although these results in this work again show interesting environmental effects on star formation in galaxies and are in agreement with our results for the Pisces-Cetus supercluster, we have used an indirect measure for star formation (the η parameter) in these galaxies. It would therefore be prudent to continue the investigation with a more robust measurement of star formation such as the equivalent width of the Hα emission line from filament galaxies.

Chapter 6

C.S.Lewis: "You can never get a cup of tea large enough or a book big enough to suit me"

Star formation in the Shapley supercluster

6.1 Introduction

Shapley (1930) observed the entire southern sky down to 18th magnitude with the 24 inch Bruce telescope at Bloemfontein, South Africa. He catalogued 76,000 galaxies and over 40 distinct clusters of galaxies. The most "noteworthy" of these was a cloud of galaxies in Centaurus. While he could not reliably estimate the population, he thought that a preliminary account was interesting due to "the great linear dimensions, the numerous population and the distinctly elongated form". This cloud is now known to be the core of the Shapley supercluster in the region around A3556, A3558 and A3562. He surmised that the cloud in Centaurus contained over 200 galaxies and "obviously was a super system that is important in our considerations of our own galactic system". Because of his amazing incites over 50 years before any real attention was payed to this area, the region was named after him and the Shapley supercluster was born.

The Shapley supercluster (SSC) is one of the most massive concentrations of galaxies in the local universe (Raychaudhury, 1989; Scaramella et al., 1989). Consisting of 29 Abell clusters (see §3.1.3) it forms the second largest supercluster in the catalogue of Raychaudhury et al. (2007). The SSC is centred around R.A.=13^h25^m

and Dec.$= -30^{\circ}$ and has a mean redshift of $z = 0.0476$. The SSC is approximately 15 degrees long, corresponding to about 50 h_{70}^{-1} Mpc. The crossing time for a cluster in this structure would be comparable to the age of the universe. Thus the SSC can not be thought of as a virialised structure, however it may be overdense enough to exhibit different environmental effects to less dense regions. X-ray work by Raychaudhury et al. (1991) showed the SSC to have a total mass exceeding $1.0 \times 10^{16}\, h_{70}^{-1}\, \mathrm{M}_{\odot}$ and our own work shows it to be $1.2 \times 10^{16}\, h_{70}^{-1}\, \mathrm{M}_{\odot}$ (see §3.4.3). These values imply that the supercluster may be close to turning around and beginning to collapse. However, the values are small enough that the system is likely to still be in or have only recently left the linear regime. More recently the SSC has proved to be important in studies of the bulk flow observed in the local universe (Radburn-Smith et al., 2006).

The SSC is located approximately 140 h_{70}^{-1} Mpc behind the Hydra-Centaurus Supercluster, which is itself approximately 60 h_{70}^{-1} Mpc from us. The SSC lies in the general direction of the motion of the local group with respects to the cosmic microwave background, as inferred from the dipole anisotropy of the cosmic microwave background (Smoot et al., 1992), and as such is a major contributor to the peculiar velocity of the local group. Bardelli et al. (2000) found a mean overdensity of over ~ 11.3 for the central region on a 10 h_{100}^{-1} Mpc scale. This central region alone was shown to contribute about 26 km s^{-1} or 7% to the 366 ± 125 km s^{-1} (Hoffman, 2001) total tidal velocity of the local group.

In the previous Chapters we have investigated the rate of star formation within the supercluster and galaxy filament environments. This has been performed with the use of the 2dFGRS η parameter, which while being shown to have a good relation to the Hα equivalent width (EW), is still an indirect measure of the star formation. In this Chapter we will investigate the star formation rates in galaxies within the SSC environment using the EWs of galaxy emission lines taken from the 6dF survey.

The six Degree Galaxy Survey (6dFGS)

The 6dF galaxy survey has obtained over 120,000 redshifts in the southern sky since it began in 2001. By the time of its final release in late 2006, the survey will have

covered an area 8 times larger than that of the 2dFGRS (but not to the same depth in redshift) and obtained peculiar velocities for over 15,000 galaxies. The survey is performed on the six-degree field multi-object fibre spectroscopy system on the UKST (6dF).

The 6dF is capable of taking 150 simultaneous spectra over a field of 5.7 degree diameter. The primary sample for the survey is the near infrared (NIR) two micron all sky survey (2MASS)(Jarrett et al., 2000). The use of a NIR survey means that the bias towards currently star forming galaxies, found in the SDSS and 2dFGRS, would be minimalised. The 2MASS total magnitudes were used where available and at lower magnitudes an estimate of the total magnitude was taken from isophotal magnitudes. These magnitudes were used to apply a cut in the K band of less than 12.75, resulting in 113,988 galaxies from the primary sample.

Thirteen other surveys were combined with the primary sample resulting in 174442 galaxies in the final sample, 150000 of which are hoped to be covered by the survey end. These additional galaxies extend the survey down to (H, J, r_f, b_J)=(13.05, 13.75, 15.6, 16.75). The instrument uses a 1032×1056 pixel CCD with R and V reflection gratings covering the wavelength ranges $4000 - 5600$ Å and $5500 - 7500$ Å respectively. Examples of combined V and R spectra can be seen in figs. 6.1 to 6.3. The survey has a median depth of $\bar{z} = 0.05$, reaching to approximately $z \sim 0.15$.

6.2 Spectroscopic data

Our data consisted of 34,649 galaxies from the entire 6dF survey with redshift of at least a quality of 3 (probable redshift or better (see Jones et al., 2004)), kindly supplied by Philip Lah. For this study, we used only star formation measures based on emission lines. When available the following equivalent emission line widths were obtained, Hα, Hβ, [OIII](5007 Å), [OIII](4959 Å), [NII](6584 Å) and [NII](6548 Å). Of the 34,649 galaxies, 17,015 had a Hα emission line detected. Due to the difficulty of defining an index with the [NII] lines surrounding the Hα line, Hα and [NII] emission were measured using the deblending option of the 'splot command' of the IRAF package. This enabled Gaussians to be fitted to a series of spectral

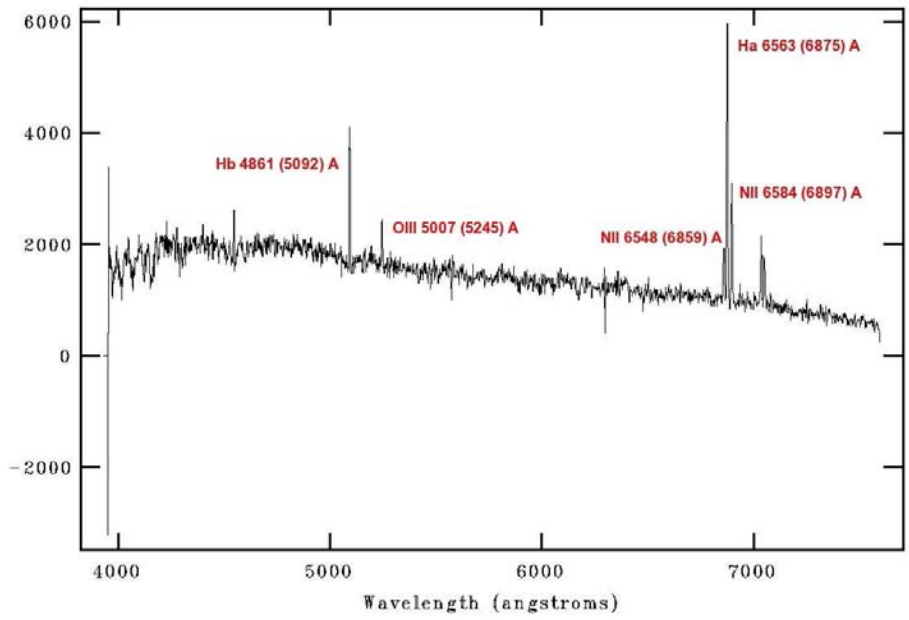

Figure 6.1: An example of the 6dF spectrum (V and R combined) of the galaxy 139654, which is part of our Shapley supercluster sample and has been classified as a starburst galaxy in §6.2. This is characterised by the large Hα emission line at 6875 Å, 6563 Å in the rest frame. (§6.1)

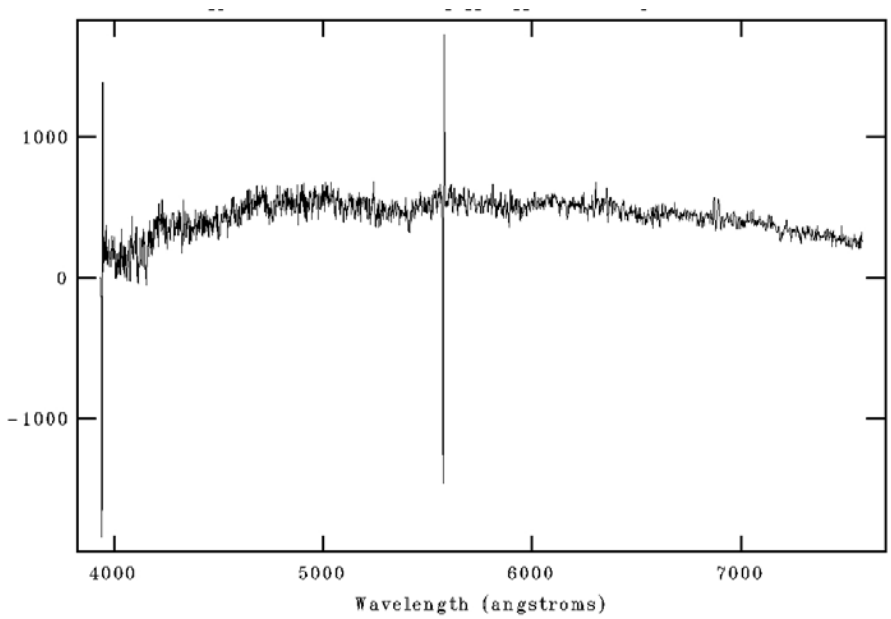

Figure 6.2: An example of the 6dF spectrum (V and R combined) of the galaxy 60930, which is part of our Shapley supercluster sample and has been classified as a passive galaxy in §6.2. It can be seen that there is no Hα emission line at 6869 Å, 6563 Å in the rest frame. (§6.1)

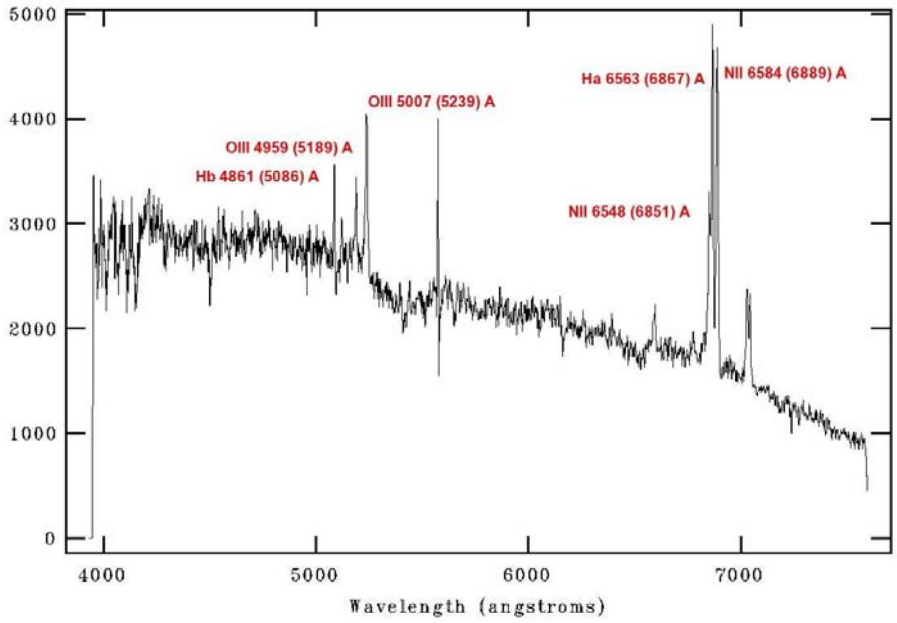

Figure 6.3: An example of the 6dF spectrum (V and R combined) of the galaxy 736, which is part of our Shapley supercluster sample and has been classified as an AGN galaxy in §6.2. This is characterised by the strong [NII] emission line at 6889 Å, 6584 Å in the rest frame and the strong [OIII] emission line at 5007 Å, 5239 Å in the rest frame. (§6.1)

lines and to measure the value of the equivalent width (EW) of each. In order that 'splot' could consistently find the continuum level to fit Gaussians to the lines, it was necessary to set the level of the spectrum away from these spectral lines to a value of exactly one. Even if there was no spectral line present "splot" tries to fit a Gaussian. This leads to fits being made of noise spikes or the continuum. Therefore, if a line had its centre more than 7 Å from its expected position it was discarded as a false reading. In addition, if the fitted Gaussian FWHM was below the instrumental resolution of the 6dF instrument (FWHM=5 Å) or very large such that they were judged to be fits to the continuum rather than real features (FWHM $>$ 12 Å), the measurement was discarded.

6.2.1 Removal of AGN

Baldwin, Phillips, & Terlevich (1981)(BPT) first showed that it was possible to distinguish type 2 Active Galactic Nuclei (AGNs) from normal star forming galaxies by considering the intensity ratios of two pairs of emission lines. This process was

refined by Veilleux & Osterbrock (1987) and it has become standard practice to classify objects in this manner. The exact demarcation between star forming galaxies and AGN derived from theory and observations has considerable uncertainty. We used the work of Kewley et al. (2001) who used detailed continuous starburst models to obtain an empirical limit, below which the galaxies are almost always starbursts as opposed to AGN. This limit is defined as:

$$\log(O_{III}/H\beta) > 0.61/[\log(N_{II}/H\alpha) - 0.47] + 1.19 \quad (6.1)$$

This definition has been applied to the Lah sample and the resulting divide in the galaxies can be seen in Fig. 6.4. This resulted in 5,977 galaxies being selected as starbursts. In addition 22,634 galaxies had no Hα measured. These were assumed to be non star forming galaxies. This results in a sample of 28,611 galaxies after the removal of the AGNs and will be referred to as the LAH06 sample. The [NII] values are those of the λ=6584 Å line and the [OIII] is the λ=5007 Å line of the doublets. Once only those galaxies that fell within the Shapley supercluster region had been selected, this resulted in a sample of 769 galaxies, 124 of them with a non zero Hα. This sample will be referred to as the SHAP769 sample.

Type 1 AGNs are characterised by broad Balmer and other permitted lines along with strong emission in the forbidden lines such as [OIII](λ=5007 Å) and [NII](λ=6584 Å). Type 2 AGN have the same narrow forbidden lines but without the broad permitted lines. The [NII](Λ=6584 Å) forbidden line in type 2 AGNs is stronger with respect to Hα than in HII region objects (normal starbursts). Collisional excitation of this line is more important in objects in regions that are partially ionised. Narrow line AGNs have a significant fraction of non thermal emission in the X-ray range. This causes a large region of Hydrogen atoms to become partially ionised resulting in more [NII](Λ=6584 Å) emission than in the HII region objects where emission is due to UV photons emitted by hot OB stars. The region of partial ionisation also has a higher number of photons that can ionise [OII] resulting in more [OIII](Λ=5007 Å) than in all but the most excited [HII] region objects. Thus type 2 AGN will have stronger EW [NII](Λ=6584 Å) lines with respect to the EW of the Hα line and strong EW [OIII](Λ=5007 Å) lines with respect to the EW of

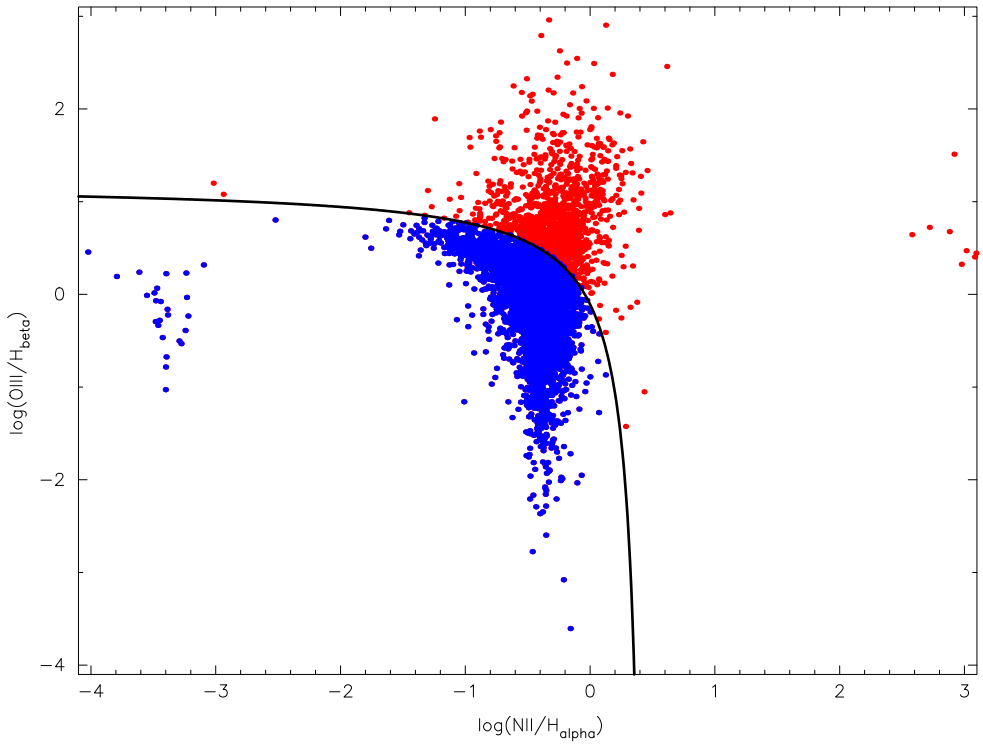

Figure 6.4: BPT diagram (used to distinguish type 2 AGNs from normal star forming galaxies) of galaxies within the Shapley supercluster region from 6dFGS spectra. The line shown is from the relation of Kewley et al. (2001) with red galaxies being categorised as AGN and the blue as normal star forming galaxies.(§6.2.1)

Hβ and be in the top right section of the BPT diagram.

6.2.2 Stellar absorption

It is well known that the Balmer emission lines can suffer contamination due to underlying stellar absorption and consequently be underestimated. Ideally the EW of the Hα line would be corrected using a population synthesis model to accurately model the observed stellar continuum (e.g., Bruzual & Charlot, 2003). This stellar continuum would then be subtracted from the spectrum of the galaxy.

However, due to time constraints it was not possible to correct the EWs that we received in this manner. It has been suggested (e.g., Hopkins et al., 2003; Balogh et al., 2004) that a common correction applied to all galaxies should be sufficient when dealing with characteristics of an entire sample rather than individual galaxies. Hopkins et al. (2003) show that an appropriate stellar absorption correction should

be at most +1.3 Å. We have therefore added 1.0 Å to our Hα and Hβ EWs.

6.2.3 Flux calculations

The 6dF data don't have spectrophotometric calibrations, so the exact fluxes in erg s^{-1} cm^{-2} will not be known. But since all the spectra were acquired with the same settings and exposures, and internally calibrated by setting the continuum flux to the same value we will assume that the equivalent widths can be converted into fluxes using a factor common to all galaxies.

Rojas et al. (2005) calculates the flux of SDSS Hα lines from,

$$F(SDSS) = \sqrt{2\pi}\sigma\kappa \times 10^{-17}, \tag{6.2}$$

where σ and κ are the widths and heights of the Gaussian fit to the line and F is the resulting flux in ergs^{-1} cm^{-2}. It can be shown that,

$$\int_{-\infty}^{\infty} \kappa \exp^{x^2}\, dx = \sqrt{\pi} \tag{6.3}$$

It can also be shown that the area under a Gaussian distribution is given by the left hand side of Eq. 6.4. Since the equivalent width of the line is equal to the area under the continuum subtracted line, represented by a Gaussian you get that,

$$\int_{-\infty}^{\infty} \kappa \exp^{y^2/2\sigma^2}\, dy = \mathrm{EW(H}\alpha), \tag{6.4}$$

where EW(Hα) is the equivalent width of the Hα emission line. Taking $x = \frac{y}{\sigma\sqrt{2}}$ and hence $dy = \sigma\sqrt{2}\, dx$ leads to,

$$\kappa\sigma\sqrt{2} \int_{-\infty}^{\infty} \exp^{-x^2}\, dx = \mathrm{EW(H}\alpha). \tag{6.5}$$

From Eq. 6.3 this means that,

$$\sqrt{2}\sigma\kappa\sqrt{\pi} = \sqrt{2\pi}\sigma\kappa = \mathrm{EW(H}\alpha). \tag{6.6}$$

Therefore, from Eq. 6.2 it follows that,

$$F(SDSS) = \mathrm{EW(H}\alpha) \times 10^{-17}. \tag{6.7}$$

Our EW(Hα) have been obtained using 3 arcsecond fibres instead of the 7 arcsecond fibres for the SDSS EW(Hα). Since the ratio of areas of the SDSS fibres to the 2dFGRS fibres is approximately 5 we adopted Eq. 6.8 for our flux calculations.

$$F = 5 \times 10^{-17}\, \mathrm{EW(H}\alpha), \tag{6.8}$$

6.2.4 Dust attenuation

The amount of dust reddening is estimated from the Balmer decrement Hα/Hβ where the Hα and Hβ EWs have been corrected for underlying stellar absorption as described above. We follow the method of Moustakas, Kennicutt, & Tremonti (2006) for correcting for dust reddening. The colour excess due to dust reddening can be expressed as,

$$\mathrm{E}(\mathrm{H}\beta - \mathrm{H}\alpha) \equiv -2.5 \log \left[\frac{(\mathrm{H}\alpha/\mathrm{H}\beta)_{int}}{(\mathrm{H}\alpha/\mathrm{H}\beta)_{obs}} \right], \tag{6.9}$$

where E(Hβ−Hα) is the colour excess between the Hβ and Hα wavelengths, (Hα / Hβ)$_{int}$) is the intrinsic Balmer decrement and (Hα/Hβ)$_{obs}$ is the observed decrement. A value of (Hα/Hβ)$_{int}$ = 2.86 is used in Eq. 6.9 (Storey & Hummer, 1995). The amount of extinction which is due only to the physics of the dust grains and hence only dependent on wavelength can be represented by an attenuation curve given by,

$$\mathrm{k}(\mathrm{H}\alpha) \equiv \mathrm{A}(\mathrm{H}\alpha)\mathrm{E}(\text{B-V}), \tag{6.10}$$

where E(B-V) is the broadband colour excess, k(Hα) is the opacity (absorption + scattering) at the wavelength of the Hα line (6563 Å) and A(Hα) is the attenuation at λ 6563Å. From the attenuation curve the colour excess is obtained as,

$$\mathrm{E}(\text{B-V}) \equiv \frac{\mathrm{E}(\mathrm{H}\beta - \mathrm{H}\alpha)}{\mathrm{k}(\mathrm{H}\beta) - \mathrm{k}(\mathrm{H}\alpha)}, \tag{6.11}$$

where k(Hβ) and k(Hα) are the opacity at 4861 and 6563 Å respectively, and is used to find the broadband colour excess. The Calzetti (2001) value of k(Hβ)-k(Hα) = 1.63 was used. Finally the Calzetti (2001) relation for the attenuated to intrinsic Balmer line ratio of

$$\mathrm{R}_{\alpha\beta} = 10^{0.4\mathrm{E}(\text{B-V})(\mathrm{k}(\mathrm{H}\beta)-\mathrm{k}(\mathrm{H}\alpha))}, \tag{6.12}$$

was used and the flux for each galaxy multiplied by R$_{\alpha\beta}$.

6.2.5 Aperture correction

Each of the fibres placed on a galaxy will not always contain the entire galaxy, and as such will not obtain the entire flux. It is therefore a possibility to apply a correction for this so as to obtain a star formation rate (SFR) for the entire galaxy, as opposed to just the central region. However, as SFR is not constant across the diameter of a galaxy this may result in artificially enhancing the SFR of the galaxy. A correction of the type,

$$F_c = F(r_g/3.5)^2, \tag{6.13}$$

could be applied where, F is the aperture uncorrected flux, F_c is the aperture corrected flux, 3.5 arcseconds is the radius of the fibre and r_g is the radius of the galaxy in arcseconds. However, considering the many uncertainties with this correction it was decided that this correction would just introduce more noise and so was not applied.

6.2.6 SFR calculation

The first step to calculate a SFR was to convert our fluxes into luminosities by,

$$L = F4\pi D^2, \tag{6.14}$$

where L is the Hα luminosity, F is the Hα flux and D is the distance to the galaxy in question. Once the luminosity was obtained the SFR was calculated using the Kennicutt (1998b) relation,

$$\mathrm{SFR} = 7.9 \times 10^{-42} \frac{L}{\mathrm{erg\ s^{-1}}} \mathrm{M_\odot yr^{-1}}. \tag{6.15}$$

It must be noted that due to the assumptions used in § 6.2.3 while calculating our fluxes this SFR will be an uncalibrated SFR (USFR), proportional to the actual SFR. However, as we are looking at general trends in SFR, this quantity should be sufficient.

6.3 Samples of galaxies in various environments

From the SHAP769 sample described in § 6.2 with dust and stellar absorption corrections applied, 3 sub samples were made:

1. Field: All galaxies ($n = 28611$) in the LAH06 sample. The large numbers in comparison with the other subsamples means that non cluster galaxies should be the dominant influence.

2. Supercluster cluster: LAH06 sample galaxies within the Abell radius of each cluster centre of the Shapley supercluster and ± 3000 km s^{-1} of the cluster mean velocity ($n = 126$).

3. Non supercluster cluster: LAH06 sample galaxies within the Abell radius of each cluster centre that is not listed in the supercluster catalogue of (Raychaudhury et al., 2007) and ± 3000 km s^{-1} of the cluster mean velocity ($n = 799$).

Fig. 6.5 shows a histogram of the USFR of galaxies in each of the three samples. The relative number of galaxies in that bin with respect to the total number of galaxies in the sample is shown. In addition, we plot the same relative numbers, but relative to the field sample, to emphasise the higher USFR bins. Although the differences are small it can be seen that the supercluster cluster sample has a higher percentage of its galaxies in the very low SFR first bin than the other samples. This may be due to the clusters being in a more dense environment, suppressing SFRs more than in clusters outside of superclusters. The field has the lowest proportion of its galaxies in the lowest USFR bin, this being consistent with it having the least dense galaxy environment.

Things are a little clearer at the high USFR end of the plot. Here it can be seen that the cluster galaxies belonging to the supercluster do not have any galaxies present in them beyond an USFR of 0.4. The non-supercluster cluster galaxies in slightly less dense environments have some galaxies present in bins up to an uncalibrated SFR of 0.65. The highest USFR bins have only galaxies which are in the relatively less dense field environment.

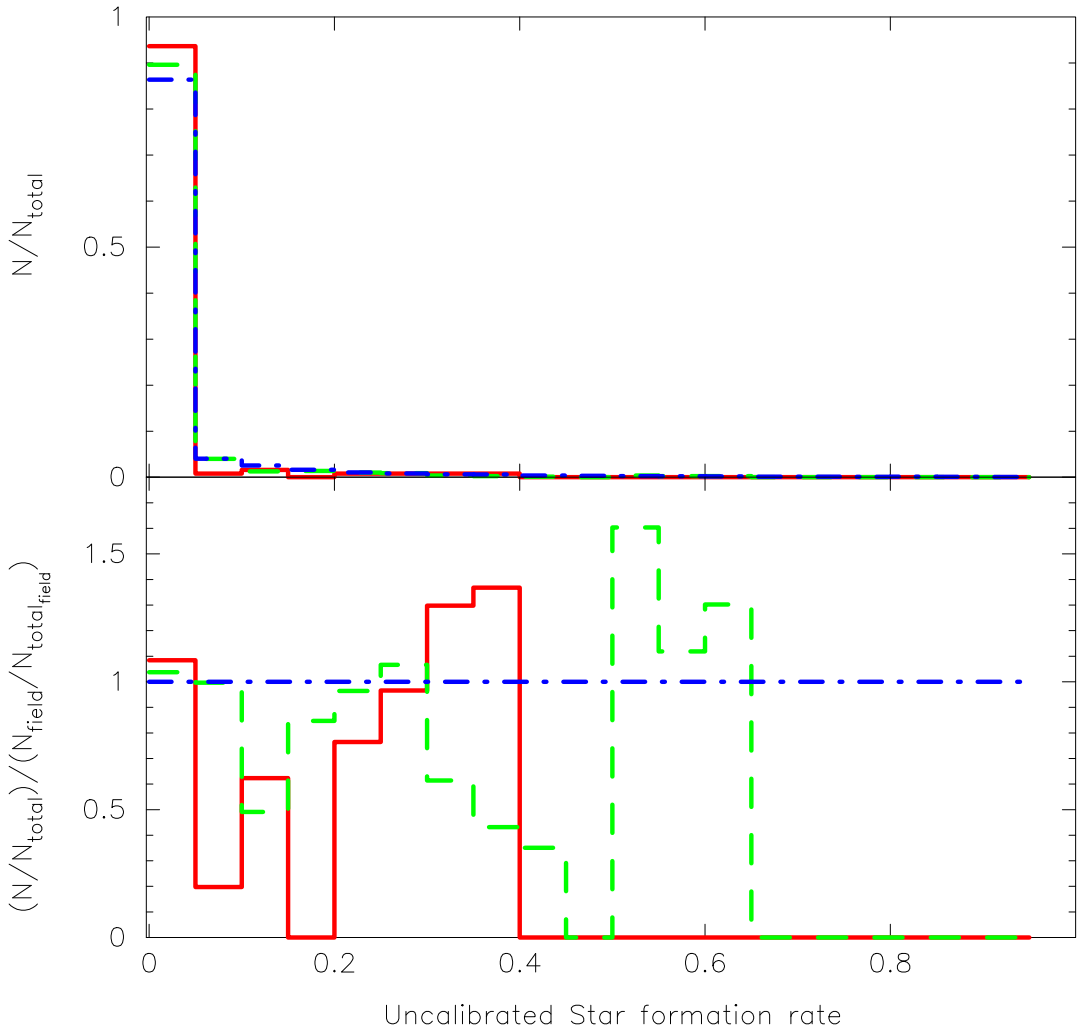

Figure 6.5: (a, top)A histogram of the of the uncalibrated star formation rate of galaxies in the Shapley supercluster region. The histogram shows the relative number of galaxies in that bin with respects to the total number of galaxies in the sample. The field, non supercluster cluster and supercluster cluster samples are represented by the blue dot-dash, green dashed and solid red lines respectively. (b, bottom) The same relative numbers as in a but now also relative to the field sample. This emphasises the higher uncalibrated star formation bins. The proportion of galaxies with no star formation for the field, non supercluster cluster and supercluster cluster samples are, 79%, 82% and 91%, respectively. (§6.3)

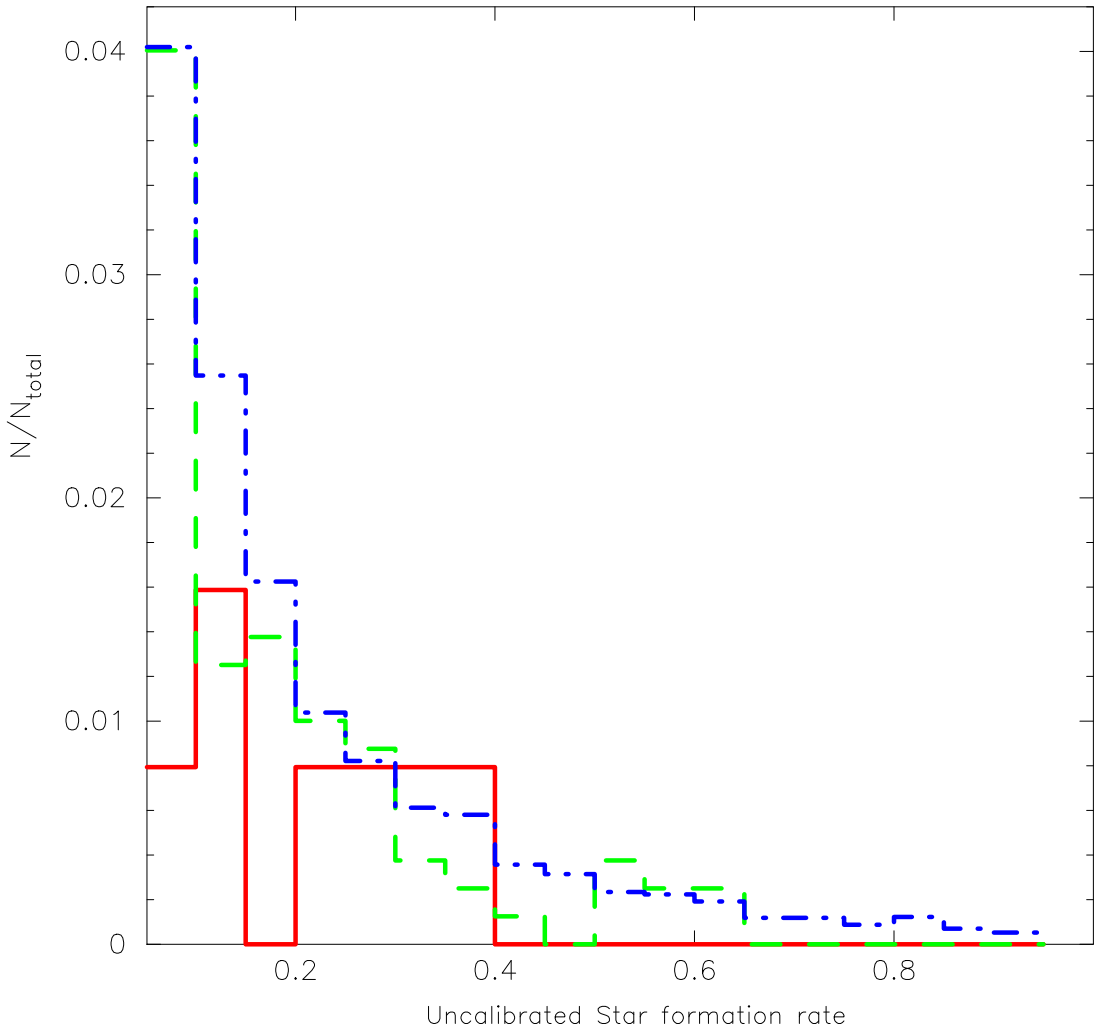

Figure 6.6: A histogram of the of the uncalibrated star formation rate of galaxies in the Shapley supercluster region. The histogram shows the relative number of galaxies in that bin with respects to the total number of galaxies in the sample. The field, non-supercluster cluster and supercluster cluster samples are represented by the blue dot-dash, green dashed and solid red lines respectively. The proportion of galaxies with no star formation for the field, non supercluster cluster and supercluster cluster samples are, 79%, 82% and 91%, respectively. The first bin of Fig. 6.5 which includes mainly non-star forming galaxies has been omitted and the Y-axis scaled accordingly to display the low USFR bins, which never the less have some star formation. (§6.3)

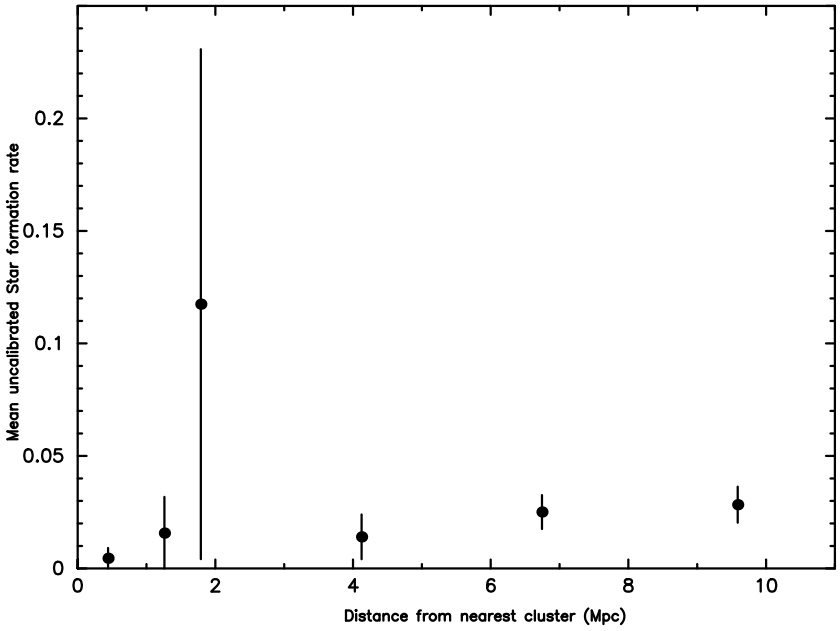

Figure 6.7: Mean uncalibrated star formation rate as a function of distance from the nearest cluster for galaxies in the Shapley region. The 6 bins in ascending order contain 38,25,20,22,77 and 103 galaxies. (§6.4)

6.4 SFR as a function of distance from a cluster

For each galaxy in the SHAP769 sample the distance from the nearest Shapley cluster was calculated using the co-moving distance formula of Hogg (1999). Distances were found using the galaxies individual redshifts unless the galaxy was classified as being a member of a cluster. Due to the lack of a comprehensive cluster catalogue in this region it was assumed that galaxies within the Abell radius of a cluster centre and 3000 km s^{-1} of the mean cluster redshift were cluster galaxies. Due to the increased peculiar velocities with respect to the filament galaxies the distances within the clusters were calculated at the mean redshift of the clusters. The galaxies were then binned as a function of the distance from the nearest cluster in 6 increasing size bins ranging from $0.5h_{70}^{-1}$ Mpc in the cluster cores up to $3h_{70}^{-1}$ Mpc bins. The mean uncalibrated star formation rate as calculated in §6.2.6 in each bin was then calculated and can be seen in Fig. 6.7.

It can clearly be seen that while in general there is a slight slope in increasing USFR from the inner bins to the outer the mean USFR in bin 3 is much higher than in any other bin. While this may suggestive of a real effect increasing the

USFR at approximately $2h_{70}^{-1}$ Mpc, the error bars are large. There are 20 galaxies in bin 3 where the peak occurs. With bins 1,2 and 4 having 38, 25 and 22 galaxies respectively, and having reasonable errors, the large errors are not due to a small number of galaxies. However, of the 20 galaxies in bin 3, only 2 are star forming and it is only these two galaxies that pull the mean USFR up to such a high value, which results in the large errors seen.

6.5 Fraction of starburst galaxies

Within the Shapley supercluster region there were 176 galaxies which had the 4 appropriate emission indices to be processed by the BPT diagram to remove AGN as described in §6.2.1. Of these galaxies, 124 were selected as being starburst galaxies rather than AGN. The distances from the nearest cluster in the Shapley supercluster were again calculated for each galaxy in these two samples and the fraction of galaxies in each bin that were starburst galaxies was calculated. The resulting plot can be seen in Fig. 6.8. There seems to be little variation in the percentage of starburst galaxies with distance from the nearest cluster, which would agree with the results of Miller et al. (2003). However, it can be seen that the small number of galaxies in the sample ($n = 15$ per bin) results in large error bars on each point and hence the significance of the results is reduced.

6.6 Fraction of passive galaxies

Out of the 769 galaxies in the SHAP769 sample 645 are classified as being passive or having no Hα emission line. In this section we have calculated the fraction of galaxies in each distance bin that are passive. It can be seen in Fig. 6.9 that as expected the maximum number of passive galaxies are found in the first bin within the cluster core. From this lowest value the fraction of passive galaxies is seen to steadily decrease with increasing distance from the cluster centre. No corresponding dip in the fraction of passive galaxies is seen in the $2h_{70}^{-1}$ Mpc region. However, once again the errors are very large on all the points giving a small significance to the

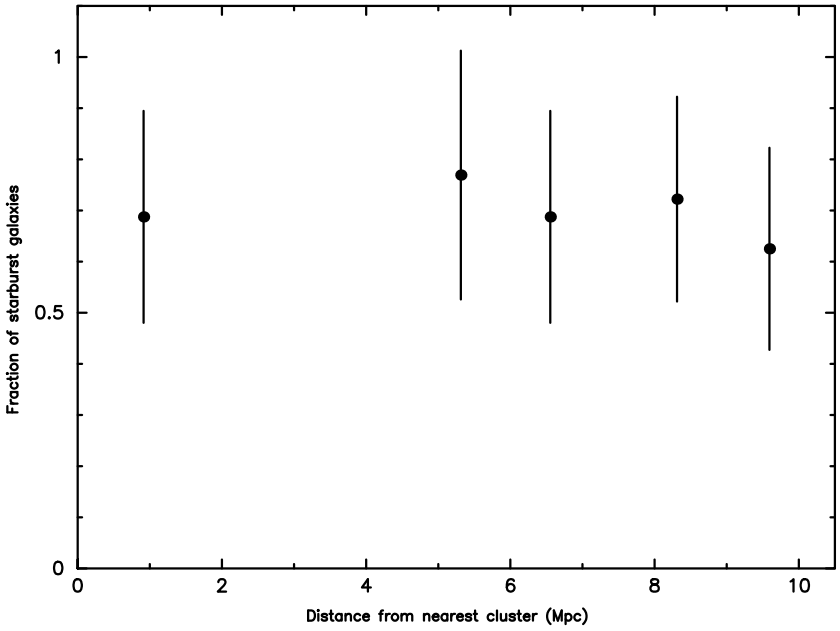

Figure 6.8: Fraction of starburst galaxies as a function of distance from the nearest cluster for galaxies in the Shapley region. (§6.5)

results.

6.7 Conclusions

For the galaxies lying in the region of the sky covered by the Shapley supercluster, we have investigated the evidence of enhanced star formation in clusters within and outside the supercluster. This has been performed using an uncalibrated star formation rate (USFR) derived from the equivalent width of the Hα emission line from 6dF spectroscopic data. Galaxies that are found to be AGN have been removed and corrections applied to the USFR for underlying stellar absorption and dust reddening.

We found that, as expected, cluster galaxies have evidence of suppressed star formation compared to galaxies in the field, but also that SFR is more suppressed within clusters in the more dense supercluster environment.

We have also investigated the environmental dependence of star formation within the Shapley supercluster. We have done this by finding the variation of the USFR with distance from the centre of the nearest cluster which is a member of the super-

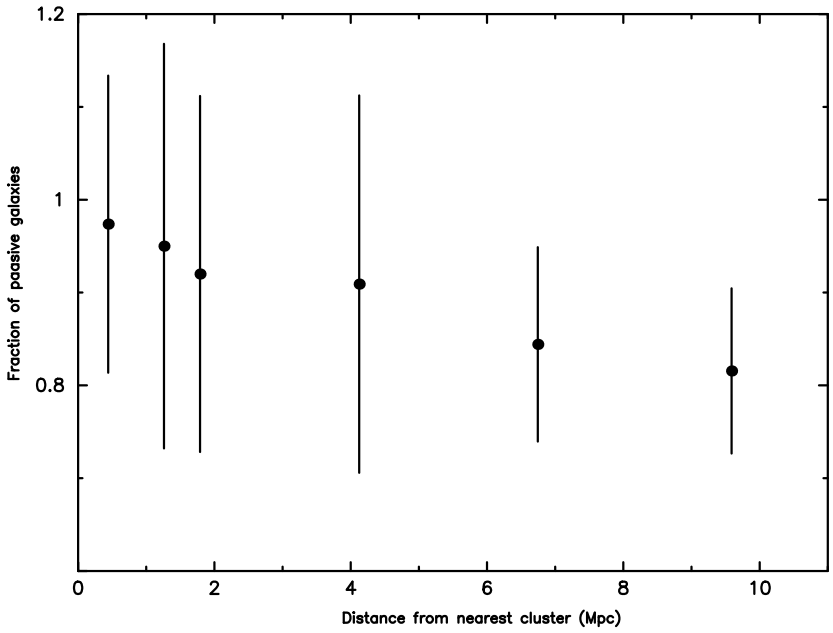

Figure 6.9: Fraction of passive galaxies as a function of distance from the nearest cluster for galaxies in the Shapley region. (§6.6)

cluster. It is well known that in the cores of rich clusters, the star formation rate in a galaxy is very low. We confirm that this is also the case for our supercluster galaxies, with the lowest mean USFR being found in the lowest distance bin. As one moves away from the cores of clusters, there is a very gradual increase in the mean USFR out to $10h_{70}^{-1}$ Mpc, but with a peak in the mean USFR at approximately $2h_{70}^{-1}$ Mpc. The gradual decrease in USFR towards the core, as discussed in §4.3, will most likely be due to galaxies encountering the Intra Cluster Medium (ICM) and an increasing density of galaxies. The galaxies will start to lose their warm gas haloes through ram pressure stripping and evaporation as the galaxys' gas interacts with the hot ICM.

We also take a look at the fraction of galaxies that are starbursts as opposed to AGN as a function of distance from the cluster cores. These results seem to show little evidence for any variation in AGN percentage with distance. However, larger numbers of galaxies would be needed to conclusively prove this.

Finally we look at the fraction of passive galaxies as a function of distance from the cluster centres. As expected the fraction was at a maximum within the cores and gradually decreased with increasing distance from the core. However, once again a

large sample of galaxies would be needed to conclusively prove this.

The results for this Chapter have once again been indicative of interesting environmental effects on star formation in galaxies. In comparison with the work in previous Chapters using the η parameter the USFR with its corrections for dust and the underlying star population is a better representation of the SFR trends within the environment. However, the overall results have suffered from small number statistics and a larger sample of galaxies is needed to conclusively prove the observed trends.

Chapter 7

Margaret Thatcher: "If my critics saw me walking over the Thames they would say it was because I couldn't swim."

Conclusions

7.1 Summary of main results

We have used survey redshifts (2dFGRS, 6dFGS, SDSS, NED and ZCAT) of galaxies to investigate the nature, extent and orientation of the Pisces-Cetus, Shapley and Horologium-Reticulum superclusters. This has been combined with photometric data from SuperCosmos to obtain estimates of the virial mass of clusters belonging to the superclusters and hence obtain minimum masses for the superclusters. These have shown the superclusters to only have mass overdensities of a few times the critical density of the universe over scales of several tens of h_{70}^{-1} Mpc and to still be in or have only recently left the linear regime. Thus they are good candidates for studying the processes present in their formation. Furthermore, this confirms that structures of the order of a $100\,h_{70}^{-1}$ Mpc are structures in their own right and hence may have different environmental effects on the evolution of galaxies.

We have used the 2dFGRS star formation rate (SFR) parameter η, which is related to the equivalent width of the Hα emission line, to show that the SFR properties of galaxies within the filaments of the Pisces-Cetus supercluster show interesting environmental effects. The SFR shows a gradual decrease from the periphery of the filament into the cluster core consistent with galaxies losing their warm gas haloes through ram pressure stripping and evaporation as the gas belonging to the galaxy interacts with the hot Intracluster Medium. However, on top of this monotonic trend with decreasing distance from the centre of a cluster, we find

a nearly instantaneous enhancement of the SFR at $\sim 3\,h_{70}^{-1}$ Mpc from its centre, which is about 1.5–2 times the virial radius of the cluster.

We conclude that the most likely reason for this sudden enhancement in SFR is either the first encounter of the infalling galaxies with the hot intracluster medium of the cluster, or galaxy-galaxy harassment due to the rapid increase of the space density of galaxies infalling along the filaments at these distances. The abruptness of the peak in SFR would indicate that the predominant process is galaxy-galaxy harassment, due to other infalling galaxies inducing tidal shocks in the still fairly intact gas reserves of the galaxies.

Further work shows the SFR is found to be at its lowest in the cluster core for both giant and dwarf galaxies demonstrating the suppression of the SFR is not dependent on mass. However, the peak in SFR is seen to be mainly due to dwarf galaxies, with the dwarf galaxies having in general a higher SFR, consistent with previous work in the literature.

There is little evidence for a difference in the position of the peak in SFR in the infall regions of high or low velocity dispersion clusters. This provides further support for galaxy harassment being the most important process in star formation properties of galaxies infalling into the cluster, and undermines the importance of the tidal effect of the dark matter haloes of the clusters involved.

Studies of groups within the filaments show that there is little variation in SFR with distance for the group galaxies taken from the whole 2dFGRS. This is in contrast with the group galaxies within the filaments which again show a peak at a few virial radii. This would suggest that the the filament environment is dominant over the group environment with respects to SFR at this distance.

A similar analysis using the 2dFGRS η parameter was also used to investigate the star formation within a larger ensemble of over 50 filaments of galaxies joining two clusters. Trends that are consistent with the smaller sample of Pisces-Cetus filament galaxies are seen, with an increase in SFR at a approximately 1.5 virial radii from the cluster cores. The results are also confirmed although to a lesser degree for a more liberally defined sample of over 300 filaments.

A more robust measurement of the SFR was sought to investigate the Shapley

supercluster region. Here, from 6dF spectra of galaxies in the Shapley supercluster region, the equivalent width of of the Hα emission line was used to obtain a SFR for galaxies in the region. Galaxies dominated by active galactic nuclei (AGN) were removed and corrections applied for dust extinction and the underlying stellar population. However, due to the lack of spectrophotometric calibrations for the 6dF data only an uncalibrated SFR could be obtained. There is some evidence for a peak in star formation at a distance of approximately $2\,h_{70}^{-1}$ Mpc from cluster cores and suppressed star formation within cluster galaxies in the supercluster, compared with those not in the supercluster, and those in the field. There appears to be little variation in the percentage of galaxies that are AGN with distance from cluster cores but some evidence for a decreasing percentage of passive galaxies with increasing distance.

7.2 Future work

The SDSS provides a massive repository of data that could be used to study SFR along filaments of galaxies in a much larger region than the 2dFGRS. We had entered into a collaboration with Biswajit Pandey and Somnath Bharadwaj with a view to using their catalogue of filaments in the SDSS (Pandey & Bharadwaj, 2006). However, we were unable to progress far with this work within the time constraints of this thesis. The spectroscopic data of the SDSS would allow us to study SFR with the use of emission lines as in Chapter 6, but with better spectrophotometric calibrations such that a true SFR could be obtained. In addition the multiple wavelength band photometry available in the SDSS would allow a study of the colour magnitude relations of the filament galaxies to investigate the possibility of an intermediate age stellar population, seen in some field galaxies, being present in filaments.

Further spectroscopic observations of galaxies at varying distances from cluster cores would allow a more significant study of the SFR properties in the Shapley region and reduce the large errors that we currently have. This could also be expanded to gain further observations of the Horologium-Reticulum region which is

more sparsely covered by 6dF than Shapley. Indeed, it would be very useful to obtain high resolution spectra of the Shapley, Horologium-Reticulum and Pisces-Cetus supercluster regions, probing deeper into the dwarf galaxy population ($M_B \approx -15$), using the Anglo-Australian Telescope 2dF or Magellan IMACS, so that the work initiated in Chapter 6 can be done properly. With a greater number of galaxies available, it may also be possible to investigate the SFR along Shapley and Horologium-Reticulum filaments rather than general spatial relations we have now.

While our results of §4.2.4 showed no relation of the position of the peak in SFR with the velocity dispersion of the nearest clusters, the results were based on only 4 clusters. A better result could be obtained by using all available redshifts and the technique used in §3.2 to obtain the velocity dispersions for all the clusters in the 52 filament sample and performing the same split into high and low velocity dispersion cluster samples.

Bibliography

Abazajian K., et al., 2005, AJ, 129, 1755

Abell G., 1958, ApJS 3, 21

Abell G., 1961 AJ, 66, 607

Abell G., Corwin H., Olowin R., 1989, ApJS 70, 1 (ACO)

Albrecht A., Steinhardt P. J., Turner M. S., Wilczek F., 1982, Physical Review Letters, 48, 1437

Andernach H., Tago E., Stengler-Larrea E., 1995, Astroph. Lett & Comm. 31, 27

Ashman K. M., Bird C. M., Zepf S. E., 1994, AJ, 108, 2348

Bagchi J., Enßlin T. A., Miniati F., Stalin C. S., Singh M., Raychaudhury S., Humeshkar N. B., 2002, New Astronomy, 7, 249

Bahcall N.A., Soneira M., 1984, ApJ, 277, 27

Bahcall N. A., 1988, Annual review of astronomy and astrophysics, 26, 631

Bahcall N. A., Fan X., 1998, ApJ, 504, 1

Bahcall N. A., 2000, Particle Physics and the Universe, Proceedings of Nobel Symposium 109, Haga Slott, Enkping, Sweden, 2000, 85, 32

Baier F.W., Godlowski W., MacGillivray H.T., 2003, A&A, 403, 847

Baldwin J. A., Phillips M. M., Terlevich R., 1981, Astronomical Society of the Pacific, Publications, 93, 5

Balogh M.L., Schade D., Morris S.L., Yee H.K.C., Carlberg R.G., Ellingson E., 1998, ApJ, 504, L75

Balogh M. L., Morris S. L., Yee H. K. C., Carlberg R. G., Ellingson E., 1999, ApJ, 527, 54

Balogh M., et al., 2004, MNRAS, 348, 1355

Bardelli S., Zucca E., Zamorani G., Moscardini L., Scaramella R., 2000, MNRAS, 312, 540

Bartelmann M., 1996, A&A, 313, 697

Basilakos S., Plionis M., 2004, MNRAS, 349, 882

Benn C.R., 1997, Observational astronomy with the new radio surveys, Conf. Proc. Astrophysics and Space Science Library 226. Kluwer, Dordrecht

Bennett C. L., et al., 1997, Bulletin of the American Astronomical Society, 29, 1353

Bharadwaj S., Sahni V., Sathyaprakash B. S., Shandarin S. F., Yess C., 2000, ApJ, 528, 21

Bharadwaj S., Bhavsar S. P., Sheth J. V., 2004, ApJ, 606, 25

Bhavsar, S. P. & Splinter, R. J. 1996, MNRAS, 282, 1461

Bhavsar, S. P., & Raychaudhury, S. 2000, Bulletin of the American Astronomical Society, 32, 1433

Binney J., & Tremaine S., 1987, Galactic Dynamics (Princeton: Princeton Univ. Press)

Bogart R. S., Wagoner R. V., 1973, ApJ, 181, 609

Böhringer H., et al., 2001, A&A, 369, 826

Böhringer, H., et al. 2000, ApJS, 129, 435

Böhringer, H., et al. 2002, ApJ, 566, 93

Böhringer H., et al., 2004, A&A, 425, 367

Bond J. R., Kofman L., Pogosyan D., 1996, Nature, 380, 603

Bower R. G., Lucey J. R., Ellis R. S., 1992, MNRAS, 254, 601

Brand K., Rawlings S., Hill G. J., Lacy M., Mitchell E., Tufts J., 2003, MNRAS, 344, 283

Breen J., Raychaudhury S., Forman W., Jones C., 1994, ApJ, 424, 59

Brinchmann J., Charlot S., White S. D. M., Tremonti C., Kauffmann G., Heckman T., Brinkmann J., 2004, MNRAS, 351, 1151

Bruzual A. G., 1983, ApJ, 273, 105

Bruzual G., Charlot S., 2003, MNRAS, 344, 1000

Burles S., Nollett K. M., Turner M. S., 2001, ApJ, 552, L1

Burns J. O., Moody J. W., Brodie J. P., Batuski D. J., 1988, ApJ, 335, 542

Burstein D., Davies R. L., Dressler A., Faber S. M., Lynden-Bell D., 1986, Galaxy distances and deviations from universal expansion; Proceedings of the NATO Advanced Research Workshop, Kona, HI, Jan. 13-17, 1986 (A87-27726 11-90). Dordrecht, D. Reidel Publishing Co., 123

Bushouse H. A., 1987, ApJ, 320, 49

Butcher H., Oemler A., Jr., 1984, ApJ, 285, 426

Calzetti D., 2001, Publications of the Astronomical Society of the Pacific, 113, 1449

Caretta C.A., Maia M.A.G., Kawasaki W., Willmer C.N.A., 2002, ApJ, 123, 1200

Cen R., Ostriker J. P., 1999, ApJ, 514, 1

Chung D.J.J., Kolb E.W., Riotto A., Tkachev I.I., 2000, Physical Review D (Particles, Fields, Gravitation, and Cosmology), 62, 043508

Colberg J.M. et al., 2000, MNRAS 319, 209

Colberg J. M., Krughoff K. S., Connolly A. J., 2005, MNRAS, 359, 272

Colín P., Avila-Reese V., Valenzuela O., 2001, Astronomical Society of the Pacific Conference Series, 230, 651

Colless M., et al., 2001, MNRAS, 328, 1039

Colless M. et al.http://msowww.anu.edu.au/2dFGRS/ (astro-ph/0306581)

Couch W.J., Sharples R.M., 1987, MNRAS, 229, 423

Couch W. J., Balogh M. L., Bower R. G., Smail I., Glazebrook K., Taylor M., 2001, ApJ, 549, 820

Cruddace R., et al., 2002, ApJS, 140, 239

Danese L., de Zotti G., di Tullio G., 1980, A&A, 82, 322

Maddox S. J., Efstathiou G., Sutherland W. J., Loveday J., 1990, MNRAS, 242, 43P

Dalton G.B., Maddox S.J., Sutherland W.J., Efstathiou G., 1997, MNRAS, 289, 263

David L. P., Forman W., Jones C., 1999, ApJ, 519, 533

Davies J. I., Roberts S., Sabatini S., 2005, MNRAS, 356, 794

dell'Antonio I. P., Geller M. J., Fabricant D. G., 1994, AJ, 107, 427

De Propris R., et al., 2002, MNRAS, 329, 87

De Propris R., et al., 2004, MNRAS, 351, 125

de Vaucouleurs G., 1953, AJ, 58, 30

de Vaucouleurs G., 1956, Vistas in Astronomy, 2, 1584

Dressler A., 1980, ApJ, 236, 351

Drinkwater M. J., Parker Q. A., Proust D., Slezak E., Quintana H., 2004, Publications of the Astronomical Society of Australia, 21, 89

Durret F., Lima Neto G.B., Forman W., Churazov E., 2003, A&A, 403, L29

Ebeling H., Voges W., Bohringer H., Edge A. C., Huchra J. P., Briel U. G., 1996, MNRAS, 281, 799

Ebeling H., Edge A., Böhringer H., Allen S.W., Crawford C.S., Fabian A.C., Voges W., Huchra J.P., 1998, MNRAS, 301, 881(BCS)

Ebeling H., Barrett E., Donovan D., 2004, ApJ, 609, L49

Edge A. C., Stewart G. C., 1991, MNRAS, 252, 414

Einasto J., Einasto M., Gramann M., 1989, MNRAS, 238, 155

Einasto J., Gramann M., Saar E., Tago E., 1993, MNRAS, 260, 705

Einasto M., Einasto J., Tago E., Dalton G. B., Andernach H., 1994, MNRAS, 269, 301

Einasto M. Tago M., Jaaniste J., Einasto J., Andernach H., 1997, A&A , 123, 119

Einasto M., Einasto J., Tago E., Muller V., Andernach H., 2001, ApJ, 122, 2222

Einasto M., Jaaniste J., Einasto J., Heinämäki P., Müller V., Tucker D. L., 2003, A&A, 405, 821

Efstathiou G., Sutherland W. J., Maddox S. J., 1990, Nature, 348, 705

Davis M., Efstathiou G., Frenk C. S., White S. D. M., 1992, Nature, 356, 489

Eke V. R. et al., 2004, MNRAS, 348, 866

Ettori S., Fabian A. C., White D. A., 1997, MNRAS, 289, 787

Fabian A.C., 1991, MNRAS, 253, 29P

Feigelson E. D., Akritas M. G., Rosenberger J. L., 1995, Astronomical Data Analysis Software and Systems IV, ASP Conference Series , 77, 311

Fleenor M. C., Rose J. A., Christiansen W. A., Hunstead R. W., Johnston-Hollitt M., Drinkwater M. J., Saunders W., 2005, AJ, 130, 957

Fleenor M. C., Rose J. A., Christiansen W. A., Johnston-Hollitt M., Hunstead R. W., Drinkwater M. J., Saunders W., 2006, AJ, 131, 1280

Frisch P., Einasto J., Einasto M., Freudling W.,Fricke K.J., Gramann M., Saar V., Toomet O., 1995, A&A 296, 611

Fritz A., Ziegler B. L., 2003, Astronomische Nachrichten, Supplementary Issue 3, Short Contributions of the Annual Scientific Meeting of the Astronomische Gesellschaft in Freiburg, September 15-20, 2003 , 324, 56

Fujita Y., 1998, ApJ, 509, 587

Fujita Y., Sarazin C.L., Kempner J.C., Rudnick L., Slee O.B., Roy A.L., Andernach H., Ehle M., 2002, ApJ, 575, 764

Fujita Y., Sarazin C.L., Kempner J.C., Rudnick L., Slee O.B., Roy A.L., Andernach H., Ehle M., 2004, ApJ, 616, 157

Fujita Y., Goto T., 2004, PASJ, 56, 621

Fukuda Y., et al., 1998, Physical Review Letters, 81, 1562

Gastaldello F., Ettori S., Molendi S., Bardelli S., Venturi T., Zucca E., 2003, A&A, 411, 21

Geller M. J., Huchra J. P., 1989, Science, 246, 897

Gallagher J. S., Hunter D. A., Tutukov A. V., 1984, ApJ, 284, 544

Gavazzi G., Catinella B., Carrasco L., Boselli A., Contursi A., 1998, AJ, 115, 1745

Gaztañaga E., 2002, MNRAS, 333, L21

Gilfanov M., Grimm H.-J., Sunyaev R., 2004, MNRAS, 347, L57

Gill S. P. D., Knebe A., Gibson B. K., 2005, MNRAS, 356, 1327

Giovannini, G.; Feretti, L., 2000, New Astronomy, 5, 335

Girardi M., Giuricin G., Mardirossian F., Mezzetti M., Boschin W., 1998, ApJ, 505, 74

Gladders M. D., Lopez-Cruz O., Yee H. K. C., Kodama T., 1998, ApJ, 501, 571

Glazebrook K., Offer A. R., Deeley K., 1998, ApJ, 492, 98

Gnedin O. Y., 2003, ApJ, 582, 141

Gómez P. L., et al., 2003, ApJ, 584, 210

Goto T., et al., 2003, Astronomical Society Japan Publications, 55, 739

Gramann M., Hütsi G., 2000, MNRAS, 316, 631

Gramann M., Hütsi G., 2001, MNRAS, 327, 538

Gramann M., Suhhonenko I., MNRAS, 2002, 337, 1417

Grimm H.-J., Gilfanov M., Sunyaev R., 2003, MNRAS, 339, 793

Gunn J. E., Gott J. R. I., 1972, ApJ, 176, 1

Guzman R., Lucey J. R., Carter D., Terlevich R. J., 1992, MNRAS, 257, 187

Haines C. P., La Barbera F., Mercurio A., Merluzzi P., Busarello G., 2006, ApJ, 647, L21

Haines C. P., Merluzzi P., Mercurio A., Gargiulo A., Krusanova N., Busarello G., La Barbera F., Capaccioli M., 2006, MNRAS, 371, 55

Hambly N. C., et al., 2001, MNRAS, 326, 1279

Hauser M. G., Peebles P. J. E., 1973, ApJ, 185, 757

Hernquist L., 1990, ApJ, 356, 359

Hoessel J.G., Gunn J.E., Thuan T.X., 1980 ApJ, 241, 486

Hoffman Y., 2001, Mining the Sky: Proceedings of the MPA/ESO/MPE Workshop Held at Garching, Germany, July 31 - August 4, 2000, ESO ASTROPHYSICS SYMPOSIA. ISBN 3-540-42468-7 , 223

Hogg, D. W. 1999, ArXiv Astrophysics e-prints, arXiv:astro-ph/9905116

Hopkins A. M., et al., 2003, ApJ, 599, 971

Horner, D., 2001, Ph.D. Thesis, University of Maryland

Howard S., Byrd G. G., 1990, AJ, 99, 1798

Hudson M. J., Smith R. J., Lucey J. R., Branchini E., 2004, MNRAS, 352, 61

Jaffe W., 1983, MNRAS, 202, 995

Jarrett T. H., Chester T., Cutri R., Schneider S., Skrutskie M., Huchra J. P., 2000, AJ, 119, 2498

Jenkins A., et al., 1998, ApJ, 499, 20

Jones C., Forman W., 1999, ApJ, 511, 65

Jones D. H., et al., 2004, MNRAS, 355, 747

Jones D. H., Saunders W., Read M., Colless M., 2005, PASA, 22, 277

Kaiser N., 1984, ApJ, 284, L9

Kaiser N., 1987, MNRAS, 227, 1

Kaldare R., Colless M., Raychaudhury S., Peterson B. A., 2003, MNRAS, 339, 652

Katgert P., Mazure A., den Hartog R., Adami C., Biviano A., Perea J., 1998, A&AS, 129, 399

Kauffmann G., et al., 2003, MNRAS, 346, 1055

Kauffmann G., White S. D. M., Heckman T. M., Ménard B., Brinchmann J., Charlot S., Tremonti C., Brinkmann J., 2004, MNRAS, 353, 713

Kawasaki W., Shimasaku K.,Doi M., Okamura S., 1998, A&AS, 130, 567

Kempner J.C., Sarazin C.L., 2002, ApJ, 579, 236

Kenney J. D. P., 1994, Astronomical Society of the Pacific Conference Series, 59, 282

Kennicutt R. C., 1983, ApJ, 272, 54

Kennicutt R. C., Jr., Roettiger K. A., Keel W. C., van der Hulst J. M., Hummel E., 1987, AJ, 93, 1011

Kennicutt R. C., Jr., 1989, ApJ, 344, 685

Kennicutt R. C., Jr., 1992, ApJ, 388, 310

Kennicutt R. C., Jr., Schweizer F., Barnes J. E., Friedli D., Martinet L., Pfenniger D., 1998, Galaxies: Interactions and Induced Star Formation, Saas-Fee Advanced Course 26. Lecture Notes 1996. Swiss Societyfor Astrophysics and Astronomy, ISBN: 3-540-63569-6

Kennicutt R. C., 1998, ARA&A, 36, 189

Kewley L. J., Heisler C. A., Dopita M. A., Lumsden S., 2001, ApJS, 132, 37

King I., 1962, AJ, 67, 471

Kolatt T., Dekel A., Ganon G., Willick J.A., 1996 ApJ, 458, 419

Kolokotronis V., Basilakos S., Plionis M., 2002, MNRAS, 331, 1020

Koranyi D.M., Geller M.J., 2000, AJ, 119, 44

Kull A., Böringer H., 1999, A&A, 341, 23

Lacy M., 2000, ApJ, 536, L1

Lahav O., et al., 2002, MNRAS, 333, 961

Lake, G., & Moore, B. 1999, IAU Symp. 186: Galaxy Interactions at Low and High Redshift, 186, 393

Larson R. B., Tinsley B. M., Caldwell C. N., 1980, ApJ, 237, 692

Ledlow M.J., Voges W., Owen F.N., Burns J.O., 2003, ApJ, 126, 2740

Le Fèvre O., et al., 2004, A&A, 417, 839

Lewis I., et al., 2002, MNRAS, 334, 673

Lidsey J. E., 1994, MNRAS, 266, 489

Lin D. N. C., Pringle J. E., Rees M. J., 1988, ApJ, 328, 103

Liu C. T., Kennicutt R. C., 1995, ApJ, 450, 547

Lucey J. R., Dickens R. J., Mitchell R. J., Dawe J. A., 1983, MNRAS, 203, 545

Lumsden S.L., Nichol R.C., Collins C.A., Guzzo L., 1992, MNRAS, 258, 1

Lumsden S.L., Collins C.A., Nichol R.C., Eke V.R., Guzzo L., 1997, MNRAS, 290, 119

Madgwick D.S., et al.(the 2dFGRS Team), 2002, MNRAS, 333, 133

Madgwick D.S., Somerville R., Lahav O., Ellis R., 2003, MNRAS, 343, 871

Mahdavi A., Geller M. J., Fabricant D. G., Kurtz M. J., Postman M., McLean B., 1996, AJ, 111, 64

Menanteau F., Ford H. C., Motta V., Benítez N., Martel A. R., Blakeslee J. P., Infante L., 2006, AJ, 131, 208

Margoniner V. E., de Carvalho R. R., Gal R. R., Djorgovski S. G., 2001, ApJ, 548, L143

Mathis H., White S.D.M., 2002, MNRAS, 337, 1193

Matković, A., & Guzmán, R. 2003, Bulletin of the American Astronomical Society, 36, 590

Mazure, A., et al.1996, A&A, 310, 31

Miller N. A., Owen F. N., 2002, AJ, 124, 2453

Miller C. J., Nichol R. C., Gómez P. L., Hopkins A. M., Bernardi M., 2003, ApJ, 597, 142

Miller L., Croom S. M., Boyle B. J., Loaring N. S., Smith R. J., Shanks T., Outram P., 2004, MNRAS, 355, 385

Mohr J. J., Geller M. J., Wegner G., 1996, AJ, 112, 1816

Moore B., Katz N., Lake G., Dressler A., Oemler A., Jr., 1996, Nature, 379, 613

Moore B., Lake G., Quinn T., Stadel J., 1999, MNRAS, 304, 465

Moran S. M., Ellis R. S., Treu T., Smail I., Dressler A., Coil A. L., Smith G. P., 2005, ApJ, 634, 977

Moustakas J., Kennicutt R. C., Jr., Tremonti C. A., 2006, ApJ, 642, 775

Mulchaey, J.S., Zabludoff A.I., 1998, ApJ, 496, 73

Mulchaey, J. S., Davis, D. S., Mushotzky, R. F., & Burstein, D. 2003, ApJS, 145, 39

Navarro J. F., Frenk C. S., White S. D. M., 1995, MNRAS, 275, 720

Navarro, J.F., Frenk, C. S., & White, S. D. M. 1996, ApJ, 462, 563

Noguchi M., 1988, A&A, 203, 259

Norberg P., et al., 2001, MNRAS, 328, 64

Olson K. M., Kwan J., 1990, ApJ, 349, 480

Osmond J., Ponman T., 2004, MNRAS, 350, 1511

O'Sullivan E., Forbes D. A., Ponman T. J., 2001, MNRAS, 328, 461

Pandey B., Bharadwaj S., 2005, MNRAS, 357, 1068

Pandey B., Bharadwaj S., 2006, MNRAS, 988

Peebles P.J.E., Schramm D.N., Turner E.L., Kron R.G., 1991, Nature, 352, 769

Peacock J.A., Nicholson D., 1991, MNRAS, 253, 307

Peacock J. A., et al., 2001, Nature, 410, 169

Pedersen K., Rasmussen J., Sommer-Larsen J., Toft S., Benson A. J., Bower R. G., 2006, NewA, 11, 465

Peebles P. J. E., 1982, ApJ, 263, L1

Percival W. J., et al., 2001, MNRAS, 327, 1297

Perlmutter S., et al., 1999, ApJ, 517, 565

Petrosian V., 1976, ApJ, 209, L1

Pimbblet K. A., Drinkwater M. J., Hawkrigg M. C., 2004, MNRAS, 354, L61

Plummer H. C., 1911, MNRAS, 71, 460

Popesso P., Biviano A., Böhringer H., Romaniello M., Voges W., 2005, A&A, 433, 431

Poggianti B. M., et al., 2006, ApJ, 642, 188

Ponman T. J., Bourner P. D. J., Ebeling H., Bohringer H., 1996, MNRAS, 283, 690

Ponman T. J., Cannon D. B., Navarro J. F., 1999, Nature, 397, 135

Press W. H., Schechter P., 1974, ApJ, 187, 425

Press W. H., Teukolsky S. A., Vetterling W. T. & Flannery B. P., 1992, Numerical Recipes in Fortran 2nd ed. (Cambridge: Cambridge University Press)

Proust D., Quintana H., Mazure A., da Souza R., Escalera E., Sodre Jr, L. and Capelato H.V., 1992, A&A, 258, 243

Proust D., et al., 2006, A&A, 447, 133

Radburn-Smith D. J., Lucey J. R., Hudson M. J., 2004, MNRAS, 355, 1378

Radburn-Smith D. J., Lucey J. R., Woudt P. A., Kraan-Korteweg R. C., Watson F. G., 2006, MNRAS, 369, 1131

Ranalli P., Comastri A., Setti G., 2003, A&A, 399, 39

Rasmussen J., Ponman T. J., Mulchaey J. S., 2006, MNRAS, 370, 453

Ravindranath S., et al., 2006, Galaxy Evolution Across the Hubble Time, International Astronomical Union. Symposium, 235

Raychaudhury S., 1989, Nature, 342, 251

Raychaudhury S., 1989, PhD Thesis, University of Cambridge

Raychaudhury S., Fabian A.C., Edge A.C., Jones C., Forman W., 1991, MNRAS 248, 101

Raychaudhury S., Bhavsar S.P., Huchra J.P., 2007, to be published

Refregier A., Valtchanov I., Pierre M., 2002, A&A, 390 ,1

Reiprich, T.H., Böhringer H., 2002, ApJ, 567, 716

Rojas R. R., Vogeley M. S., Hoyle F., Brinkmann J., 2005, ApJ, 624, 571

Rose J. A., Gaba A. E., Christiansen W. A., Davis D. S., Caldwell N., Hunstead R. W., Johnston-Hollitt M., 2002, AJ, 123, 1216

Rubin V. C., Ford W. K. J., 1970, ApJ, 159, 379

Ruderman J. T., Ebeling H., 2005, ApJ, 623, L81

Ruffle P. M. E., Zijlstra A. A., Walsh J. R., Gray M. D., Gesicki K., Minniti D., Comeron F., 2004, MNRAS, 353, 796

Scaramella R., Baiesi-Pillastrini G., Chincarini G., Vettolani G., Zamorani G., 1989, Nature, 338, 562

Schwope A., Hasinger G., Lehmann I., Schwarz R., Brunner H., Neizvestny S., Ugryumov A., Balega Yu., Trmper J., Voges W., 2000, Astronomische Nachrichten, 321, 1, 1

Sekiguchi K., Wolstencroft R. D., 1993, MNRAS, 263, 349

Shandarin S. F., Sheth J. V., Sahni V., 2004, MNRAS, 353, 162

Shapley H., 1930, Ball Harvard Observatory Bulletin, 874, 9

Shapley H., 1930, Harvard College Observatory Circlular, 350, 1

Shapley H., 1933, Proc. Nat. Acad. Sci. USA 19, 591

Shapley H., 1935, Annals of the Astronomical Observatory of Harvard College, 88, 105

Shen, Mulchaey, Raychaudhury, Rasmussen, Ponman, 2007, Submitted to ApJ letters

Simon P., Schneider P., Erben T., Schirmer M., Wolf C., Meisenheimer K., 2004, Proceedings of "Baryons in Dark Matter Halos". Novigrad, Croatia, 5-9 Oct 2004. Editors: R. Dettmar, U. Klein, P. Salucci. Published by SISSA, Proceedings of Science, 97

Slee O. B., Roy A. L., Murgia M., Andernach H., Ehle M., 2001, AJ, 122, 1172

Smoot G. F., et al., 1992, ApJ, 396, L1

Spergel D. N., et al., 2003, ApJS, 148, 175

Springel V., Yoshida N., White S.D.M., 2001 New Astronomy, 6, 79

Springel V., 2005, MNRAS, 364, 1105

Storey P. J., Hummer D. G., 1995, MNRAS, 272, 41

Struble M.F., Rood, H.J., 1999, ApJS, 125, 35

Struck-Marcell C., Scalo J. M., 1987, ApJS, 64, 39

Tremonti C. A., et al., 2004, ApJ, 613, 898

Tully R. B., 1986, ApJ, 303, 25

Tully R. B., 1987, ApJ, 323, 1

Tully R. B., 1988, International Astronomical Union Symposia, 130, 243

van Dokkum P. G., Franx M., 2001, ApJ, 553, 90

van Dokkum P. G., Stanford S. A., 2003, ApJ, 585, 78

Veilleux S., Osterbrock D. E., 1987, ApJS, 63, 295

Veilleux S., Cecil G., Bland-Hawthorn J., Tully R. B., Filippenko A. V., Sargent W. L. W., 1994, ApJ, 433, 48

Viana P. T. P., Nichol R. C., Liddle A. R., 2002, ApJ, 569, L75

White S. D. M., Frenk C. S., Davis M., 1983, ApJ, 274, L1

White S. D. M., Davis M., Frenk C. S., 1984, MNRAS, 209, 27P

White M., 2006, http://astro.berkeley.edu/ mwhite/modelcmp.html

Wu X.P., Xue, Y.J., 1999, ApJ, 524, 22

Xu C., Sulentic J. W., 1991, ApJ, 374, 407

Xue Y., Wu X., 2000, ApJ, 538, 65

Zel'Dovich Y. B., 1970, A&A, 5, 84

Zeng N., White S. D. M., 1991, ApJ, 374, 1

Zucca E., Zamorani G., Scaramella R., Vettolani G., 1993, ApJ, 407, 470

Zwicky F., 1933, Helvetica Physica Acta, 6, 110

Zwicky F., Herzog E., Wild P., Karpowicz M., Kowal C.T., 1961-1968, Catalogue of Galaxies and Clusters of Galaxies (California Institute of Technology, Pasadena)

Appendix A

Optical Surface brightness fits to clusters in the Pisces-Cetus supercluster

In section 3.2.1 we fitted the Navarro Frenk White (NFW) X-ray surface brightness model to optical surface brightness profiles of clusters of galaxies in superclusters, using SuperCOSMOS data (UK Schmidt blue (Bj)). This enables us to obtain an estimate of the virial mass of each of the clusters. This appendix contains plots of the surface brightness profiles of the clusters of the Pisces-Cetus supercluster and the best fit line of the NFW model to the curves.

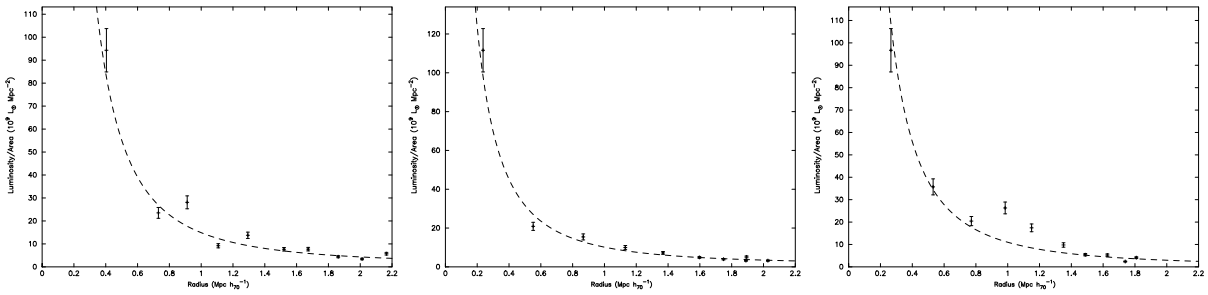

Figure A.1: Optical (B_j) radial surface brightness profiles with the best-fit projected NFW model (Eq. 3.7) superposed for A0014, A0027 and A0074. Member galaxies are binned in annuli around the cluster centre, such that each annulus contains an equal number of galaxies.

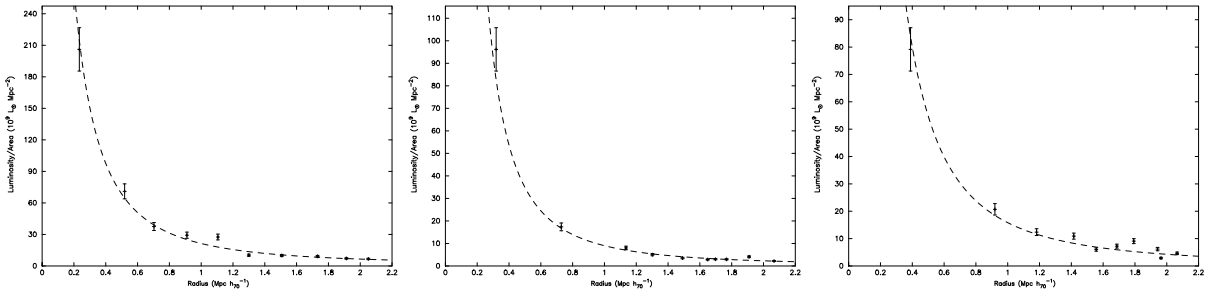

Figure A.2: Optical (B_j) radial surface brightness profiles with the best-fit projected NFW model (Eq. 3.7) superposed for A0085, A0086 and A0087. Member alaxies are binned in annuli around the cluster centre, such that each annulus contains an equal number of galaxies.

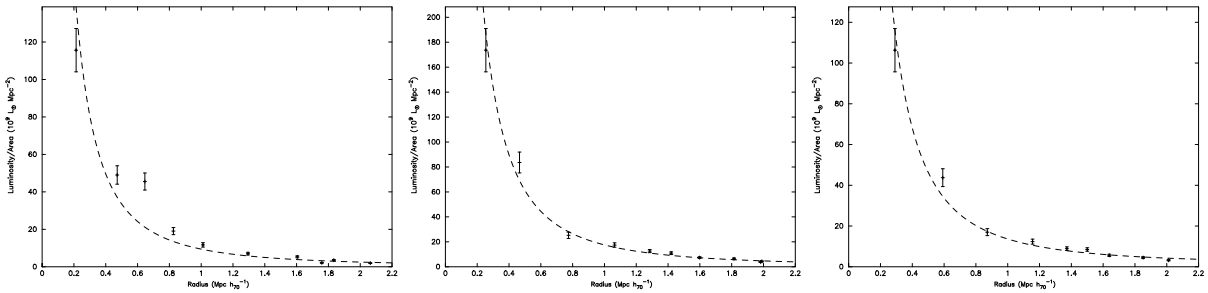

Figure A.3: Optical (B_j) radial surface brightness profiles with the best-fit projected NFW model (Eq. 3.7) superposed for A0114, A0117 and A0126. Member galaxies are binned in annuli around the cluster centre, such that each annulus contains an equal number of galaxies.

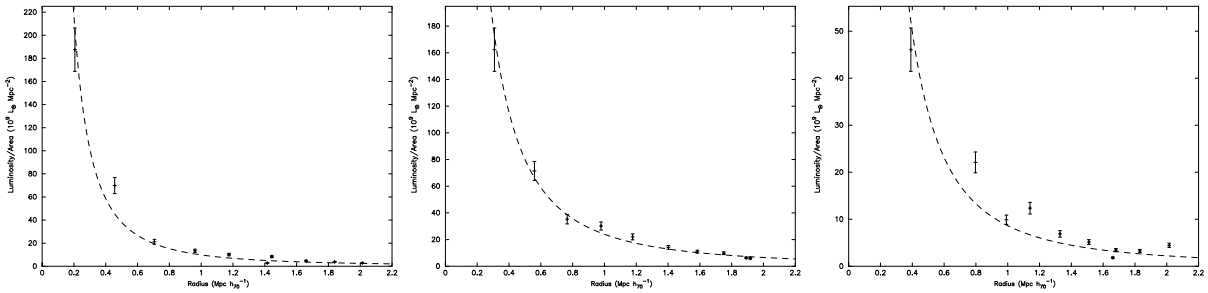

Figure A.4: Optical (B_j) radial surface brightness profiles with the best-fit projected NFW model (Eq. 3.7) superposed for A0133, A0151 and A2660. Member galaxies are binned in annuli around the cluster centre, such that each annulus contains an equal number of galaxies.

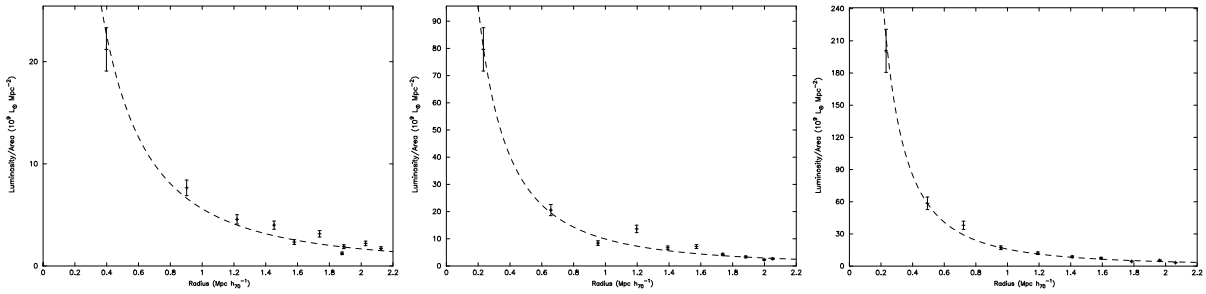

Figure A.5: Optical (B_j) radial surface brightness profiles with the best-fit projected NFW model (Eq. 3.7) superposed for A2683, A2716 and A2734. Member galaxies are binned in annuli around the cluster centre, such that each annulus contains an equal number of galaxies.

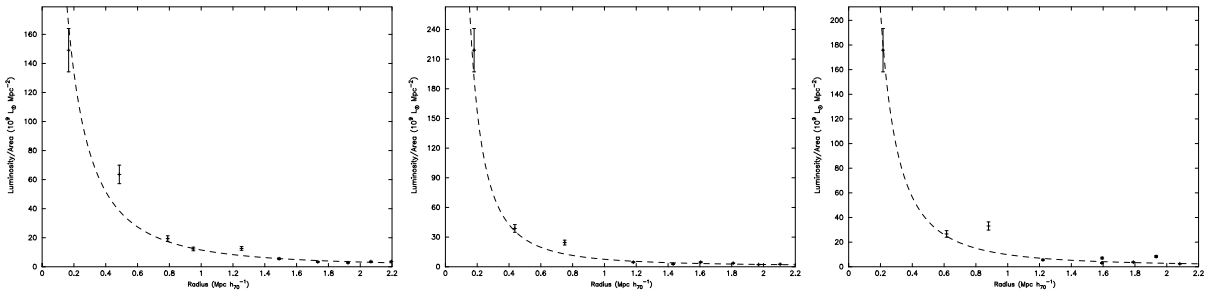

Figure A.6: Optical (B_j) radial surface brightness profiles with the best-fit projected NFW model (Eq. 3.7) superposed for A2800, A2824, and A4053. Member galaxies are binned in annuli around the cluster centre, such that each annulus contains an equal number of galaxies.

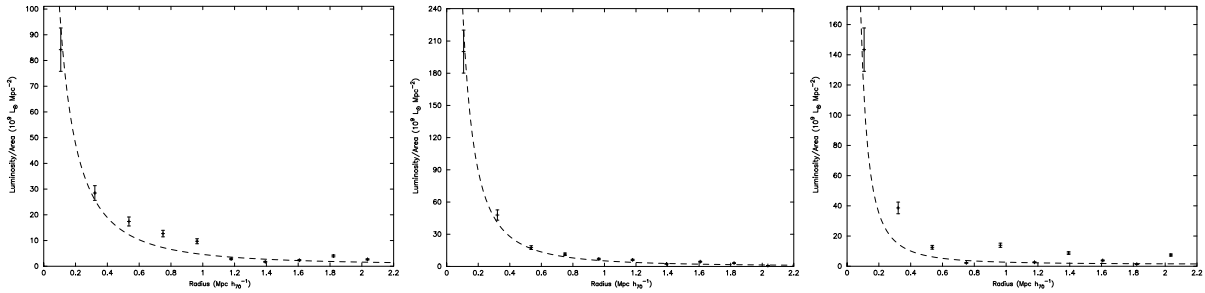

Figure A.7: Optical (B_j) radial surface brightness profiles with the best-fit projected NFW model (Eq. 3.7) superposed for A2794, S1136 and S1155. Member galaxies are binned in annuli around the cluster centre, such that each annulus has a constant radius.

Appendix B

Optical Surface brightness fits to clusters in the Horologium-Reticulum supercluster

In section 3.2.1 we fitted the Navarro Frenk White (NFW) X-ray surface brightness model to optical surface brightness profiles of clusters of galaxies in superclusters, using SuperCOSMOS data (UK Schmidt blue (Bj)). This enables us to obtain an estimate of the virial mass of each of the clusters. This appendix contains plots of the surface brightness profiles of the clusters of the Horologium-Reticulum supercluster and the best fit line of the NFW model to the curves.

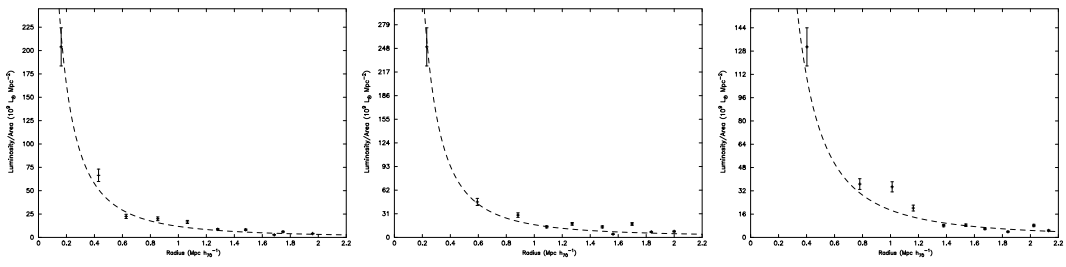

Figure B.1: Optical (B_j) radial surface brightness profiles with the best-fit projected NFW model (Eq. 3.7) superposed for A2988, A3004 and A3009. Member galaxies are binned in annuli around the cluster centre, such that each annulus has a constant number of galaxies.

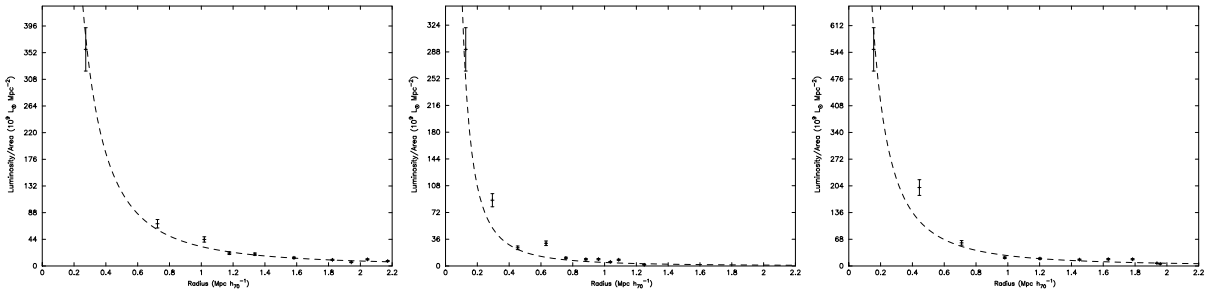

Figure B.2: Optical (B_j) radial surface brightness profiles with the best-fit projected NFW model (Eq. 3.7) superposed for A3074, A3078 and A3089. Member galaxies are binned in annuli around the cluster centre, such that each annulus has a constant number of galaxies.

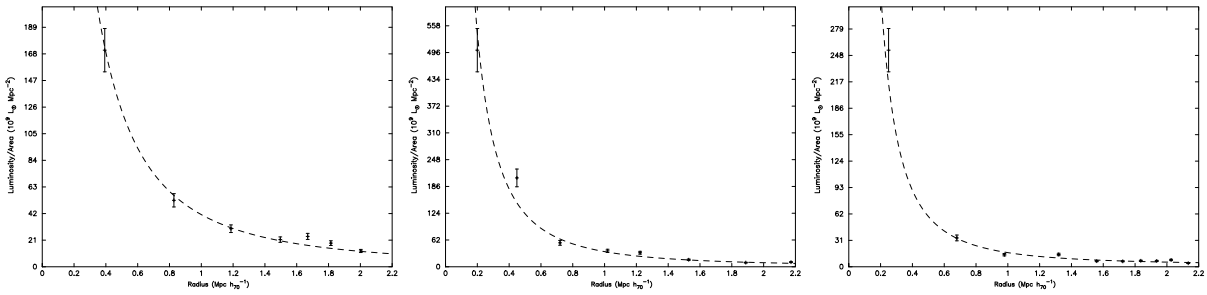

Figure B.3: Optical (B_j) radial surface brightness profiles with the best-fit projected NFW model (Eq. 3.7) superposed for A3093, A3098 and A3100. Member galaxies are binned in annuli around the cluster centre, such that each annulus has a constant number of galaxies.

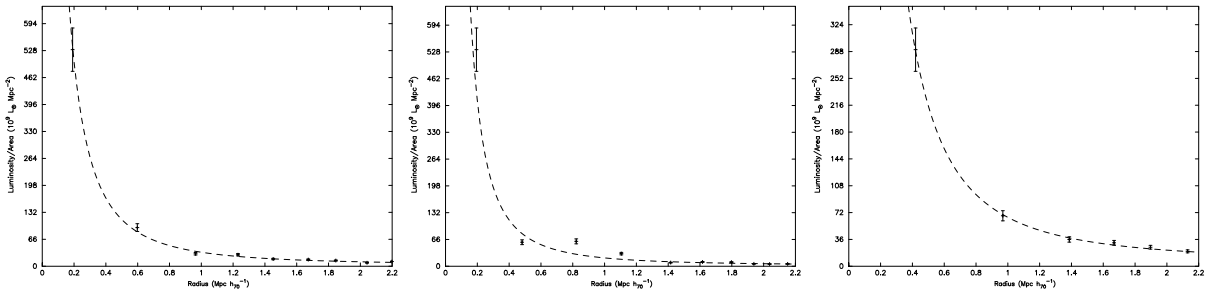

Figure B.4: Optical (B_j) radial surface brightness profiles with the best-fit projected NFW model (Eq. 3.7) superposed for A3104, A3106 and A3109. Member galaxies are binned in annuli around the cluster centre, such that each annulus has a constant number of galaxies.

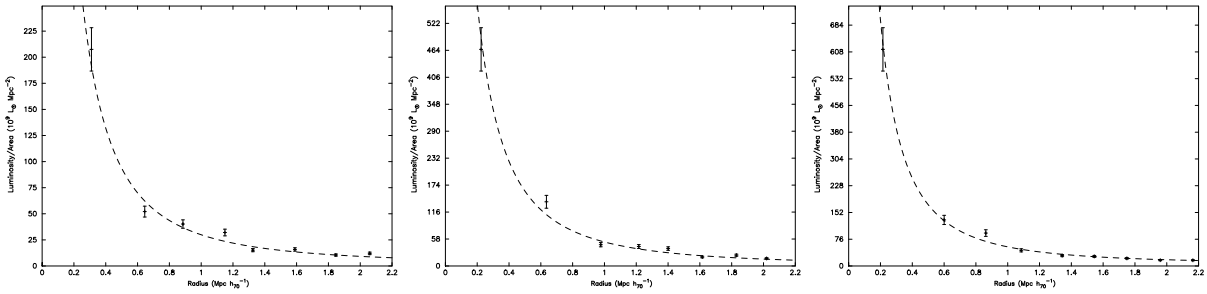

Figure B.5: Optical (B_j) radial surface brightness profiles with the best-fit projected NFW model (Eq. 3.7) superposed for A3110, A3111 and A3112. Member galaxies are binned in annuli around the cluster centre, such that each annulus has a constant number of galaxies.

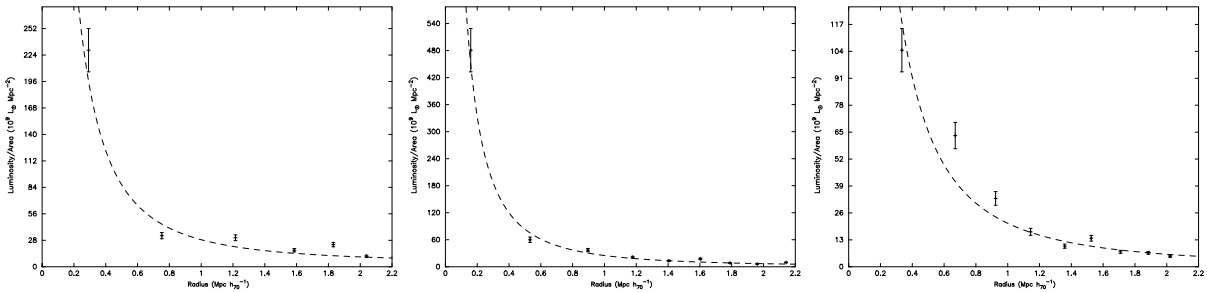

Figure B.6: Optical (B_j) radial surface brightness profiles with the best-fit projected NFW model (Eq. 3.7) superposed for A3116, A3120 and A3122. Member galaxies are binned in annuli around the cluster centre, such that each annulus has a constant number of galaxies.

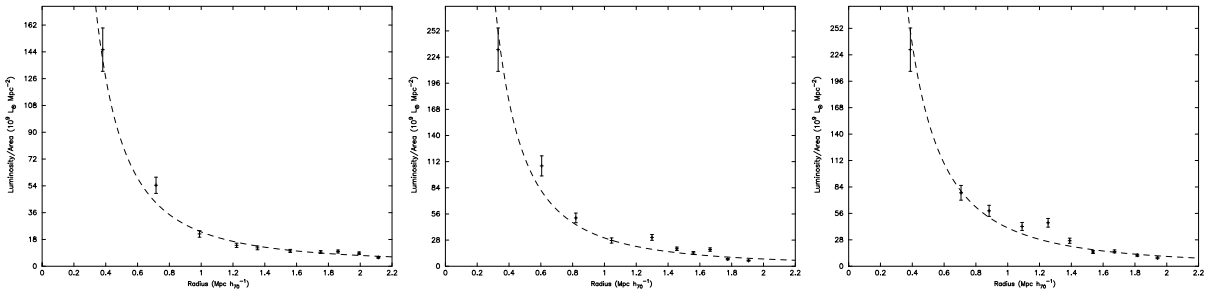

Figure B.7: Optical (B_j) radial surface brightness profiles with the best-fit projected NFW model (Eq. 3.7) superposed for A3123, A3125 and A3128. Member galaxies are binned in annuli around the cluster centre, such that each annulus has a constant number of galaxies.

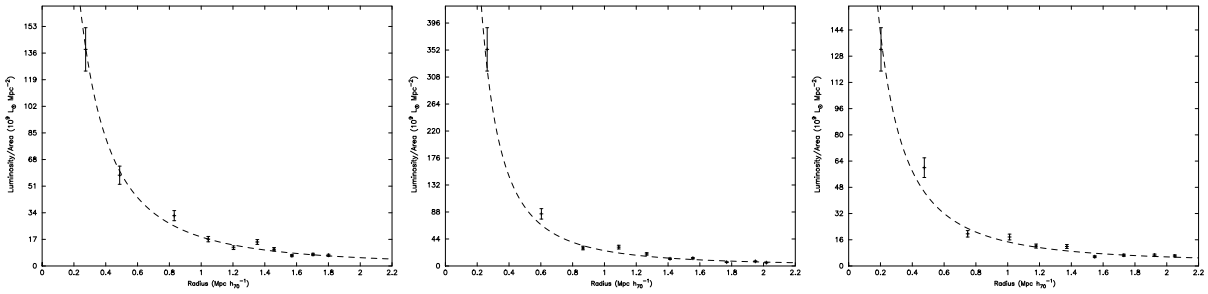

Figure B.8: Optical (B_j) radial surface brightness profiles with the best-fit projected NFW model (Eq. 3.7) superposed for A3133, A3135 and A3140. Member galaxies are binned in annuli around the cluster centre, such that each annulus has a constant number of galaxies.

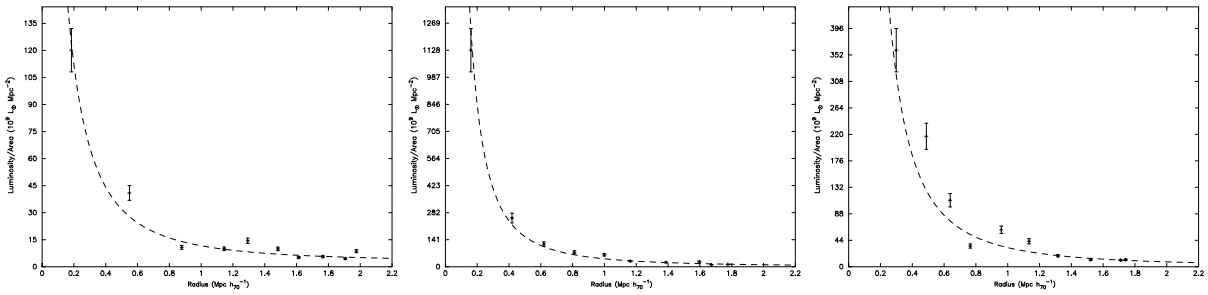

Figure B.9: Optical (B_j) radial surface brightness profiles with the best-fit projected NFW model (Eq. 3.7) superposed for A3145, A3158 and A3164. Member galaxies are binned in annuli around the cluster centre, such that each annulus has a constant number of galaxies.

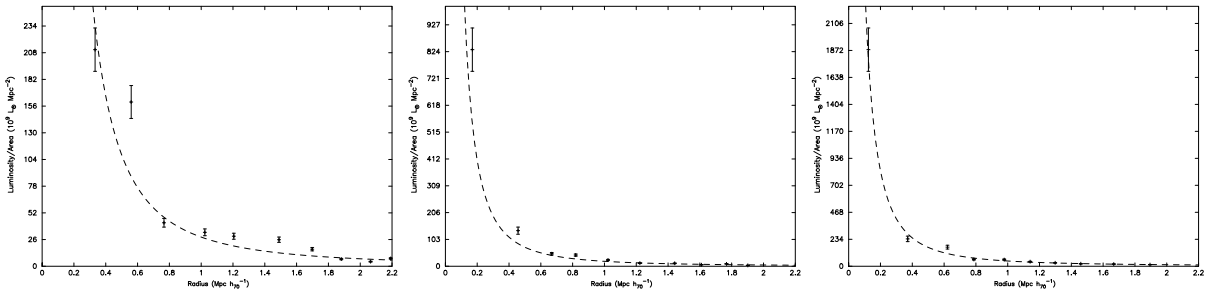

Figure B.10: Optical (B_j) radial surface brightness profiles with the best-fit projected NFW model (Eq. 3.7) superposed for A3202, A3225 and A3266. Member galaxies are binned in annuli around the cluster centre, such that each annulus has a constant number of galaxies.

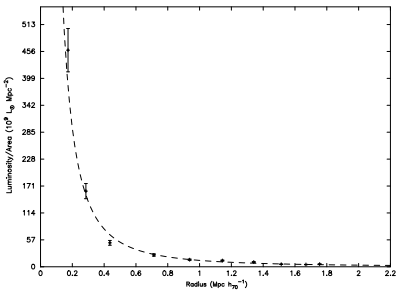

Figure B.11: Optical (B_j) radial surface brightness profiles with the best-fit projected NFW model (Eq. 3.7) superposed for A3312. Member galaxies are binned in annuli around the cluster centre, such that each annulus has a constant number of galaxies.

Appendix C

Optical Surface brightness fits to clusters in the Shapley supercluster

In section 3.2.1 we fitted the Navarro Frenk White (NFW) X-ray surface brightness model to optical surface brightness profiles of clusters of galaxies in superclusters, using SuperCOSMOS data (UK Schmidt blue (Bj)). This enables us to obtain an estimate of the virial mass of each of the clusters. This appendix contains plots of the surface brightness profiles of the clusters of the Shapley supercluster and the best fit line of the NFW model to the curves.

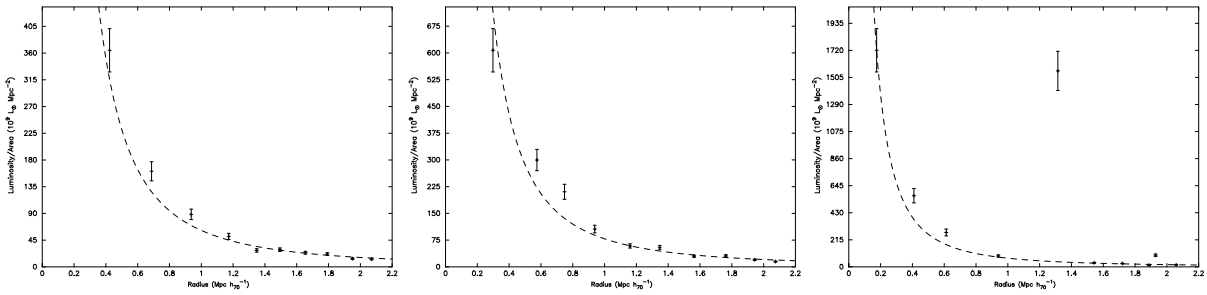

Figure C.1: Optical (B_j) radial surface brightness profiles with the best-fit projected NFW model (Eq. 3.7) superposed for A1631, A1644 and A1709. Member galaxies are binned in annuli around the cluster centre, such that each annulus has a onstant radius.

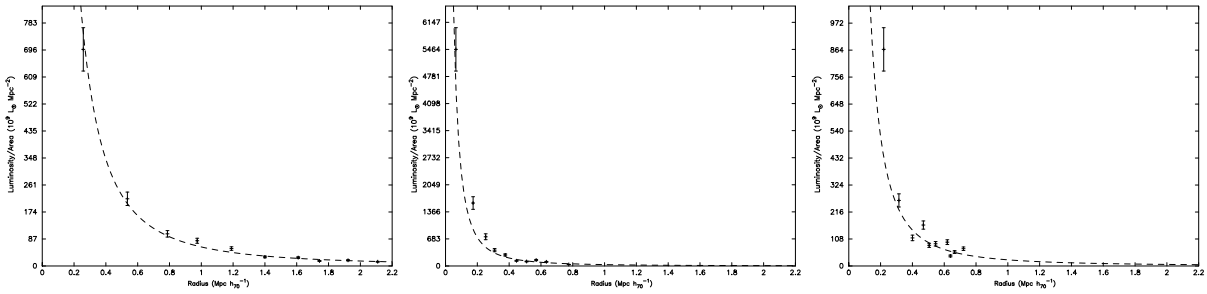

Figure C.2: Optical (B_j) radial surface brightness profiles with the best-fit projected NFW model (Eq. 3.7) superposed for A1736, A3528N and A3528S. Member galaxies are binned in annuli around the cluster centre, such that each annulus has a onstant radius.

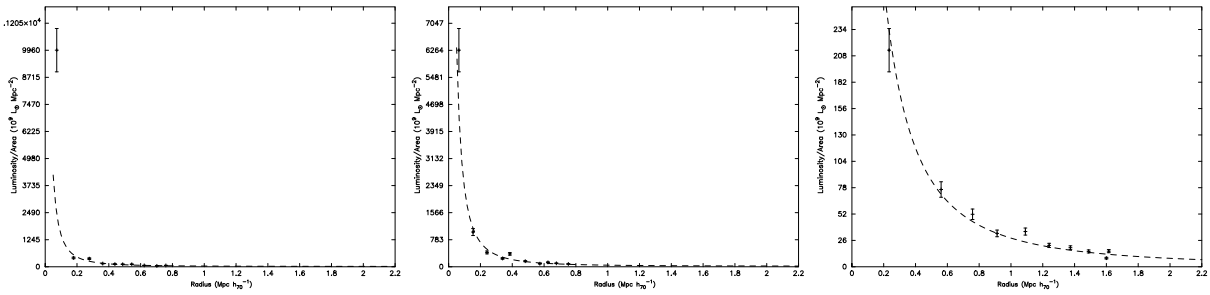

Figure C.3: Optical (B_j) radial surface brightness profiles with the best-fit projected NFW model (Eq. 3.7) superposed for A3530, A3532 and A3546. Member galaxies are binned in annuli around the cluster centre, such that each annulus has a onstant radius.

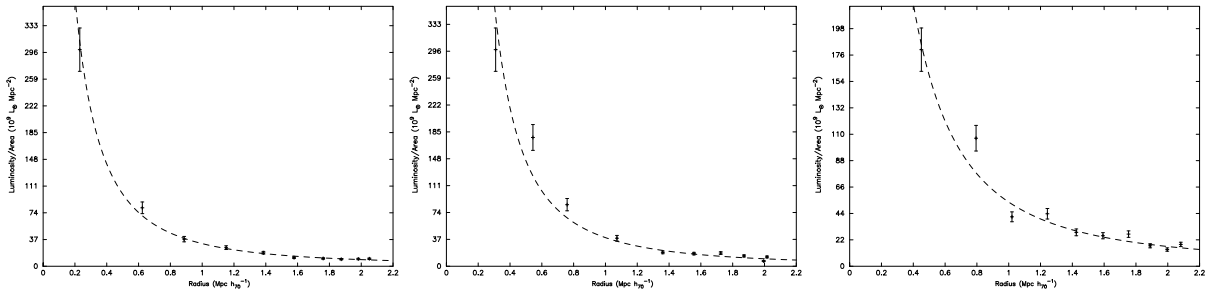

Figure C.4: Optical (B_j) radial surface brightness profiles with the best-fit projected NFW model (Eq. 3.7) superposed for A3552, A3555 and A3556. Member galaxies are binned in annuli around the cluster centre, such that each annulus has a costant number of galxies in it.

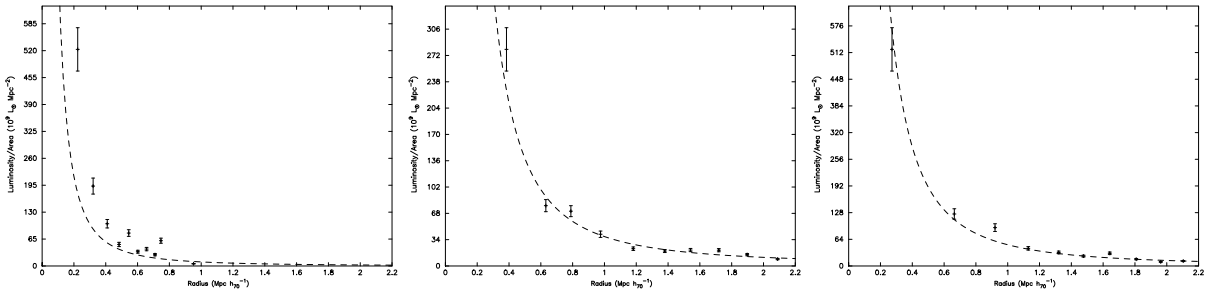

Figure C.5: Optical (B_j) radial surface brightness profiles with the best-fit projected NFW model (Eq. 3.7) superposed for A3558, A3559 and A3560. Member galaxies are binned in annuli around the cluster centre, such that each annulus has a constant number of galaxies.

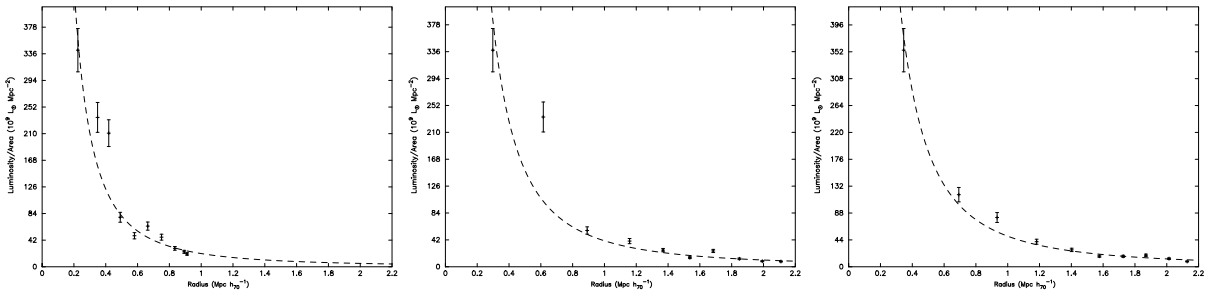

Figure C.6: Optical (B_j) radial surface brightness profiles with the best-fit projected NFW model (Eq. 3.7) superposed for A3562, A3564 and A3566. Member galaxies are binned in annuli around the cluster centre, such that each annulus has a constant number of galaxies.

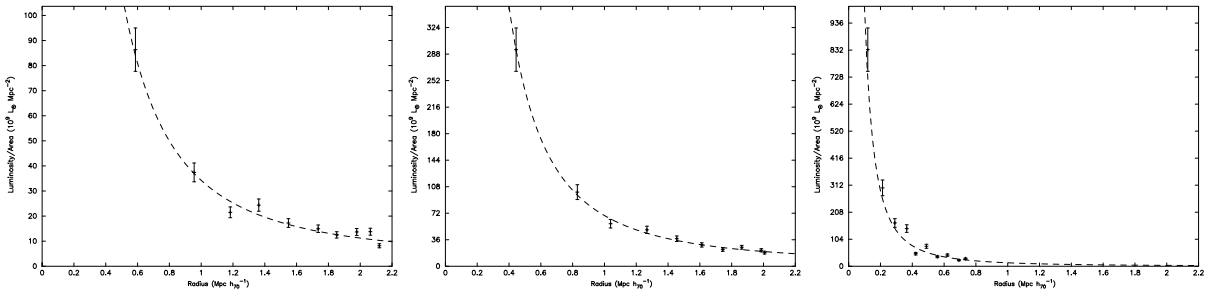

Figure C.7: Optical (B_j) radial surface brightness profiles with the best-fit projected NFW model (Eq. 3.7) superposed for A3568, A3570 and A3571. Member galaxies are binned in annuli around the cluster centre, such that each annulus has a constant number of galaxies.

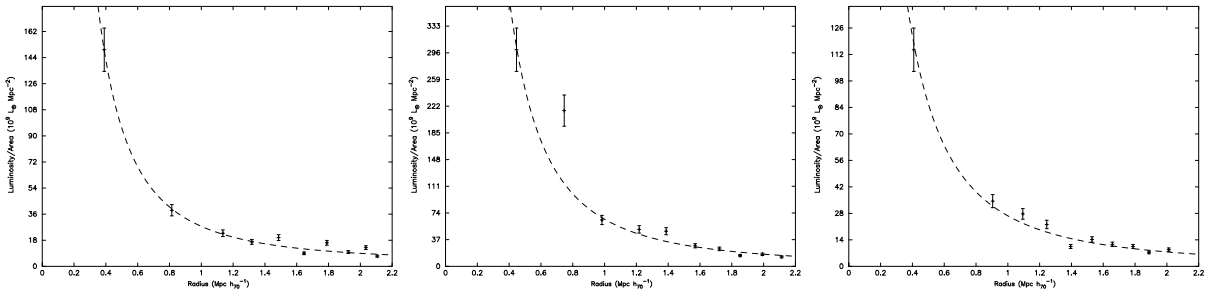

Figure C.8: Optical (B_j) radial surface brightness profiles with the best-fit projected NFW model (Eq. 3.7) superposed for A3575, A3577 and A3578. Member galaxies are binned in annuli around the cluster centre, such that each annulus has a constant number of galaxies.

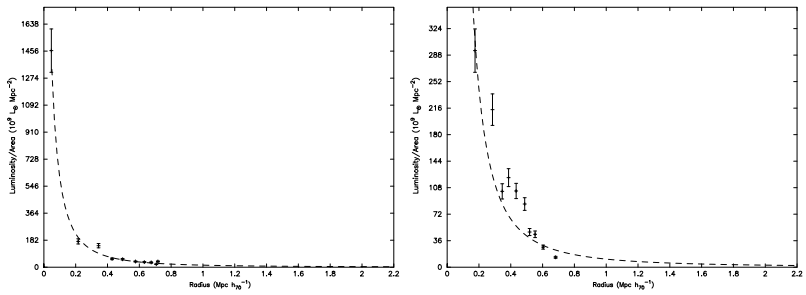

Figure C.9: Optical (B_j) radial surface brightness profiles with the best-fit projected NFW model (Eq. 3.7) superposed for SC1327 and SC1329. Member galaxies are binned in annuli around the cluster centre, such that each annulus has a constant number of galaxies.

Appendix D

X-ray analysis of the Pisces-Cetus supercluster

D.1 X-Ray observations

For the clusters that form the Pisces-Cetus supercluster (see §3.1.1), relevant X-ray observations were taken from the data archives of the respective observatories, via the High Energy Astrophysics Science Archive Research Center (HEASARC). The X-ray observations were used to confirm the presence and location of the cluster, whenever possible and determine the centre of the cluster. Where X-ray observations were available from multiple sources, ROSAT PSPC pointed observations were preferentially used. If these were not available, ROSAT All-Sky Survey data (short PSPC observations) or Einstein data were used.

D.1.1 ROSAT archival pointed observations

Where archival data were available for a cluster, reduction was performed using the Asterix software package (http://www.sr.bham.ac.uk/asterix-docs). The initial data were background subtracted, using backgrounds with point sources extracted. The background was then flattened and used to estimate vignetting and the image adaptively smoothed using asmooth. An estimate of the variance was found using smooth on the largest Gaussian used in asmooth, and then this variance array

used to form a background error map. The smoothed image was then background subtracted and divided by the background standard deviation (σ) map, to get the number of σ above the background map. This does mean that the significance of contours in the less heavily smoothed regions is actually an over-estimate of the significance. The contours were then overlaid on to an optical DSS image. Contour levels are at 5 10 20 40 ... σ above the background. The overlays for the clusters with pointed ROSAT data can be seen in Fig. D.1.

D.1.2 Rosat all-sky Survey and Einstein IPC observations

For the clusters for which pointed X-ray observations were not available in the archives, the ROSAT all-sky (RASS) data were inspected. If an inspection by eye of the image, reconstructed from the event map in the energy range of 0.1-2.4 kev, showed an extended X-ray source in the vicinity of the cluster coordinates, an X-ray contour overlay was created using the GAIA software package. The X-ray data was convolved with an elliptical Gaussian function and overlayed on a 20 arcminute DSS image of centred on the cluster centre. The contour levels were linear, and chosen to obtain a sensible contour image. The overlays for the clusters with RASS data can be seen in Fig. D.1. A similar method to the above was used for Einstein IPC data, contour overlays obtained and these can also be found in Fig. D.1.

D.1.3 The L_X–σ relation

Theory

If it is assumed that hot gas traces the gravitating mass profile and radiates most of its energy through bremsstrahlung radiation then,

$$L_x \propto f_{gas}^2 T^2, \tag{D.1.1}$$

(Ponman, Cannon, & Navarro, 1999) where f_{gas} is the gas fraction or the ratio of the gas to the total mass and T is the X-ray temperature. In the case of self similarity, the gas fraction is assumed to be constant. Thus the relation becomes,

$$L_x \propto T^2, \tag{D.1.2}$$

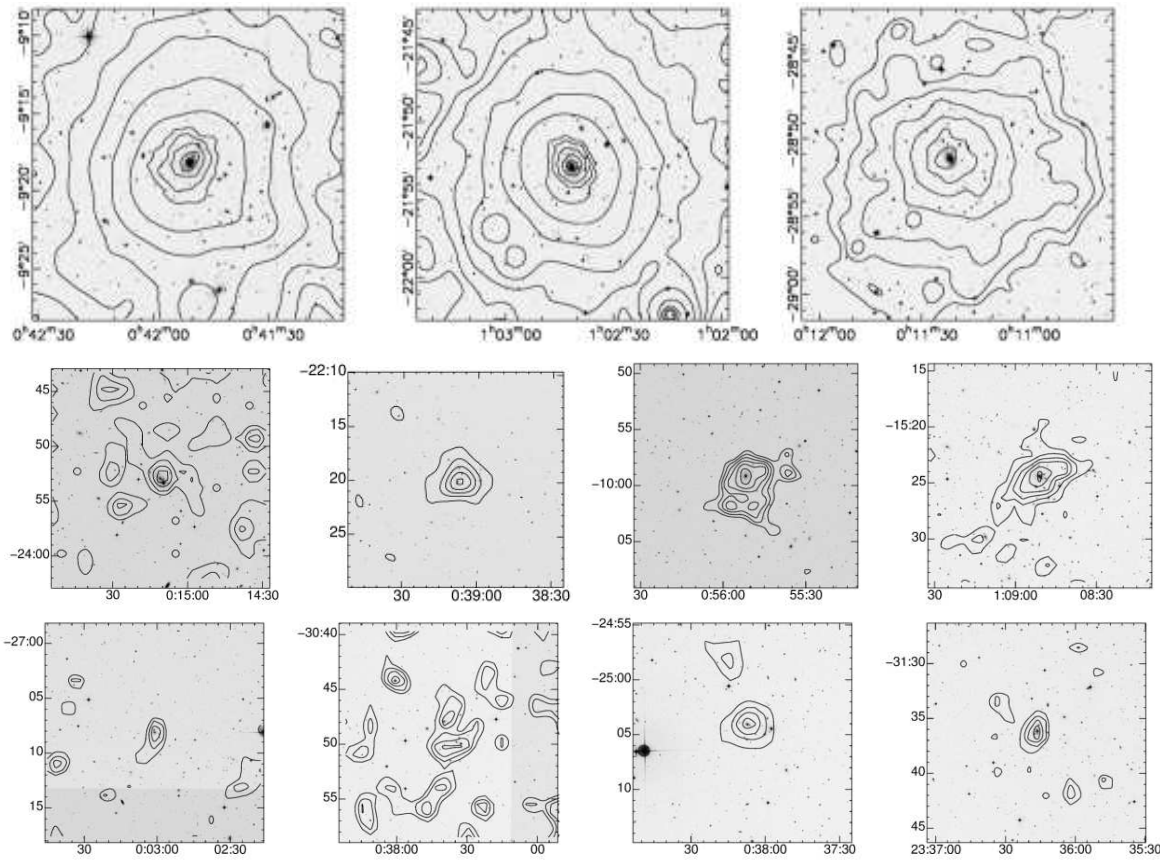

Figure D.1: (Top row) X-ray contours from pointed ROSAT PSPC observations, superposed on optical (Blue) DSS images of the clusters Abell 85, Abell 133 and Abell 2734. (Middle row) Similar images of Abell 14 (RASS), Abell 74 & Abell 117 (Einstein IPC), Abell 151 (RASS), and (Bottom row) of Abell 2716, Abell 2794, Abell 2800, and Abell S1136 (all RASS).

If the virial theorem holds it follows that

$$\sigma_{clus}^2 \propto \frac{M}{R_v}, \tag{D.1.3}$$

where σ_{clus} is the line of sight velocity dispersion, M is the mass of the cluster and R_v is the virial radius. Hence,

$$\sigma_{clus} \propto T^{0.5}, \tag{D.1.4}$$

This gives rise to,

$$L_x \propto \sigma_{clus}^4, \tag{D.1.5}$$

Therefore, we would expect a gradient of 4 to the $\log L_x$–$\log \sigma$ relation of our clusters if the above assumptions hold.

D.1.4 Pisces-Cetus supercluster results

X-ray luminosities (L_x) for the individual clusters from the literature (See Table 3.1) were converted into values of L_x in the bolometric energy range and normalised for the Hubble constant used. The conversion was performed in PIMMS using a Raymond-Smith model with a temperature estimated from the velocity dispersion-temperature relation of Osmond & Ponman (2004) and a suitable H I Column Density using the HESEARC tools (http://heasarc.gsfc.nasa.gov/cgi-bin/Tools/w3nh/w3nh.pl).

The X-ray luminosity and velocity dispersion for those of our clusters which have both values are plotted in Fig.D.2. The line of best fit for our data gives $\log L_x = 6.67 \log \sigma + 24.84$. We compare our results with those of Wu & Xue (1999), who used a sample of 156 clusters from literature and obtained the relation, $L_x = 10^{-14.57}\sigma^{5.24}$. For groups, Osmond & Ponman (2004) used ROSAT data for a sample of 60 groups and obtained the relation, $\log L_x = 3.1 \log \sigma - 2\log(h) + 34.27$. However, Mulchaey & Zabludoff (1998) found the relation $\log L_x = 4.29 \log \sigma - 2\log(h) + 31.61$ for a sample of 12 groups with ROSAT data. These three relations are plotted for comparison with our own in Fig. D.2 along with the data points of Osmond & Ponman (2004).

A Kolmogorov-Smirnov (KS) test was performed to find the significance of the differences between each of the above relations and our own. It was found that the

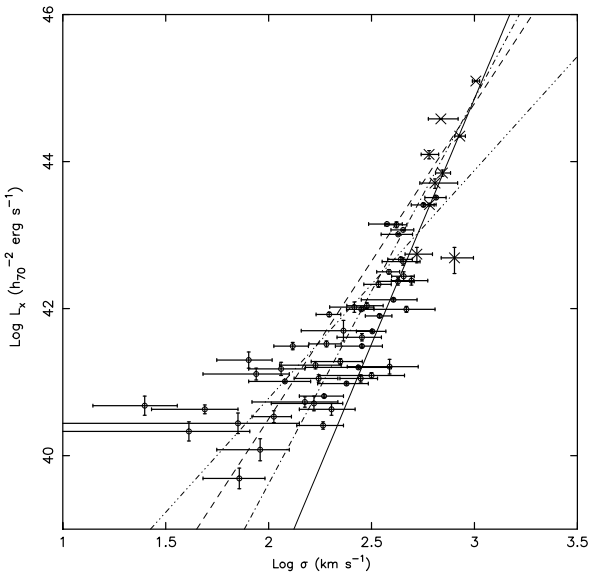

Figure D.2: The relationship between L_x and σ for clusters in the Pisces-Cetus supercluster, with available X-ray data. Cross symbols are our cluster data points while the open circle symbols are the points for (Osmond & Ponman, 2004) for groups. Solid= best fit to the data points, dot-dash=(Wu & Xue, 1999), dashed=(Mulchaey & Zabludoff, 1998), dash-dot-dot-dot=(Osmond & Ponman, 2004) All values of L_x are in the bolometric energy range

probability that the Mulchaey & Zabludoff (1998) relation was drawn from the same L_x–σ distribution as our own relation is 21.8 %. However, the relation of (Osmond & Ponman, 2004) was found to have only a 1.8 % probability of being drawn from the same L_x–σ distribution as our relation. The relatively low probability for the Osmond & Ponman (2004) relation implies a possible steepening of the $L_X - \sigma$ relation for clusters. This is in agreement with the results of Xue & Wu (2000) who also found a steepening for the cluster relation.

The relation of Wu & Xue (1999) was found to have a 54.2% probability of being drawn from the same distribution as our own relation showing a fair agreement between the two. This would suggest little difference in the L_X–σ relation of clusters inside and out of a supercluster.

Discussion

From Eq.D.1.5, we would expect a gradient of 4 to the L_x–σ relation of our clusters. However, our line of best fit is seen to have a steeper gradient of 5.33. This would be consistent with the presence of pre-heating of the Intergalactic Medium, which could

systematically reduce the luminosity of the clusters, with a greater effect on the lower mass clusters. A possible mechanism for the pre-heating would be the shocking of the intergalactic medium during the formation of the large scale filaments, present in the supercluster region, as suggested by Cen & Ostriker (1999).

Our results also show that clusters in the Pisces-Cetus supercluster have a steeper L_x–σ relation than for groups not in a supercluster. However, there is no significant difference in the relation for clusters that are in the Pisces-Cetus supercluster and clusters which are not in a superluster. The flattening of the L_x–σ relation for groups has been covered extensively in papers such as dell'Antonio, Geller, & Fabricant (1994); Ponman et al. (1996); Xue & Wu (2000). Ponman et al. (1996) find that their flattening of their L_x–σ relation for groups is not statistically significant and attribute the flattening seen in dell'Antonio, Geller, & Fabricant (1994) to the additional X-ray emission of individual galaxies, which had not been removed. As the contribution of the individual galaxies to the group emission has not been removed for all of our data points taken from the literature, this may be the reason for our flattening of the L_x–σ relation for groups.

In addition the method of conversion to bolometric luminosities, based on an uncertain temperature estimate, also reduces the validity of the comparison. Due to the lack of a measured temperature for some clusters estimates were found using the velocity dispersion-temperature relation of Osmond & Ponman (2004). Therefore, the X-ray luminosities derived from these estimates are slightly dependent on the velocity dispersion for the cluster. We therefore decided not to include this analysis in our published paper, but include it in this dissertation as evidence of substantial exploratory work undertaken in course of this investigation.

Appendix E

The 2dFGRS "clean sample" of filaments

In section 5.3.1 we describe the 52 filaments that make up the 2dFGRS "clean sample" (see Table 5.2). This appendix contains plots of the spatial distribution of the galaxies that form each of the filaments in the "clean sample" and a plot of the mean η and mean percentage of passive galaxies as a function of distance from the nearest cluster for the filament galaxies.

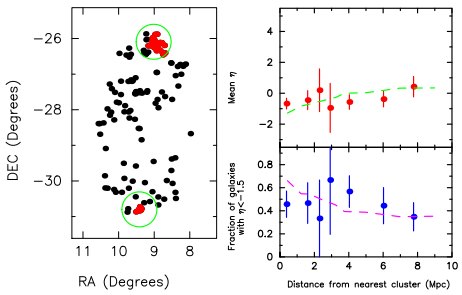

Figure E.1: Galaxy position, mean η and mean percentage of passive galaxies in the filaments joining the clusters: APMCC 0094 and EDCC 0457. Cluster galaxies as defined in §5.3.1 are shown in red.

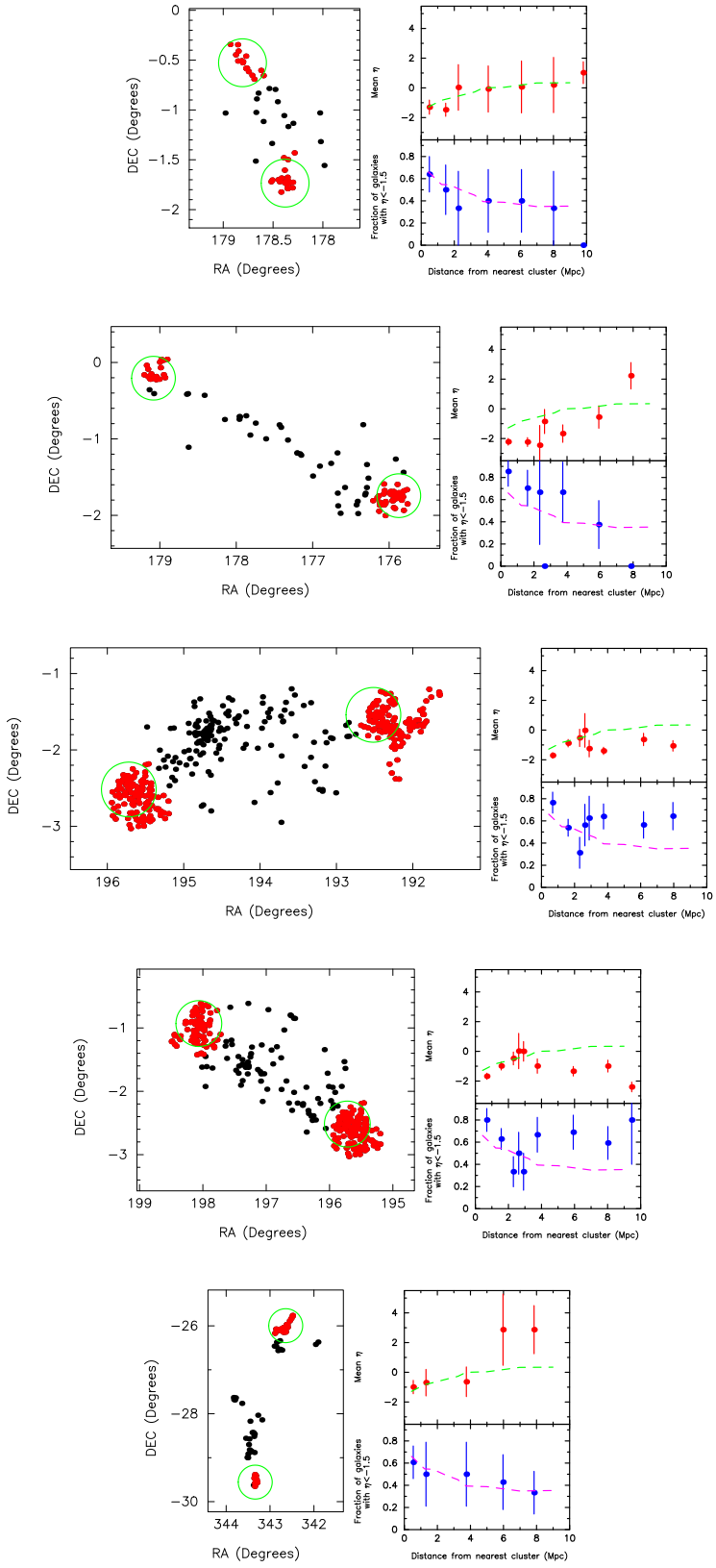

Figure E.2: Galaxy position, mean η and mean percentage of passive galaxies in the filaments joining the clusters: Abell 1411 Abell 1407, Abell 1419 Abell 1364, Abell 1620 Abell 1663, Abell 1692 Abell 1663 and Abell 2493 EDCC 0215. Cluster galaxies as defined in §5.3.1 are shown in red.

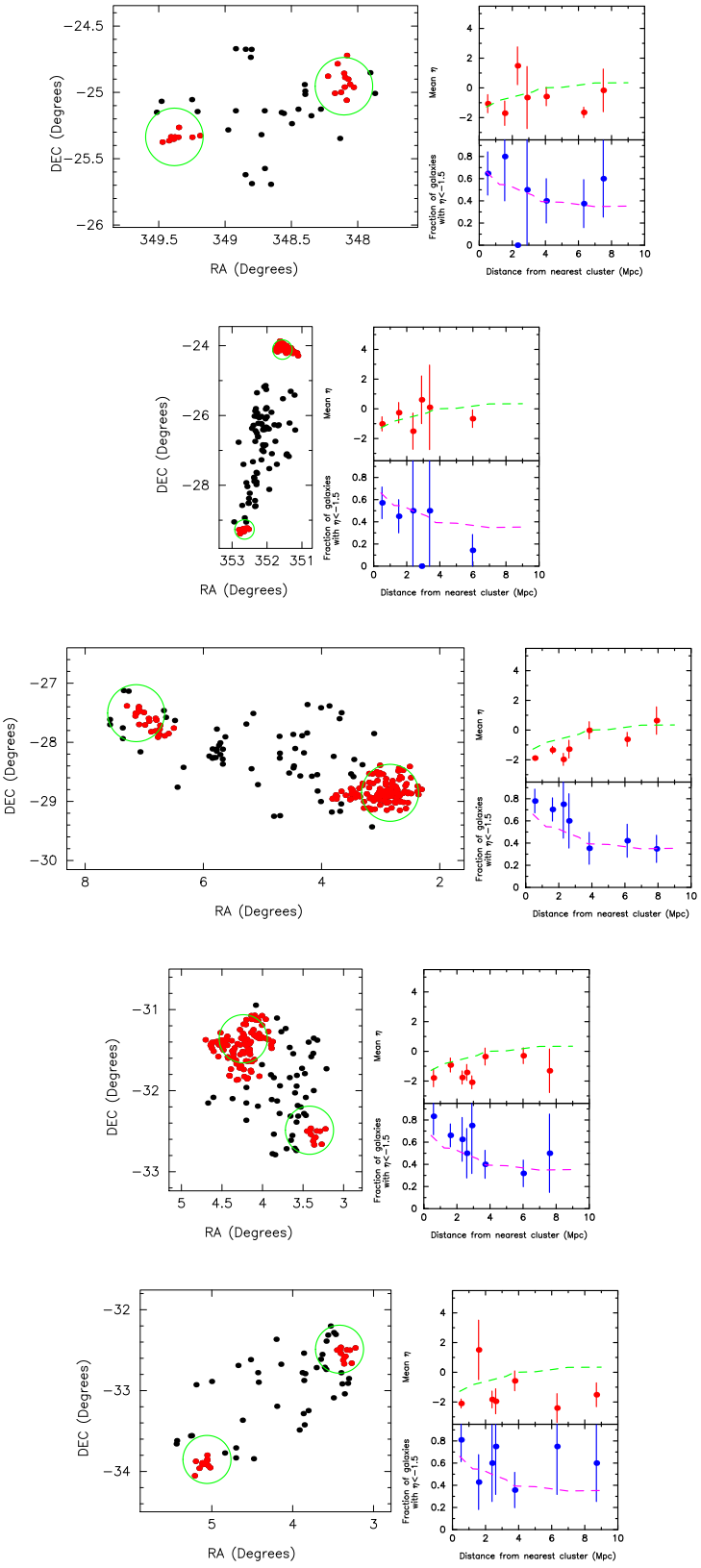

Figure E.3: Galaxy position, mean η and mean percentage of passive galaxies in the filaments joining the clusters: Abell 2553 EDCC 0275, Abell 2601 Abell 4009, Abell 2734 EDCC 0445, Abell 2741 APMCC 0039 and Abell 2741 APMCC 0051. Cluster galaxies as defined in §5.3.1 are shown in red.

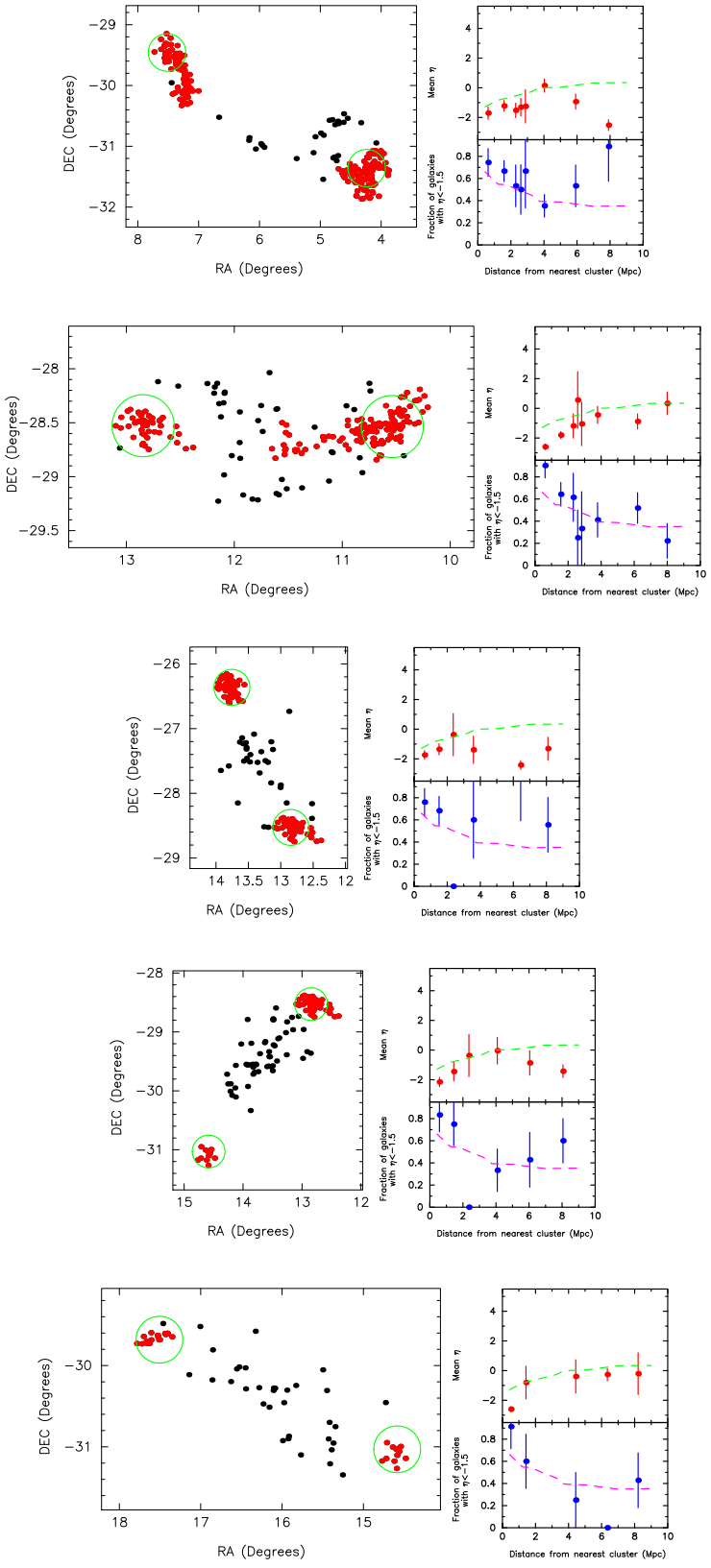

Figure E.4: Galaxy position, mean η and mean percentage of passive galaxies in the filaments joining the clusters: Abell 2780 APMCC 0039 Abell 2814 Abell 2829, Abell 2829 Abell 0118, Abell 2829 EDCC 0511 and Abell 2878 EDCC 0511. Cluster galaxies as defined in §5.3.1 are shown in red.

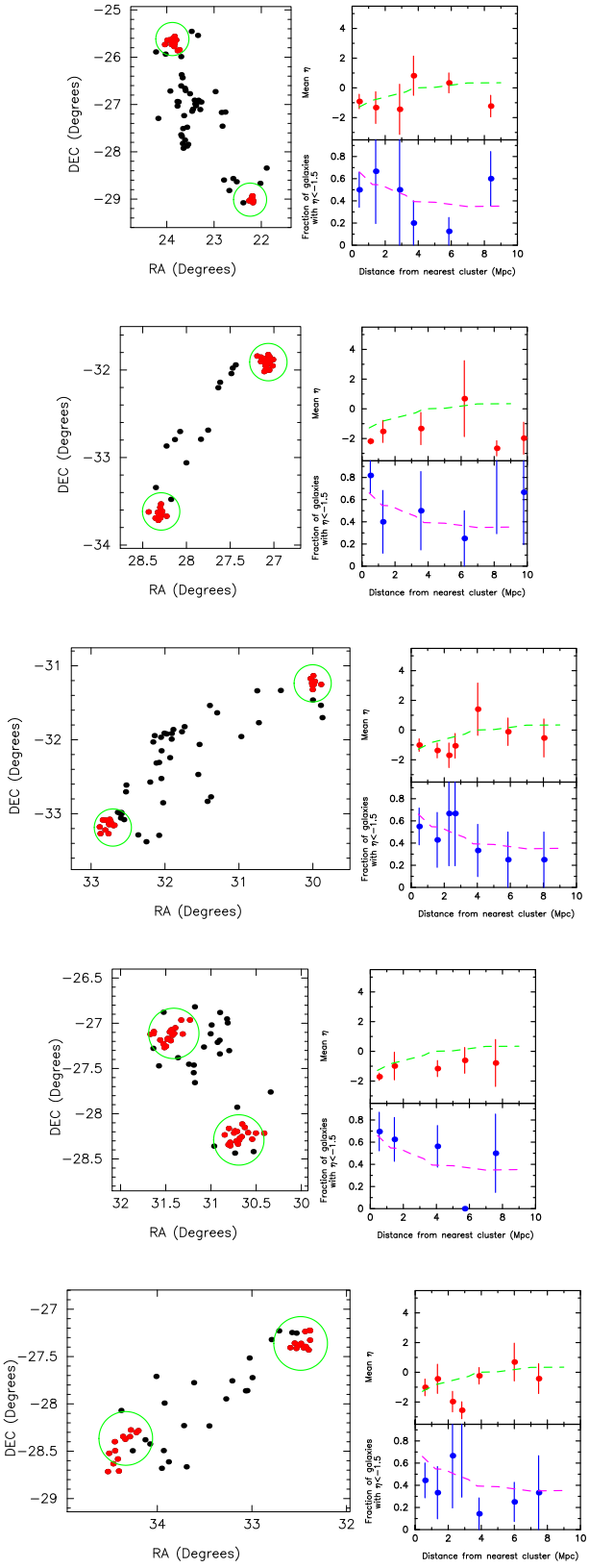

Figure E.5: Galaxy position, mean η and mean percentage of passive galaxies in the filaments joining the clusters: Abell 2915 EDCC 0581 Abell 2943 APMCC 0222, Abell 2961 APMCC 0245, Abell 2967 Abell 2972 and Abell 2981 Abell 2999. Cluster galaxies as defined in §5.3.1 are shown in red.

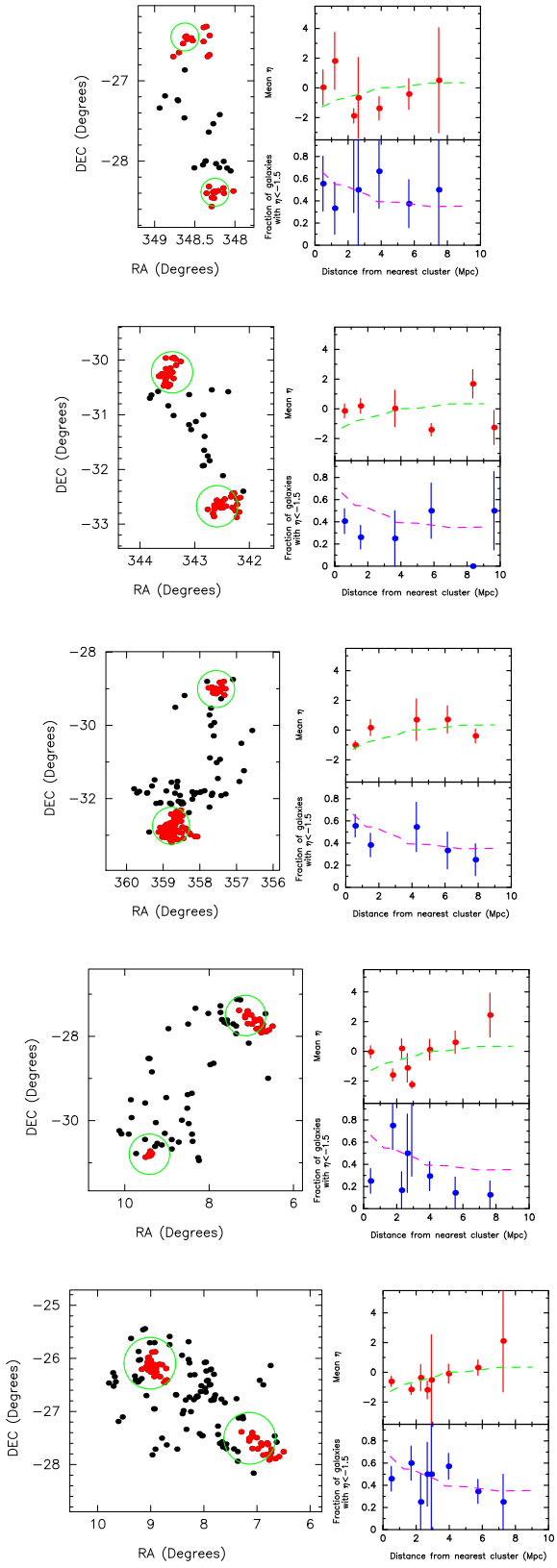

Figure E.6: Galaxy position, mean η and mean percentage of passive galaxies in the filaments joining the clusters: Abell 3980 EDCC 0268, EDCC 0217 EDCC 0202, EDCC 0365 Abell S1155, EDCC 0445 APMCC 0094 and EDCC 0457 EDCC 0445. Cluster galaxies as defined in §5.3.1 are shown in red.

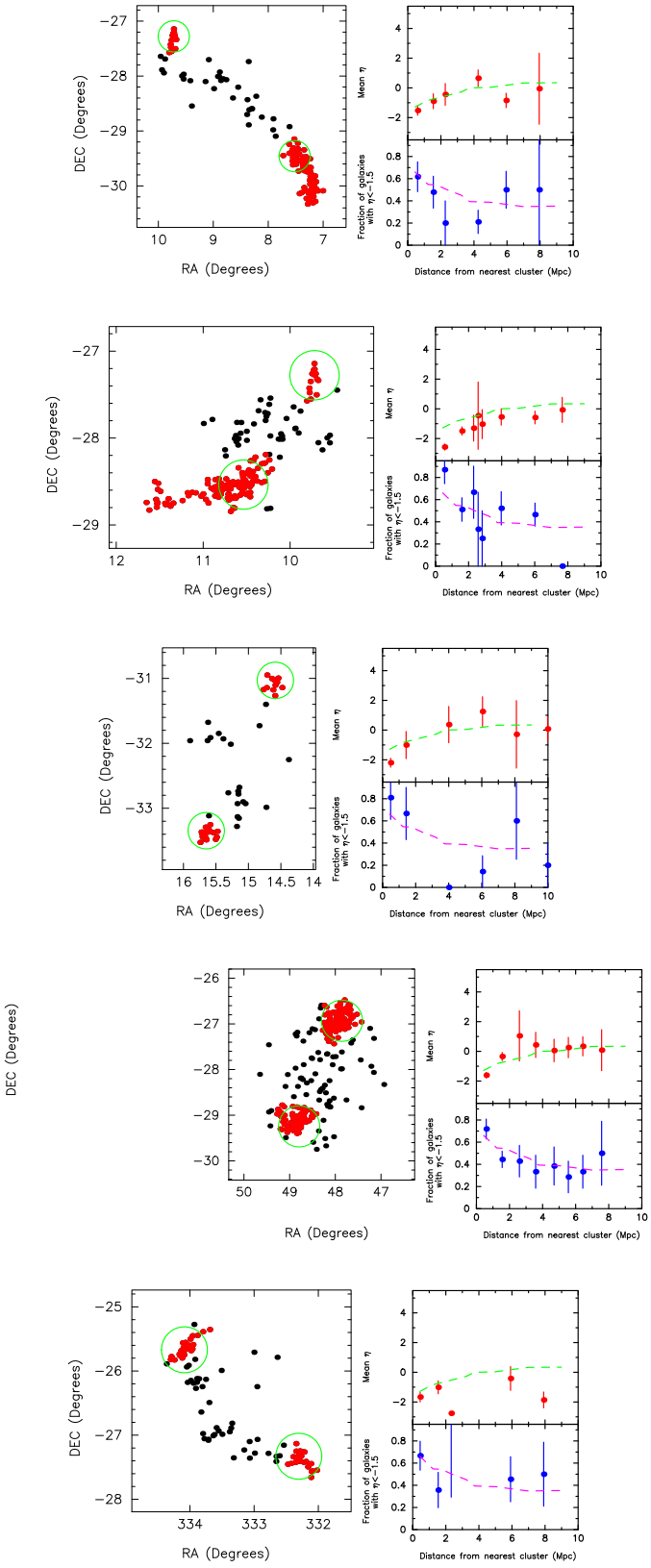

Figure E.7: Galaxy position, mean η and mean percentage of passive galaxies in the filaments joining the clusters: EDCC 0465 Abell 2780, EDCC 0465 Abell 2814, EDCC 0517 EDCC 0511, Abell S0333 Abell 3094 and EDCC 0119 Abell 3837. Cluster galaxies as defined in §5.3.1 are shown in red.

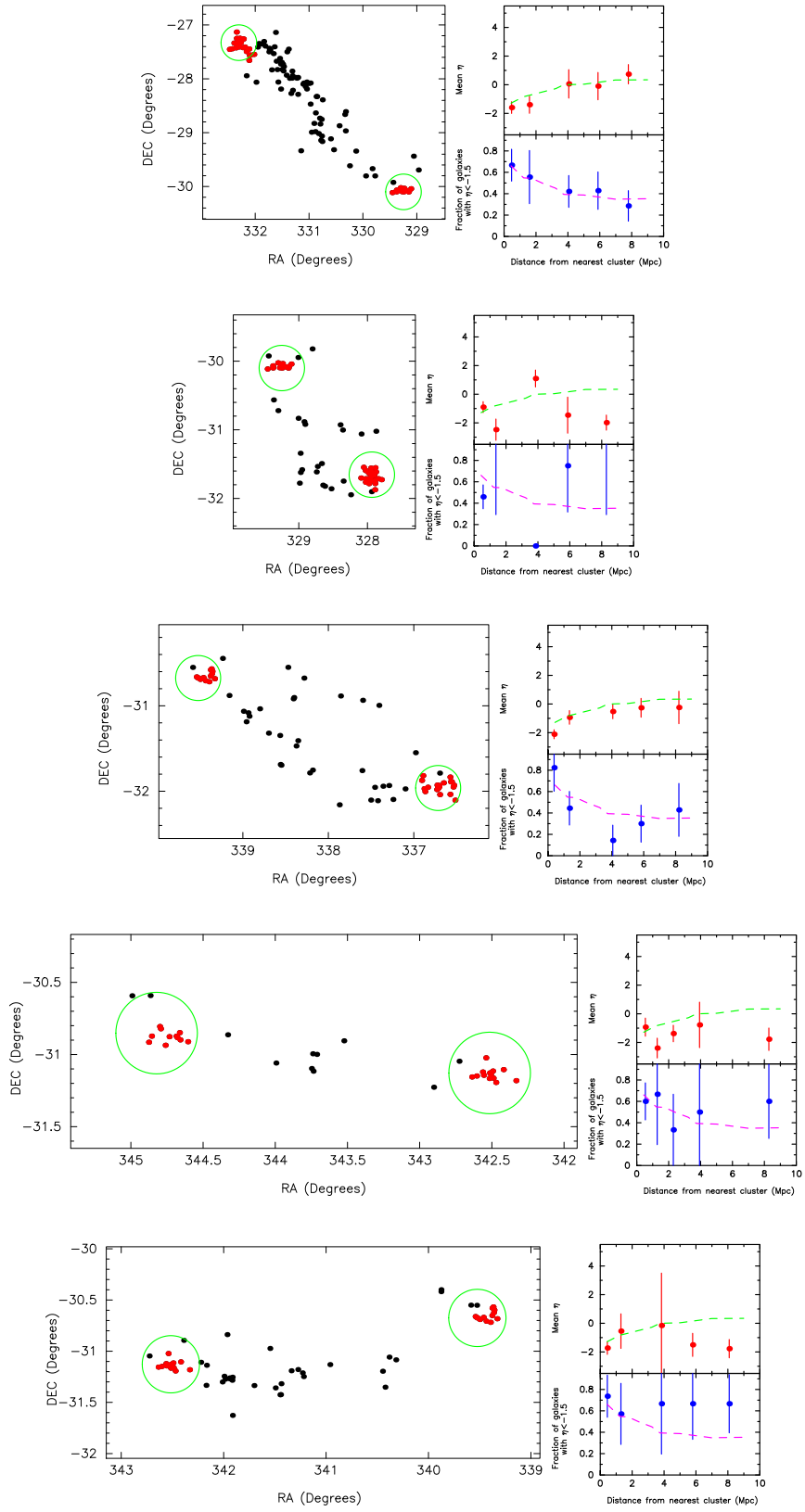

Figure E.8: Galaxy position, mean η and mean percentage of passive galaxies in the filaments joining the clusters: EDCC 0057 Abell 3837, EDCC 0057 APMCC 0721, Abell 3878 Abell 3892, EDCC 0230 APMCC 0827 and APMCC 0827 Abell 3892. Cluster galaxies as defined in §5.3.1 are shown in red.

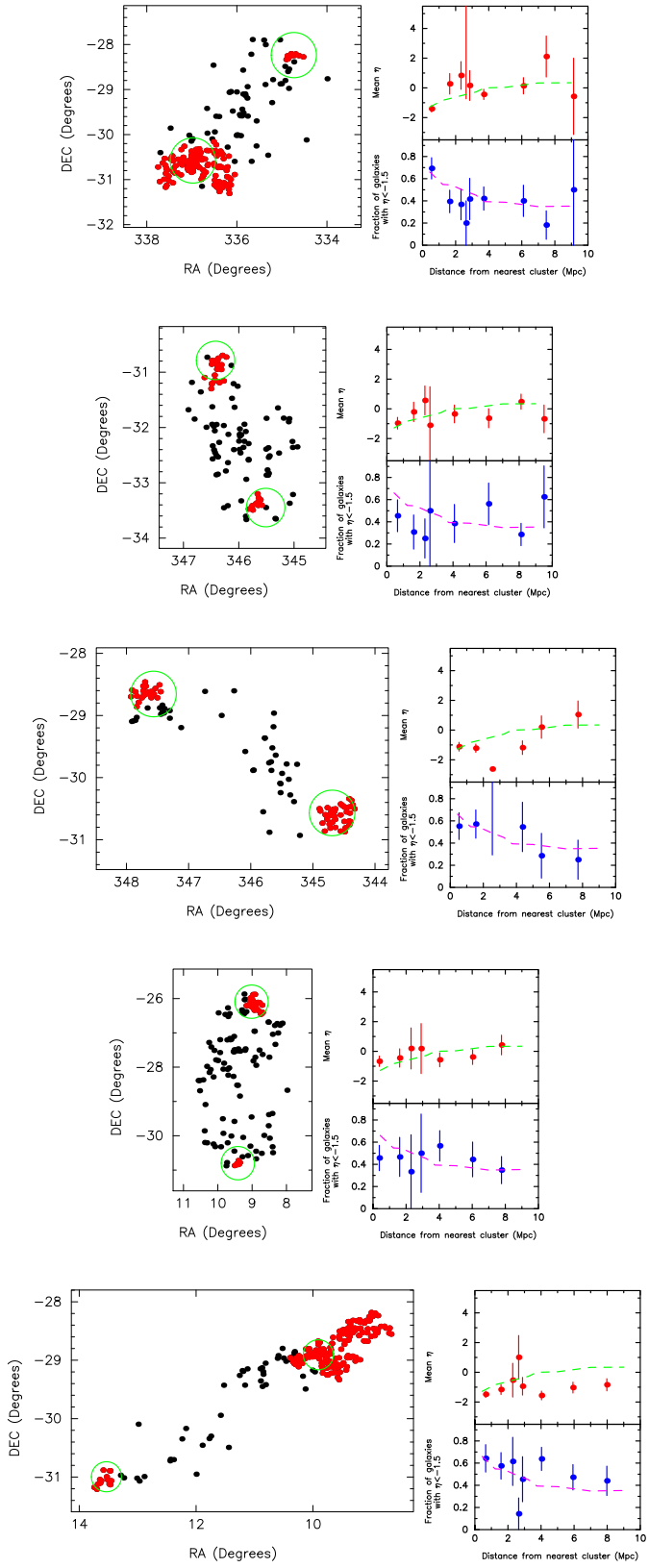

Figure E.9: Galaxy position, mean η and mean percentage of passive galaxies in the filaments joining the clusters: EDCC 0128 Abell 3880, Abell 3959 APMCC 0853, Abell S1075 APMCC 0167, EDCC 0457 Abell 2794, EDCC 0492 Abell 2804. Cluster galaxies as defined in §5.3.1 are shown in red.

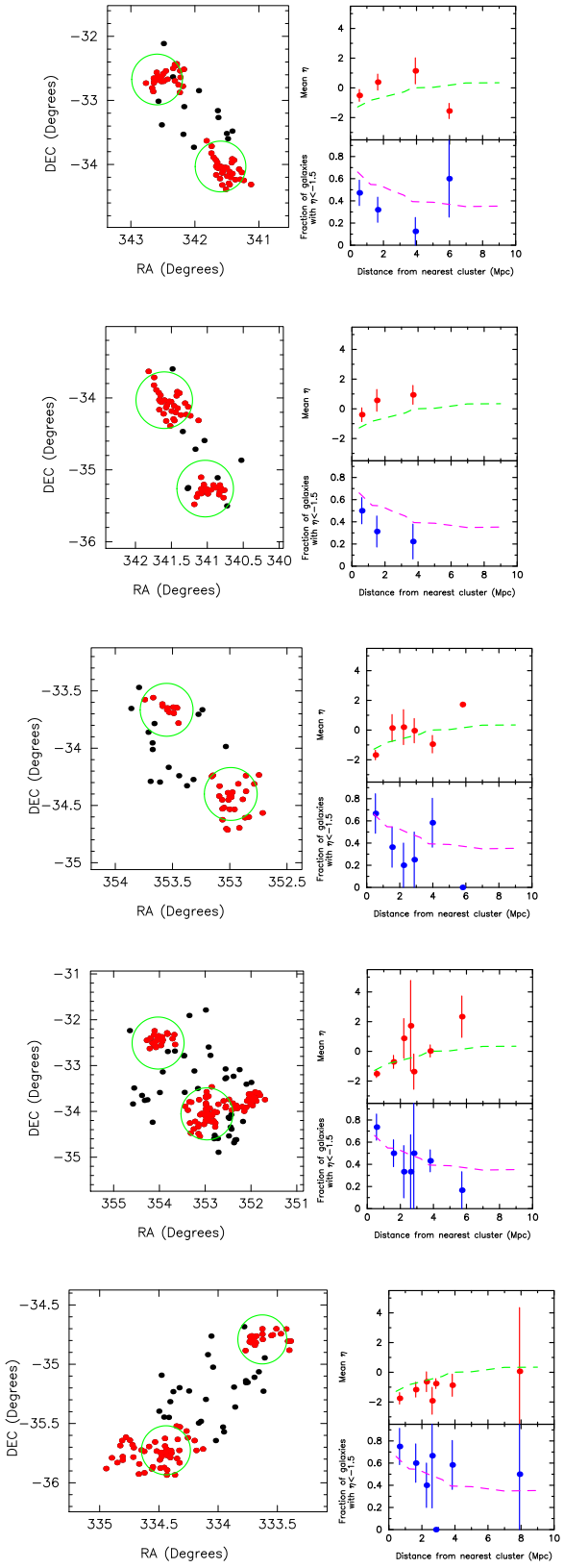

Figure E.10: Galaxy position, mean η and mean percentage of passive galaxies in the filaments joining the clusters: EDCC 0202 EDCCC 0187, EDCC 0187 APMCC 0810, EDCC 0317 APMCC 4011, EDCC 0323 APMCC 4012 and Abell 3854 Abell 3844. Cluster galaxies as defined in §5.3.1 are shown in red.

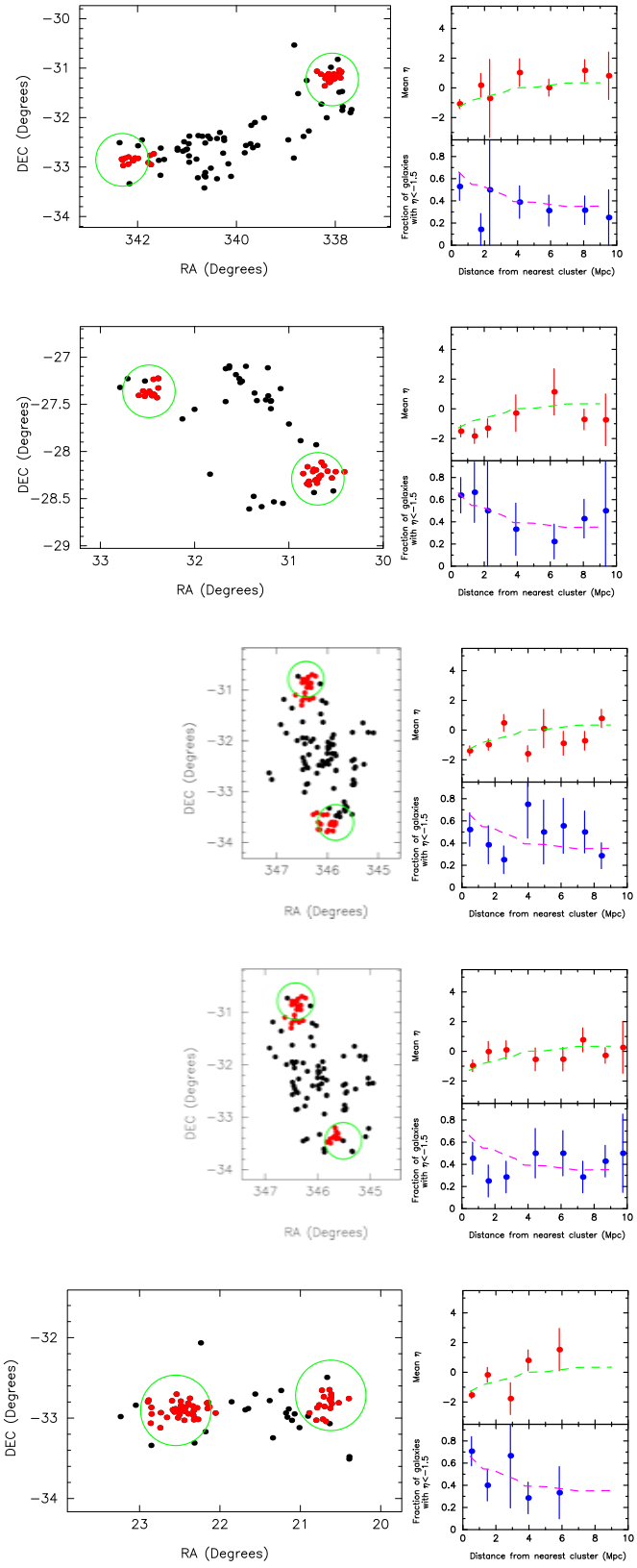

Figure E.11: Galaxy position, mean η and mean percentage of passive galaxies in the filaments joining the clusters: Abell S1064 EDCCC 0153, Abell 2967 EDCCC 2981, EDCC 0239 APMCC 0853, EDCC 0248 Abell 3959 and APMCC 0167 Abell S0160. Cluster galaxies as defined in §5.3.1 are shown in red.

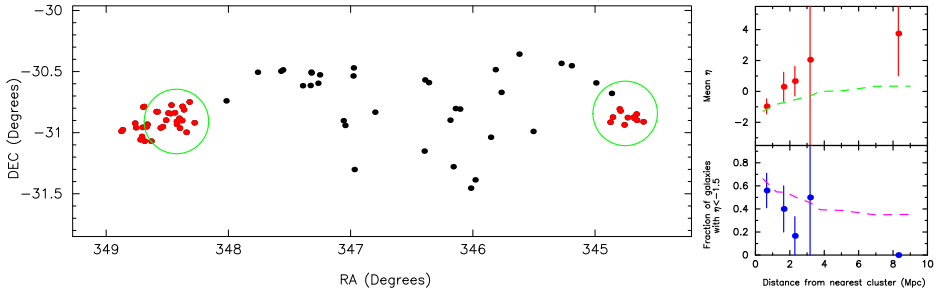

Figure E.12: Galaxy position, mean η and mean percentage of passive galaxies in the filaments joining the clusters: APMCC 0869 and APMCC 0840. Cluster galaxies as defined in §5.3.1 are shown in red.